37th NOAA Climate Diagnostics and Prediction Workshop
Special Issue

Climate Prediction S&T Digest

January 2013

NWS Science & Technology Infusion Climate Bulletin Supplement

Inside this issue:

NOAA's National Weather Service

Office of Science and Technology
1325 East West Highway
Silver Spring, MD 20910

Climate Prediction Center
5830 University Research Court
College Park, MD 20740

Although the skill of current operational climate prediction is limited and the research on the topic presents many challenges, there are promises of improvement on the horizon. To accelerate advancement in climate services, an effective mechanism of S&T infusion from research to operation for application is much needed. This bulletin has been established to clarify science-related problems and relevant issues identified in operation, helping our partners in the research community to understand which R&D activities are needed to "shoot arrows at the target".

Science and Technology Infusion Climate Bulletin
http://www.nws.noaa.gov/ost/climate/STIP/index.htm

National Weather Service
National Oceanic and Atmospheric Administration
U.S. Department of Commerce

PREFACE

It is with great pleasure that the Climate Prediction Center and the Office of Science and Technology offer you this synthesis of the 37th Climate Diagnostics and Prediction Workshop. The CDPW brought together over 100 participants to share their research results and perspectives on a broad range of climate prediction and monitoring topics. As in previous years, the CDPW included plenary sessions and poster sessions, but this year also featured coordinated activities with a "Drought Task Force" organized by the NOAA Climate Program Office and focused on challenges in drought monitoring and prediction. Thus, the CDPW continues to be an important and timely way for the climate prediction community to stay connected.

As is clearly evident in this digest, the climate community continues to make major strides in the foundational research necessary to improve understanding and to advance climate prediction and monitoring capabilities. The purpose of this digest is to help keep you informed of these advances and to ensure that they are shared with the broader climate community and transitioned into operations. This is especially important as NOAA works to enhance climate services across the agency and with external partners. We hope you find this digest to be useful and stimulating. And please drop me a note if you have suggestions to improve the digest.

Finally, I would like to thank Dr. Jiayu Zhou of the Office of Science and Technology / NWS, for developing the digest concept and for sustaining it year after year. This partnership between OST and CPC is an essential element of NOAA climate services.

Wayne Higgins

Director, Climate Prediction Center
National Centers for Environmental Prediction
NOAA's National Weather Service

CONTENTS

OVERVIEW

NOAA's 37th Climate Diagnostics and Prediction Workshop was held in Fort Collins, Colorado, on 22-25 October 2012. It was hosted by the Colorado State University (CSU) and the Cooperative Institute for Research in the Atmosphere (CIRA); and co-sponsored by the Climate Prediction Center (CPC) of the National Centers for Environmental Prediction and the National Climatic Data Center (NCDC). The American Meteorological Society was a cooperating sponsor.

The workshop addressed the status and prospects for advancing climate prediction, monitoring, and diagnostics, with emphasis on five major themes:

1. Improving climate prediction tools and techniques through dynamical and statistical models and methods, forecaster practices and protocols, data and model improvements, and scientific concepts.
2. Prospects for improved understanding, prediction, and simulation of intra-seasonal, seasonal, and inter-annual climate variability, including the extratropical annular modes, stratosphere/troposphere coupling, tropical-extratropical interactions, land-surface forcing, etc.
3. Climate variability and prediction in relation to the hydrologic cycle and in particular Western water resources.
4. Prediction and attribution of recent high impact weather and climate events.
5. Improving climate services through the application of new technologies, including GIS, statistical tools, and software development practices.

This Digest is a collection of extended summaries of the presentations contributed by participants. The workshop is continuing to grow and expect to provide a stimulus for further improvements in climate monitoring, diagnostics, prediction, applications and services.

1. ANNUAL REVIEW OF WEATHER & CLIMATE

AND CLIMATE OPERATION

Science and Technology Infusion Climate Bulletin
NOAA's National Weather Service
37th NOAA Annual Climate Diagnostics and Prediction Workshop
Fort Collins, CO, 22-25 October 2012

US Climate Review of 2012: The Hot and Dry

Melissa Ou

Climate Prediction Center, NCEP/NWS/NOAA, MD

1. Introduction

The climate across the Contiguous U.S. (CONUS) was dominated by above normal temperatures during 2012, even record setting temperatures in many locations. Northern areas of the CONUS experienced anomalously low snow cover this winter and widespread hot and dry conditions across the CONUS during the summer. This report discusses some of these major climatic events, their impacts, and some attribution studies up to the end of October 2012.

2. Discussion

a. A warm winter and spring

The majority of 2012 was above normal for most of the CONUS, until the end of summer (August and September) when anomalous warm focused in the western half of the CONUS. January through August was the warmest first eight months of any year on record for the CONUS. The largest temperature departures for Jan-Mar 2012 occurred across the Midwest and New England. Much of the west coast was below normal.

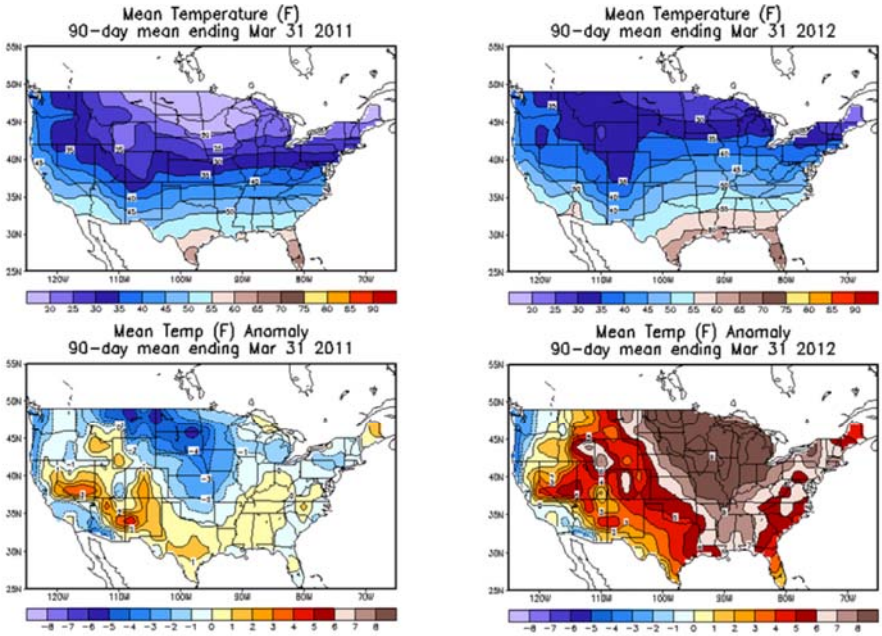

Fig. 1 Jan - Mar averaged temperatures (top row) and anomalies (bottom row) for 2011 (left) and 2012 (right). Units in degrees Fahrenheit. (Source: Climate Prediction Center's temperature analyses web page).

The long-term time series of Jan-March (JFM) averaged temperatures (from 1895-2012) showed that this past Jan-Mar had the highest CONUS temperature in the long-term time series. The value was about 43 degrees Fahrenheit, which is about 6 degrees above the long-term average.

A comparison of last year's Jan-Mar averaged CONUS temperatures and anomalies to this year's (Fig. 1) shows that this year had a very different pattern than 2011. Last year, a large area of CONUS experienced below-average temperatures, whereas this year most of the country saw above-average temperatures. Some areas across the Midwest experienced temperature anomalies of 8 degrees (F) above normal (indicated by the dark brown shaded areas in Fig. 1). The west coast in both years had below-normal temperatures. In 2012, the sea surface temperatures off the west coast were colder than normal, likely keeping temperatures along the west coast cool.

Correspondence to: Melissa Ou, Climate Prediction Center, NCEP/NWS/NOAA, 5830 University Research Court, College Park, MD 20740-3818; E-mail: Melissa.Ou@noaa.gov.

The large-scale winter flow is examined to find some features that could be attributed to the anomalously warm winter temperatures. December-February (DJF) 500mb heights are used to look at the large-scale synoptic pattern of last year's winter compared to this year's winter. The DJF season was used because it is thought to best capture the cold season pattern. According to NCDC's state of the climate, the frequent development of cold upper-level systems over the west, and lack of frequent and persistent cold outbreaks in the east led to above-normal temperatures over much of the country east of the Rockies. Fig. 2 shows plots of 500mb heights and anomalies of 2011 and 2012. Last year's plots show below-normal heights across the eastern US, whereas this year this region had above-normal heights, which may reflect the below average frequency of storm systems in the east. This upper-level pattern of ridging across the eastern US is consistent with a positive Arctic-Oscillation (AO) pattern during the winter season.

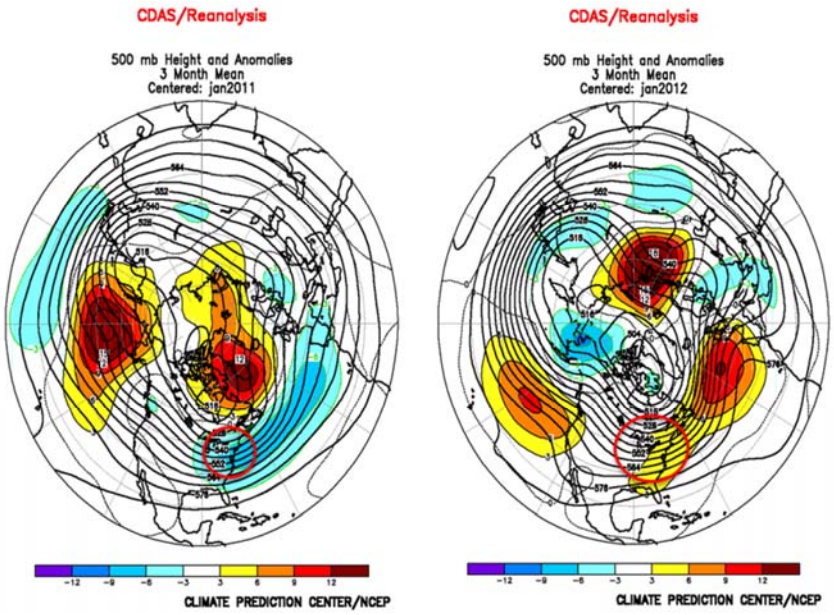

Fig. 2 Dec-Feb averaged 500mb heights (contour) and anomalies (shaded) for last year (left) and this year (right). Circled areas in red are mentioned in the text. (Source: Climate Prediction Center)

One impact from the lack of cold outbreaks was anomalously low snow cover across many parts of the CONUS. There were fewer days than normal that received snow cover during January and February of this year. Large areas across the Northern Plains had 25% fewer days than normal of snow cover than climatology. This was the 3rd smallest winter snow cover in the 46-year satellite period, especially in the west.

b. Impacts from a warm winter and spring

Some impacts from the warm winter and spring include earlier migration of animals and spring flower blooms. Cherry trees in Washington D.C., a popular tourist attraction, bloomed 2 weeks earlier than normal in 2012. Typically the average peak bloom is near April 4, whereas this year it occurred on March 20. There were also large profit losses to ski areas. Many areas did not have enough snow to open, and many of those that did open had to close early due to lack of sufficient snow. These warm conditions also led to an early start to wildfires across the nation.

c. A dry, hot summer

Above-normal temperatures continued across most of the CONUS during the summer, accompanied by persistent dry conditions. Plot of June-August average temperature departure from normal (Fig. 3) shows that the summer season was warmer than average for a large portion of the CONUS, with the exception of the Southeast and parts of the Northwest. It was the 3rd hottest

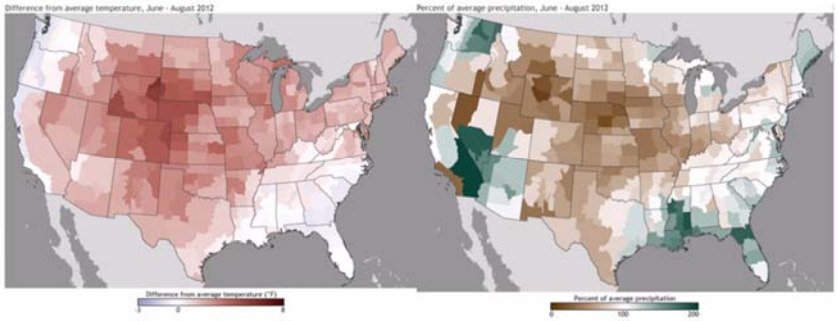

Fig. 3 U.S. Temperature (left) (ºF) and precipitation (right) (percent of average precipitation) departures from normal averaged over June-August 2012. (Source: NCDC)

summer on record according to NCDC. In fact, the average CONUS temperature was more than 2 degrees Fahrenheit above the 20th century average.

Many areas across the US experienced a heat wave in June, with most of them occurring over the CONUS. 645 locations experienced record heat, with 410 records broken, and 235 of them tied with previous records. Several Midwestern locations saw multiple days of extremes, which are reminiscent of the country's legendary "Dust Bowl Days" of the 1930s.

The long-term timeseries of CONUS temperature averaged June-August (JJA) (Fig. 4) shows that this year's JJA was the second highest temperature on record at 74.28 º F, closely beat by 1936 at 74.45 º F. The long-term average is displayed on the plot in Fig. 4 as the solid gray line. This value is at about 72.1, making this year's summer temperature about 2 degrees higher than the long-term average.

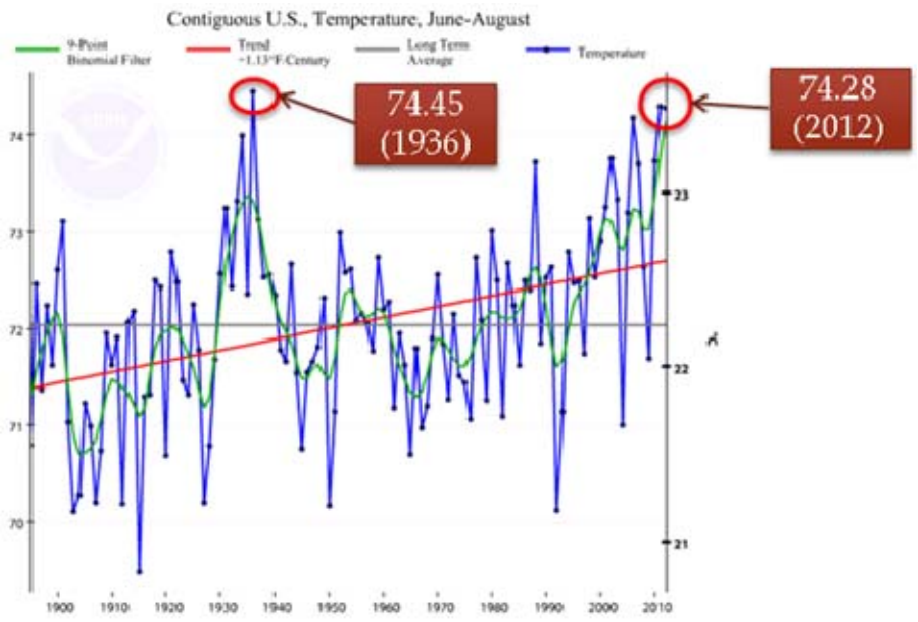

Fig. 4 Long-term timeseries of June-August averaged CONUS temperature from 1895 - 2012. The highest 2 values are circled in red. (Source: National Climatic Data Center)

The average June-August (JJA) CONUS precipitation was below average at 188 mm (average is about 210 mm), although was not as record-breaking as the temperature. This JJA was much drier overall, than the previous year. Last year the CONUS on average during JJA received above-normal precipitation (238 mm).

Even though the overall average CONUS precipitation is not as impressive in terms of the long term records, some of the localized precipitation rankings reached record driest. The central part of the CONUS had many areas of much-below normal to record driest precipitation. Last year, the most arid areas were focused across the south, especially Texas, whereas this year most of the driest areas in JJA were in central US. Most of the record breaking dry conditions this year were seen in Nebraska. In contrast, Florida had its wettest summer on record this year, partially driven by tropical storm Debby in June and Isaac in August.

Many parts of the CONUS received below-normal precipitation, especially central CONUS, which resulted in large spatial coverage of moderate to exceptional drought. According to the North American Drought Monitor (NADM) created July 31, 2012, 62.9% of the nation was in moderate to exceptional drought (D1 to D4 NADM categories). The maximum value of coverage of 63.9% occurred on July 24, 2012, which was a record spatial coverage in the 13-year of the U.S. Drought monitor (USDM) history (according to the NCDC State of the Climate report).

Unfortunately, despite the fact that the 2012 Atlantic hurricane season was relatively active, the tropical storms and hurricanes that made landfall did little to improve drought. A comparison of the drought monitoring maps before and after hurricane Isaac made landfall (Fig. 5) delineates the fact that the areas with the most severe drought in the Central and Southern Plains and the southeast saw little improvement associated with precipitation from Isaac. The track of hurricane Isaac was located too far east to result in significant rain supporting drought improvement in these areas.

Hurricane Isaac had a larger impact to flooding than drought. Above average streamflow observations in the southeast after Isaac made landfall highlight this fact.

d. Examination of precipitation and drought analogs for July 2012

I examine some of the atmospheric variables for precipitation and drought analog years to July 2012 to attempt to glean some information about similarities and differences of the synoptic pattern associated with these analogs. July 2012 was selected for investigation because July 24, 2012 broke the 13-year U.S. Drought Monitor (USDM) history for the greatest spatial coverage of areas with moderate to exceptional drought (D1 - D4). Based on numerous characteristics regarding the spatial pattern and intensity of various climate indicators, the National Climatic Data Center identified 1954 as a good analog for July drought, and 1936 as a good July precipitation analog. Drought in July 1936 was worse than 1954, but 1954 was the last time such drought occurred and was identified by NCDC to have more similar characteristics overall to July 2012.

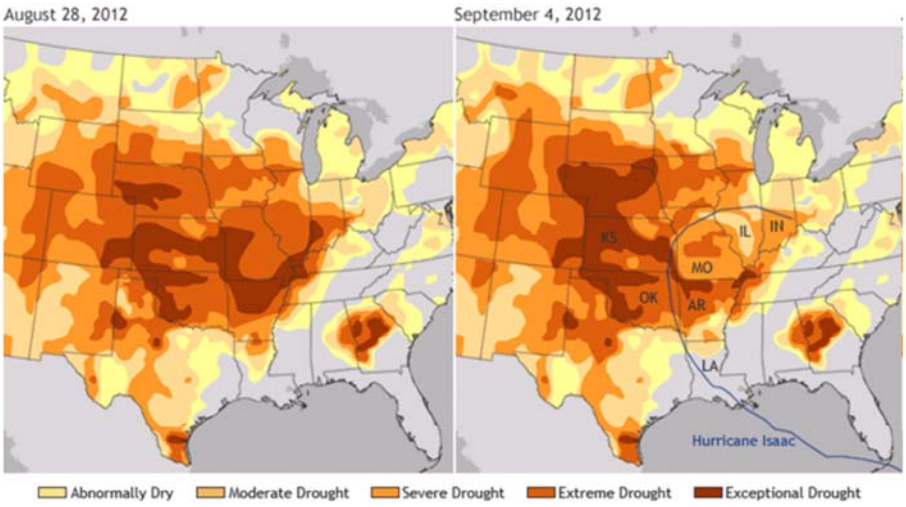

Fig. 5 Drought monitoring maps for the week of August 28, 2012, and September 4, 2012, which was made before and after landfall of Hurricane Isaac, respectively. The track of Isaac is outlined in blue. (Source: National Climatic Data Center, created by Climate Portal at climate.gov)

First, I will discuss the July 1954 and 2012 drought analogs by looking at synoptic pattern information such as 500mb heights as well as the surface air temperature anomalies, and drought blends of these years (Fig. 6). The drought blend is a short-term drought indicator, which approximates drought-related impacts that respond to precipitation on time scales ranging from a few days to a few months, such as wildfire danger, non-irrigated agriculture, topsoil moisture, range and pasture conditions, and unregulated streamflows.

The 500 mb flow of both July 1954 and 2012 were dominated by an upper-level ridge covering much of the CONUS. However, more of the CONUS was impacted by higher heights in 1954 than 2012. The shaded red area, indicating high 500 mb heights in Fig. 6, stretches further west into California during 1954, compared to 2012. There were more areas in California in 1954 that experienced above normal temperatures than 2012 likely associated with this impact from the upper-level ridging, although it did not seem to lead to more areas of drought in California.

Maps of temperature anomalies (Fig. 6) indicate that the values across central US had similar amplitudes between 2012 and 1954, but that there was a wider area of greater temperature anomalies across this area during 2012 than 1954. This feature may have supported a more condensed area of severe drought compared to 1954 which had more scattered areas with the most severe drought.

Another synoptic feature difference is that in 1954 the upper-level trough axis was negatively tilted and along the east coast, whereas in 2012 it was positively tilted and situated further inland across the east coast states (trough axis highlighted in dashed white lines on Fig. 6). This means that in 1954, there were more states in eastern CONUS impacted by the persistent upper-level ridge pattern which may have resulted in less precipitation from storms in eastern states than in 2012. This can be indicated by more areas of severe drought extending further eastward in 1954 than in 2012.

It should also be noted that even though July 1954 had greater spatial coverage of severe to exceptional drought (D1-D4) of 53.34% compared to 40.28% in 2012, July 2012 had slightly greater spatial coverage of exceptional drought (D4) (10.86% in 2012 compared to 9.69% in 1954).

In terms of precipitation analogs to July 2012, 1936 was identified as a good analog by NCDC. July 1936 was the most anomalous, historically, in terms of extreme drought coverage and dry conditions. Fig. 7 shows 500mb heights, surface air temperature anomalies, and statewide precipitation for July 1936 and 2012.

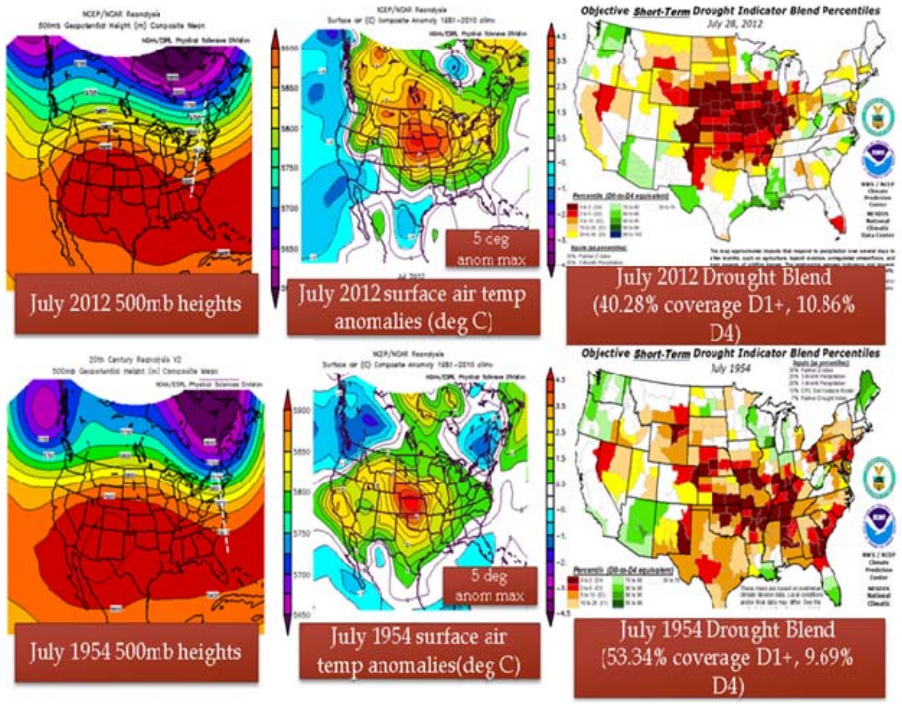

Fig. 6 500mb heights (left), surface air temperature anomalies in deg Celsius (center), and the objective short-term drought blend (right) for 1954 (bottom) and top (2012). 1954 was an identified drought analog for July 2012. (Sources: 500mb heights and surface air temperature anomalies created using composite web application by Earth System Research Laboratory, objective short-term drought blends from Climate Prediction Center)

A comparison of the 500 mb height pattern for July 1936 and 2012 reveals that in 1936 the upper-level ridge had a larger spatial extent than in 2012. This likely supported the larger magnitude and more widespread coverage of positive temperature anomalies over central CONUS. Maps of surface air temperature anomalies (center, Fig. 7) indicate greater maximum temperature anomalies of 9 degrees Kelvin during 1936 than 2012, which had values of 5 degrees Celsius (2012) (Fahrenheit and Kelvin are identical if comparing degree differences). This more widespread anomalous heat and ridging in 1936 was likely the main cause of the worst dry conditions in the Midwest historically. The statewide precipitation maps reflect the more widespread and severe dry conditions in 1936 than in 2012. Many of the Midwest states had record driest categories in 1936, whereas 2012 had no states categorized as record driest.

It is interesting to note that when applied to the temperature pattern for July 2012, several Julys from the 1930s (1934, 1935, 1936) are a close match in many regions.

Record-setting hot, dry, and windy conditions during the last week of June supported widespread fire activity, especially in the west. Colorado had multiple days at or above 100 º F (NCDC State of the Climate). Many of the fires were caused by lightning, with the hot, dry conditions providing an environment conducive for fire initiation and spread. The Waldo Canyon Fire, which started on June 23, 2012, is considered the most destructive fire in Colorado state history.

Increased fire activity burned thousands of acres, leading to hundreds of destroyed homes and thousands of people evacuated. Impacts negatively affected tourism, water resources, and energy interests. The primary corn and soybean agricultural belt was severely impacted. According to NYTimes.com, this year's U.S. corn yield is projected to be the lowest since 1995. Widespread burning also led to devastated crops and livestock from the Great Plains to the Midwest, which elevated prices for domestic and international food and animal feed. There was a significant stress on water resources and increased fish kills due to dried up rivers and increased water temperatures.

e. Southwest monsoon report

This summer's onset of the North American (Southwest) monsoon was considered normal. Typically the monsoon season runs from early July to end of September. The noticeable spike in Tucson's daily dewpoint tracker during early July most likely indicates the onset of the monsoon.

Overall, precipitation was slightly above normal in the southwest during the monsoon season. The accumulated precipitation plots (Fig. 8) indicates that the precipitation observations (black curve) were greater than the climatology (green dashed curves) for most of the time in most of the zones, excluding zone 3, 4, and 6 (zones 4 and 6 results not shown).

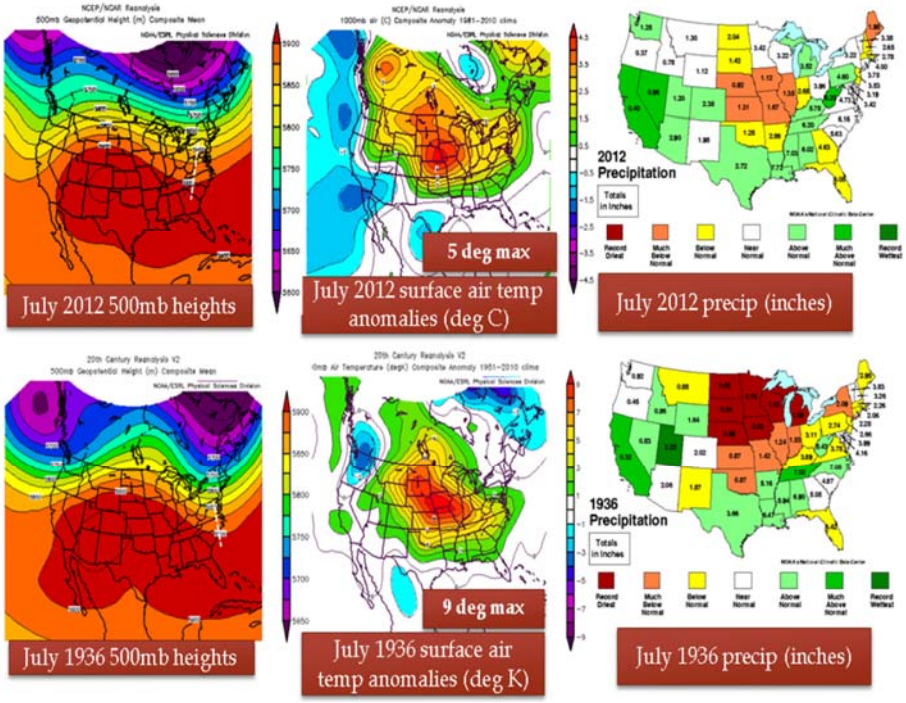

Fig. 7 500mb heights (left), surface air temperature anomalies in deg Celsius (center), and the statewide precipitation in inches (right) for 1936 (bottom) and top (2012). 1936 was an identified precipitation analog for July 2012. (Sources: 500mb heights and surface air temperature anomalies created using composite web application by Earth System Research Laboratory, objective short-term drought blends from Climate Prediction Center)

Verification of models' monsoon related accumulated precipitation forecasts shows that the high resolution CFS with April initial conditions and the GSFC with March initial conditions did the best over most of the U.S. southwest regions, although typically the GSFC over predicted the amount of accumulated precipitation (Fig. 8). The exclusion of this is in zone 8, where the lower resolution CFS with March initial conditions performed the best.

f. Most recent conditions (September/October 2012)

During September 2012, most of the west experienced above-normal temperatures. Parts of the northwest, upper Midwest, California, and the southeast received below normal precipitation. Much of the northwest and the upper Midwest had much below to record driest September precipitation. These warm and dry conditions led to another month of above average wildfire in the northwest. Above-normal temperatures and lack of sufficient precipitation exacerbated severe drought conditions, especially across the Great Plains. Another impact of this warm, dry environment was enhanced likelihood for wildfires. At Rocky Mountain Park, CO - many areas were in very high risk for fires. According to DenverPost.com, the fire started on October 9 and increased by 40 acres more of burning on October 20.

3. Summary

Much of the CONUS was dominated by above-normal temperatures during the winter and spring. This is most likely attributed to more cold upper-level low pressure systems over the west, and less persistent cold outbreaks in the east, which is consistent with a positive Arctic-Oscillation (AO) pattern.

Hot, dry conditions pervaded during the summer over CONUS, which led to widespread severe drought over much of the country. Much of this drought occurred over agriculturally significant areas which severely impacted many of the country's most important crops and livestock, especially corn and soybeans and the

feed and water used to sustain livestock. Dry conditions supported widespread fires, resulting in the destruction of many homes and evacuations. The most recent conditions as of October 2012 were anomalous warm and dry conditions across the northwest, upper Midwest, and southeast, and widespread extreme drought across the Great Plains.

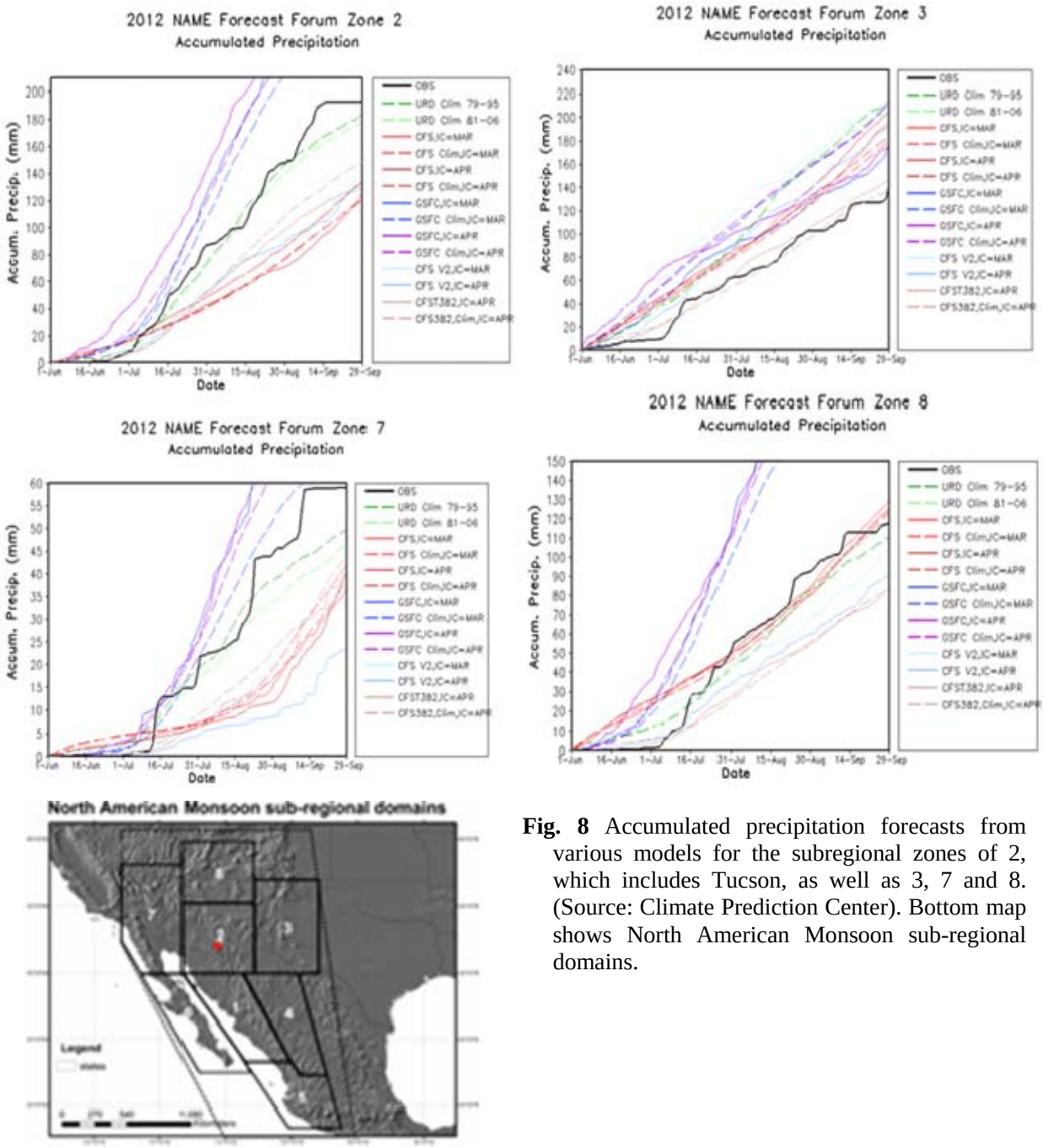

Fig. 8 Accumulated precipitation forecasts from various models for the subregional zones of 2, which includes Tucson, as well as 3, 7 and 8. (Source: Climate Prediction Center). Bottom map shows North American Monsoon sub-regional domains.

Science and Technology Infusion Climate Bulletin
NOAA's National Weather Service
37th NOAA Annual Climate Diagnostics and Prediction Workshop
Fort Collins, CO, 22-25 October 2012

The Current State of Arctic Sea Ice

Gregory J. Deemer[1], Uma S. Bhatt[1], Hajo Eicken[2], Jennifer Hutchings[3], Pamela Posey[4], Rick Allard[4], Gary Hufford[5], and Robert Raye[6]

[1]*Department of Atmospheric Science, University of Alaska Fairbanks, Fairbanks, AK*
[2]*Geophysical Institute, University of Alaska Fairbanks, Fairbanks, AK*
[3]*International Arctic Research Center, University of Alaska Fairbanks, Fairbanks, AK*
[4]*U.S. Naval Research Laboratory, Stennis Space Center, MS*
[5]*NOAA's National Weather Service Alaska Region Headquarters, Anchorage, AK*
[6]*Shell Global Solutions, Houston, TX*

1. Introduction

Arctic sea-ice extent reached a new record minimum in 2012. Although shattering the previous record set in 2007 was not entirely unforeseen, the swift return to a record year places increased attention on our polar regions. This report discusses long-term trends that have led up to today's conditions of a younger and thinner ice cover, and thus an ice cover that is more vulnerable to rapid and record summertime retreat.

2. Discussion

a. Rapid and record summer retreat, 2012

One of the simplest methods used to characterize the state of the ice cover is the extent, or the area of ocean covered with at least 15% sea ice coverage. Figure 1, displays five months of the annual Arctic sea ice cycle and shows that the extent near the onset of the breakup season in 2012 was within two standard deviations of the 20-year base period. But as the melt season progressed, the departure from the long-term average became increasingly large. The Arctic also experienced a large sea-ice loss event in early August before reaching the new record minimum of 3.41 million km^2. The new record is approximately 50% below the climatological mean minimum extent and surpassed the previous record minimum values by over 760 thousand km^2.

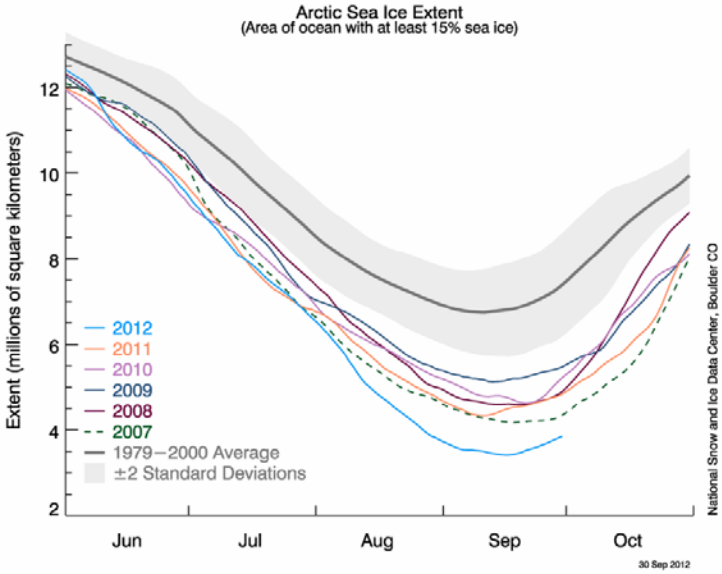

Fig. 1 Arctic sea ice extent progression (Source: NSIDC Arctic Sea Ice News and Analysis, 30 September 2012).

b. Substantial losses of multiyear ice

Another descriptor of the state of the ice cover is ice age, which commonly serves as a proxy for ice thickness, as the oldest ice is in the Arctic basin is often the thickest ice. Figure 2 displays a satellite-derived ice age product showing the progression of loss of the oldest ice types within the Arctic. A precipitous decline of multiyear ice is notable beginning around the year 2002, and has continued over the past decade.

The distribution of individual ice age classes that contributes to the total Arctic ice extent (Figure 3) indicates that the oldest ice classes are nearly depleted. Because of

Correspondence to: Gregory J. Deemer, Department of Atmospheric Science, University of Alaska Fairbanks, Fairbanks, AK 99775 ; E-mail: gjdeemer@alaska.edu.

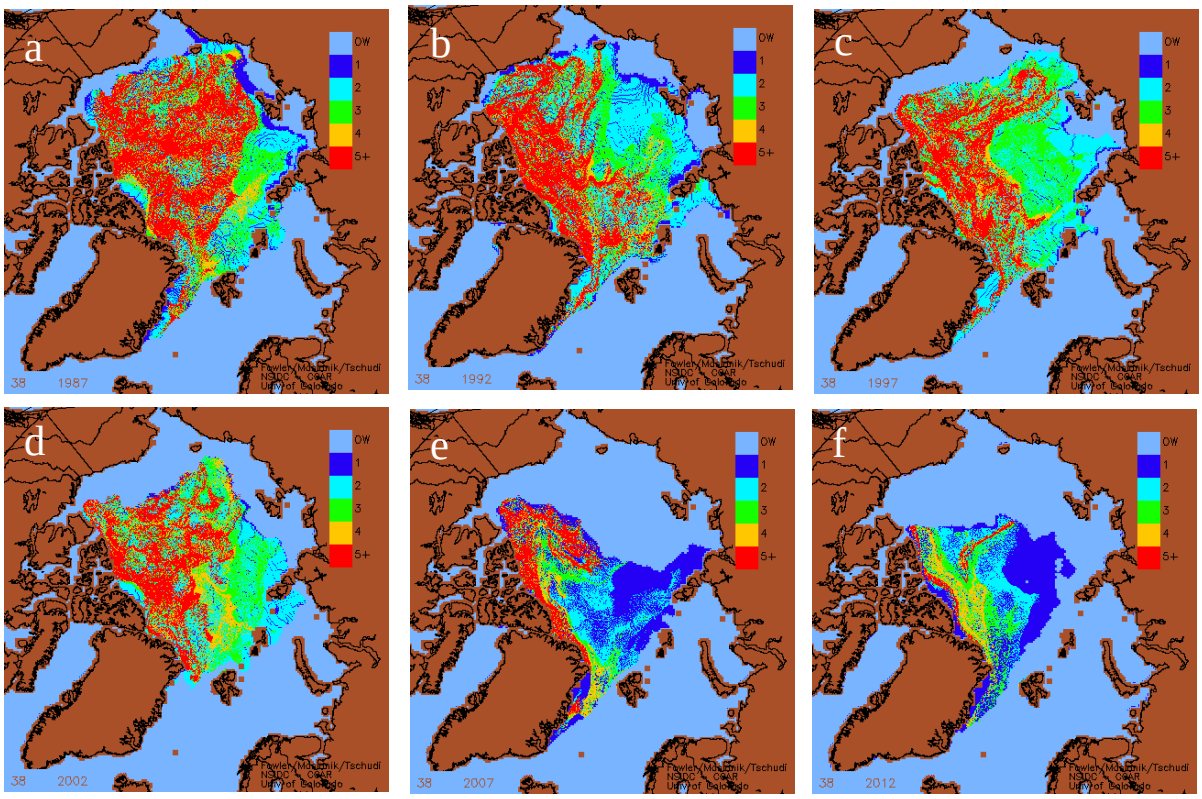

Fig. 2 Ice age product, courtesy of Fowler, C., Maslanik, J., Tschudi, M., Dept. of Aerospace Engr., Univ. of CO, Boulder, CO. Each panel shows Week 38, corresponding to the typical September minimum ice extent for a) 1987, b) 1992, c) 1997, d) 2002, e) 2007, and f) 2012, respectively. The oldest ice (5+years) is in red.

substantial losses of multiyear ice, the Arctic now contains more thin, first-year ice that is more susceptible to export by dynamical forcing and often melts entirely by the end of the summer retreat.

c. Declining trend in sea ice volume

The most important variable in describing the state of the sea ice cover on a climate-scale is the ice volume. Accurate sea-ice thickness measurements needed for the assessment of ice volume are in short supply, but there are a number of different guidance products that have been created by the modeling community. The output from one of the better-known models, the Pan-Arctic Ice Ocean Modeling and Assimilation System (PIOMAS) indicates a declining trend in total ice volume of 2 – 4 thousand km^3 per decade (Figure 4). In the most recent years, ice volume has repeatedly dipped below the second standard deviation of the long-term trend during the melt season. This indicates that not only are large losses of sea ice occurring in the Arctic, but the Arctic is also losing much of its multiyear ice cover.

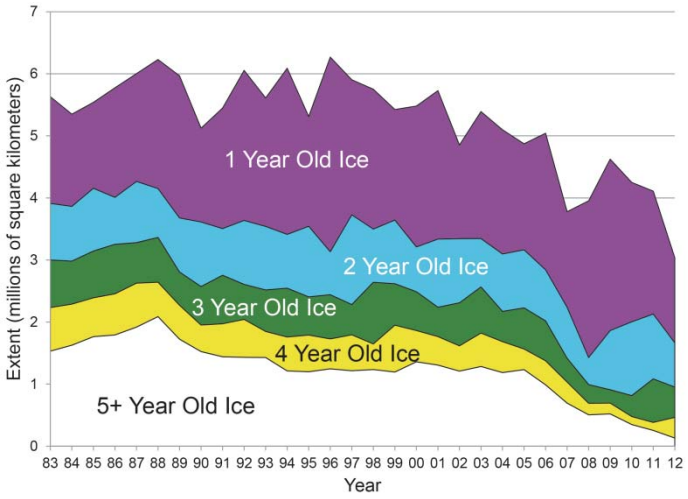

Fig. 3 Changes in multiyear ice extent from 1983 to 2002. (Source: NSIDC Arctic Sea Ice News and Analysis, 2 October 2012).

d. The Arctic storm of 2012

An intense Arctic cyclone that developed in northern Siberia may be the cause of the large ice loss event, which occurred in early August

(Figure 1). After formation, the system ejected off the northern coast of Chukotka where it quickly intensified to reach a minimum central pressure of 964 hPa. The storm reached its peak intensity before encountering the ice edge located in the north-central Beaufort Sea and then began to fill. This event was associated with high winds and seas, warmer temperatures, and dense cloud cover; processes that favor sea-ice destruction. Ground-truth verification of the effects that this storm had on the state of the ice cover in 2012 are difficult quantify due to data scarcity, and the contribution of this event to the total ice loss will for now be left to speculation.

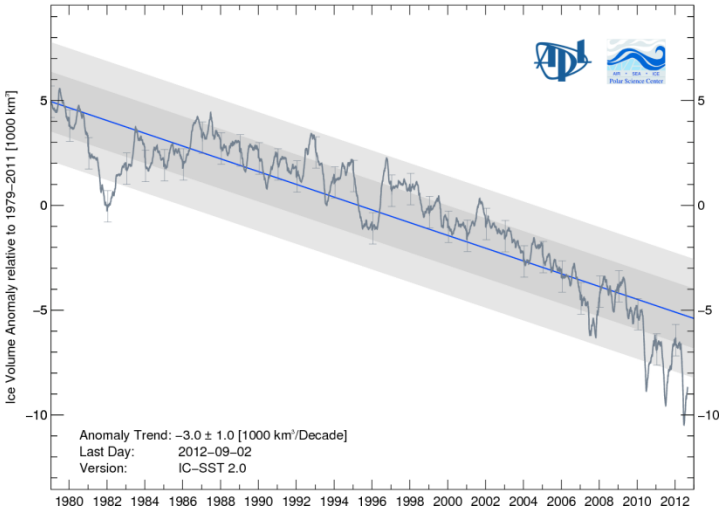

Fig. 4 Pan-Arctic Ice Ocean Modeling and Assimilation System (PIOMAS) Arctic sea ice volume and trend (Source: University of Washington – PSC web page).

3. Summary

Long-term trends of Arctic sea-ice thinning preconditioned 2012 for record retreat. Much of the oldest ice within the Arctic has been lost, which leaves a thinner more mobile ice cover that is subject to rapid export and melt. This year, a strong Arctic cyclone impacted the Pacific sector of the Arctic and is a likely candidate for rapid sea ice retreat in August but exact effects of the storm have yet to be fully apportioned.

References

Arctic Sea Ice News & Analysis, 2012: Poles apart: A record-breaking summer and winter. http://nsidc.org/arcticseaicenews/2012/10/poles-apart-a-record-breaking-summer-and-winter/

Polar Science Center, 2012: Arctic sea ice volume anomaly, version 2. http://psc.apl.washington.edu/wordpress/research/projects/arctic-sea-ice-volume-anomaly/

Science and Technology Infusion Climate Bulletin
NOAA's National Weather Service
36th NOAA Annual Climate Di7agnostics and Prediction Workshop
Fort Collins, CO, 22-25 October 2012

NWS Efforts to Improve Weather to Climate Based-Services

Jiayu Zhou, S&TI Climate Mission, Office of Science and Technology
Wayne Higgins and Mike Halpert, Climate Prediction Center/NCEP

NOAA's National Weather Service

1. Introduction

The promise of NWS operational climate monitoring and prediction improvement relies on research advancement and its successful transition to operation. This summary highlights recent advances identified by NWS that can improve weather-climate based services.

2. Embracing a unified weather-climate modeling strategy

a. Weather-climate connection in model prediction

In recent years, the development of seamless prediction has been increasingly praised, which advocates the importance of scale interactions between weather and climate. The NCEP Climate Forecast System (CFS) has been built on the operational weather forecast model in order to benefit from the weather model improvement. It is expected that the better the weather statistics is simulated by the model, the more reliable the climate prediction would be.

The significance of model climate improvement to advancing the weather forecast has not been taken seriously until recently, when outstanding researches (van den Dool 2012, Fan 2012) demonstrated that the foremost weather forecast error is not due to random processes, nor to local factors, but rather to large-scale climate biases (Fig. 1). The improved understanding of ocean-atmosphere interactions has also pointed out that ocean mesoscale eddies have a large influence on weather system development, and the improved hurricane and coastal weather forecasts can be achieved using a high-resolution model coupled with an eddy resolved ocean model. Evidently, the ocean influence on weather forecast should no longer be ignored. As a result, a weather-climate two-way truly unified modeling framework is recommended for mutual benefits and acceleration of model improvement.

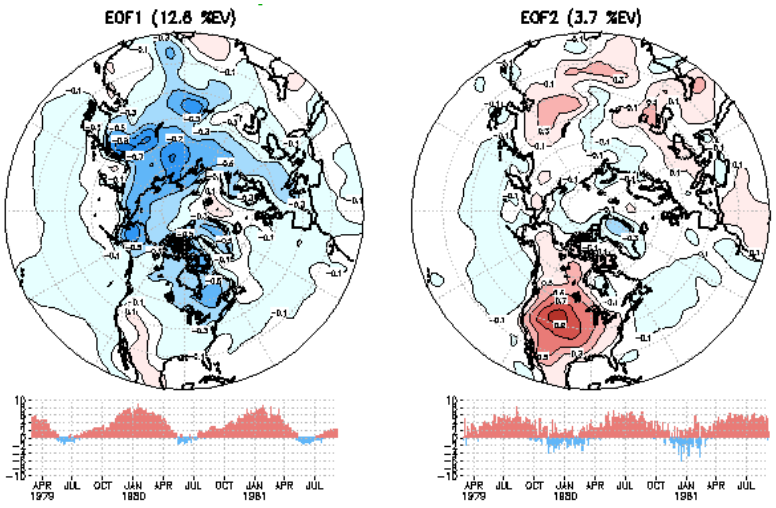

Fig. 1 The leading two EOF modes of NCEP Climate Forecast System (CFS) 975 hPa temperature 5-day forecast error (1979-12). (van den Dool, *CFS v2 Evaluation Workshop, May 2012*)

b. Cloud resolving vs. optimized physics ensemble

Due to increases in computational power, weather-climate model development has achieved more realistic representations of physical processes, thereby improving prediction skill.

Global cloud resolving model with modern turbulence parameterization and multi-scale framework explicitly formulates mesoscale organization without closure assumptions and triggers. It simulates

Correspondence to: Jiayu Zhou, Office of Science and Technology, NOAA's National Weather Service, Silver Spring, MD 20910; E-mail: jiayu.zhou@noaa.gov.

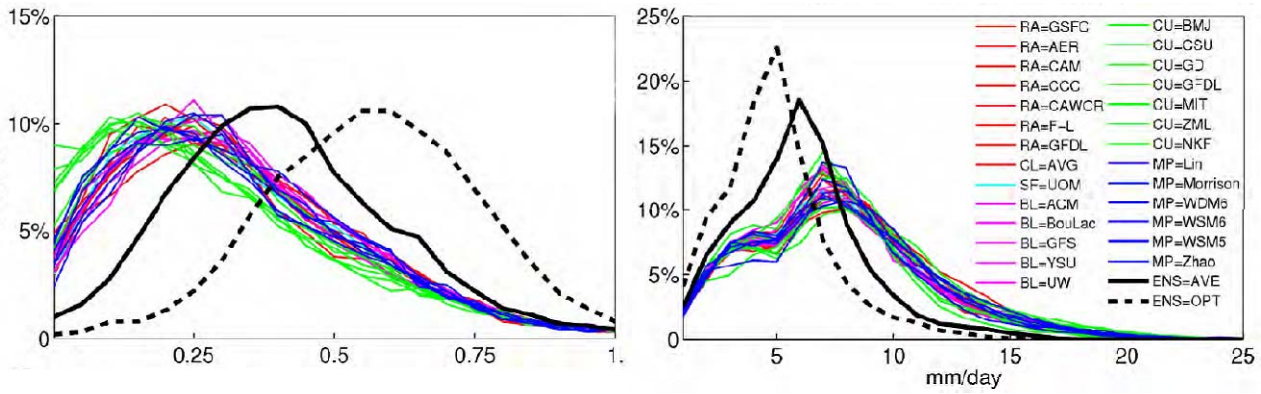

Fig. 2 Spatial frequency distribution of correlations (left) and RMS errors (right) between CWRF and observed daily mean rainfall variations in summer 1993. Each color line depicts a specific configuration in a group of key physical processes. The ensemble result is the average of all runs with equal (AVE, black solid line) or optimal (OPT, black dashed line) weights. (Liang, *Climate Prediction Center Seminar, June 2012*)

variability more realistically, *e.g.* the memory of delay in convective response, and shows tremendous potential (Randall 2012). The progress has also been made in developing multiple physics ensemble configuration, which incorporates a comprehensive list of alternative parameterization schemes for key physical processes. Since individual physical parameterization scheme has predictive ability depending on the weather or climate regime as well as the application, no single scheme performs uniformly well under all circumstances. Figure 2 shows superior skill of multiple physics ensemble over those using a single model configuration (Liang 2012).

3. Accelerating research to operations

a. Prediction of 2010-2011 "double dip" La Nina

During 2010-11, the tropical Pacific experienced prolonged cooler-than-normal conditions. More than 20 models have been used to make real-time forecasts of equatorial Pacific SST (see details at the IRI website http://portal.iri.columbia.edu). Most models failed to forecast Niño 3.4 SST from June 2010 initial conditions. However, one intermediate coupled model, UMD/ESSIC ICM, made a good prediction of the 2011 cold SST conditions in the tropical Pacific (Fig. 3).

To understand why, the relationships among various anomaly fields were analyzed. It was found that the thermocline feedback, which was explicitly represented by the relationship between the temperature of subsurface water entrained into the mixed layer and sea level, was a crucial factor affecting the second cooling in 2011. Sensitivity experiments showed that second cooling in 2011 would not occur if the intensity of thermocline feedback was underestimated below certain levels in the UMD/ESSIC ICM (Zhang 2012).

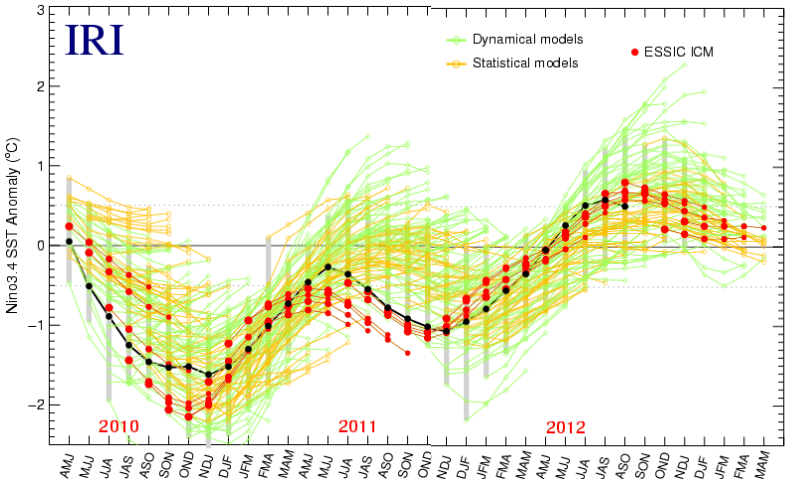

Fig. 3 UMD/ESSIC ICM performance of Nino 3.4 SST predictions (red) in comparison with performances of dynamical models (green) and statistical models (yellow). The observation is plotted in black. (Xue, *CPC Ocean Briefing, 2012*)

b. Representation of daily mean surface air temperature

Hourly (from minute) observations have become popular since the

Automated Surface Observing System (ASOS) deployed in 1991. There are many potential benefits of automated measurements that have not been realized.

Research demonstrated that current daily mean surface air temperature (T_a) defined by (T_{max}+T_{min})/2, which could be strongly affected by transient factors (*e.g.*, cloud cover *etc.*), is distinctly different from the true daily mean of 24-hour average (Fig. 4). The difference has a significant impact on applications, *e.g.* model-data comparisons, trend assessment, *etc.* It is recommended to archive 24-hour average Ta, as well as daily maximum and minimum T_a, to produce the monthly mean T_a for the climate data record (Zeng 2012).

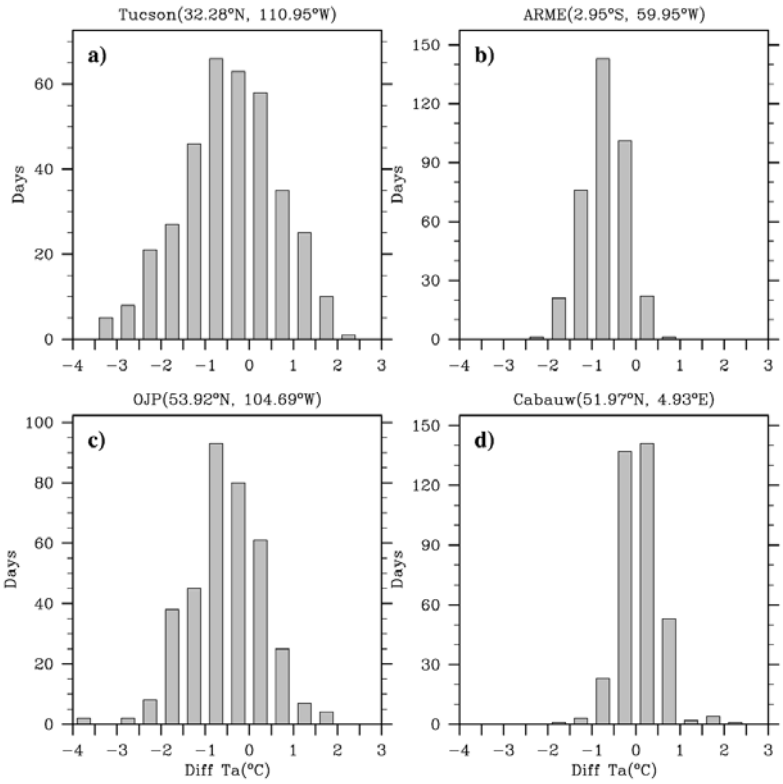

Fig. 4 The statistics of daily differences between 24-hr average and (T_{max} +T_{min})/2 at locations of distinct climatologies. (Zeng, *4th WCRP International Conference, May 2012*)

4. Climate information and user needs

An analysis of scenario planning approaches employed by national climate assessment demonstrated all science information can be "actionable" (Hartmann 2012).

The science oriented top-down approach, which focuses on characterizing uncertainties based on modeling studies, identifies climate system sensitivity to the external forces, resulting in different adaptation options for probable futures that are hardly actionable for stakeholders.

The community bottom-up approach, which puts emphasis on reducing uncertainty through participatory processes, shares values, goals and visions and builds preparedness toward one probable future. The results are more relevant to and actionable for stakeholders but less reliable for a range of possibilities.

More recent advancement in scenario planning calls for embracing uncertainty. Due to long-term uncontrollable external forces and limited predictability, the new development incorporates the advantages of above two approaches by using them interconnectively to maintain a multi-dimensional view, looking for common elements on various pathways, meanwhile incrementally implementing options close by to meet strategic adaptation challenges.

Acknowledgements. We thank Drs. Huug van den Dool (Climate Prediction Center), Yun Fan (Meteorological Development Laboratory), David Randall (Colorado State University), Xin-Zhong Liang, Rong-Hua Zhang (ESSIC/University of Maryland), Xubin Zeng and Holly Hartmann (University of Arizona) for their sincere support of S&TI mission to improve NWS climate prediction and services.

References

Fan, Y., 2012: The most dominant weather forecast errors: climate biases. *NWS Office of Science & Technology Seminar*, Silver Spring, MD, 3 May 2012.

Hartmann, H. C., 2012: A framework for integrating scenario studies across applications. *10th Climate Prediction Application Science Workshop*, Miami, FL, 13 March 2012.

Liang, X.-Z.., 2012: CWRF advances for NCEP operational use. *Climate Prediction Center Seminar*, Camp Springs, MD, 22 June 2012.

Randall, D., 2012: Three ways to use cloud-resolving models to improve global models. *NOAA Climate Test Bed Joint Seminar Series*, Camp Springs, MD, 27 June 2012.

van den Doll, H., 2012: CFS v2 in the context of NMME and IMME. *NOAA Climate Test Bed CFS v2 Evaluation Workshop*, Riverdale, MD, 30 April 2012.

Xue, Y., 2012: *NCEP Climate Prediction Center Annual Ocean Review*. Camp Springs, MD, 8 February 2012.

Zeng, X., 2012: Development of global 0.5º hourly land surface air temperature data. *4th WCRP International Conference on Reanalyses*. Silver Spring, MD, 9 May 2012.

2. IMPROVING AND EVALUATING

REANALYSES AND FORECASTS

Science and Technology Infusion Climate Bulletin
NOAA's National Weather Service
37th NOAA Annual Climate Diagnostics and Prediction Workshop
Fort Collins, CO, 22-25 October 2012

A Comparison of Skill of CFSv1 and CFSv2 Hindcasts of Nino3.4 SST

Anthony G. Barnston[1] and Michael K. Tippett[1, 2]

[1]*International Research Institute for Climate and Society,*
The Earth Institute at Columbia University, Lamont Campus, Palisades, NY 10964

[2]*Center of Excellence for Climate Change Research, Dept. of Meteorology,*
King Abdulaziz University, Jeddah, Saudi Arabia

1. Background

The first version of the NOAA/NCEP Climate Forecast System coupled model (CFSv1; Saha *et al.* 2006) was used operationally between 2004 and 2011. In 2011 it was supplanted by the second version, CFSv2 (Saha *et al.* 2013). Some basic characteristics of the two model versions are shown in Table 1. The CFSv2 carries several major improvements. Besides changes in the model dynamics and increases in forecast resolution and ensemble size, the CO_2 concentration in CFSv2 evolves realistically over time, while for CFSv1 the CO_2 value is fixed at the observed 1988 concentration. Another difference is in the initial conditions: In CFSv2, initial conditions come from the Climate Forecast System Reanalysis (CFSR) (Saha *et al.* 2010), while in CFSv1 they come from NCEP/DOE Reanalysis-2 (R-2). It is stated in Saha *et al.* (2010) that the atmospheric analysis, and therefore the initial conditions, based on the CFSR is more realistic than for the R-2.

	CFSv1	**CFSv2**
Horizontal & Vertical Resolution	T62 (~2°), 64 levels	T126 (~1°), 64 levels
Atmospheric Model	GFS from 2003	GFS from 2009
Ocean Model	MOM3	MOM4
No. Ensemble Members / Month	15	24
Source of Initial Condition Data	NCEP/DOE Reanalysis	Climate Forecast Sys. Reanalysis (CFSR)
Sea Ice	Climatology	Predicted
Carbon Dioxide Concentration Setting	Fixed at 1988 level	Evolving with time

Table 1 Some basic specifications for CFSv1 and CFSv2

Given the improvements in CFSv2 compared with CFSv1, one would expect relatively better predictive skill in CFSv2. However, a discontinuity at year 1999 in the CFSR, related to a change in the atmospheric observing system, induced a change in the characteristics of the SST used for the initial conditions for the CFSv2 hindcast integrations beginning that year—especially those in the tropical Pacific (Xue *et al.* 2011; Kumar *et al.* 2012). Here we compare the skill of predictions of Nino 3.4 SST in the tropical Pacific by CFSv2 to those of CFSv1, and examine which features of the skill differences may be related to CFS model improvement, or to the 1999 discontinuity in the initial conditions due to the CFSR.

2. Results

Here the skill results include verification measures for deterministic predictions, including trend analysis and forecast timing error analysis, and also reliability analysis for the probabilistic aspect of the predictions.

a. Anomaly correlation and RMSE

The anomaly correlations between predictions and observations of Nino3.4 SST are shown in the left column of Fig. 1 as a function of target month and lead time for CFSv1 and CFSv2. The most noticeable skill

Correspondence to: Anthony G. Barnston, International Research Institute for Climate and Society, The Earth Institute at Columbia University, Lamont Campus, Palisades, NY 10964; E-mail: tonyb@iri.columbia.edu.

difference is found in forecasts for northern summer at medium and long lead times, where CFSv1 has relatively low skill (correlations of 0.5 or lower) while CFSv2 shows higher skill (0.6 to 0.7).

These forecasts are for target months beyond the northern spring ENSO predictability barrier that are made before that barrier—the condition known to present greatest predictive difficulty. However, another skill difference — in the opposite direction — is found for predictions for times near the mature stage of an ENSO episode made from start times after the beginning of the episode (*e.g.*, a forecast for February made in July). These "easier" predictions appear to be made better by CFSv1 than CFSv2. Why would this be the case for a model that outperforms its predecessor in the most difficult prediction conditions?

Figure 2 shows the error of CFSv1 and CFSv2 predictions as a function of start time for all seasons and leads through the 28 year hindcast period. A discontinuity in the CFSv1 errors appears near 1991, and a larger one is seen in CFSv2 errors near 1999.

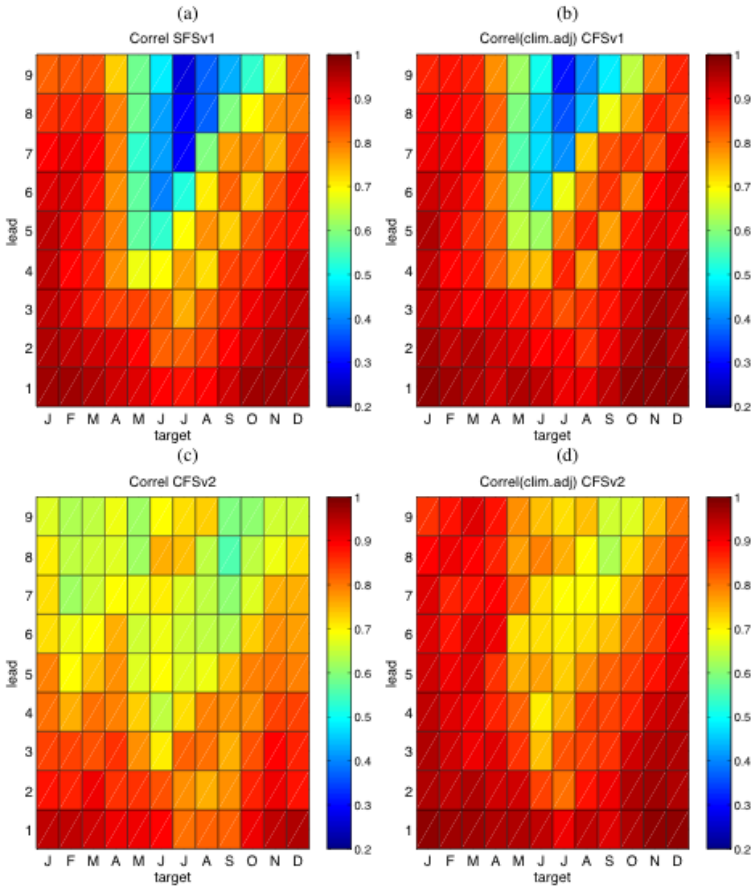

Fig. 1 Temporal correlation between (a) CFSv1 and (c) CFSv2 predictions of Nino3.4 SST and verifying observations over the 1982-2009 period. The target month is indicated on the horizontal axis, and lead time on the vertical axis. A lead time of 1 month implies a prediction made at the very beginning of the target month using data up to the end of the previous month. Right column shows temporal correlation for (b) CFSv1 and (d) CFSv2 following elimination of discontinuities in the predictions of each model by using two separate climatologies (see text).

Such discontinuities would be expected to degrade all verification measures relative to discontinuity-free errors, including temporal correlation. The source of the 1991 change in CFSv1 error has been attributed to a problem in the use of bathythermograph (XBT) measurements prior to 1991 (Berringer and Xue 2004), and is not examined further here. The CFSv2 error discontinuity, on the other hand, is associated with a discontinuity at year 1999 in the CFSR reanalysis data (Saha *et al.* 2010) that induced a change in the characteristics of the SST— particularly in the tropical Pacific (Xue *et al.* 2011; Kumar *et al.* 2012). This SST change has been attributed to the introduction of the ATOVS[1] data in the atmospheric assimilation beginning in late 1998 (Zhang *et al.* 2012), due to forcing from the atmospheric to the oceanic aspects of the Reanalysis (Xue *et al.* 2011). The positive change in central tropical Pacific SST in 1999 does not coincide with observed SST trends documented in other studies, which have been slightly downward (*e.g.* Kumar *et al.* 2012; Deser *et al.* 2010; Kumar *et al.* 2010; Lyon and DeWitt 2012), and is therefore seen as artificial. Such a positive change in tropical Pacific SST behavior around 1999 would be important because the SST in that region, besides reflecting the ENSO state in its own right, would affect remote teleconnections to seasonal climate. A change in the climatology of tropical Pacific reanalyzed SST in 1999 implies a change in the initial conditions used to begin a prediction run of CFSv2. Changes beginning in 1999 in the CFSv2 predictions have indeed been noted in SST and related oceanic and atmospheric fields in

[1] ATOVS refers to the Advanced Television and Infrared Observation Satellite (TIROS) Operational Vertical Sounder radiation data system.

several studies, noted most strongly in the general vicinity of the tropical Pacific (Wang *et al.* 2011; Chelliah *et al.* 2011; Ebisuzaki *et al.* 2011). It will be shown below that the signature of the 1999 discontinuity in the predictions of Nino3.4 SST appears in the shortest lead time, propagates to longer lead times, and exhibits some seasonal dependence.

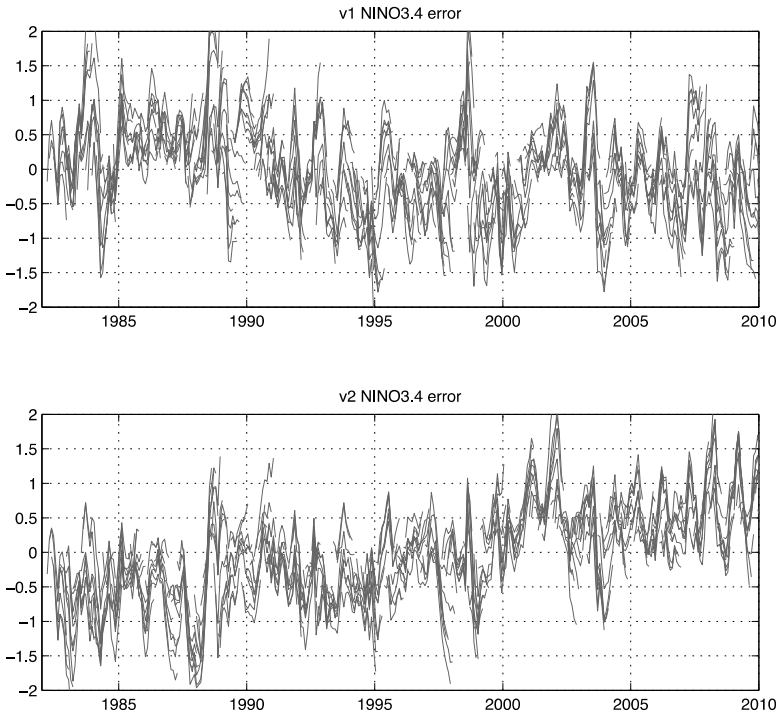

Fig. 2 Error (°C) in Nino3.4 SST predictions of CFSv1 (top) and CFSv2 (bottom) for start times (indicated on horizontal axis) over the course of the 1982-2009 period. Errors for predictions at all lead times are shown.

To free the evaluation of the effects of discontinuities in both CFS versions, dual climatologies from which to form anomalies are developed (1982-1990 and 1991-2009 for CFSv1; 1982-1998 and 1999-2009 for CFSv2), and the evaluations are repeated. Results following this adjustment (or correction) are shown in the right column of Fig. 1. Improvements are noted in the cases of both model versions, but are more substantial in CFSv2 than CFSv1. In CFSv2, higher correlations are seen in all seasons and leads, but most notably for predictions for late northern autumn and winter made during summer or later — forecasts considered least challenging but relatively lacking in skill compared with CFSv1 before the correction. A summary of the correlation differences between CFSv2 and CFSv1 before and after the discontinuity corrections for both models is shown in Fig. 3 in terms of the difference in squared correlation (where negative signs are retained upon squaring).

The relative superiority of CFSv2 for long lead predictions through the northern spring predictability barrier is clear with or without the correction, but with the correction CFSv2 no longer presents a degradation for moderate and long lead predictions for northern winter made from earlier within the same ENSO cycle. It may be noted, however, that CFSv1 performed about as well for these predictions as CFSv2. Following the correction, then, the better performance of CFSv2 applies to most seasons and leads.

A similar skill comparison is conducted for RMSE using standardized anomalies[2], with results shown in Fig. 4. The results for RMSE differ noticeably in pattern to those of correlation because biases in both mean and in amplitude contribute to RMSE but not to correlation.

RMSE scores are reduced considerably with the dual climatology correction for both model versions, indicating the importance of the sub-period biases that can greatly exacerbate the squares of the largest errors in the direction of the bias. Comparing the RMSE for the corrected versions of the two model versions, it is seen again that the main difference is a substantial improvement in CFSv2 in the errors of predictions traversing the northern spring predictability barrier, particularly for late northern summer target months made early in the calendar year. Such predictions are for ENSO conditions generally not yet observed at the time of the forecast.

[2] Here the RMSE is standardized for each season individually to scale it so that climatology forecasts (zero anomaly) would result in the same RMSE-based skill (of zero) for all seasons, and all seasons' RMSE would contribute equally to a seasonally combined RMSE.

b. Standard Deviation Ratio

Figure 5 shows the ratio of the interannual standard deviation of the model predictions to that of the corresponding observations for each model version for each target month and lead time, both before and after correcting biases by forming two climatologies in place of a single discontinuous one.

Ideally the standard deviation ratio would be no higher than unity throughout all seasons and leads, and lower to the extent that predictive skill is imperfect: Theoretically, it should be the square root of the fraction of observed variance explained by the predictions. While the correction results mainly in subtle changes in the ratios, a noticeable decrease toward unity is found in the case of CFSv2 for short to intermediate lead times for target months in the second half of the year. More importantly, the ratio of CFSv1 is noted to be too high (>1.5) even following the correction for intermediate lead predictions for northern spring season when the observed standard deviation is at its seasonal minimum. CFSv2 lacks this weakness and, following the bias correction, shows ratios fairly close to unity for many seasons and leads. In keeping with the expected lower skill expected for forecasts traversing the northern spring predictability barrier, ratios of less than unity are noted in CFSv2 for predictions for June to October made at medium and long leads.

c. Target month slippage

"Target month slippage" is a systematic error that occurs when predictions verify with higher skill for target months earlier or later than those intended (Tippet et al. 2012; Barnston et al. 2012), such as a 4-month lead prediction intended for July verifying better against observations of May or June. Typically slippage occurs with predictions late in reproducing observed changes, such as onsets or endings of ENSO episodes. Slippage cannot be

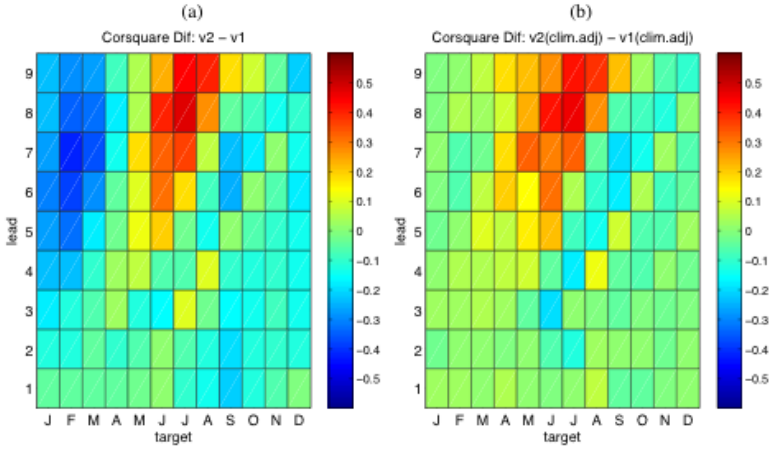

Fig. 3 Difference in squared correlation (of predictions vs. observations) of CFSv2 and CFSv1 without treatment for discontinuities and following treatment using dual climatologies for each model version (a and b, respectively). Negative sign is retained upon squaring. The target months and lead times are as described above in caption of Fig. 1.

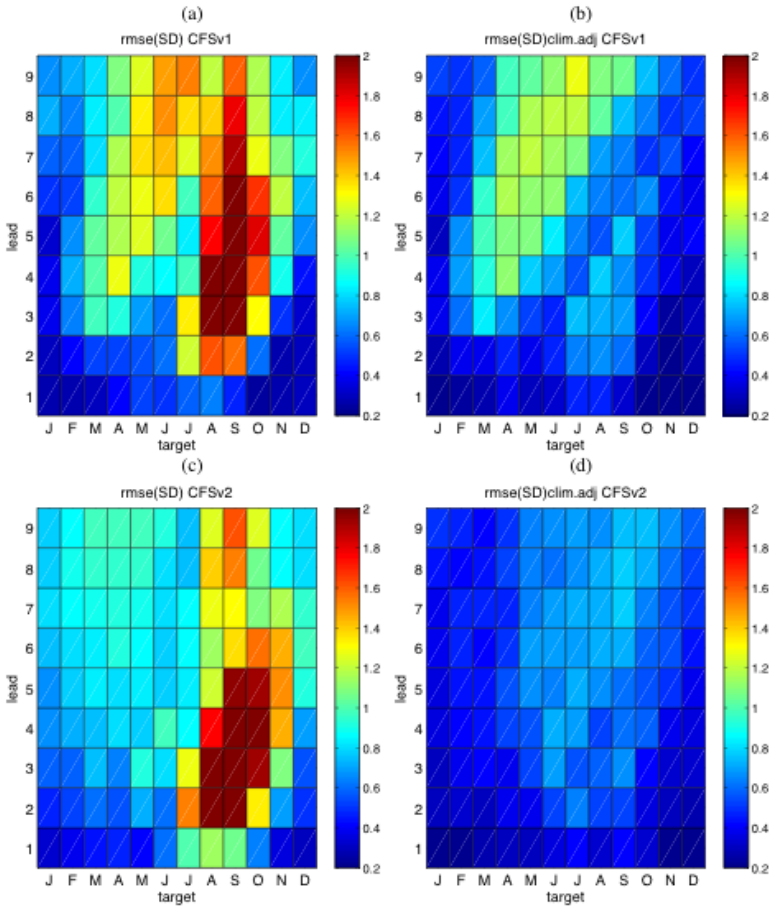

Fig. 4 Root mean squared error of predicted vs. observed standardized anomalies of (a) CFSv1 and (c) CFSv2 without treatment for discontinuities and following treatment using dual climatologies for each model version (b and d, respectively). In the absence of any skill, RMSE of 1.41 is expected. The target months and lead times are as described above in caption of Fig. 1.

diagnosed from the usual skill measures, which only compare forecasts with the verifying observations of the intended target time. Although slippage is a systematic temporal error, it is indistinguishable from a random error when forecasts at different leads are evaluated independently. It is most likely to occur when prediction is most difficult, such a prediction made in March for targets of July and beyond. Because CFSv1 is seen to underperform CFSv2 in such predictions crossing the northern spring predictability barrier, greater slippage might be expected in CFSv1 than CFSv2.

Slippage is shown in plots of skill as a function of the lag time between the measured target period and the intended one. To overcome the small sample issue, the diagnosis is made for all seasons together. To the extent that slippage is systematic, it can be corrected using statistical methods, such as multiple regression, that define optimum shifts of the model's forecasts to targets different from those originally intended (Tippett et al. 2012). Here we apply such a multiple regression-based correction to the forecasts of CFSv1 and CFSv2, to increase an MSE-based skill metric. Figures 6 and 7 show slippage and skill results for CFSv1 and CFSv2, respectively, before and after the correction.

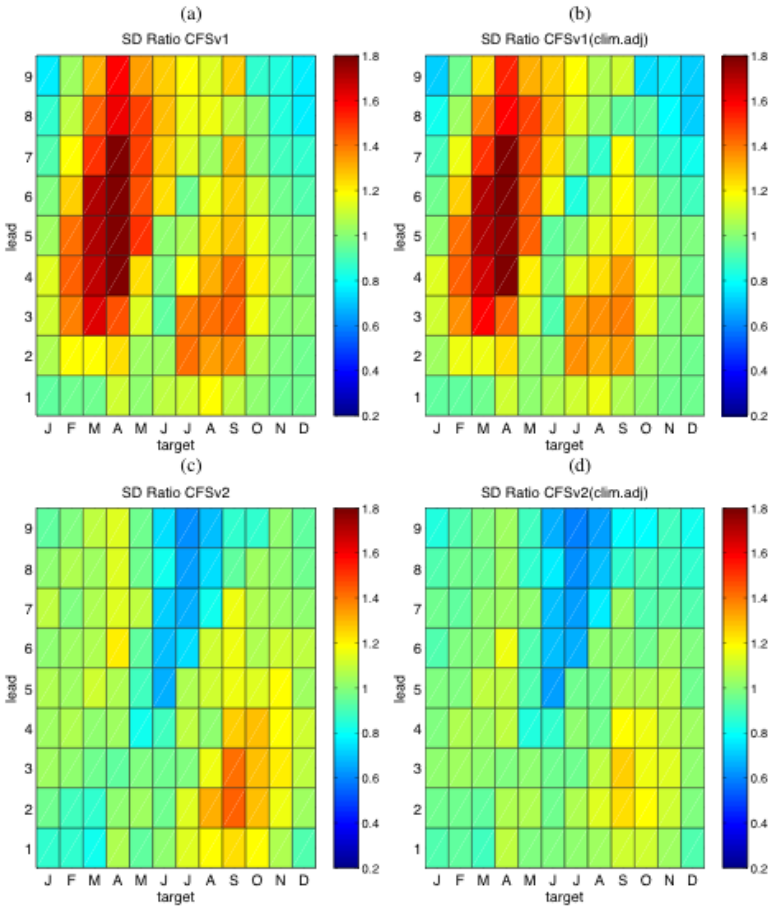

Fig. 5 Ratio of interannual standard deviation of predicted vs. observed anomalies of CFSv1 (a) and CFSv2 (c) without treatment for discontinuities and following treatment using dual climatologies for each model version (b and d, respectively). Ideally, the ratio is unity or less. The target months and lead times are as described above in caption of Fig. 1.

Slippage is obvious in CFSv1 (top left panel of Fig. 6), and it increases with increasing lead times. The MSE-based skill score (bottom left panel) indicates sub-zero skill for long-lead CFSv1 forecasts for northern summer. After the statistical correction (right panels) slippage is decreased and the skill of the long-lead summer forecasts is improved. The same diagnostics for CFSv2 (Fig. 7) indicate little original slippage, and the correction does little to improve the already good performance.

d. Trend Bias

The time-conditional biases indicated in the CFSv1 and CFSv2 predictions discussed earlier (Fig. 2) create trend biases in the sense that a linear trend fit to the predictions exhibit slopes that do not appear in such a fit to the observations. Each model also exhibits more gradual trends within each of its sub-periods, particularly for start months around northern autumn. Figure 8 shows Nino3.4 predictions for the first month from each model version, along with the corresponding observations, for start times of 1 August, 1 September and 1 October for each year of the hindcast period. As expected from the earlier discussion, CFSv1 exhibits a positive bias before 1991 and negative bias from 1991 onward, while CFSv2 shows negative bias before 1999 and positive bias from 1999 onward. Additionally, the magnitude of the negative biases in CFSv2 appears to decrease with time up to 1999, and of positive biases to increase with time from 1999 forward.

At the earliest lead time, predictions are expected to be influenced heavily by the initial conditions. The systematic discrepancies between the short-lead predictions and the observations shown in Fig. 8 are thus indicative of biases in the SST initial conditions, and in this case these are most prominent for the August, September and October start times. Figure 9 shows biases in the slope of the least-squares linear trend for predictions of CFSv1 and CFSv2 for each target month at each lead time. The CFSv2 positive trend biases for the shortest lead predictions of August, September and October are noted in the bottom row of cells. Figure 9 (right) shows that these northern autumn biases amplify as they propagate to predictions at later target months with increasing lead times.

The initial condition bias is thus seen to be responsible for the initially noted lower skills of CFSv2 than CFSv1 for predictions made during the less challenging seasons of the year if the data are not corrected by using two separate climatologies. This relatively simple correction is sufficient to uncover evidence of the substantial general improvement in predictive skill of CFSv2 compared to CFSv1.

A reason for a remaining gradual positive trend in CFSv2 predictions relative to observations even after the discontinuity correction using dual climatologies is not obvious, but may reflect a problem of radiation balance in the model. This possibility may be an issue for consideration in the development of the future version of the CFS.

The trend bias in CFSv1 is negative for virtually all months and leads, mainly because of the discontinuity in 1991 but also to some degree because of a gradual trend within the sub-periods. In contrast to CFSv2, trend biases in CFSv1 do not appear at short leads, indicating a likely lack of major biases in initial conditions. However, CFSv1 has the disadvantage of

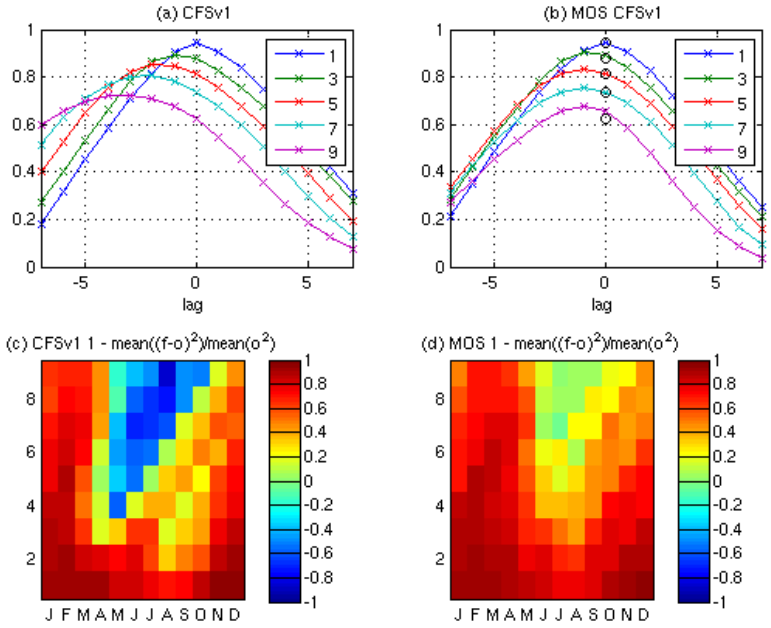

Fig. 6 Target period slippage, and its correction, in CFSv1: (top) Correlation between predictions and observations as a function of lag time between verified target month and intended target month, for leads of 1, 3, 5, 7 and 9 months before (left) and after (right) a MOS correction for slippage based on multiple regression. Predictions free of slippage should have maximum correlation at zero lag. The hollow circles in the right figure show the correlation at zero lag prior to the correction. (bottom) Mean squared error (MSE) skill score as a function of target month and lead time before (left) and after (right) the MOS correction.

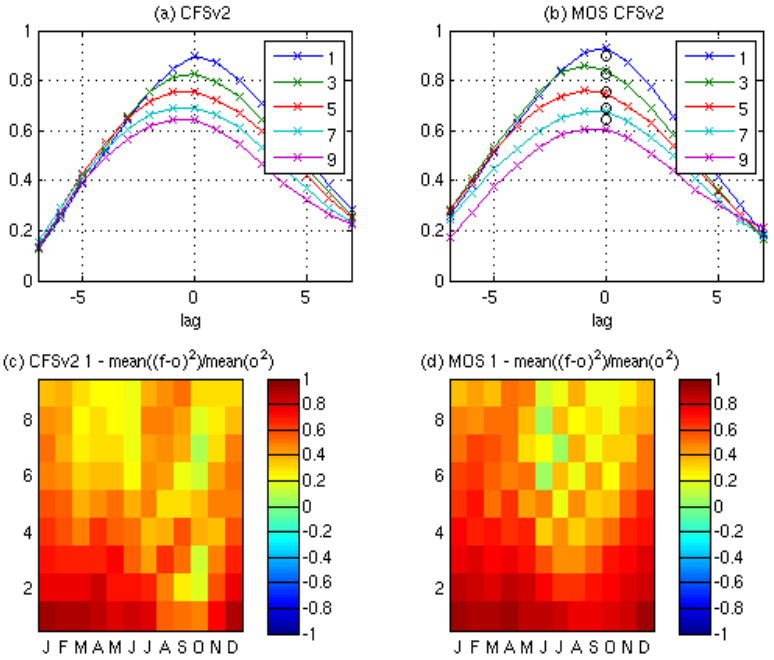

Fig. 7 As in Fig. 6, except for CFSv2 slippage and its correction.

a non-evolving CO_2 concentration setting, and this is one possible reason for the slowly declining Nino3.4 SST predictions relative to the observed SST.

e. Probabilistic reliability

We assess the reliability and sharpness of the probabilistic predictions of Nino3.4 SST from the two CFS versions using reliability analysis. For any prediction, probabilities for the below-, near- and above-normal categories are defined by counting the proportion of ensemble members whose predictions are in each respective category, where the categories are defined using tercile cutoffs for the study period. The observations are categorized likewise. The three categories may be loosely representative of La Nina, neutral and El Nino conditions. Reliability analysis is carried out for the above and below normal forecast categories separately. We ignore the near-normal category, which has repeatedly been demonstrated to have weak performance.

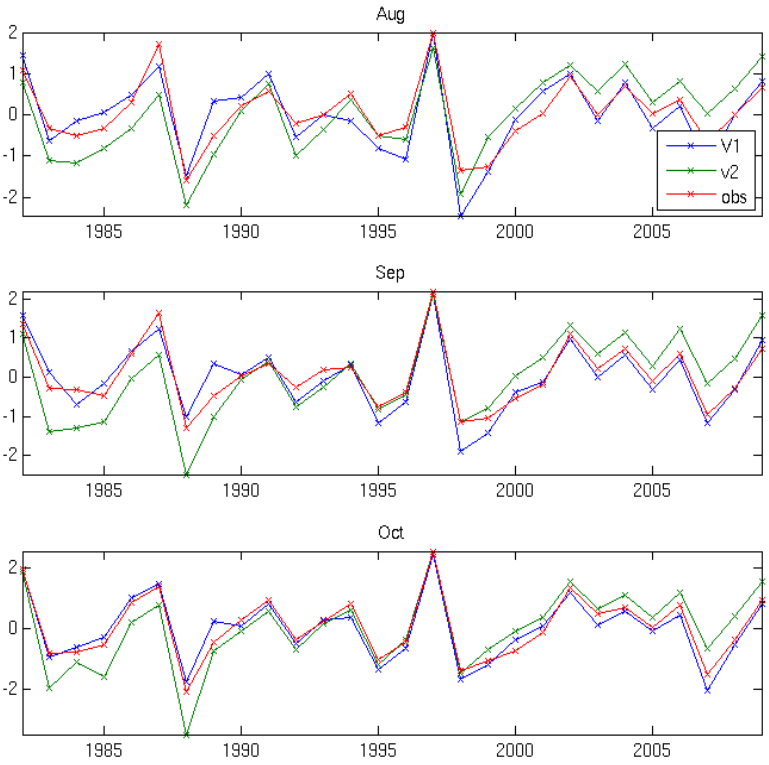

Fig. 8 Shortest-lead Nino3.4 SST anomaly predictions of CFSv1 (blue) and CFSv2 (green) and corresponding observations (red) for start times at beginning of August (top), September (middle) and October (bottom) over the 1982-2009 period.

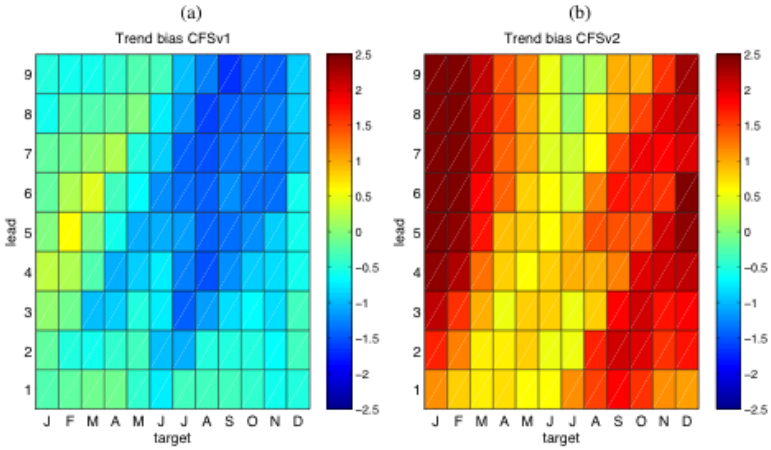

Fig. 9 Bias, relative to observations, in the slope of the linear trend fit over the 1982-2009 (°C per 28 yr) period for Nino3.4 predictions of (a) CFSv1 and (b) CFSv2 as a function of target month and lead time.

Reliability is a measure of the correspondence between the forecast probabilities and their subsequent observed relative frequencies, spanning the full range of issued forecast probabilities. Perfect reliability would be achieved, for example, if for the 20 instances when the above normal Nino3.4 SST category is assigned a probability of 40%, the corresponding later observed anomalies were above normal category in 8 (40%) cases. Here we examine just the 6-month lead predictions, and combine all target months. We form eleven 10%-wide forecast probability bins. Then there are (28×12) = 336 predictions, resulting in an expected average of about 31 predictions per probability bin.

The reliability diagrams for the below and above normal categories are shown for the two CFS model versions, with uncorrected climatologies, in Fig. 10 as the red and green curves, respectively. For each category, forecasts are binned for forecast probability spanning from lowest to highest (x-axis), and are compared to their corresponding observed relative frequencies of occurrence (y-axis). The diagonal line (y=x) represents perfectly reliable forecasts. The plots insets below the main panel show the percentage of forecasts having probabilities in each bin.

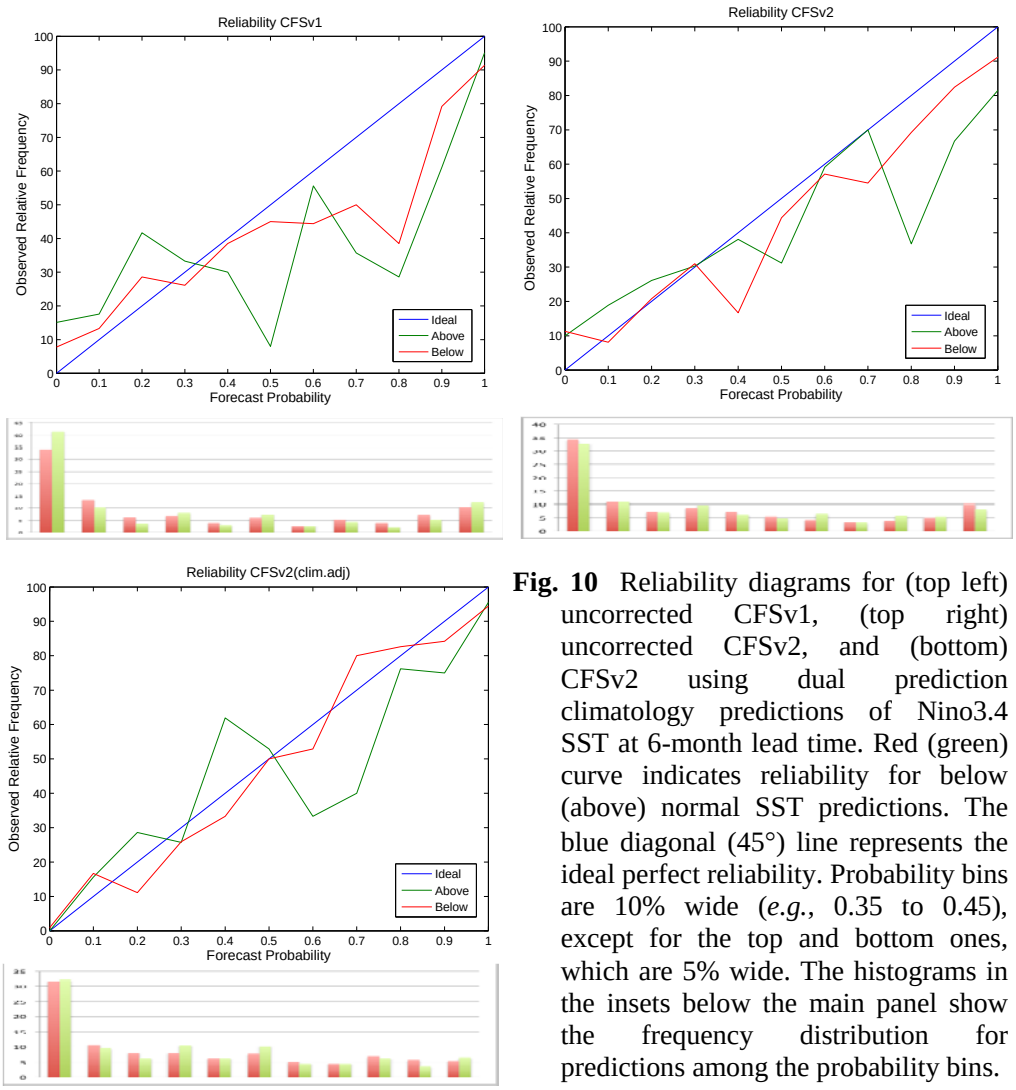

Fig. 10 Reliability diagrams for (top left) uncorrected CFSv1, (top right) uncorrected CFSv2, and (bottom) CFSv2 using dual prediction climatology predictions of Nino3.4 SST at 6-month lead time. Red (green) curve indicates reliability for below (above) normal SST predictions. The blue diagonal (45°) line represents the ideal perfect reliability. Probability bins are 10% wide (*e.g.*, 0.35 to 0.45), except for the top and bottom ones, which are 5% wide. The histograms in the insets below the main panel show the frequency distribution for predictions among the probability bins.

For CFSv1 (Fig. 10a), positive skill is evidenced by the fact that predictions with increasing probabilities for both below and above normal SST tend to be associated with increasing observed relative frequencies of occurrence. The curves are not smooth because of sampling variability related to the somewhat small sample sizes per bin. However, the average slope of both curves is seen to be somewhat less than unity. Thus, forecasts with very low (high) probabilities do not result in comparably low (high) frequencies of occurrence — *i.e.* the forecasts exhibit overconfidence, particularly for probabilities between 0.7 and 0.9 for both categories, and for probabilities of 0.0 for above normal predictions. The inset plot at the bottom shows that the lowest bin (0 to 0.05) is by far the most frequently issued probability, followed by the highest bin (0.95 to 1.00) and the second lowest bin (0.05 to 0.15). The U-shaped curve described by the histogram bars indicates high forecast sharpness (*i.e.*, probabilities deviating strongly and frequently from climatology), and the fact that the slope of the lines is <1 indicates that this degree of sharpness is not warranted, given the level of predictive skill achieved at the 6-month lead time.

The reliability result for the uncorrected CFSv2 (Fig. 10, upper right), while roughy similar to that of CFSv1, shows milder overconfidence: the curves have slope closer to (but still less than) unity, with smaller deviations below the ideal reliability (45°) line for bins for 0.50 and higher probability. Similarly, the lower inset shows that zero-probability predictions for above normal SST that are issued more than 41% of the time by CFSv1 are issued only 33% of the time by CFSv2, indicating a greater expressed forecast uncertainty.

The somewhat more reliable probabilistic predictions seen in CFSv2 than in CFSv1 are attributable to a combination of its generally higher skill (Figs. 1 and 3) and its slightly less sharp, more conservative probabilities that better reflect the true level of uncertainty in the model's reproduction of the ocean-atmosphere system. This outcome is consistent with the greater inflation above unity of the standard deviation ratio of CFSv1 than CFSv2 noted above, especially at medium to long lead times (left panels of Fig. 5). Elimination of the discontinuities in the climatology of the predictions slightly helps to remedy the inflated standard deviation ratio of CFSv2 (lower right panel of Fig. 5), and a similar improvement would be expected

in the reliability analysis. To confirm this expectation, the CFSv2 analysis is applied using dual climatologies for the tercile boundary definitions for the model prediction category. Results (Fig. 10c) indicate an overall slope closer to unity than when using a single prediction climatology; and the observed relative frequencies associated with forecasts of zero probability are less than 2%, suggesting that now such sharply low probabilities are justified in the absence of the spurious change in the forecast climatology within the hindcast period. Likewise, forecasts with 100% probability are met with correctly verifying observations in about 95% of cases for the dual climatologies, rather than only about 80% (90%) for the above (below) normal category without the climatology adjustment. All told, the adjustment results in an improvement in probabilitistic reliability for CFSv2—most noticeably for forecasts deviating most sharply from climatology. That the extreme probability forecasts are most able to be improved in reliability makes sense in view of the expected effect of an artificial mean shift in the climatological on forecasts probabilities that heavily define the reliability curve, both because they are issued frequently (in this example) and because they form the end points of the curve.

3. Conclusion

Given the large amount of time and resources used to achieve an improved CFSv2 compared with the earlier CFSv1, one would expect relatively better predictive skill in CFSv2. Here we examine the skill difference between CFSv1 to CFSv2 in predictions of the ENSO state, as represented by Nino3.4 SST anomaly.

CFSv2 is better able to predict the ENSO state than CFSv1 through the northern spring predictability barrier, the time of year when the need for better predictions is greatest. By contrast, on initial examination CFSv2 appears to fall short of CFSv1 in ENSO prediction skill for northern summer and autumn start times — times for which ENSO prediction is known to be least challenging and skill is highest. However, CFSv2 is found to be affected by a significant discontinuity in initial condition climatology near 1999 associated with a corresponding discontinuity in the high resolution Reanalysis observations generated using CFSv2 (the CFSR). The size and impact of this discontinuity turns out to be most prominent in the tropical Pacific region (Xue *et al.* 2011; Kumar *et al.* 2012). Here, focusing on the skill for Nino3.4 SST anomaly, we highlight differences in skill diagnostics that may be related to model improvement, or on the other hand caused by the discontinuity.

The initial condition discontinuity masks CFSv2's net predictive skill and its general superiority over CFSv1 in prediction Niño3.4 SST. This impediment is most noticeable for northern autumn start times when skill is highest, when CFSv1 already achieves a high skill level that is difficult to exceed. The skill impact of the discontinuity is evaluated by examining skill with versus without the benefit of correction of the discontinuity by defining two separate climatologies from which to form anomalies. After correcting for the 1999 discontinuity, performance of CFSv2 is found to equal or exceed that of CFSv1 more generally at nearly all times of the year in terms of anomaly correlation, RMSE, and interannual standard deviation ratio with respect to the observations. CFSv2 also exhibits better probabilistic reliability than CFSv1, mainly because of its lesser degree of probabilistic overconfidence, and the climatology correction still further increases this margin of superiority. Finally, CFSv2 largely lacks "target month slippage" compared with CFSv1— *i.e.*, it does not tend to verify better on target times earlier than those intended due to being slow to reproduce major transitions in the ENSO state.

Comparing verifications before and after the climatology correction, the measures seen to be most noticeably adversely affected by the uncorrected 1999 change are first the RMSE, and secondly the temporal anomaly correlation. The standard deviation ratio and probabilistic reliability analyses are noticeably, but less dramatically, affected. When one realizes that the problem is one of a changing calibration, it is easy to expect *all* verification measures to be degraded without a correction. A constant miscalibration is easily corrected, and the lack of a correction would not degrade measures such as the anomaly correlation or the slope of the reliability curves. However, a changing miscalibration becomes equivalent to a nonsystematic error unless the time series is examined by eye (*e.g.*, Fig. 2) and the problem identified and treated with a combination of human intervention and machine automation (*i.e.*, choosing the appropriate correction procedure).

CFSv2 is shown to have a larger upward trend in Nino3.4 SST than found in the observations, apart from the 1999 discontinuity. This appears despite the specification of realistic time-evolving CO_2 concentrations—an improvement over CFSv1, which had a fixed and outdated CO_2 concentration. This exaggerated positive trend may be related to a problem in the radiation budget, and indicates a potential area of improvement for the next improved version of CFS.

Although the discontinuity has clearly discernible effects on predictions of ENSO-related SST by CFSv2, they are not so large as to materially degrade the model's predictions of climate across much of the globe. In fact, performance in climate predictions has been found significantly better than that of CFSv1, including for example in the United States during winter when ENSO is a major governing factor (Peng *et al.* 2013) and reproduction of the MJO (Weaver *et al.* 2011). The skill of CFSv2 is found competitive with that of ECMWF system 4 for winter climate predictions over North America, despite relative shortcomings in predictions of ENSO and the globally averaged tropical climate (Kim *et al.* 2012).

References

Barcikowska, M., F. Feser, and H. von Storch, 2012: Usability of best track data in climate statistics in the western north pacific. *Mon. Wea. Rev.*, **140**, 2818-2830.

Barnston, A. G., M. K. Tippett, M. L. L'Heureux, S. Li, and D. G. DeWitt, 2012: Skill of real-time seasonal ENSO model predictions during 2002-11: Is our capability increasing? *Bull. Amer. Meteor. Soc.*, **93**, 631-651.

Behringer, D.W., and Y. Xue, 2004: Evaluation of the global ocean data assimilation system at NCEP: The Pacific Ocean. *Eighth Symposium on Integrated Observing and Assimilation Systems for Atmosphere, Oceans, and Land Surface*, AMS 84th Annual Meeting, Washington State Convention and Trade Center, Seattle, Washington, 11-15.

Chelliah, M., W. Ebisuzaki, S. Weaver, and A. Kumar, 2011: Evaluating the tropospheric variability in National Centers for Environmental Prediction's climate forecast system reanalysis. *J. Geophys. Res. (Atmos.)*, **116**, Art. No. D17107, doi: 10.1029/2011JD015707.

Deser, C., A. S. Philips, and M. A. Alexander, 2010: Twentieth century tropical sea surface temperature trends revisited. *Geophys. Res. Lett.*, **37**, doi:10.1029/2010GL043321.

Ebisuzaki, W., and L. Zhang, 2011: Assessing the performance of the CFSR by an ensemble of analyses. *Clim. Dyn*., **37**, 2541-2550.

Kim, H. M., P. J. Webster and J. A. Curry, 2012: Seasonal prediction skill of ECMWF System 4 and NCEP CFSv2 retrospective forecast for the Northern Hemisphere Winter, *Clim. Dyn.*, **39**, 2957–2973, doi: 10.1007/s00382-012-1364-6.

Kumar, A., J. Bhaskar, and M. L'heureux, 2010: Are tropical SST trends changing the global teleconnection during La Nina? *Geophys. Res. Lett.*, **37**, L12702, doi:10.1029/2010GL043394.

—, M. Chen, L. Zhang, W. Wang, Y. Xue, C. Wen, L. Marx, and B. Huang, 2012: An analysis of the non-stationarity in the bias of sea surface temperature forecasts for the NCEP climate forecast system (CFS) version 2. *Mon. Wea. Rev*., **140**, 3003-3016.

Lyon, B., and D. G. DeWitt, 2012: A recent and abrupt decline in the East African long rains. *Geophys. Res. Lett*., **39**, L02702, doi: 10.1029/2011GL050337.

Peng, P., A. G. Barnston, and A. Kumar, 2013: A Comparison of Skill between Two Versions of the NCEP Climate Forecast System (CFS) and CPC's Operational Short-Lead Seasonal Outlooks. *Weather and Forecasting*, **27**, in press.

Saha, S., and Coauthors, 2006: The NCEP Climate Forecast System. *J. Climate*, **19**, 3483–3517.

—, and Coauthors, 2010: The NCEP Climate Forecast System Reanalysis. *Bull. Amer. Meteor. Soc.*, **91,** 1015-1057. doi: 10.1175/2010BAMS3001.1

—, and Coauthors, 2013: The NCEP Climate Forecast System Version 2. *J. Climate*, **19**, submitted.

Tippett, M. K., A. G. Barnston, and S. Li, 2012: Performance of recent multimodel ENSO forecasts. *J. Appl. Meteor. Climatol.*, **9**, 637–654.

Wang, W., P. Xie, S. H. Yo, Y. Xue, A. Kumar, and X. Wu, 2011: An assessment of the surface climate in the NCEP Climate Forecast System Reanalysis. *Clim. Dyn.*, **37**, 1601-1620. doi: 10.1007/s00382-010-0935-7.

Weaver, S. J., W. Q. Wang, M. Y. Chen, and A. Kumar, 2011: Representation of MJO variability in the NCEP Climate Forecast System. *J. Climate*, **24**, 4676-4694.

Xue, Y., B. Huang, Z.-Z. Hu, A. Kumar, C. Wen, D. Behringer, and S. Nadiga, 2011: An assessment of oceanic variability in the NCEP climate forecast system reanalysis. *Clim. Dyn.*, **37**, 2511-2539, doi:10.1007/s00382-010-0954-4.

Zhang, L., A. K Kumar, and W. Wang, 2012: Influence of changes in observations on reanalysis products: A Case Study for the CFSR. *J. Geophys. Res. - Atmosphere.* Conditionally accepted.

Science and Technology Infusion Climate Bulletin
NOAA's National Weather Service
37th NOAA Annual Climate Diagnostics and Prediction Workshop
Fort Collins, CO, 22-25 October 2012

Improvement of Grand Multi-model Ensemble Prediction Skills for the Coupled Models of APCC/ENSEMBLES Using a Climate Filter

Doo Young Lee[1, 2], Joong-Bae Ahn[2], Karumuri Ashok[3], and Andrea Alessandri[4]

[1]*APEC Climate Center, Busan, Republic of Korea*

[2]*Department of Atmospheric Sciences, Pusan National University, Busan, Republic of Korea*

[3] *Centre for Climate Change Research, Indian Institute of Tropical Meteorology, Pune, India*

[4]*Italian National Agency for New Technologies, Energy and Sustainable Economic Development (ENEA), Roma, Italy*

1. Introduction

In this work, we apply the concept of the climate filter (Lee *et al.* 2011) for potential improvement of a grand MME, derived from a combination of APEC Climate Center (APCC) MME seasonal prediction system (Lee *et al.* 2009) and ENSEMBLES (Weisheimer *et al.* 2009; Alessandri *et al.* 2011) in order to explore whether the methodology can improve the skills of the grand MME, constituent MMEs, and individual models.

2. Data and methodology

2.1 Data

- Target seasons and Periods

The boreal winter (December through February, DJF) hindcast outputs for the period of 1983-2005

- Model data set

Seven coupled models involved in the operational 6-month MME seasonal prediction system of the APCC and five coupled models from the European Commission FP7 project called ENSEMBLES for seasonal to annual predictions – totaling twelve coupled model hindcast sets – are used in this study.

- Observed data set

The atmospheric variables (NCEP-DOE R2, Kanamitsu *et al.* 2002), precipitation (CMAP, Xie and Arkin 1997) and sea surface temperature (OISST V.2, Reynolds *et al.* 2002) from 1983 to 2005 are also used as observations.

2.2 Statistical methods

For MME prediction, we adopt a simple composite method (Peng *et al.*, 2002; Lee *et al.* 2009, 2011), known as simple arithmetic mean of bias corrected predictions, with equal weights to predictions from individual models.

The standard *t*-test (Wilks 1995) is employed to compute the statistical significance of the correlations. The degrees of freedom for the temporal correlation is estimated as N-2, where N is 23, the number of winter seasons during the study period. To find the significance levels for spatial pattern correlations, we use the effective spatial degree of freedom (ESDOF) (Wang and Shen 1999).

Finally, to calculate seasonal anomalies of each model parameter as well as those from observations for each year, we follow the standard leave-one-out cross validation method (Jolliffe and Stephenson 2003). We also use the cross validation method in each target year while applying the climate filter for all hindcast periods.

Correspondence to: Doo Young Lee, APEC Climate Center and Department of Atmospheric Sciences, Pusan National University, Busan, Republic of Korea; E-mail: dylee@apcc21.net.

3. Results

3.1 Climate Filter

At the temporal correlation pattern of Figure 1, high correlations with magnitudes of more than 0.4, significant at 95% confidence level from a *t*-test, are generally located along 10°S-10°N. Especially, there is a strong association of the local rainfall in the central and western tropical Pacific with the zonal circulation.

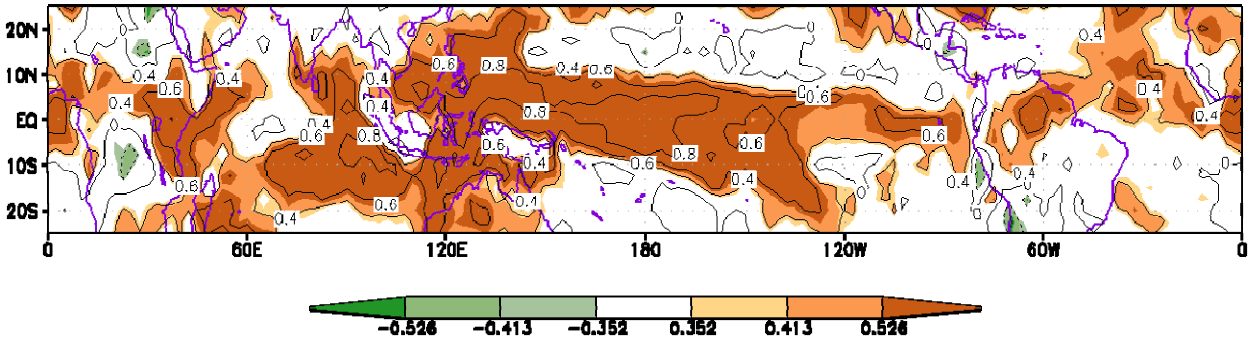

Fig. 1 Temporal correlation patterns between the observed Walker circulation and precipitation for the boreal winter (DJF) during the period of 1983-2005. Shading indicates statistically significant correlation coefficients at the 90% (0.352), 95% (0.413) and 99% (0.526) confidence levels from a Student's two-tailed t-test.

From the relationship in Figure 2, it can be discerned that the strong relationship between the observed Walker circulation with Niño 3.4 (-0.9, significant at 99% confidence level from a *t*-test) is well reproduced by hindcasts of all model Walker circulations. We utilize the coefficient of variation (*i.e.*, the squared correlation coefficient) between the Walker circulation and the Niño 3.4 index as a weight for the Walker circulation field to compute the ENSO-associated Walker circulation. Based on these points, we believe that it is an important measure of model fidelity to predict the tropical rainfall from model simulations of ENSO-associated Walker circulation in the tropical Pacific and also minimum requirement for any model with necessary fidelity.

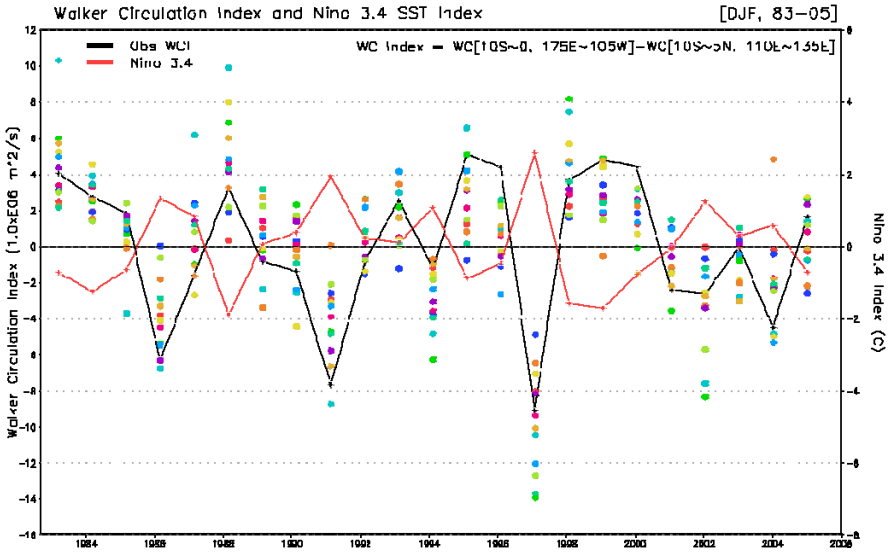

Fig. 2 Time series of SST anomalies from Niño 3.4 (solid red line), and Walker circulation index of observation (solid black line) and individual models (colored circles), which is defined by difference of Walker circulation between the tropical eastern Pacific (10°S-0°, 175°E-105°W) and the tropical western Pacific (10°S-5°N, 110°E-135°E) from 1983 to 2005.

3.2 Evaluation of the hindcast relationship in the tropical Pacific

Specifically, we use two empirical criteria to grade the individual model skills.

(i) The slope of the regression line fitted between the observed and simulated pattern correlations of tropical rainfall and ENSO-associated Walker circulation should be larger than 0.5 and less than 1.5.

(ii) Statistically significant temporal correlation between these observed and simulated pattern correlations is more than 0.5 (significant at ~99% confidence level from a Student's two-tailed *t*-test).

Four out of 12 models, namely, model 2, 5, 8 and 9 (Figures 3b, 3e, 3h and 3i) successfully represent the realistic rainfall relationship with the local ENSO-associated Walker circulation in the tropical Pacific (100°E~60°W, 10°S~10°N) for the boreal winter season.

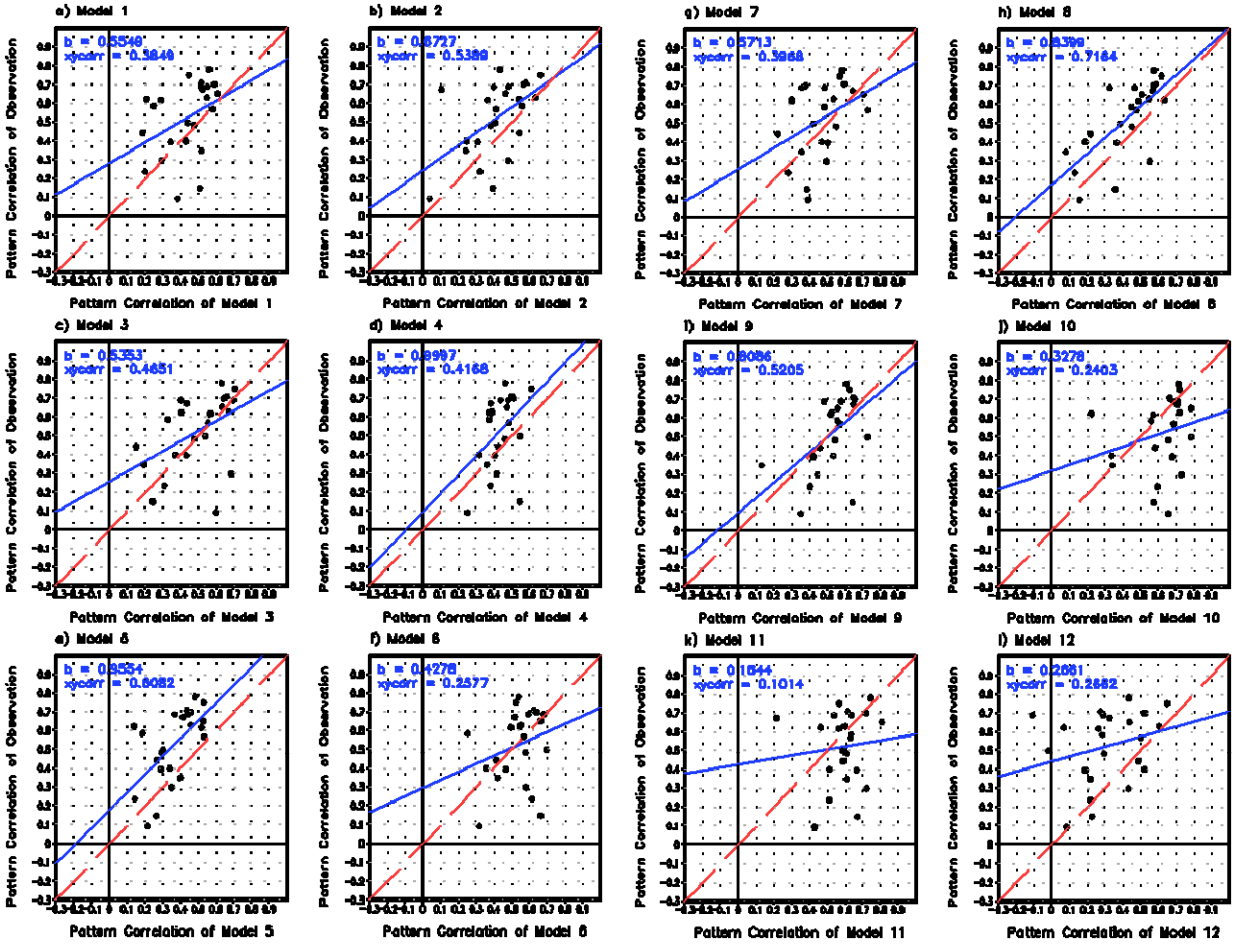

Fig. 3 Scatter diagrams depicting spatial pattern correlation between the ENSO-associated walker circulation and precipitation from observation (Y-axis) over the tropical Pacific region, for 23 boreal winters, plotted against those from the individual models (X-axis). The slope 'b' from the fitted regression line is provided in the upper left. The 'xycorr' represents the temporal correlations of each model with observation.

3.3 Sensitivity of the fidelity of various MME

We implement three separate MME hindcast experiments, which are, for convenience, named as the M12 (essentially a grand MME involving hindcasts from all the 12 models), the A4 (means a filtered grand MME involving hindcasts from the four performing models), and the B8 (uses the rest of the model hindcasts). Figure 4 indicates the time averages of the spatial pattern correlations between the observed and the simulated rainfall and temperature at 850 hPa from all the three MME experiments for six arbitrary regions. In the global and tropical regions, slightly better performances of the M12 are essentially due to the relatively better performances of the B8 predictions in these regions. Meanwhile, in the four extratropical regions, the gap between the MME prediction skills of the A4 and those of the B8 is significantly different.

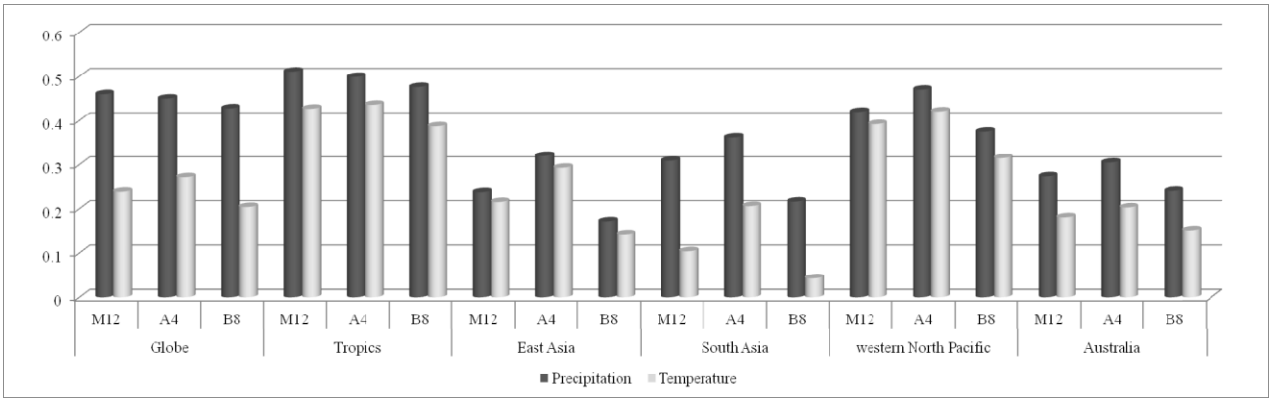

Fig. 4 Time average of pattern correlations between the observed and simulated precipitations and those for the temperature at 850 hPa from M12, A4, and B8 over the six regions of the Global region (0°-360°E, 90°S-90°N), Tropics (0°-360°E, 20°S-20°N), East Asia (90°E-150°E, 20°N-50°N), South Asia (60°E-120°E, 10°N-40°N), western North Pacific (120°E-160°E, 10°N-40°N), and Australia (110°E-180°E, 50°S-10°S).

4. Summary and conclusion

In order to grade the individual model hindcast performances of two different MME systems, we utilize a climate filter concept using evaluation of the relative capabilities of each model. We explore the possible use of this climate filter method to filter models with better fidelity, and finally introduce an optimized MME suite with enhanced seasonal prediction skills. We find that the MME prediction skills from four better performing models are indeed significantly higher as compared to those from the rest of the non-performing models, and those from the all-inclusive 12 model grand MME. This research indicates that the MME is better skilled if models that can reproduce realistic observed feature are used.

References

Alessandri, A., and Co-authors, 2011: Evaluation of probabilistic quality and value of the ENSEMBLES multi-model seasonal forecasts: comparison with DEMETER. *Mon. Wea. Rev.*, **139**, 581-607.

Jolliffe, IT, and D.B. Stephenson, 2003: *Forecast Verification: A Practitioner's Guide in Atmospheric Science*. John Wiley & Sons, Chichester.

Kanamitsu, M., and Co-authors, 2002: NCEP-DOE AMIP-II Reanalysis (R-2). *Bull. Amer. Meteor. Soc.*, **83**, 1631-1643.

Lee, W-J, and Co-authors, 2009: *APEC Climate Center for Climate Information Services*, APCC 2009 Final Report. http://www.apcc21.org/eng/research/pub/repo/japcc040602_lst.jsp

Lee, D.Y., K. Ashok and J.-B. Ahn, 2011: Toward enhancement of prediction skills of multimodel ensemble seasonal prediction: A climate filter concept. *J. Geophys. Res.*, **116**, D06116, doi:10.1029/2010JD014610.

Peng, P., A. Kumar, H. van den Dool, A.G. Barnston, 2002: An analysis of multimodel ensemble predictions for seasonal climate anomalies. *J. Geophys. Res.*, **107**, 4710, doi:10.1029/2002JD002712.

Reynolds, R.W., N.A. Rayner, T.M. Smith, D.C. Stokes, and W. Wang, 2002: An improved in situ and satellite SST analysis for climate. *J. Climate*, **15**, 1609-1625.

Wang, X., and S. S. Shen, 1999: Estimation of Spatial Degrees of Freedom of a Climate Field. *J. Climate*, **12**, 1280-1291.

Weisheimer A, and Co-authors, 2009: ENSEMBLES: A new multi-model ensemble for seasonal-to-annual predictions-Skill and progress beyond DEMETER in forecasting tropical Pacific SSTs. *Geophys. Res. Lett.*, **36**, L21711, doi:10.1029/2009GL040896.

Wilks, D.S., 1995: *Statistical Methods in the Atmospheric Sciences*. Academic Press, New York.

Xie, P., P.A. Arkin, 1997: Global precipitation: A 17-year monthly analysis based on gauge observations, satellite estimates, and numerical model outputs. *Bull. Amer. Meteor. Soc.*, **78**, 2539-2558.

Science and Technology Infusion Climate Bulletin
NOAA's National Weather Service
37th NOAA Annual Climate Diagnostics and Prediction Workshop
Fort Collins, CO, 22-25 October 2012

Assessing the Daily and Radiative Performence of the CFSR, ERA-interim and MERRA

Wesley Ebisuzaki[1], Li Zhang[1, 2], S. K. Yang[1, 2], Arun Kumar[1]

[1]*Climate Prediction Center, NCEP/NWS/NOAA, College Park, MD*
[2]*Wyle Information Systems, McLean, Virginia*

1. Introduction

Uses of reanalyses tend to fall into one of three categories, interest in the instantaneous or daily analyses, interest in the physical cycles diagnosis often conducted through a budget study and interest in the monthly to longer term variability often for climate monitoring.

In the first part, this study uses the procedure of Ebisuzaki and Zhang (2011) to evaluate the performance of the daily analyses from the newer reanalyses (CFSR, ERA-interim and MERRA). Using an ensemble of operational analyses as the reference, the various reanalyses were examined for the year 2007. For the tropospheric variables, the newer reanalyses are better than the previous generation of reanalyses. In comparison with the operational analyses, the ERA-interim was the best of the newer reanalyses for the year 2007.

In the second part of this study we look at the top-of-the-atmosphere (TOA) radiation budget. The TOA radiation is the primary driver behind the atmospheric circulation and can be directly compared with satellite observations. For satellite observations, we use the Clouds and Earth's Radiant Energy System (CERES) level 3 data. The newer reanalyses have a global net upward radiative flux of 0.6 to 1.4 W/m/m (3/2000-2/2009) which is much better than the older reanalyses.

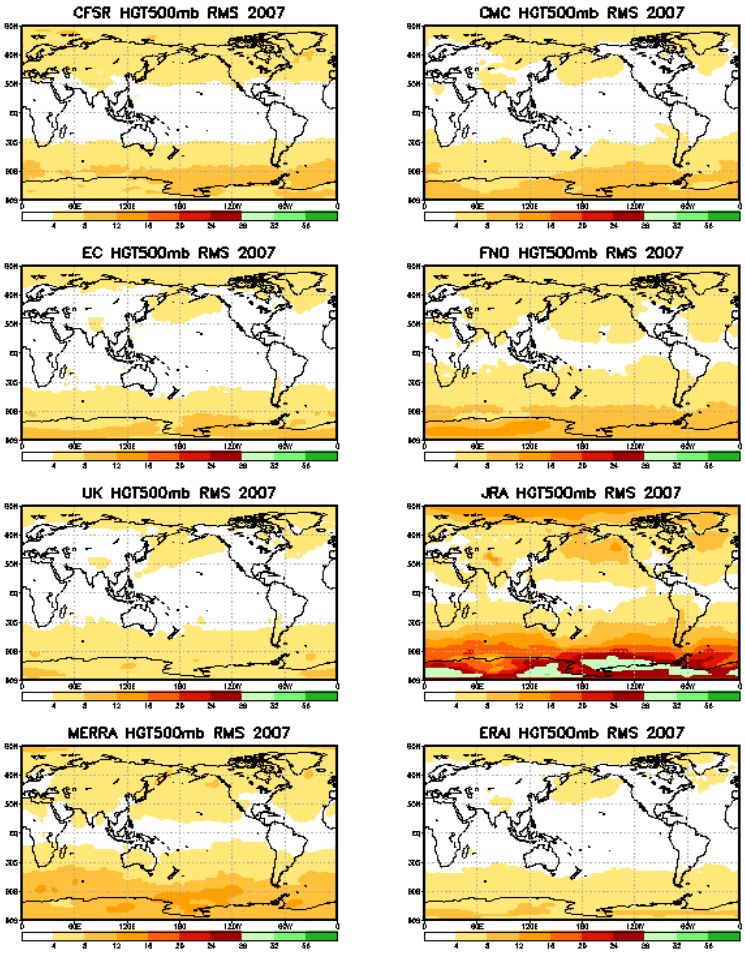

Fig. 1 Analysis of daily 500 mb height variability described by RSM of the various analyses (indicated in each panel's title) from the ensemble mean of operational analyses for 2007.

2. Data

i) Ensemble members: twice daily (0000 and 12000 UTC) for 2007 on a 2.5 x 2.5 degree grid

CFSR: Reanalysis from CFS version 2 (used in place of NCEP GDAS/FNL)
CMC: Operational analyses from the Canadian Meteorological Centre

Correspondence to: Wesley Ebisuzaki, Climate Prediction Center, NCEP/NWS/NOAA, 5830 University Research Court, College Park, MD 20740-3818; E-mail: Wesly.Ebisuzaki@noaa.gov.

EC: Operational analyses from the European Centre for Medium Range Weather Forecasts

FNO: NOGAPS analysis from the Fleet Numerical Ocean and Meteorological Center

UK: Operational analysis from the UK MetOffice

ii) Observed TOA radiation: CERES level 3 (v2.6r, 12/2011) March 2000-Dec 2011, monthly means

iii) Reanalyses: CFSR (NCEP), ERA-interim (ECMWF), MERRA (GMAO/NASA), JRA-25 (CRIEPI, JMA), R1 (NCEP/NCAR), R2 (NCEP/DOE)

3. Results

a) Analyses of daily 500 mb height variability (2007)

Using the ensemble of operational analyses as the "truth", the RMS of the various analyses from the ensemble mean for the 500 mb Height RMS are plotted for 2007. Figure 1 shows the modern analyses have less land-sea contrast, indicating that the newer systems are making a better use of satellite data. The ERA-interim is the best reanalysis for this statistic.

b) Analysis of daily 200 mb zonal wind variability (2007)

The RMS of the 200 mb zonal wind (UGRD) analyses from the mean of the operational ensemble is shown by Figure 2. Again the land-sea contrast is stronger in the older reanalyses. Of the newer reanalyses, the ERA-interim is best for this variable followed by CFSR and MERRA. The eastern tropical Pacific was a region of higher uncertainty.

Many tropospheric fields were checked using the same procedure. The general result was that ERA-interim was best of the three newer reanalyses in capturing the daily variability.

c) January OLR climatologies (2001-2011)

The observed Outgoing Long-wave Radiation (OLR) from CERES is compared with the various reanalyses on

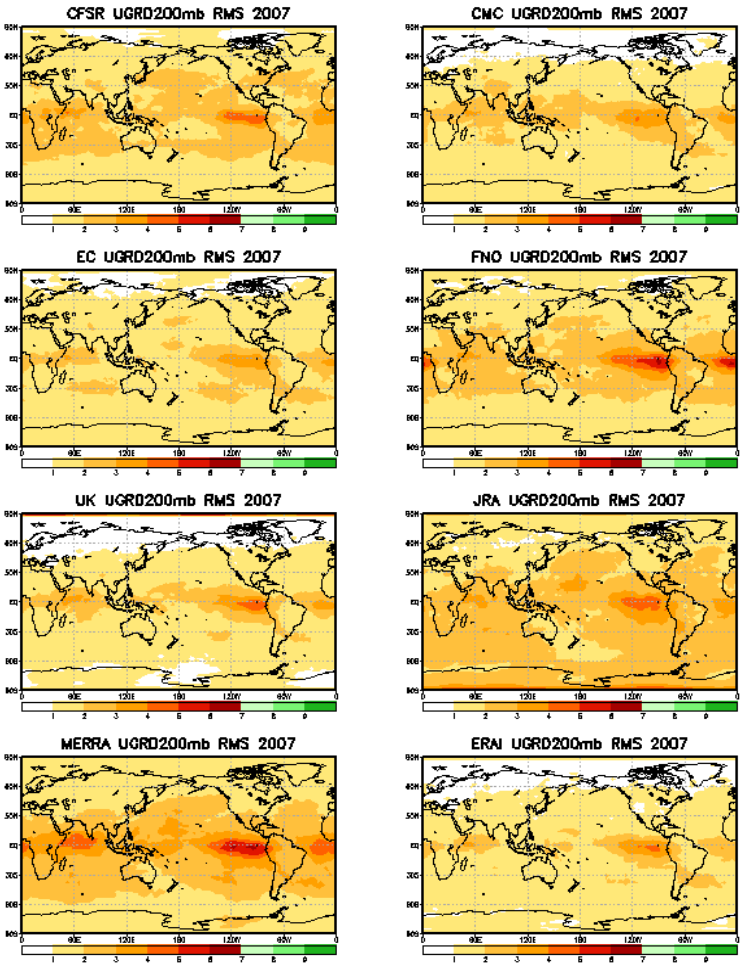

Fig. 2 Same as Figure 1 except for 200 mb zonal wind.

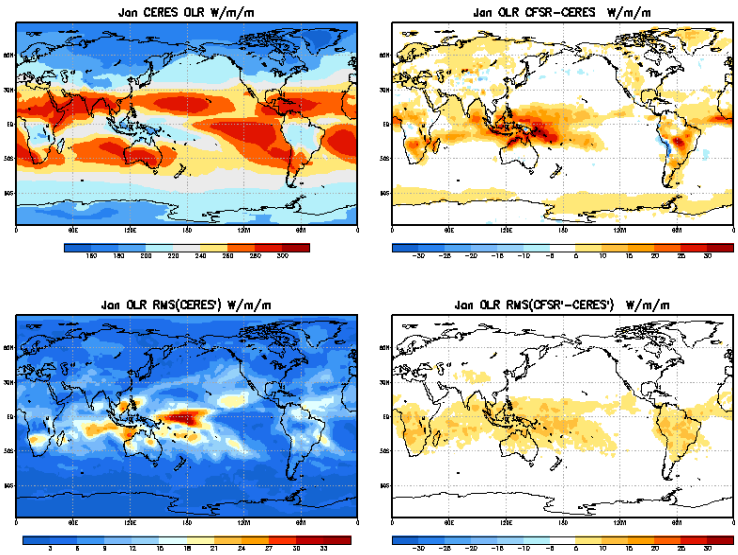

Fig. 3 Left column: observed January OLR (top) and RMS (bottom). Right column: the differences between CFSR and the observed January OLR (top) and the RMS of (CFS-OBS) anomalies.

climatological mean and variability of anomalies. The comparison with the January means is shown (Figs. 3-5). Overall there is no clear best reanalysis for January OLR. "Best" depends on the region of interest. The newer reanalyses are much better than the older R1, R2 (not shown) and JRA-25.

d) January outgoing short-wave radiation

The comparison of observed January outgoing short-wave radiation (OSR) with that of the reanalyses is shown in Fig. 6. It revealed the OSR wasn't as well represented as the OLR. However, the OSR showed a similar feature. The systematic error was larger than the error in the anomalies.

e) Trends in the OLR and OSR

The global mean OLR, OSR and the net radiation at the top of atmosphere (TOA) are inspected. OLR shows CFSR, ERA-interim and MERRA are 2-6 W/m/m more than CERES (Fig. 7a). OSR shows CFSR, ERA-interim and MERRA are clustered about CERES. The newer reanalyses display some trends (Fig. 7b). The net global radiation shows the March 2000 - February 2009 (net) upward flux is 0.6 (CFSR), 1.4 (ERA-interim), and 0.7 (MERRA) W/m/m. The older R1 and R2 have a 13 and 7 W/m/m (respectively) net radiative upward flux (Fig. 7c).

4. Summary

The CFSR was very good representing

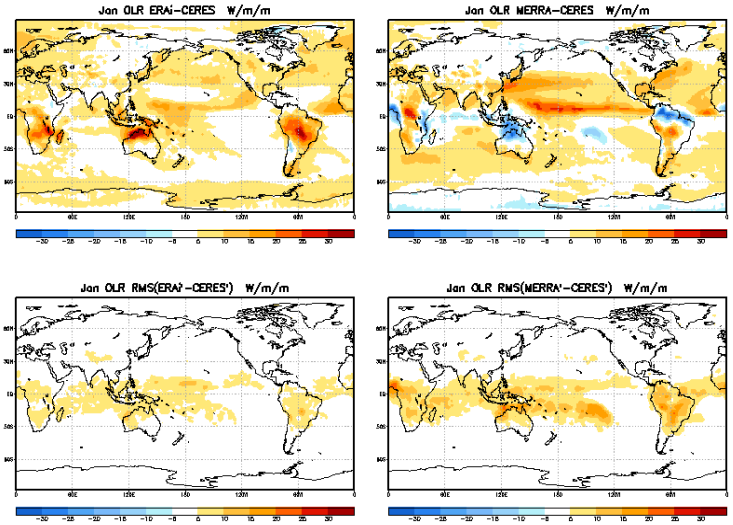

Fig. 4 Same as the right column of Figure 3 but for ERA-interim (left) and MERRA (right).

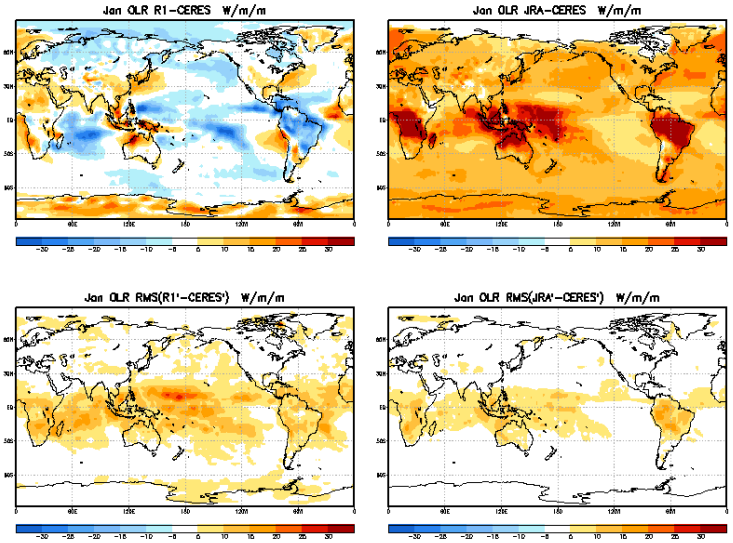

Fig. 5 Same as the right column of Fig. 3 but for R1 (left) and JRA-25 (right).

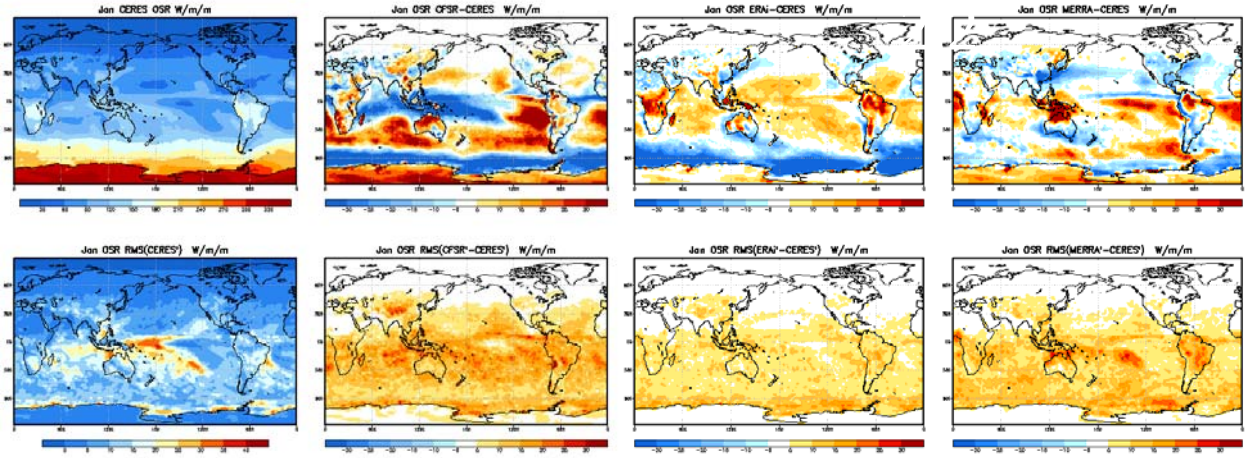

Fig. 6 January OSR (top left) and RSM of anomalies (bottom left) for 2001-2011 from CERES in comparison with counter-parts of CFSR (2nd column), ERA-interim (3rd column) and MERRA (last column on right).

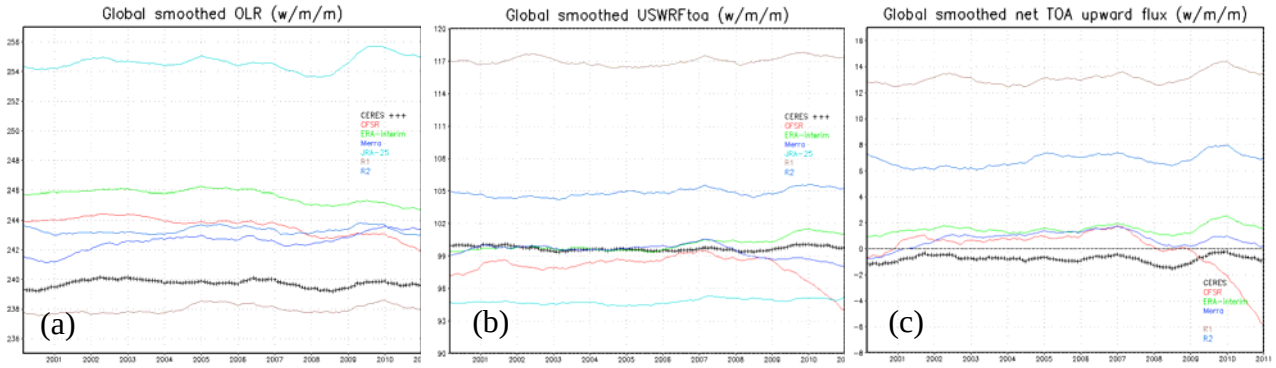

Fig. 7 Global OLR (a), OSR (b) and the net radiation (c) with a 12-month running mean.

the daily variability in the current environment. For various fields examined, the CFSR did well and was comparable to the operational models *circa* 2007. Compared with the older R1 and R2, the CFSR did better at capturing the daily variability. The biggest improvements were over the oceans which were the result of improved satellite instruments and the improved data assimilation of the satellite data. Over the well observed land areas, the improvements over R1 and R2 were smaller. Overall, the ERA-interim did the best on the primary tropospheric fields.

The newer reanalyses have improved their OLR in both the systematic and the time varying components with the systematic error being larger than the errors in the anomalies. The OSR was not as well represented as the OLR.

The global TOA radiation budget was better simulated in the recent reanalyses. The net global flux averaged 0.6 (CFSR), 1.4 (ERA-interim) and 0.7 (MERRA) W/m/m upward for the period March 2000-Feb 2009.

All the newer reanalyses showed trends in the TOA fluxes, some larger than others.

References

Ebisuzaki, W., and L. Zhang, 2011: Assessing the performance of the CFSR by an ensemble of analyses. *Clim. Dyn.*, **37**, 2541-2550.

Science and Technology Infusion Climate Bulletin
NOAA's National Weather Service
37th NOAA Annual Climate Diagnostics and Prediction Workshop
Fort Collins, CO, 22-25 October 2012

Combining Sub-seasonal and Seasonal Precipitation Forecasts over Indonesia

Andrew W. Robertson[1], Dong Eun Lee[2], Vincent Moron[3,1], and Shuhua Li[1]

[1]*International Research Institute for Climate and Society, Columbia University, New York*
[2]*Lamont-Doherty Earth Observatory, Columbia University, New York*
[3]*Aix-Marseille University, France*

1. Introduction

The onset of Maritime Continent monsoon during September to December is strongly influenced by El Niño-Southern Oscillation (ENSO). Timely information on ENSO status has been known to be helpful for the Indonesian agriculture, as it enables the local farmers to plan their rice planting (Naylor *et al.* 2001). Using Tropical Pacific July sea surface temperature (SST) as a predictor, Moron *et al.* (2009) were able to construct onset date forecasts that exhibited some skill over parts of Indonesia.

Precipitation over the Maritime Continent is also strongly influenced by the Madden-Julian Oscillation (MJO), leading to the hypothesis that SST-based forecasts of monsoon onset dates could be improved using MJO information. The goal of this work is to develop and test a statistical forecast model of monsoon onset date over Indonesia, incorporating both ENSO and MJO information.

2. Data

Two precipitation data sets are used to derive the onset dates: gridded pentad CMAP on 2.5×2.5 from 1979-2009 (Xie and Arkin 1996), and daily rainfall gauge data from 99 stations over Indonesia, compiled from the NCDC and CPC GSOD datasets, and the dataset of Hamada and Sribimawati (1998). The local onset is defined when the accumulated precipitation reaches 20 cm, counted from July 30. Figure 1 shows the mean onset dates thus calculated, which compare well with previous estimates (Moron *et al.* 2009).

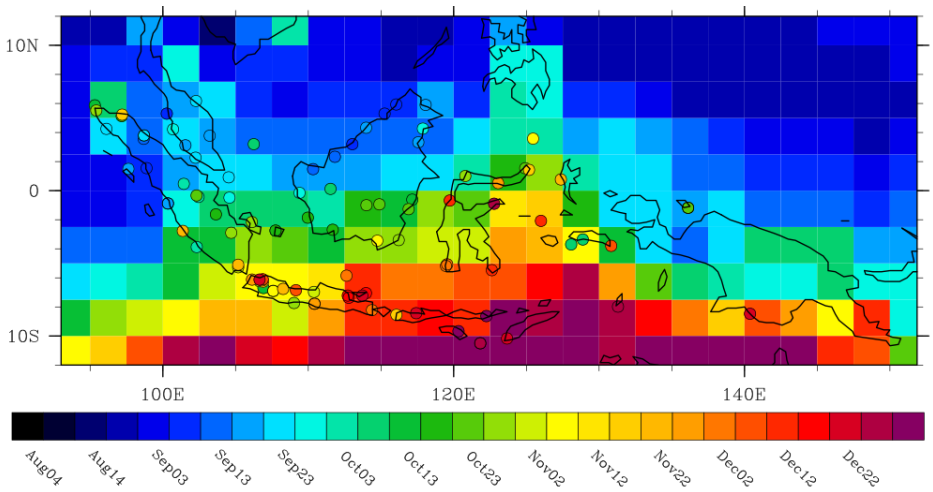

Fig. 1 Onset dates averaged over all years 1979-2009, derived from gridded CMAP and station data.

Predictor variables are constructed from OLR pentad data obtained from NOAA-NCEP-CPC (Liebmann and Smith, 1996), and NOAA ERSST data (Smith *et al.* 1998), both 1979–2009.

3. Methodology

Empirical forecast models for local onset date are built using multivariate (pattern) regression based on cross-validated Canonical Correlation Analysis (CCA), using IRI's CPT Toolkit (http://iri.columbia.edu/climate/tools).

Correspondence to: Andrew W. Robertson, International Research Institute for Climate and Society, Columbia University, NY; E-mail: awr@iri.columbia.edu.

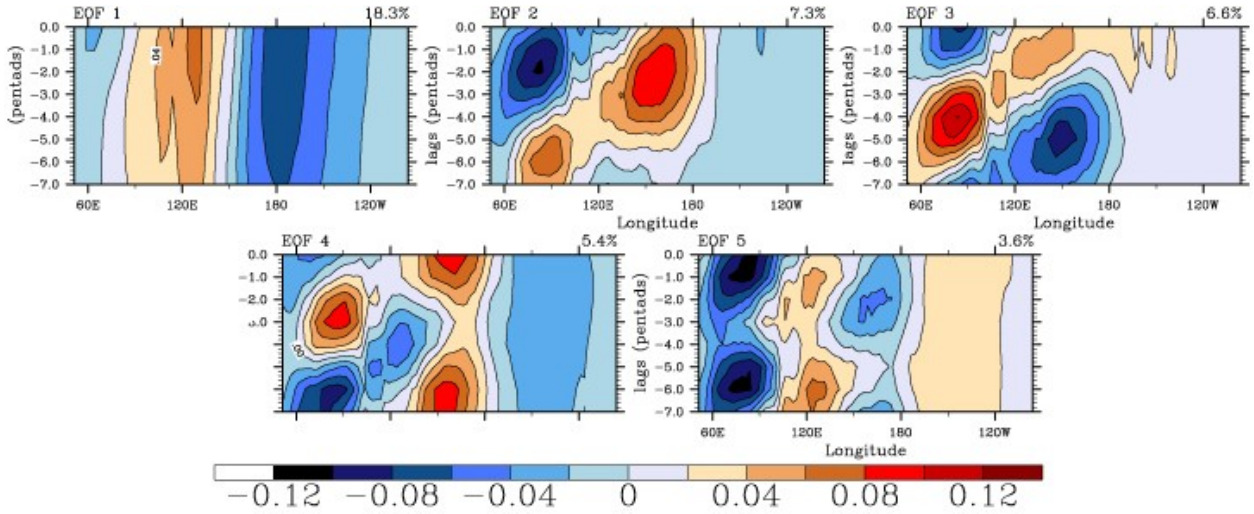

Fig. 2 Leading 5 extended EOFs of latitude-averaged OLR [10ºS-10ºN]. Percentage of variance explained is given above each panel.

In the case of OLR, extended EOFs are applied to the OLR data, so as to include the 8 pentads before the forecast start date. Start dates are taken at each pentad, beginning Jul 15–19, and ending Dec 13–17. The CCA uses PCs of 5 extended EOFs (EEOFs) of latitude-averaged OLR [10ºS-10ºN] vs. PCs of onset date (4 EOF modes), for the Aug–Dec season, with the seasonal cycle subtracted from the OLR data.

4. Results

The leading five EEOFs of latitude-averaged OLR are shown in Fig. 2 as a function of time lag. The leading mode varies slowly in time, and its timeseries is dominated by interannual periods (not shown). EEOFs 2-4 are dominated by sub-seasonal periods and eastward propagation.

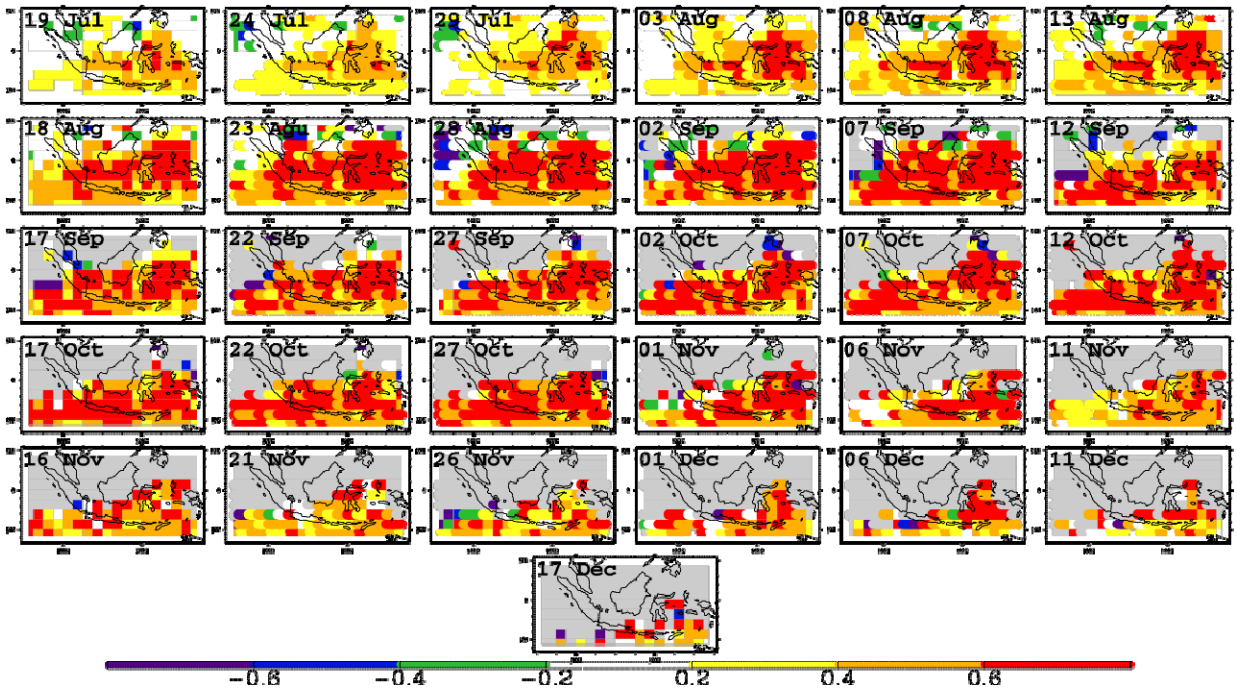

Fig. 3 Anomaly correlation skill of cross-validated hindcasts of local onset date, based on OLR conditions at consecutive pentads. The start dates are given in each panel.

Hindcasts of gridded onset date were made at different lead times, and their cross-validated anomaly correlation skill plotted in Fig. 3. Each panel shows the skill for a particular pentad start date. Skill levels rise as the climatological onset date approaches, which propagates seasonally from north to south (Fig. 1). Grey regions in Fig. 3 denote locations where the climatological onset date has already passed. We have repeated the hindcasts using only EEOFs 2-4, thus filtering out the ENSO-related predictive information in EEOF 1. The resulting skill levels are generally much lower, except over eastern Java during Nov–Dec (*i.e.* close to onset date there, not shown).

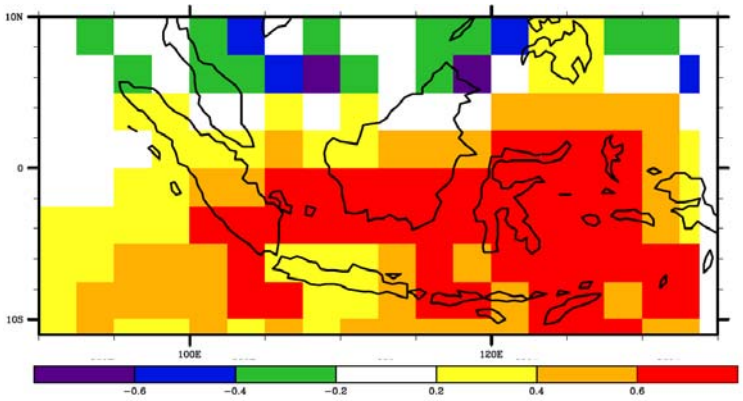

Fig. 4 Anomaly correlation skill of cross-validated hindcasts, based on July SST.

The OLR-based hindcasts in Fig. 3 can be compared with July SST-based hindcasts, shown in Fig. 4. Skill levels based on SST and OLR are comparable, but the latter are markedly higher locally as the onset approaches.

4. Concluding remarks

The work reported here suggests that subseasonal OLR observations have the potential to augment the skill of onset date forecasts over Indonesia at shorter lead times, compared to that obtained from July SST. The regions of skill at shorter lead times are found to migrate southward with the monsoon. Most of the increased skill is found to be associated with updating of the interannual predictive signal, rather than to intra-seasonal modes of variability.

Acknowledgements. This work was supported by USAID award AID-OAA-A-11-00011, and by NOAA Climate Program Office through a block grant to the IRI.

References

Hamada, J.-I., and T. Sribimawati, 1998: Catalogue and sample plotting of daily rainfall for 1961–90 at 157 stations in Indonesia. *Climatology of Indonesian Maritime Continent*. M.D. Yamanaka, Ed., Research Report Topic 08041107, Kyoto University, 17-90.

Liebmann, B., and C.A. Smith, 1996: Description of a complete (interpolated) outgoing longwave radiation dataset. *Bull. Amer. Meteor. Soc.*, **77**, 1275 –1277.

Moron, V., A. W. Robertson, and R. Boer, 2009: Spatial coherence and seasonal predictability of monsoon onset over Indonesia. *J. Climate*, **22**, 840-850.

Naylor, R., W.P. Falcon, D. Rochberg, and N. Wada, 2001: Using El Nino/Southern Oscillation climate data to predict rice production in Indonesia. *Climatic Change*, **50**, 255-265.

Smith, T.M., R.W. Reynolds, T. C. Peterson, and J. Lawrimore, 2008: Improvements to NOAA's historical merged land-ocean surface temperature analysis (1880-2006). *J. Climate*, **21**, 2283-2296.

Xie, P., and P. A. Arkin, 1996: Analyses of global monthly precipitation using gauge observations, satellite estimates, and numerical model predictions. *J. Climate*, **9**, 840 -858.

Science and Technology Infusion Climate Bulletin
NOAA's National Weather Service
37th NOAA Annual Climate Diagnostics and Prediction Workshop
Fort Collins, CO, 22-25 October 2012

Homogeneous and Heterogeneous Predictability and Forecast Skill in MME

Huug van den Dool[1], Emily Becker[1] and Malaquias Pena[2]

[1]*Climate Prediction Center, NCEP/NWS/NOAA, College Park, MD*
[2]*IMSG at Environmental Modeling Center, NCEP/NWS/NOAA*

1. Introduction

Forecast skill and potential predictability of 2 m temperature are assessed using hindcast data from Phase 1 of the National Multi-Model Ensemble (NMME) project. Forecast skill was examined using the anomaly correlation (AC) of the ensemble mean (EM) of an individual model forecast against the observed value. Predictability was considered from two angles: homogeneous, where one model is verified against a single member from its own ensemble, and heterogeneous, where a model's EM is compared to a single member from another model. This study provides insight both into the NMME and its contributing models and into the physical predictability of the 2 m temperature field.

2. The National Multi-Model Ensemble project

The NMME is a forecasting system consisting of coupled models from U.S. and, more recently, Canadian modeling centers. The multi-model ensemble approach has been proven to produce better prediction quality than any single model ensemble, motivating the NMME undertaking. The environmental variables included

	Hindcast Situation YEAR 1					Model resident Resolutions		
	Start months available NOW	Period	Members	Arrangement of Members	Lead (months)	Atmosphere	Ocean	Reference
NCEP-CFSv1	12	1981-2009	15	1st 0Z +/-2days, 11th 0Z+/-2d, 21st 0Z+/-2d	0-9	T62L64	MOM3L40 0.30 deq Eq	Saha et al 2006
NCEP-CFSv2	12	1982-2010	24(28)	4 members (0,6,12,18Z) every 5th day	0-9	T126L64	MOM4 L40 0.25 deg Eq	Saha et al 2012
GFDL-CM2.1	12	1982-2010	10	All 1st of the month 0Z	0-11	2x2.5deg L24	MOM4 L50 0.25 deg Eq	Delworth et al 2006
IRI-Echam4-f	12	1982-2010	12	All 1st of the month	0-7	T42L19	MOM3 L25 0.5 deg Eq	DeWitt MWR2005
IRI-Echam4-a	12	1982-2010	12	All 1st of the month	0-7	T42L19	MOM3 L25 0.5 deg Eq	"
NCAR-CCSM3.0	12	1982-2010	6	All 1st of the month	0-11	T85L26	POP L40 0.3 deg Eq	Kirtman and Min 2009
NASA	12	1981-2010	6	1 member every 5th day as CFSv2	0-9	1x1.25deg L72	MOM4 L40 0.25 deg Eq	Rienecker et al 2008

Table 1 All models included in the National Multi-Model Ensemble project, year 1 of Phase 1 (August 2011 – August 2012).

Correspondence to: Huug van den Dool, Climate Prediction Center, NCEP/NWS/NOAA, 5830 University Research Court, College Park, MD 20740-3818; E-mail: Huug.Vandendool@noaa.gov.

in the first year of Phase I (Aug. 2011 – July 2012) were 2m surface temperature, SST, and precipitation rate; real-time and archived forecast graphics from Aug. 2011 – present are available at www.cpc.ncep.noaa.gov/products/NMME. Hindcast and forecast data is archived at the International Research Institute for Climate and Society (IRI), accessible from the NMME homepage. Table 1 lists the models included in the 1st year of Phase 1. All model outputs have 1.0° latitude by 1.0° longitude resolution and forecast leads of 1 – 7 months. 29 years of hindcasts (1982-2010) were available for all models except CFSv1 (28 years: 1982-2009). Model real-time forecasts are produced by no later than the 8th of each month, and graphical forecasts are available on the 9th of each month. Phase I forecasts were all delivered on time in year 1.

3. Forecast skill and predictability

This study assessed prediction skill, homogeneous predictability, and heterogeneous predictability for the 29 years of hindcasts for all models, using the anomaly correlation (AC). The AC is a measure of the association between the anomalies of (usually) gridpoint forecast and observed values (Wilks 1995, van den Dool 2007). By "prediction skill", we mean one model's ensemble mean (EM) forecast versus the observed value. The verification field for 2 m temperature (T2m) is the station observation-based GHCN+CAMS (Fan and van den Dool 2008). GHCN+CAMS has a native resolution of 0.5˚ latitude x 0.5˚ longitude, and was regridded to 1.0˚ x 1.0˚ for this study.

One common method of defining potential predictability, *i.e.* the physical extent to which a parameter can be predicted under the best of circumstances, is to evaluate one model forecast versus another (Lorenz 1982). Hence, we are testing how effective the model is at predicting itself, and therefore the limit of predictability, if we assume the model is a replica of reality. In this context, we apply the so-called 'perfect' model assumption, *i.e.* the forecast and proxy-observation are taken from the same world and there are no systematic errors to be corrected. Homogeneous predictability assesses one model's EM, based on N-1 members, against the one member that is left out (the proxy-observation). Heterogeneous predictability refers to one model's EM (based on all N members) versus one member of another model.

All values in Table 2 represent the 29-year hindcast timeseries. Leads 1-3, and all 12 start months are combined, and the area-averages are done over all land north of 23°N and south of 75°N. Model anomalies are relative to each model's individual climatology (from the 29-year reforecast). No cross-validation is applied for the prediction skill calculations, which may be a problem, except for homogeneous predictability.

TMP2m Northern Hemisphere Leads 1-3

	cfsv1	cfsv2	echa ma	echa mf	gfdl	nasa	ncar	obs (EM skill)	EM RMSE (C)	EM SD
cfsv1 EM	0.19	0.08	0.05	0.06	0.07	0.09	0.04	0.06	2.07	0.81
cfsv2 EM	0.09	0.27	0.09	0.08	0.16	0.19	0.01	0.19	1.98	0.77
echama EM	0.04	0.08	0.15	0.16	0.08	0.08	0.05	0.08	2.06	0.76
echamf EM	0.06	0.07	0.16	0.15	0.08	0.08	0.05	0.07	2.07	0.76
gfdl EM	0.06	0.14	0.07	0.06	0.25	0.15	0.01	0.15	2.08	1.05
nasa EM	0.07	0.14	0.07	0.05	0.15	0.27	0.00	0.14	2.06	0.93
ncar EM	0.03	0.01	0.04	0.04	-0.01	0.00	0.12	-0.01	2.24	1.07
singmem & obs SD	2.28	2.09	2.13	2.09	2.37	1.99	2.26	2.14		

Table 2 Anomaly correlations showing 2 m temperature forecast skill (model ensemble mean (EM) verified against observations), homogeneous predictability (model EM of N-1 members verified against remaining member), and heterogeneous predictability (model EM verified against a single member of another model) for the seven models in NMME Phase 1. ACs are aggregated over leads 1-3, all start months, land 23°N – 75°N. Also shown are standard deviation for each model's EM (EM SD, right column) and a single member (singmem & obs SD, lower row).

4. Results

The following discussion refers to Table 2. First, some comments on the size of the anomalies. The standard deviation (sd; bottom row) of all models (*i.e.* from individual model runs) agrees very well with the observations; all are in the range of 2.0° - 2.4°C. This is high praise, and different from earlier impressions (mainly from Demeter) that models are underdispersive. The sd of

the model ensemble means (EM; far right column) is about 0.75° to 1.0°C, which is appropriately smaller than the sd of either the individual ensemble members or the observations. This decrease in sd follows from damping of the noise (leaving mainly the signal in the EM) by 1/sqrt(N), where N is the number of (effectively) independent ensemble members. Models with higher N have a greater reduction of their sd.

Prediction skill, measured here by the AC (blue column), varies from -0.01 to +0.19. These are modest numbers, but +0.19 is highly significant because it is based on a huge sample. (Also, a trustworthy +0.19 tends to correspond to large areas and many targets times with little or no skill at all and a few areas and limited target times with much higher skill.) The homogeneous predictability (the yellow diagonal) ranges from 0.12 to 0.27. This is higher than the reported skill (<= 0.19), which means that we can do better eventually, but not hugely so. It is probably disappointing that among the seven independent opinions about predictability, none is better than 0.27, leaving not much to pick from. The heterogeneous predictability ranges from 0.0 to 0.19, exactly the range of skill already achieved. Heterogeneous predictability and the actual skill suffer equally from a mismatch in climate between model and verification – only homogeneous predictability estimates are based with justification on a perfect model assumption. The days when models predicted each other better than they predict reality appear to be over (at least for monthly means at long lead). In summary, all models predict themselves better than they predict other models (or reality).

Regarding heterogeneous predictability (black off-diagonal elements), we note that Table 2 is largely symmetric. This means that “to predict” and “to be predicted” is similar, *i.e.* if Model A (EM) can predict Model B (single member), then the reverse is also true. Curiously, the NCAR model is exceptional in a way: it has a hard time to predict anomalies in the other models, or to be predicted by the other models. In and of itself we appreciate orthogonal behavior, but since NCAR also poorly verifies against the observations, its orthogonality may be erroneous. The trio GFDL, NASA, CFSv2 correlates the most to each other, and have the highest skill against observations. That raises (unaddressed) questions of redundancy. The two IRI models predict each other almost as well as they predict themselves. These models are in fact the same, and our decision to treat the fully coupled ensemble of 12 and the anomaly coupled ensemble of 12 as two separate ensembles may be debatable. (At IRI the two sets were merged into one ensemble.) The CFSv1 and CFSv2 have a shared pedigree obviously, but in contrast to the IRI, the two NCEP model do not predict each other very well.

We finally note that prediction skill is low at present for NCAR and the two IRI-ECHAM models, and this is in part because these models have only ocean initialization, *i.e.* their atmosphere and land initial state is random and unlikely to be realistic. This impacts skill of predicting T2m negatively. CFS, GFDL and NASA attempt to have a realistic atmosphere and land initial state, in addition to a realistic initial ocean.

Acknowledgements: Other team members: Suranjana Saha, Peitao Peng; all data suppliers (NCAR, GFDL, NASA, IRI *etc.*), funding agents (CPO *etc*.).

References

Fan, Y., and H. van den Dool, 2008: A global monthly land surface air temperature analysis for 1948-present. *J. Geophys. Res.*, **113**, D01103, doi:10.1029/2007JD008470.

Lorenz, E. N., 1982: Atmospheric predictability experiments with a large numerical model. *Tellus*, **23**, 243-254.

Van den Dool, H., 2007: *Empirical Methods in Short-Term Climate Prediction*. Oxford University Press, 215 pp.

Wilks, D., 1995: *Statistical Methods in the Atmospheric Sciences*. Academic Press, 467 pp.

Science and Technology Infusion Climate Bulletin
NOAA's National Weather Service
36th NOAA Annual Climate Di7agnostics and Prediction Workshop
Fort Collins, CO, 22-25 October 2012

Evaluation of the National Multi-Model Ensemble System for Seasonal and Monthly Prediction

Emily Becker[1], Qin Zhang[1], Huug van den Dool[1], Suranjana Saha[2], Peitao Peng[1], Malaquias Peña[2], Patrick Tripp[2], and Jin Huang[1]

[1]*Climate Prediction Center, NCEP/NWS/NOAA*
[2]*Environmental Modeling Center, NCEP/NWS/NOAA*

1. Introduction

The National Multi-Model Ensemble (NMME) project supplies routine guidance to users. Phase I (experimental) ran from August 2011 to July 2012. Phase II is in operation now. This assessment focuses on the results of Phase I, and includes diagnostic verification of NMME seasonal and monthly prediction. Evaluation metrics include anomaly correlations (AC) calculated from 29 years of hindcasts (1982-2010) and Heidke skill scores (HSS) for the realtime seasonal and monthly 2 meter surface temperature (T2m) and precipitation rate (Prate) forecasts from August 2011 to July 2012 over the contiguous United States. Prediction of the winter for December-January-February (DJF) 2011/12 is used as a case study. This study is motivated by the desire to provide skill benchmarks for future improvements of the NMME seasonal and monthly prediction system.

2. The National Multi-Model Ensemble project

The NMME is a forecasting system consisting of coupled models from U.S. and Canadian modeling centers. The multi-model ensemble approach has been proven to produce better prediction quality than any single model ensemble, motivating the NMME undertaking. The environmental variables included in Phase I (Aug. 2011 – July 2012) were T2m, sea surface temperature (SST), and Prate; and realtime and archived forecast graphics from Aug. 2011 – present are available at www.cpc.ncep.noaa.gov/products/NMME. Hindcast and forecast data are archived at the International Research Institute for Climate and Society (IRI), accessible from the NMME homepage.

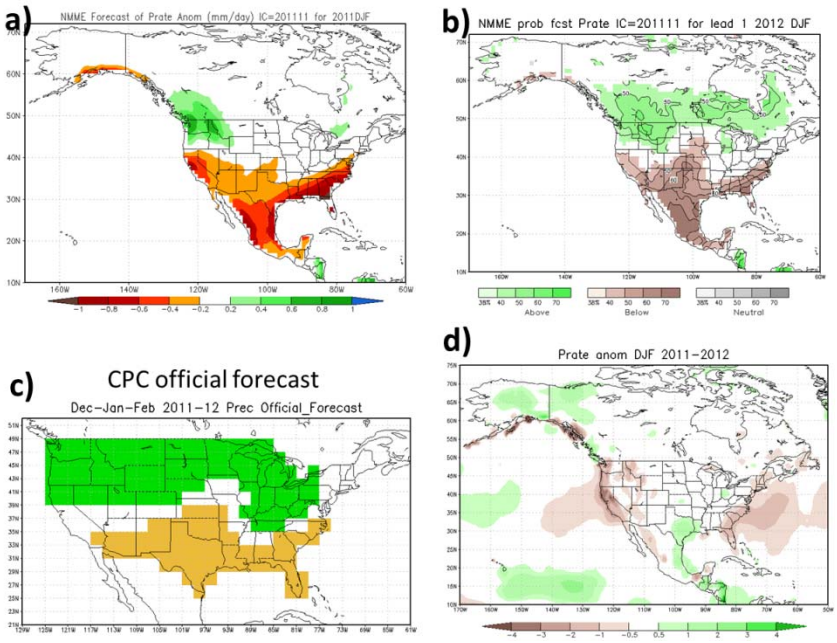

Fig. 1 NMME Prate anomaly forecast (a), probability forecast (b), Climate Prediction Center official forecast (c), and observed Prate anomaly from CPC URD (d) for DJF 2011-2012.

NMME Phase I activities included the following models:

- NCEP CFS version 1: 15 ensemble members
- NCEP CFS version 2: 24 ensemble members

Correspondence to: Emily Becker, Climate Prediction Center, NCEP/NWS/NOAA, 5830 University Research Court, College Park, MD 20740-3818; E-mail: Emily.Becker@noaa.gov.

- GFDL CM2.1: 10 ensemble members
- IRI ECHAM4-f: 12 ensemble members
- IRI ECHAM4-a: 12 ensemble members
- NCAR-CCSM3.0: 6 ensemble members
- NASA: 6 ensemble members

All models have 1.0° latitude by 1.0° longitude resolution and forecast leads of 1 – 7 months. 29 years of hindcasts (1982-2010) were available for all models except CFSv1 (28 years: 1982-2009). Model forecasts are produced by the 8th of each month, and graphical forecasts are available on the 9th of each month. Phase I forecasts were all delivered on time.

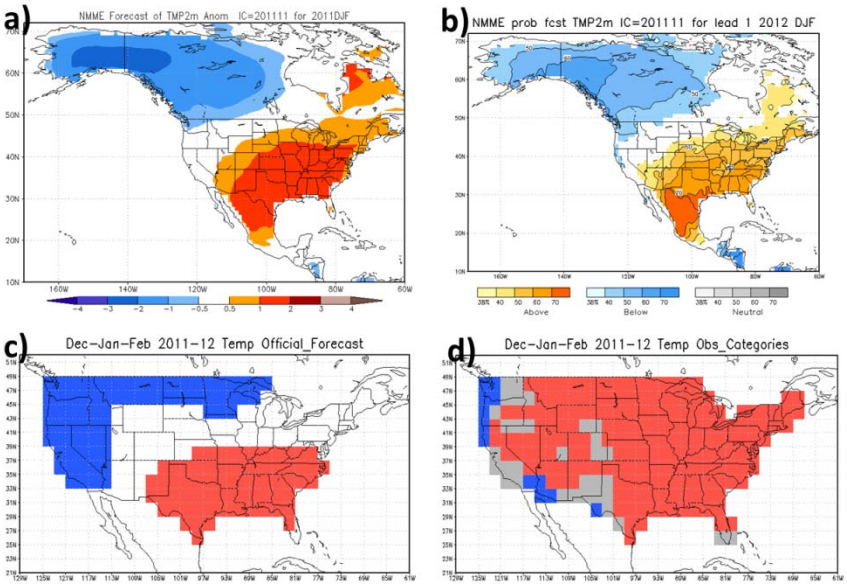

Fig. 2 NMME T2m anomaly forecast (a), probability forecast (b), Climate Prediction Center official forecast (c), and observed T2m anomaly from GHCN+CAMS (d) for DJF 2011-2012.

3. Forecast assessment metrics

Anomaly correlations (AC) were assessed for each model over the 29 years (28 for CFSv1) of hindcasts. Global maps and area averages over the Northern and Southern Hemispheres as well as the tropics were produced for T2m, Prate, and SST. Heidke skill scores (HSS) were used to assess forecast verification of Phase 1 probability forecasts. Verifying data sets used comprise GHCN+CAMS T2m, regridded to 1° x 1° (Fan and van den Dool 2008), CPC global Unified Rain-Gauge Database (URD), regridded to 1° x 1° (Xie *et al.* 2010), and OI-2 Sea-surface temperature (Reynolds *et al.* 2002), native resolution of 1° x 1°.

4. Results

Analysis of ACs (not shown) reveal that ACs for DJF seasonal forecasts at lead 1 month are higher for NMME forecasts than for individual models for all three fields. This holds for all area averaged ACs.

DJF 2011-2012 Prate anomaly forecast (Fig 1a), probability forecast (Fig 1b), CPC official forecast (Fig 1c), and observed precipitation (Fig 1d) reveal a low HSS, -04, for this season over the contiguous United States. Forecasts for T2m (Fig. 2), with a HSS of 47, were reasonably good.

Winter 2012 was a difficult case for forecasting. Looking at the scores for monthly forecasts beginning with September 2011 initial conditions (lead-1 month forecast for October 2012) through May 2012 initial

	Oct 2011	Nov 2011	Dec 2011	Jan 2012	Feb 2012	Mar 2012	Apr 2012	May 2012	Jun 2012	Jul 2012
201109	-03	-02	-31	27	12	23	15			
201110		0	-16	41	12	17	11	33		
201111			-31	34	06	09	04	58	35	
201112				18	15	11	05	39	60	05
201201					20	10	14	40	54	39
201202						15	15	40	49	21
201203							13	46	53	28
201204								46	33	09
201205									32	36

Table 1 Precipitation rate Heidke skill scores over the CONUS for monthly forecasts from September 2011 – May 2012 initial conditions. Forecast initial month is in the first column; target months read across.

conditions, higher scores are found for both Prate (Table 1) and T2m (Table 2) for the January – July period, even at leads of 6-7 months. This is encouraging, as the late winter, spring and early summer of 2012 produced unusually hot and dry conditions over the CONUS.

	Oct 2011	Nov 2011	Dec 2011	Jan 2012	Feb 2012	Mar 2012	Apr 2012	May 2012	Jun 2012	Jul 2012
201109	35	17	36	85	30	65	51			
201110		24	0	83	23	64	58	59		
201111			17	69	48	70	54	64	46	
201112				62	21	58	31	12	44	39
201201					34	71	61	61	42	18
201202						76	59	61	38	61
201203							55	53	28	64
201204								49	35	40
201205									28	62

Table 2 Same as Table 1, but for T2m.

5. Summary

At lead 1 month, NMME anomaly correlations for DJF forecast are higher than those of individual models. DJF 2011-2012 was a difficult case, but lead-1 month T2m forecasts over CONUS were reasonably good; precipitation rate forecast had low skill. The very warm and dry late winter through early summer over CONUS were fairly well forecasted, even at long leads. This is a preliminary examination of the forecast verification. A full verification analysis should help to identify sources of strength and weakness.

References

Fan, Y., and H. van den Dool, 2008: A global monthly land surface 714 air temperature analysis for 1948-present. *J. Geophys. Res.*, **113**, D01103, doi:10.1029/2007JD008470.

Reynolds, R.W., N. A. Rayner, T. M. Smith, D. C. Stokes, and W. Wang, 2002: An improved in situ and satellite SST analysis for climate. *J. Climate*, **15**, 1609–1625.

Xie, P., M. Chen, and W. Shi, 2010: CPC unified gauge analysis of global daily precipitation. To be submitted to *J. Hydrometeor*.

Science and Technology Infusion Climate Bulletin
NOAA's National Weather Service
37th NOAA Annual Climate Diagnostics and Prediction Workshop
Fort Collins, CO, 22-25 October 2012

A Comparison of Skill between Two Versions of the NCAP Climate Forecast System (CFS) and CPC's Operational Short-Lead Seasonal Outlooks

Peitao Peng[1], Anthony G. Barnston[2], and Arun Kumar[1]

[1]*Climate Prediction Center, NCEP/NWS/NOAA, MD*

[2]*International Research Institute for Climate and Society, Earth Institute of Columbia University*

ABSTRACT

Analysis of the relative prediction skills of NOAA's Climate Forecast System version 1 and 2 (CFSv1 and CFSv2), and the NOAA Climate Prediction Center's (CPC) operational seasonal outlook, is conducted over the 15-year common period of 1995-2009. The analyses are applied to predictions of seasonal mean surface temperature and total precipitation over the conterminous United States for the shortest and most commonly used lead time of 0.5 months. The assessments include both categorical and probabilistic verification diagnostics—their seasonality, spatial distributions, and probabilistic reliability. Attribution of skill to specific physical sources is attempted when possible. Motivations for the analysis are to document improvements in skill between the two generations of NOAA's dynamical seasonal prediction system and to inform the user community the forecast products skill of the CFS model now in use (CFSv2) to help guide the users' decision making processes.

The CFSv2 model is found to deliver generally higher mean predictive skill than CFSv1 (Fig. 1). This result is the strongest for surface temperature predictions and potentially may be related to the use of time-evolving CO_2 concentration in CFSv2, in contrast to a fixed (and now outdated) concentration used in CFSv1. CFSv2, and especially CFSv1, exhibit more forecast "overconfidence" than the official seasonal outlooks, despite that the CFSv2 hindcasts have outperformed the outlooks more than half of the time. Results justify the weight given to CFSv2 in developing the final outlooks, which is more than that given to previous dynamical input tools (*e.g.*, CFSv1), and indicate that CFSv2 should be of greater interest to users.

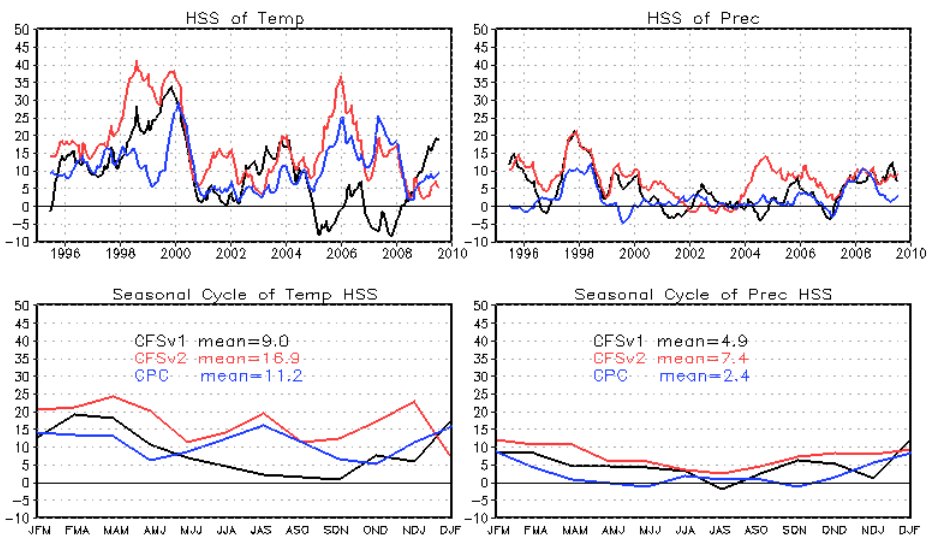

Fig. 1 Time series of spatial mean of Heidke skill score (HSS) over the US for CFSv1 (black), CFSv2 (red), and CPC official seasonal forecast (blue) of temperature (top left) and precipitation (top right); seasonal march of the mean HSS over the 15-year study period for the three forecast sources of temperature (bottom left) and precipitation (bottom right).

This work is to be published shortly in *Weather and Forecasting*.

Correspondence to: Peitao Peng, Climate Prediction Center, NCEP/NWS/NOAA, 5830 University Research Court, College Park, MD 20740-3818; E-mail: Peitao.Peng@noaa.gov.

Science and Technology Infusion Climate Bulletin
NOAA's National Weather Service
37th NOAA Annual Climate Diagnostics and Prediction Workshop
Fort Collins, CO, 22-25 October 2012

Sea Surface Temperature - Precipitation Relationship in Different Reanalyses

Li Zhang[1, 2], Arun Kumar[1], Wanqiu Wang[1]

[1]*Climate Prediction Center, NCEP/NWS/NOAA, College Park, MD*
[2]*Wyle Science Technology and Engineering, McLean, Virginia*

ABSTRACT

The focus of this investigation is how the relationship at intraseasonal time scales between sea surface temperature (SST) and precipitation (SST-P) varies among different reanalyses. The SST-P relationship in observation is much better reproduced in CFSR, the Modern Era-Retrospective-analysis for Research and Applications (MERRA) and the ECMWF Re-Analysis Interim (ERAI) compared to that in the NCEP/NCAR reanalysis (R1) and the NCEP/DOE reanalysis (R2) (Fig.1, top panel). The differences in SST-P relationship at intraseasonal time scales across different reanalyses are not due to whether the reanalysis system is coupled or atmosphere alone, but are due to the specification of different SSTs. The SST-P relationship in different reanalyses, when computed against a single SST for the benchmark, demonstrates a relationship that is common across all the reanalyses and observations (Fig. 1, bottom panel). The results also demonstrate that the MERRA and ERAI overestimate the intraseasonal variability in precipitation compared to the observation.

Part of this work has been published in *Monthly Weather Review* in 2012.

Paper published

Kumar, A., L. Zhang and W. Wang, 2012: Sea surface temperature - precipitation relationship in different reanalyses. *Mon. Wea. Rev.*, doi: http://dx.doi.org/10.1175/MWR-D-12-00214.1.

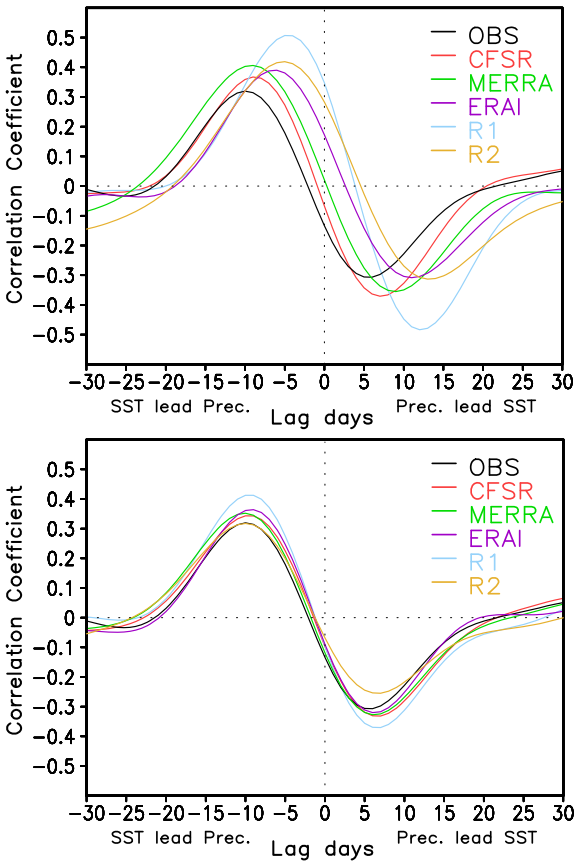

Fig. 1 Lead-lag SST-precipitation correlation for various reanalyses and for observations over the tropical western Pacific (averaged over 10°S–10°N, 130°–150°E) for respective SSTs were used (top panel), and for NCDC SST as the benchmark (bottom panel). Negative (positive) lag in days on the x axis indicates days by which the SST leads (lags) the precipitation.

Correspondence to: Li Zhang, Climate Prediction Center, NCEP/NWS/NOAA, 5830 University Research Court, College Park, MD 20740-3818; E-mail: leigh.zhang@noaa.gov.

Science and Technology Infusion Climate Bulletin
NOAA's National Weather Service
37th NOAA Annual Climate Diagnostics and Prediction Workshop
Fort Collins, CO, 22-25 October 2012

Prediction Skill of Monthly SST in the North Atlantic Ocean in NCEP Climate Forecast System Version 2

Zeng-Zhen Hu[1], Arun Kumar[1], Bohua Huang[2, 3], Wanqiu Wang[1], Jieshun Zhu[3], and Caihong Wen[1,4]

[1]*Climate Prediction Center, NCEP/NWS/NOAA, MD*
[2]*Department of Atmospheric, Oceanic, and Earth Sciences, Gorge Mason University, VA*
[3]*Center for Ocean-Land-Atmosphere Studies, MD*
[4]*WYLE Science, Technology and Engineering Group, McLean, Virginia*

ABSTRACT

This work evaluates the skill of retrospective predictions of the second version of the NCEP Climate Forecast System (CFSv2) for the North Atlantic sea surface temperature (SST) and investigates the influence of El Niño-Southern Oscillation (ENSO) and North Atlantic Oscillation (NAO) on the prediction skill over this region. It is shown that the CFSv2 prediction skill with 0-8 month lead displays a "tripole"-like pattern with areas of higher skills in the high latitude and tropical North Atlantic, surrounding the area of lower skills in the mid-latitude western North Atlantic (Fig. 1). This "tripole"-like prediction skill pattern is mainly due to the persistency of SST anomalies (SSTAs), which is related to the influence of ENSO and NAO over the North Atlantic. The influences of ENSO and NAO, and their seasonality, result in the prediction skill in the tropical North Atlantic the highest in spring and the lowest in summer. In CFSv2, the ENSO influence over the North Atlantic is overestimated but the impact of NAO over the North Atlantic is not well simulated. However, compared with CFSv1, the overall skills of CFSv2 are slightly higher over the whole North Atlantic, particularly in the high latitudes and the northwest North Atlantic.

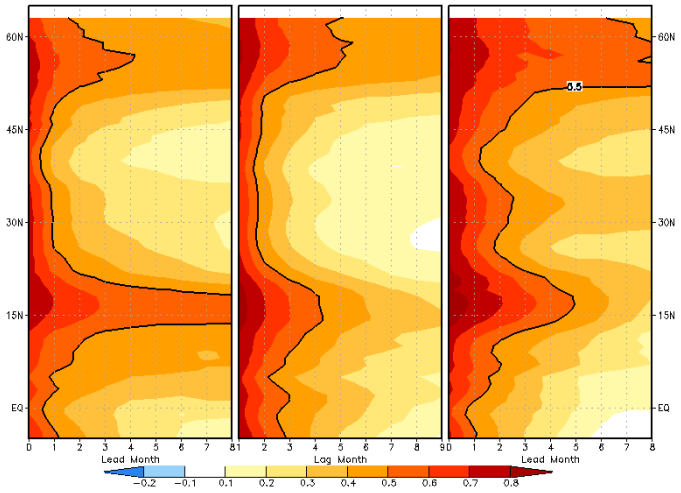

Fig. 1 Zonal averages over the North Atlantic Ocean for correlations between OIv2 SSTA and CFSv2 predicted SSTA (left), lag correlations of OIv2 SSTA (middle), and correlations of SSTA between initial conditions and 0-8 month predictions of CFSv2 (right). Only 0.5 contour is plotted.

The model prediction skill beyond the persistency initially presents in the mid-latitudes of the North Atlantic and extends to the low latitudes with time. That might suggest that the model captures the associated air-sea interaction in the North Atlantic. The CFSv2 prediction is less skillful than that of SSTA persistency in the high latitudes, implying that over this region the persistency is even better than CFSv2 predictions. Also, both persistent and CFSv2 predictions have relatively low skills along the Gulf Stream.

This work has been published in *Climate Dynamics* in 2012.

Paper published

Hu, Z.-Z., A. Kumar, B. Huang, W. Wang, J. Zhu, and C. Wen, 2012: Prediction skill of monthly SST in the North Atlantic Ocean in NCEP Climate Forecast System version 2. *Clim. Dyn.*, doi: 10.1007/s00382-012-1431-z (published online).

Correspondence to: Zeng-Zhen Hu, Climate Prediction Center, NCEP/NWS/NOAA, 5830 University Research Court, College Park, MD 20740-3818; E-mail: Zeng-Zhen.Hu@noaa.gov.

Science and Technology Infusion Climate Bulletin
NOAA's National Weather Service
37th NOAA Annual Climate Diagnostics and Prediction Workshop
Fort Collins, CO, 22-25 October 2012

Characteristics of Oceanic Response to ENSO Estimated from Simulations with the NCEP Climate Forecast System

Hui Wang[1,2], Arun Kumar[1], and Wanqiu Wang[1]

[1]*Climate Prediction Center, NCEP/NWS/NOAA, College Park, Maryland*
[2]*Wyle Science, Technology and Engineering Group, McLean, Virginia*

ABSTRACT

The ocean temperature response to El Niño–Southern Oscillation (ENSO) is examined based on 31-yr (1981–2011) simulations with the National Centers for Environmental Prediction (NCEP) Climate Forecast System (CFS) coupled model. The model sea surface temperature (SST) in the tropical Pacific is relaxed to observations to ensure realistic ENSO variability in the simulations.

In the tropical Pacific, the subsurface temperature response to the ENSO SST is closely related to the variability of thermocline. The early temperature response is stronger and deeper in the tropical Indian Ocean than in the tropical Atlantic. The analysis at three selected locations (Fig. 1) reveals that the peak response of the subsurface temperature to ENSO lags the Niño-3.4 SST by 4, 7, and 7 months, respectively, in the tropical Indian Ocean, subtropical Atlantic, and North Pacific, where SSTs are known to be strongly influenced by ENSO. The ENSO-forced temperature anomalies tend to penetrate to deeper ocean with time in the North Pacific and subtropical Atlantic, but not in the tropical Indian Ocean where peak anomalies are found at month 4 over all depths above the 300 m depth. The longer (shorter) response timescale in the North Pacific and subtropical Atlantic (tropical Indian Ocean) is closely related to more (less) persistent local surface wind stress anomaly forced by ENSO. The results presented in this study may help understand the attributions for SST anomalies and oceanic variability in different ocean basins and their link to the ENSO variability.

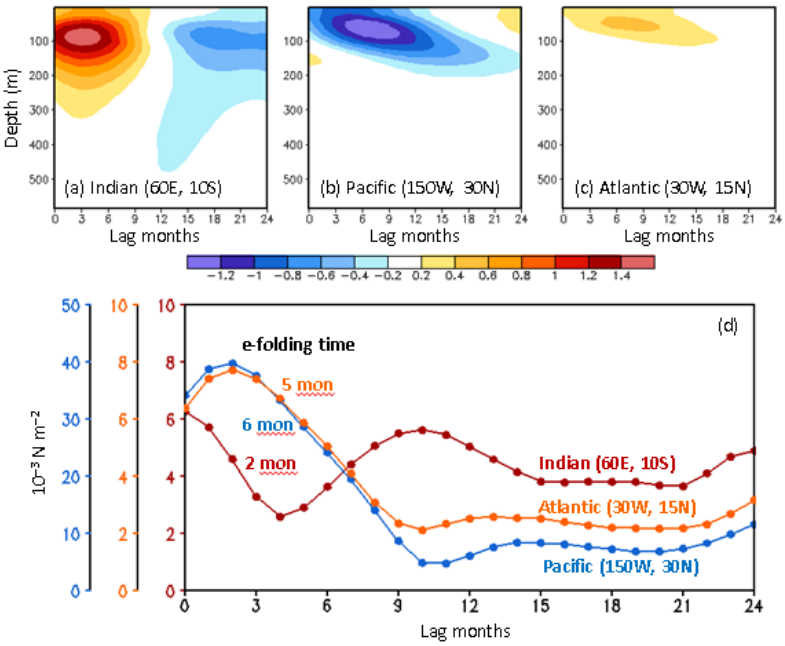

Fig. 1 Ocean temperature anomalies at (a) tropical Indian Ocean (60ºE, 10ºS), (b) North Pacific (150ºW, 30ºN), and (c) subtropical Atlantic (30ºW, 15ºN) and (d) corresponding amplitude of surface wind stress anomalies at 60ºE, 10ºS (red), 150ºW, 30ºN (blue), and 30ºW, 15ºN (orange) obtained based on lagged linear regressions against the Niño-3.4 index for individual CFS simulations and then averaged over the nine members. The anomalies correspond to a two-standard-deviation Niño-3.4 SST anomaly (1.8ºC) and lag the Niño-3.4 SST anomaly from 0 month to 24 months.

This work has been submitted to *Journal of Climate*.

Correspondence to: Hui Wang, Climate Prediction Center, NCEP/NWS/NOAA, 5830 University Research Court, NCWCP, College Park, MD 20740-3818; E-mail: hui.wang@noaa.gov.

3. PREDICTION AND ATTRIBUTION OF HIGH IMPACT WEATHER AND CLIMATE EVENTS

Science and Technology Infusion Climate Bulletin
NOAA's National Weather Service
37th NOAA Annual Climate Diagnostics and Prediction Workshop
Fort Collins, CO, 22-25 October 2012

Wet Weeks in the Warm Season: Processes Supporting Widespread, Multi-day Precipitation Episodes

Russ S. Schumacher

Department of Atmospheric Science, Colorado State University, Fort Collins, CO

1. Introduction

Multi-day periods in the warm season in which heavy precipitation falls across a large region are not always well predicted even a few days in advance of the onset of heavy rain. Yet these events are also very important in the context of seasonal climate prediction, as an event of this type can result in a large fraction of the rainfall in a particular region. This research will outline some of the processes typically associated with widespread heavy rainfall and will evaluate the performance of global ensemble prediction systems for several recent events.

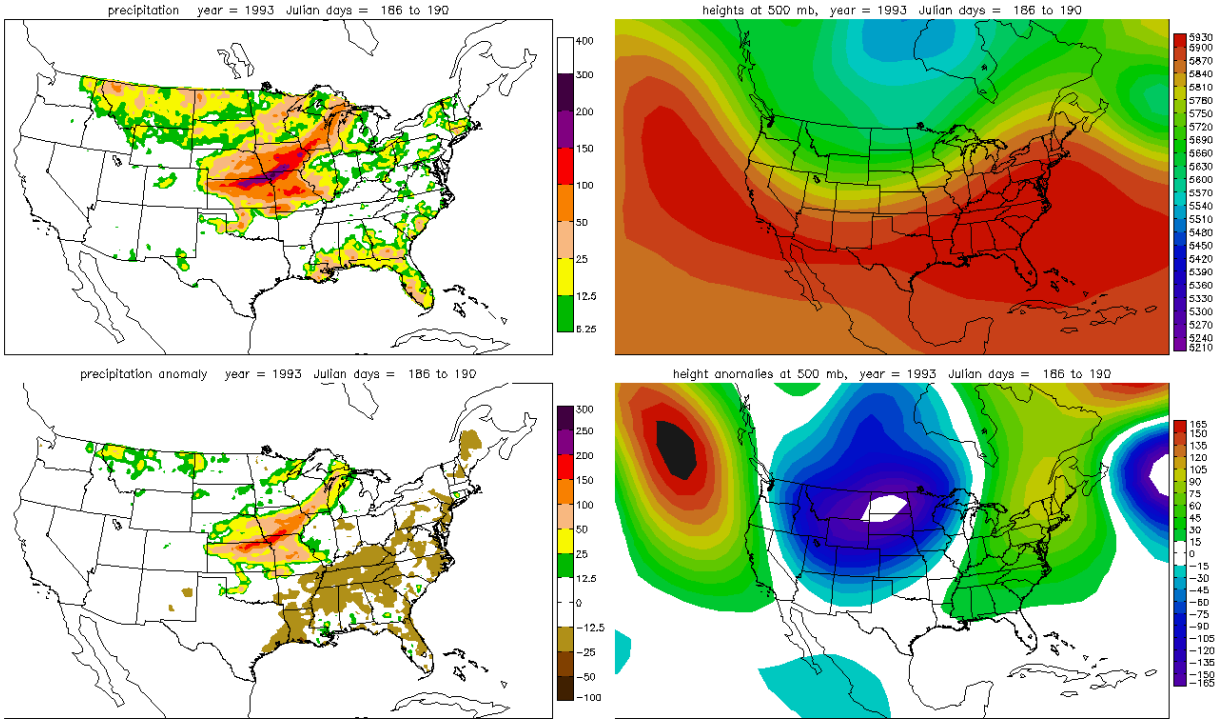

Fig. 1 (upper left) CPC analysis of total precipitation (mm) from 1200 UTC 3 July to 1200 UTC 8 July 1993. (lower left) As in the upper left, but for the precipitation anomaly. (upper right) Average 500-hPa geopotential height (m) from 4-8 July 1993 from the NCEP-NCAR Reanalysis (Kalnay et al. 1996). (lower right) 500-hPa geopotential height anomaly from 4-8 July 1993.

2. Case selection

The Climate Prediction Center's (CPC) US daily precipitation analysis (Chen *et al.* 2008), which has 0.25° grid spacing, was used to identify all 5-day periods during 1948—2011 where over 350 grid points had precipitation exceeding 100 mm (4 inches) of rainfall. Over this period, there were 22 cases identified in June, July, and August, after removing overlapping 5-day periods.

Correspondence to: Russ Schumacher, Department of Atmospheric Science, Colorado State University, 1371 Campus Delivery, Fort Collins, CO 80523; E-mail: russ.schumacher@colostate.edu.

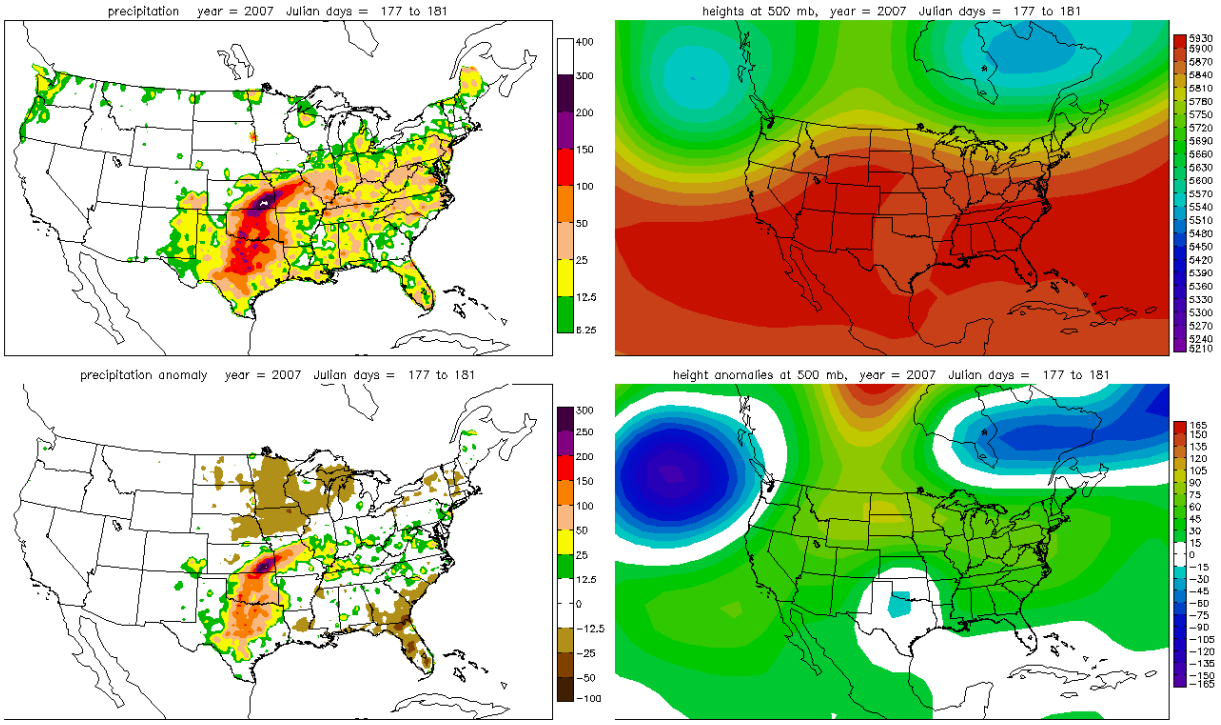

Fig. 2 As in Fig. 1, except the precipitation totals are for 1200 UTC 25 June to 1200 UTC 30 June 2007, and heights are for 26-30 June 2007.

3. Weather systems associated with widespread heavy rainfall in the warm season

Of the 22 warm-season events taking place during 1948—2011, 13 were associated with tropical cyclones. These events, while clearly important and impactful, were not the primary focus of this work. Six of the 22 events were associated with persistent, anomalous synoptic-scale troughs over the US. An archetypal example of this pattern was the widespread heavy rain and flooding during July of 1993 in the Midwest (Fig. 1). The June 2008 Midwest floods were also very similar to the 1993 floods in terms of their large-scale pattern (e.g., Bodner *et al.* 2011).

Two of the 22 events were associated with "predecessor rain events" (Galarneau *et al*. 2010), which occur when tropical moisture is transported ahead of an extratropical cyclone and lifted along a baroclinic zone in the midlatitudes. These occurred ahead of tropical cyclone Grace in 2003 and tropical cyclone Erin in 2007.

The last of the warm-season events identified here was associated with a long-lived mesoscale convective vortex (MCV) that remained nearly stationary for over a week from 24 June-1 July 2007 (Fig. 2; Schumacher 2011). Schumacher and Davis (2010) showed that at the medium range, this event was very poorly predicted in the European Centre for Medium Range Weather Forecasts (ECMWF; Fig. 3a) ensemble prediction system relative to other events of similar spatial and temporal scale. Lynch (2012) extended this analysis to the NCEP and UK Met Office global ensemble prediction systems and found similar results. (Fig. 3b).

4. The June 2007 extreme rainfall in the Southern Plains

Ensemble-based synoptic analysis (*e.g.*, Hakim and Torn 2008) was employed using the ECMWF ensemble forecast initialized at 0000 UTC 24 June 2007. Schumacher (2011) found that the strength of an anticyclone over the southwestern U.S. was one of the key determining factors in the genesis and longevity of the MCV and associated rainfall over the Southern Plains. In ensemble members with a weaker anticyclone in the southwest, which was closer to the observed evolution, the incipient vortex encountered relatively weak vertical wind shear. This allowed deep convection to repeatedly form near the center of the vortex, which in turn caused the vortex to intensify, and so on (Fig. 4a). In members with a stronger anticyclone, however, the vortex experienced stronger vertical wind shear, which led to stronger steering flow as well as convection

developing downshear of the vortex center, and the incipient vortex moved southwestward into Mexico and decayed without producing any extreme precipitation (Fig. 4b). These small differences in the midlevel flow configuration were associated with large differences in the location and intensity of precipitation over the southern Plains, and were thus responsible for the low skill and high uncertainty in the global ensemble forecasts.

5. Summary and conclusions

This research illustrates the variety of synoptic-scale patterns that can lead to widespread heavy precipitation in the warm season, including tropical cyclones, anomalous troughs, predecessor rain events, and long-lived mesoscale convective vortices. The upscale growth of mesoscale convection in late June 2007 led to rainfall of sufficient intensity and coverage to be relevant to regional climate, yet this event was poorly predicted and likely had low intrinsic predictability.

Acknowledgements. Precipitation analyses were obtained from the CPC, and ensemble forecast output was obtained from the TIGGE archive at ECMWF (http://tigge.ecmwf.int). Thanks to Chris Davis, Samantha Lynch, and Heather Vazquez for their contributions to the research summarized in this report.

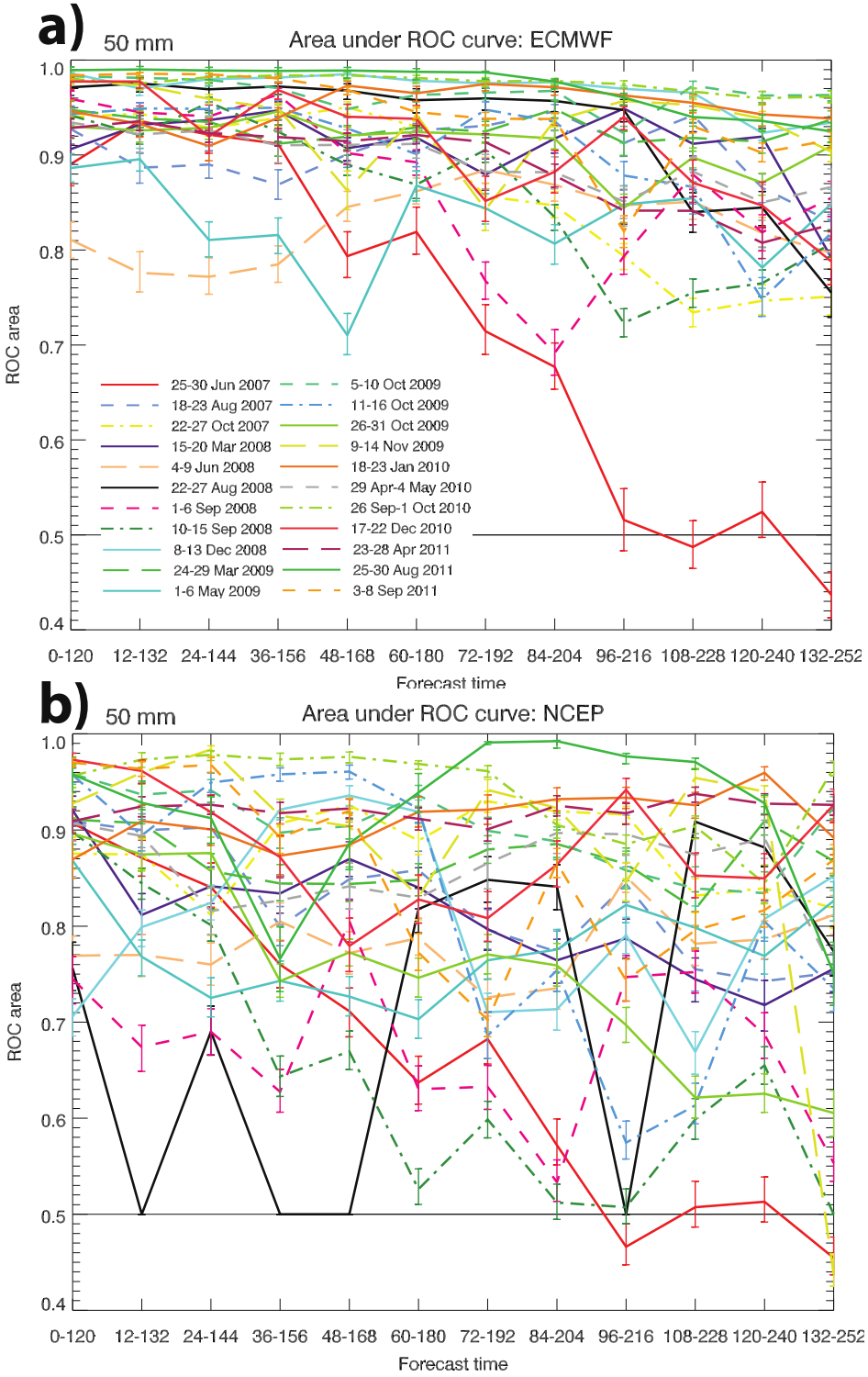

Fig. 3 Area under the receiver operating characteristic (ROC) curve for forecasts of 50 mm of rainfall in the (a) ECMWF and (b) NCEP ensemble prediction systems. Confidence intervals were calculated using a 1000-sample bootstrap resampling. A perfect forecast has ROC area of 1; a random reference forecast has area 0.5. The red lines represent the June 2007 event discussed in section 4. From Lynch (2012).

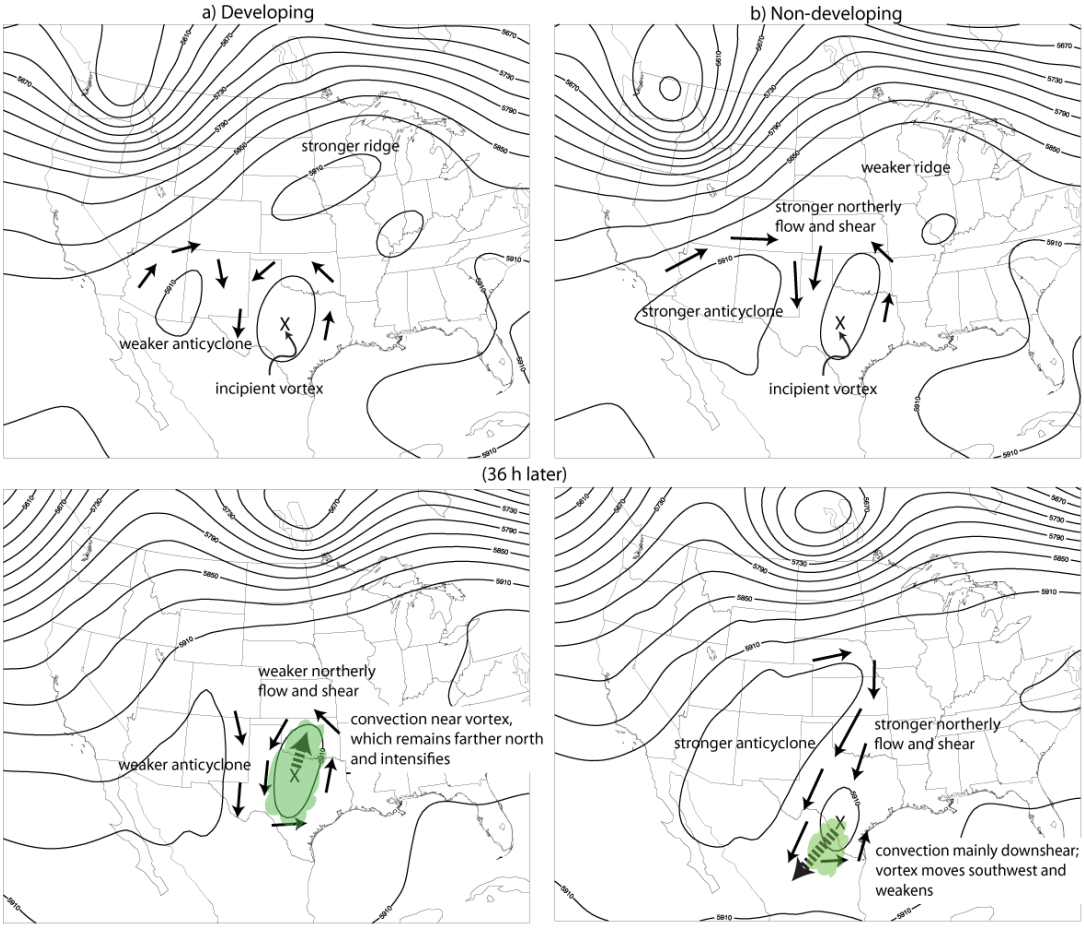

Fig. 4 Schematic diagram illustrating the large-scale factors leading to (a) development and (b) non-development of a long-lived vortex and associated widespread rainfall, as indicated by differing ensemble members. The 500-hPa height pattern at an earlier time, and 36 later, are shown for both instances. Black arrows denote representative flow vectors. The ``X" indicates the location of the 500-hPa vorticity maximum, gray shading indicates the location of deep convection, and the dotted arrow indicates the movement of the vortex over time. From Schumacher (2011).

References

Bodner, M.J., N.W. Junker, R.H. Grumm, and R.S. Schumacher, 2011: Comparison of atmospheric circulation patterns during the 2008 and 1993 historic Midwest floods. *Nat. Wea. Digest,* **35,** 103-119.

Chen, M., W. Shi, P. Xie, V. B. S. Silva, V. E. Kousky, R. W. Higgins, and J. E. Janowiak, 2008: Assessing objective techniques for gauge-based analyses of global daily precipitation. *J. Geophys. Res.*, **113**, D04110, doi:10.1029/2007JD009132.

Galarneau, T.J., Jr., L.F. Bosart, and R.S. Schumacher**,** 2010**:** Predecessor rain events ahead of tropical cyclones. *Mon. Wea. Rev.*, **138,** 3272-3297.

Hakim, G. J., and R. D. Torn, 2008: Ensemble synoptic analysis. *Synoptic-Dynamic Meteorology and Weather Analysis and Forecasting: A Tribute to Fred Sanders, Meteor. Monogr.*, No. 55, Amer. Meteor. Soc., 147–161.

Lynch, S. L., 2012: Ensemble-based analysis of extreme precipitation events from 2007-2011. M.S. thesis, Colorado State University.

Schumacher, R.S., 2011: Ensemble-based analysis of factors leading to the development of a multi-day warm-season heavy rain event. *Mon. Wea. Rev.*, **139,** 3016-3035.

Schumacher, R.S.**,** and C.A. Davis, 2010**:** Ensemble-based uncertainty analysis of diverse heavy rainfall events. *Wea. Forecasting*, **25,** 1103-1122.

Science and Technology Infusion Climate Bulletin
NOAA's National Weather Service
37th NOAA Annual Climate Diagnostics and Prediction Workshop
Fort Collins, CO, 22-25 October 2012

Changes in Activity of the Intense Tropical Cyclones for the Western North Pacific During the Last Decades, Derived From a Regional Climate Model Simulation

Monika Barcikowska, Frauke Feser, and Hans von Storch

Institute for Coastal Research, Helmholtz-Zentrum Geesthacht, Geesthacht, Germany
and
Cluster of Excellence 'Integrated Climate System Analysis and Prediction' (CliSAP)
of the University of Hamburg, Germany

1. Introduction

The observation-based studies so far haven't reached consensus regarding the trends of tropical cyclones (TCs) in the western North Pacific (WNP) during the last six decades. Such results are related to deficient (Barcikowska 2012; Song *et al.* 2010; Landsea *et al.*) observational data sets (best track data sets, hereafter referred to BTD), containing inhomogeneities introduced by operational practices which are changing over time and measurement techniques. This limits the reliability of derived TC climatologies and also the feasibility to associate the TC activity with environmental factors.

As for an alternative data set, which is long and homogenous enough to derive climate statistics, an atmospheric regional climate model was employed. In this study, we analyze TC activity over the WNP, derived from dynamically downscaled NCEP/NCAR re-analyses for the period 1948-2011.

Section 2 describes the data and methods used for this study. Section 3 examines the spatial and temporal changes in TC activity. Section 4 shows the relation of given changes to large-scale environmental patterns.

2. Data and methods

The regional climate model applied to simulate long-term TC climate is COSMO-CLM (CCLM, www.clm-community.eu; Rockel *et al.* 2008; Steppeler *et al.* 2003). The model domain covers the western North Pacific and South-East Asia (Fig. 1) with a horizontal resolution of 0.5° (~ 55 km) and 32 vertical levels. The model runs in non-hydrostatic mode and the Kain-Fritsch scheme (Kain 2004) is used as convective parameterization.

CCLM is driven by large-scale fields provided by global NCEP-NCAR reanalyses I (Kalnay *et al.* 1996; Kistler *et al.* 2001), hereafter called NCEP, at a horizontal resolution of T62 (~ 210 km)) as boundary and initial conditions. Additionally, the spectral nudging technique (von Storch *et al.* 2000) was applied to the whole model domain, and only for the horizontal wind components.

The influence of large-scale circulation patterns on hindcasted TC variability was quantified with a Canonical Correlation Analysis (*e.g.* von Storch and

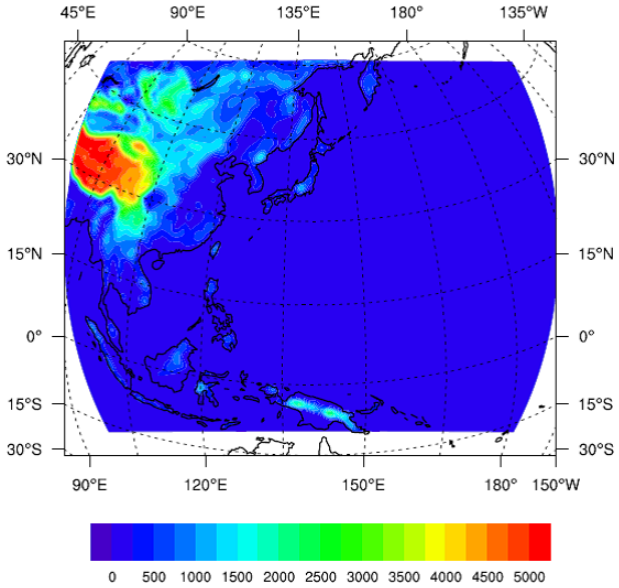

Fig. 1 CCLM model domain and surface elevation (m) of the CCLM simulation for Southeast Asia and the western North Pacific with a grid distance of 0.5° latitude x 0.5° longitude.

Correspondence to: Monika Barcikowska, Institute for Coastal Research, Helmholtz-Zentrum Geesthacht, Geesthacht, Germany; E-mail: monika.barcikowska@hzg.de.

Zwiers 1999). The method estimates the maximum correlation between two multidimensional data sets. Here we analyzed the association of TC spatial density with Maximum Potential Intensity (MPI) patterns and Genesis Potential Index (GPI). For this purpose the first ten EOFs were computed using yearly anomalies of atmospheric variables calculated during JASO (July-October, hereafter JASO months) months. It is assumed that the first ten EOFs represent the main patterns of variability and those were used for further analysis (Leoncini *et al.* 2008; von Storch and Zwiers 1999).

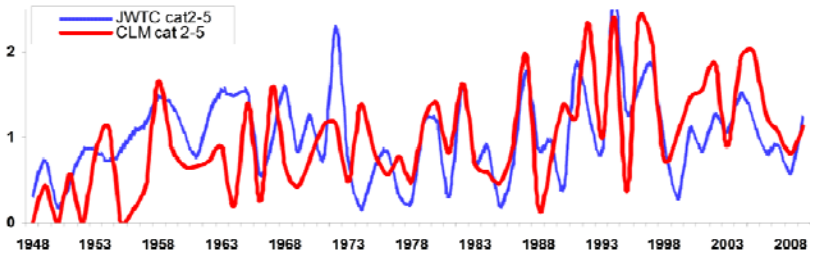

Fig. 2 Annual numbers for the intense TC days counted for July-October seasons, normalized by their climatological mean values for the period 1948-2011, CCLM (red) and JTWC (blue).

The MPI (Emanuel 1988) is computed with a program provided by K. Emanuel on the website ftp://texmex.mit.edu/pub/emanuel/TCMAX/. The yearly values of MPI for the WNP region were calculated with the sea surface temperature (SST) fields that were used to drive the regional model. The GPI is defined by (Emanuel and Nolan 2004).

Simulated TC activity is compared with the BTD observations, provided by Joint Warning Typhoon Center (http://www.usno.navy.mil/JTWC/).

3. Changes of TC activity over the western North Pacific for the years 1948-2011

Impact of TCs on coastal populations depends on their frequency, duration, intensity and location. Therefore we analyse the number of days for intense TCs, which account for the first three given parameters. Figure 2 presents simulated and observed annual numbers for the intense TC days normalized by their mean values for the period 1948-2011.

For the period 1978-2011 yearly TC variability in CCLM (CLM cat2_5) is comparable with the observations, given by BTD set (hereafter referred to JTWC cat2-5,). For the previous period, prior to the satellite-measurement era, observations show higher TC activity numbers. These differences may be related to the limited spatial/temporal coverage of observations and limited accuracy of TC measurement techniques.

Long-term trends in CCLM time series show an increasing trend for the period 1948-2011, with a slope coefficient of 0.02 for the intense TCs. The maximum of the TC activity occurs in the 1990s with a slight shift towards less numbers in the last decade.

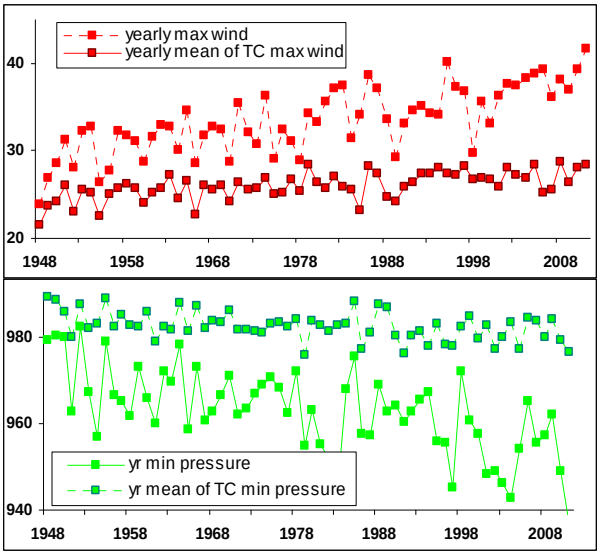

Fig. 3 Annual maxima of TC intensity (dashed line) and annual mean of TC intensity from all derived TCs (solid line). Intensity is shown in terms of maximum wind speed (top) and minimum pressure (bottom). The x-axis shows years. The y-axis shows (top) wind speed (units: m s^{-1}) and (bottom) pressure (units: hPa).

Increasing frequency of the intense TCs is consistent with increasing intensity of the intense TCs. Figure 3 shows the annual maxima of TC intensity simulated by CCLM, in terms of maximum wind speed and minimum pressure. The 50th percentile of annual maxima for TC intensities during the analysed period are ~ 34 m s^{-1} and ~ 962 hPa for wind speed and pressure, respectively. Time series clearly show an increasing trend for maximum wind speed and a decreasing trend for minimum pressure. TC cores are deepening from ~ 970 hPa in the early 1960s, to ~ 950 hPa in the 2000s.

Figure 4 shows that TCs that reach an intensity higher than the 50th percentile of TC intensity annual maxima (~ 34 m s^{-1} for wind speed and ~ 962 hPa for pressure) occur mainly in the second part of the analysed period and their frequency increases.

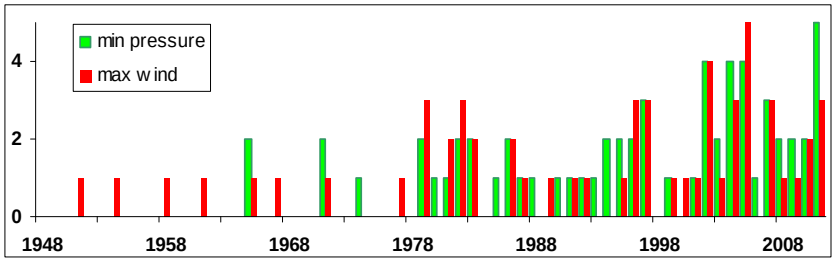

Fig. 4 Number of TCs reaching the intensity threshold (50th percentile of annual maxima of TC intensity for the period 1948-2011). Intensity is represented as maximum wind speed (red) and minimum pressure (green).

Spatial features of TC activity changes are presented in Fig. 5. The picture presents long-term spatial density trends for intense TCs. Trends were derived with a linear regression using a least squares fit, for every grid box. TC activity shows an increase along the South Asian coast, eastward from the northern part of the Phillipines and extends towards the southern flanks of Japan. The maximum is located in the subtropical latitudes, in the vicinity of Taiwan (Barcikowska *et al.* 2012, submitted). Downward tendencies of TC activity are focused mainly in the south-eastern part (130-150°E, 10-20°N) of the WNP. Overall, the constructed TC climatology shows an increase and a north-westward shift of intense TC tracks for the period 1948-2011.

Several observational studies that analysed the impact of TCs in the WNP for shorter time periods (Ho *et al.* 2004; Wu *et al.* 2005) confirm partly our findings. Tu *et al.* (2009) found strong TC variability after 1982 and an abrupt shift of TC activity in the vicinity of Taiwan in the 2000s. The authors concluded that there is a northward shift of typhoon tracks. Wu *et al.* (2005) identified a westward shift of TC track patterns in the WNP for the last decades and stated that there is a rising influence of TCs on subtropical East Asia.

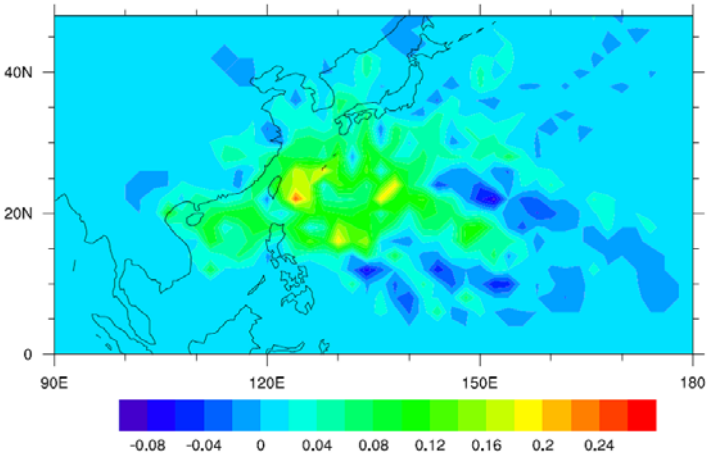

Fig. 5 Trends for yearly intense TC occurrences, estimated with a linear regression using a least squares fit derived for every 2° latitude x 2° longitude grid box; for the period 1948-2011.

4. Relationship of TC activity with large-scale environmental patterns

Variability of TC activity is determined by many environmental factors. High sea surface temperature, high moisture content in the lower troposphere, conditional convective instability, cyclonic vorticity and weak vertical shear of horizontal winds are necessary conditions, although not sufficient for tropical cyclogenesis to occur (Gray 1968).

We utilize two indexes (MPI and GPI), combining given parameters, to estimate and explain derived yearly variability of intense TCs. The MPI (Emanuel 1988) is determined by: sea surface temperature, the outflow temperature and convective available potential energy. It represents thermodynamic conditions which influence TC genesis and intensification. The GPI combines additionally dynamical factors, *e.g.* vertical wind shear, absolute vorticity. Thus GPI indicates how favourable thermodynamical and dynamical conditions are for TC genesis and development.

In order to quantify the relation between yearly variability of intense TCs and large –scale environmental patterns (represented by MPI and GPI), we apply canonical correlation analysis (CCA). CCA results are two pairs of correlating patterns. Figure 6a and 6b show the pattern of anomalies for: 3-yr MPI fields and 3-yr spatial density of the intense TCs. Figure 6c presents the time series of those patterns. The time series of CCA pattern for the intense TCs explains 71 % of total variability. Figure 7 shows in the same manner the relationship between intense TC activity and GPI.

CCA patterns for 3-yr MPI and TCs share a correlation of 68 %. The relationship represented by CCA patterns indicates that anomalously positive MPI along the SE Asian coast is strongly related to an anomalously high activity of the intense TCs in the same region. Time series of given patterns share a correlation of 0.65. Both time series show an increasing activity with the maximum in the early 2000s.

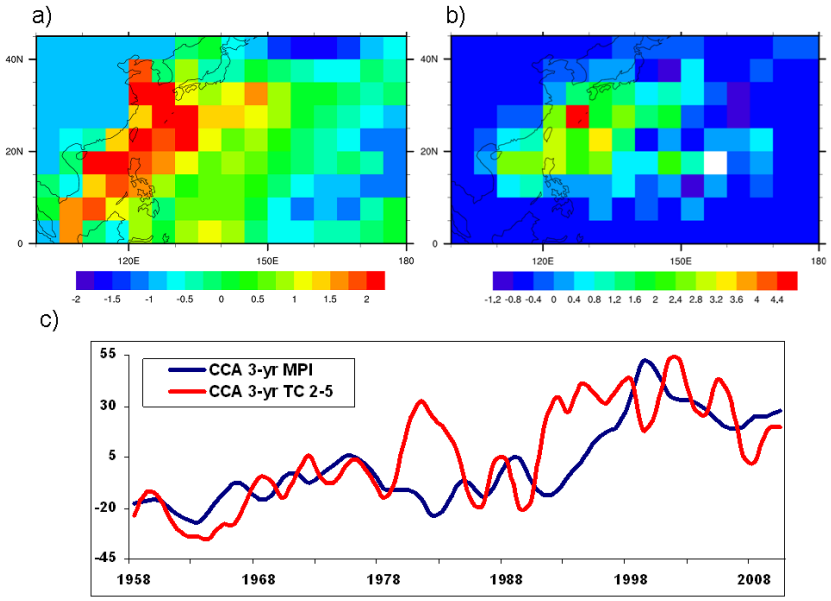

Fig. 6 The canonical correlation patterns derived between: (a) 3-yr spatial density anomalies of the intense TCs (CCA TC) and (b) 3-yr fields of Maximum Potential Intensity anomalies (CCA MPI). The CCA patterns share a correlation of 68 %. Time series for correlating CCA TC and CCA MPI patterns are shown in c).

However, anomalously high TC activity in 1982/83 and in the early 1990s cannot be explained with the derived MPI pattern, which in these years is rather inactive (Fig. 6c). In these years, other modes of variability might reduce the strength of the derived MPI pattern, particularly ENSO variability, which was in a strong, positive phase (El Niño) in 1982/83 and the early 1990s. At that time the sea surface temperature (and consequently MPI) shows positive anomalies in the equatorial central and eastern Pacific, but – negative anomalies in the western North Pacific. Consequently the positive anomalies of these factors, which are visible along the SE Asian coast in the first CCA MPI pattern (Fig. 6a), are diminished during the warm ENSO phase.

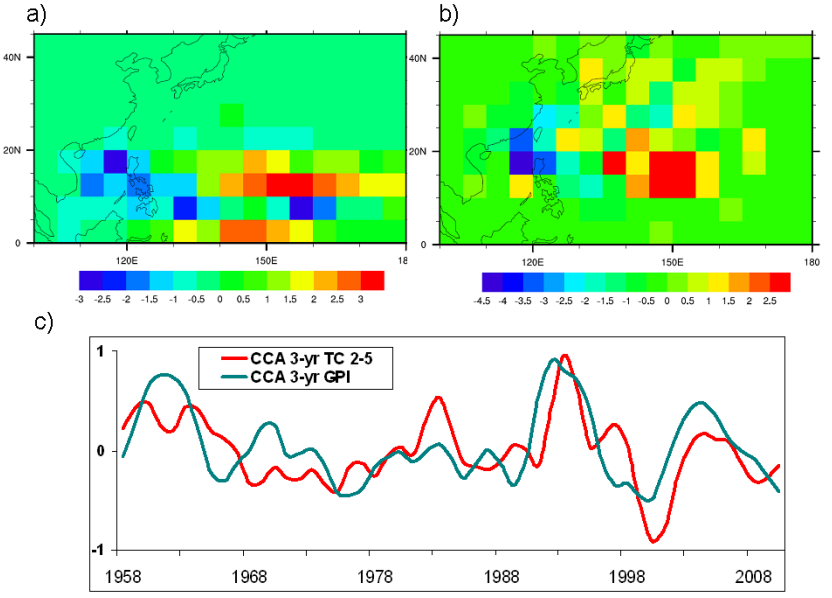

Fig. 7 The canonical correlation patterns derived between: (a) 3-yr spatial density anomalies of the intense TCs (CCA TC) and (b) 3-yr fields of Genesis Potential Index anomalies (CCA GPI). The CCA patterns share a correlation of 45%. Time series for correlating CCA TC and CCA GPI patterns are shown in c).

To find a potential reason for anomalously high TC activity in 1982/83 and the early 1990s we analysed its relation to GPI. Figure 7a, b represents the first canonical correlation patterns derived between anomalies of GPI and TCs (CCA GPI and CCA TC, respectively). The patterns share a correlation of 45 %. The CCA GPI (Fig. 7a) captures the ENSO signal quite clearly, indicating positive anomalies in the eastern part of the western North Pacific and negative anomalies in coastal regions. CCA TC reflects the spatial features of the GPI pattern. The time series of CCA patterns confirm an influence of ENSO on TC activity. The magnitude of GPI values (Fig. 7c) clearly indicates strong ENSO phases in 1982/1983, in the 1990s and 1999/2000. This corresponds to high TC activity in El Nino phases (1982/1983 and 1990s), and low TC activity in La Nina (1999/2000). The time series of the given patterns show a correlation of 60 %.

5. Summary

This paper presents the TC activity over the western North Pacific for the last six decades. In order to construct a TC data set, we employed a regional atmospheric model (CCLM) to dynamically downscale NCEP-NCAR reanalyses.

Comparisons of the resulting data set with more recent observations (1978-2008) show that the simulated TC climatology represents realistic features of TC activity variability on inter-annual to inter-decadal time scales.

The constructed long-term TC climatology shows an increase and a north-westward shift of intense TC tracks for the period 1948-2011. The variability of TC activity shows a relationship with large-scale environmental patterns, represented by MPI and GPI.

Increasing TC activity over the last decades along the SE Asian coast shows a relation with the MPI pattern. The pattern and its time series indicate a change of thermodynamic conditions in the same region towards conditions which are more favourable for TC genesis and intensification. Another mode of TC variability shows a link with ENSO, represented by the GPI pattern. The given relationships explain high TC activity: in the 1990s mainly due to the warm ENSO mode; in the 2000s due to favourable thermodynamic TC genesis and development conditions which occurred over coastal regions of the WNP.

References

Barcikowska, M., F. Feser, and H. von Storch, 2012: Usability of best track data in climate statistics in the western north pacific. *Mon. Wea. Rev.*, **140**, 2818-2830.

Emanuel, K. A, 1988: The maximum intensity of hurricanes. *J. Atmos. Sci.*, **45**,1143–1155.

—, and D. S. Nolan, 2004: Tropical cyclone activity and the global climate system. *Proceedings of 26th Conference on Hurricanes and Tropical Meteorology*, American Meteorological Society, Miami, FL., 240–241.

Gray, W. M., 1968: A global view of the origin of tropical disturbances and storms. *Mon. Wea. Rev.*, **96**, 669–700.

Ho, C.-H., J.-J. Baik, J.-H. Kim, and D.-Y. Gong, 2004: Interdecadal changes in summertime typhoon tracks. *J. Climate*, 17, 1767-1776.

Kain, J. S., 2004: The kain-fritsch convective parameterization: An update. *J. Appl. Meteor.*, **43**, 170–181.

Kalnay, E., M. Kanamitsu, R. Kistler, W. Collins, D. Deaven, L. Gandin, M. Iredell, S. Saha, G. White, J. Woollen, Y. Zhu, A. Leetmaa, R. Reynolds, M. Chelliah, W Ebisuzaki, W. Higgins, J. Janowiak, K.C. Mo, C. Ropelewski, J. Wang, R. Jenne, and D. Joseph, 1996: The NCEP/NCAR 40-year reanalysis project. *Bull. Amer. Meteor. Soc.*, **77**, 437–470.

Kistler, R., and Co-authors, 2001: The NCEP-NCAR 50-year reanalysis: Monthly means CD-ROM and documentation. *Bull. Amer. Meteor. Soc.*, **82**, 247–267.

Landsea, C. W., B. A. Harper, K. Hoarau, and J. A. Knaff, 2006: Can we detect trends in extreme tropical cyclones? *Science*, **313**, 452–454.

Leoncini, G., R. A. Sr Pielke, and P. Gabriel, 2008: From model based parameterizations to lookup tables: An EOF approach. *Wea. Forecasting*, **23**, 1127-1145.

Rockel B., A. Will, and A. Hense, 2008: The regional climate model COSMO-CLM (CCLM). *Editorial, Meteorol. Zeitschrift*, **17**, 347–348.

Song, J.-J., Y. Wang, and L. Wu, 2010: Trend discrepancies among three best track data sets of western north pacific tropical cyclones. *J. Geophys. Res.*, **115**, D12128, doi:10.1029/2009JD013058.

Steppeler, J., G. Doms, U. Schättler, H.-W. Bitzer, A. Gassmann, U. Damrath, and G. Gregoric, 2003: Meso-gamma scale forecasts using the nonhydrostatic model LM. *Meteorol. Atmos. Phys.*, **82**, 75–96.

Tu, J.-Y., C. Chou, and P.-S. Chu, 2009: The abrupt shift of typhoon activity in the vicinity of taiwan and its association with western north pacific-east asian climate change. *J. Climate*, **22**, 3617–3628.

von Storch, H., H. Langenberg, and F. Feser, 2000: A spectral nudging technique for dynamical downscaling purposes. *Mon. Wea. Rev.*, **128**, 3664–3673.

—, and F. W. Zwiers, 1999: *Statistical analysis in climate research.* Cambridge University Press, 484 pp.

Wu, L., B. Wang, and S. Geng, 2005: Growing typhoon influence on East Asia. *Geophys. Res. Lett.*, 32, L18703, doi:10.1029/2005GL022937.

Science and Technology Infusion Climate Bulletin
NOAA's National Weather Service
37th NOAA Annual Climate Diagnostics and Prediction Workshop
Fort Collins, CO, 22-25 October 2012

El Niño-Southern Oscillation, the Madden-Julian Oscillation and Atlantic Basin Tropical Cyclone Rapid Intensification

Philip Klotzbach

Department of Atmospheric Science, Colorado State University, Fort Collins, CO

1. Introduction

El Niño-Southern Oscillation (ENSO) is a large-scale mode of coupled atmospheric/oceanic variability that impacts weather and climate around the globe (Rasmusson and Carpenter 1982). ENSO has significant impacts on tropical cyclone (TC) activity worldwide (Camargo *et al.*, 2007), with its notable impacts on seasonal Atlantic basin TC activity as well as U.S. hurricane landfalls being noted in a large number of studies (*e.g.*, Klotzbach 2011 and references therein). The Madden-Julian Oscillation (MJO) is a large-scale mode of tropical variability that propagates around the globe on an approximately 30-60-day timescale (Madden and Julian 1972). As it does, it alters large-scale fields such as vertical wind shear, sea level pressure (SLP), mid-level moisture and vertical motion. Klotzbach (2010) showed that when the convectively active phase of the MJO was located over Africa or in the western Indian Ocean (Phases 1-2 of the Wheeler-Hendon (WH) index (Wheeler and Hendon 2004)), Atlantic TC activity was enhanced.

Given that climate conditions appear more favorable for Atlantic basin storm formation in particular phases of the MJO and ENSO than in others, this study examines the possibility that these impacts extend to RI events as well. Section 2 describes the data utilized, while Section 3 examines the impacts of ENSO on Atlantic basin RI. Section 4 examines how RI frequency changes with MJO phase, while the strength of the relationship between RI and the combined MJO/ENSO index is considered in Section 5. Section 6 concludes the manuscript and provides ideas for future work.

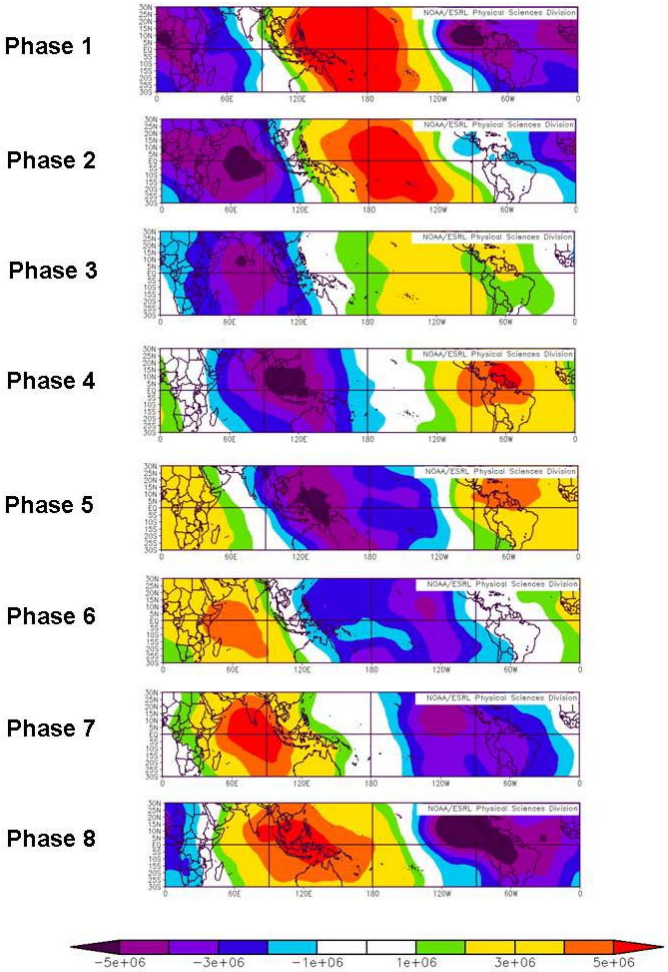

Fig. 1 200-mb velocity potential anomalies ($m^2 s^{-1}$) for the top 200 days for each MJO phase from July-October for each phase of the WH index. Cool colors indicate upper-level divergence while warm colors indicate upper-level convergence.

2. Data

The Multivariate ENSO Index (MEI) was utilized to classify ENSO events (Wolter and Timlin 1998). The MEI index is calculated using a bi-monthly average (*e.g.*, August-September). For the Atlantic hurricane season, the average of

Correspondence to: Philip Klotzbach, Department of Atmospheric Science, Colorado State University, Fort Collins, CO; E-mail: philk@atmos.colostate.edu.

the August-September and September-October MEI values are utilized. The ten highest values of the index since 1974 are classified as El Niño, the ten lowest values are classified as La Niña while the sixteen years in the middle are classified as neutral. All years since 1974 (excluding 1978) are utilized in this analysis, since this is when the MJO index is available in real-time.

The index utilized to classify the MJO was developed by Wheeler and Hendon (2004). The WH index is available from 1974-present, with data missing from April-December 1978 when OLR was unavailable. For this study, the period from 1974-2010 (except 1978) was examined. Figure 1 displays 200-mb velocity potential anomalies for the 200 days where the MJO is of the strongest amplitude for each of the eight phases of the MJO as defined by the WH index. Negative velocity potentials (cool colors) denote areas of upper-level divergence where convection is enhanced, while positive velocity potentials (warm colors) indicate areas where convection is suppressed.

An additional index is one that analyzes a similar tropical convective signal to that analyzed by the WH index but with ENSO and the 120-day-mean retained. This index is utilized to approximate the combined signal of MJO and ENSO in this analysis and is referred to as the WH-Combined index throughout the remainder of this manuscript. All calculations for both MJO indices are done for systems where the index (RMM1 + RMM2) (Wheeler and Hendon 2004) is greater than one (approximately 60% of days during the hurricane season). This helps to separate out periods when the MJO is inactive.

TC statistics were calculated from the National Hurrican Center's Best Track file available online at http://www.nhc.noaa.gov/data/hurdat/tracks1851to2010_atl_reanal.txt. Rapid intensification (RI) events were defined when a system intensified by 25-, 30-, 35-, and 40 or more knots in a 24-hour period.

The National Centers for Environmental Prediction/National Center for Atmospheric Research (NCEP/NCAR) Reanalysis I (Kistler *et al.* 2001) was utilized for all large-scale field calculations. All large-scale fields are calculated over the Main Development Region (MDR), which is defined to be 7.5-22.5°N, 75-20°W for this analysis, in keeping with the definition utilized by Klotzbach (2010).

3. ENSO's impacts on Atlantic basin RI

ENSO's impacts on Atlantic basin TCs have been related to a variety of physical fields, including changes in vertical wind shear, mid-level moisture, upper-tropospheric temperature and static stability (Tang and Neelin 2004; Klotzbach 2010). Given previous research, it is expected that Atlantic basin RI frequency might also be increased in La Niña years. Figure 2 displays the number of 24-hour RI events for various categories (from 25 to 40+ knots in 24 hours) for the MDR. The ratio differences between La Niña and El Niño reach approximately 6:1 when the MDR is considered.

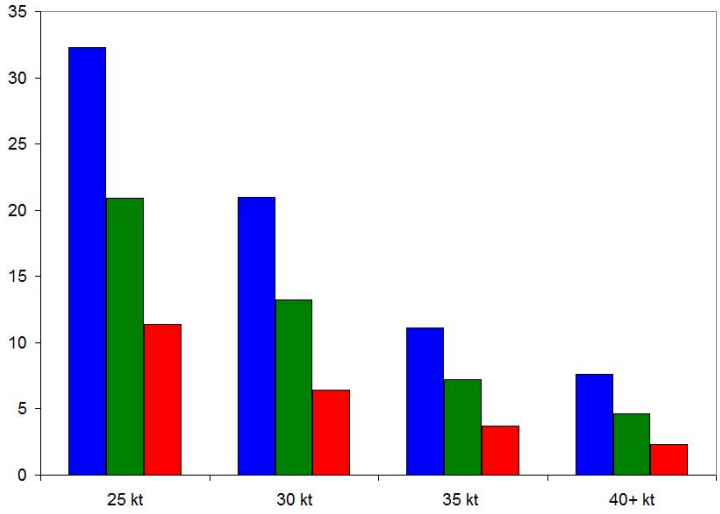

Fig. 2 Average numbers of events per-year for systems undergoing RI of 25-knot, 30-knot, 35-knot and 40+-knot thresholds for the entire Atlantic basin within a 24-hour period for years classified as La Niña (blue column), neutral (green column) and El Niño (red column). See text for ENSO classification scheme.

Another way to evaluate ENSO's impacts on RI is to examine the frequency of storms intensifying by various RI thresholds given a particular phase of ENSO. For example, 32% of systems forming in the MDR in a La Niña year undergo at least one 40+ knot RI at some point during their lifetime, while only 12% of systems forming in the MDR in an El Niño year undergo this level of RI.

Table 1 Number of 24-hour periods for systems undergoing RI of 25-knot, 30-knot, 35-knot and 40+-knot thresholds for systems forming in the MDR. Also provided are values normalized by the number of days that the MJO spends in each phase for July-October for systems forming in the MDR. These normalized values are multiplied by 100, so they can be interpreted as the number of 24-hour periods that one should expect given 100 days in a particular MJO phase. Ratios between Phases 1+2 and Phases 6+7 are provided for the normalized values.

MDR Systems								
	24 Hour Periods				Normalized Values			
MJO Phase	25 Kt	30 Kt	35 Kt	40+ Kt	25 Kt	30Kt	35 Kt	40+ Kt
1	98	61	36	27	22.0	13.7	8.1	6.1
2	89	58	37	27	22.4	14.6	9.3	6.8
3	15	6	3	2	6.9	2.8	1.4	0.9
4	37	23	11	7	14.5	9.0	4.3	2.7
5	31	22	11	8	6.8	4.8	2.4	1.8
6	21	12	6	2	6.8	3.9	1.9	0.6
7	3	1	1	0	1.5	0.5	0.5	0.0
8	13	10	5	2	5.8	4.5	2.2	0.9
Phases 1+2 / Phases 6+7					5.4	6.3	7.2	18.6

4. MJO's impacts on Atlantic basin RI

Since predicting TC RI remains one of the great challenges in hurricane forecasting (Sampson *et al.*, 2011), the knowledge of RI likelihood given what phase of the MJO a particular storm forms in is likely to be useful to TC forecasters. While several studies have examined the impacts of the MJO on Atlantic basin TC activity, to the author's knowledge, no study has explicitly studied RI. All calculations displayed in the following paragraphs are done for systems when the MJO is greater than or equal to one SD. When the WH index is less than one SD, the MJO is likely not playing a significant role in altering tropical convection.

Strong relationships are found between the MJO and systems forming in the MDR. Table 1 displays the number of 24-hour periods for each RI threshold for all TCs forming in the MDR. Also provided are normalized values, given that the MJO, as defined by Wheeler and Hendon (2004), spends more time in some phases than in others.

5. Combined MJO/ENSO impacts on Atlantic basin RI

In order to evaluate the MJO and ENSO in combination, the WH index with ENSO and the 120-day mean retained is now considered. As is the case with the WH index with ENSO and the 120-day-mean removed, the WH-Combined index is divided into eight phases spanning the globe. Since the ENSO phase is retained in the WH-Combined index, certain phases of the index are preferentially experienced during the hurricane season in El Niño versus La Niña years. Significantly

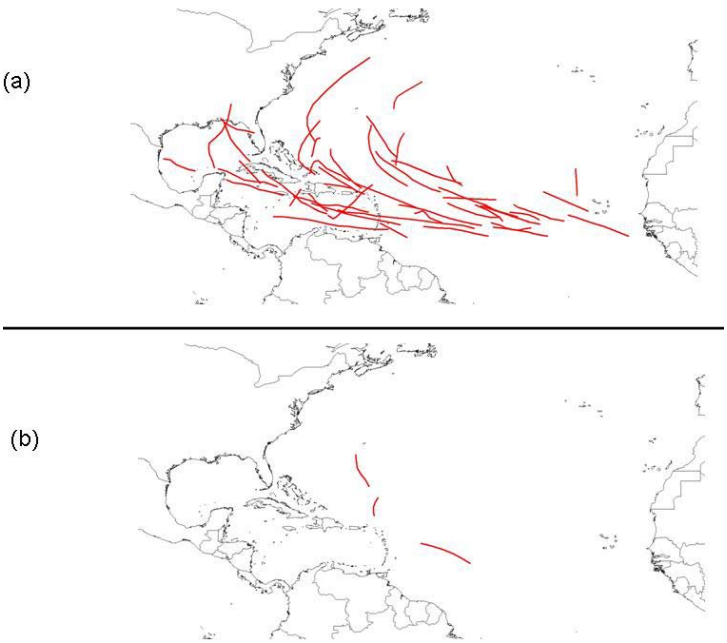

Fig. 3 Tracks of TCs undergoing an RI of 30 knots or greater in 24 hours during (a) Phases 2+3 defined by the WH-Combined index and (b) Phases 7+8 defined by the WH-Combined index. Normalized ratio differences between these phases is 38:1.

reduced levels of vertical wind shear are observed in Phases 2+3 of the WH-Combined index, while significantly increased levels of vertical wind shear are observed in Phases 7+8 of the WH-Combined index.

As would be expected given the dramatic changes in vertical shear, the largest differences are observed between Phases 2+3 and Phases 7+8. All differences in the mean between Phases 2+3 and Phases 7+8 are statistically significant at the 1% level for systems forming in the MDR. The difference in means are somewhat greater when the WH-Combined index is considered compared with the WH index by itself, indicating that considering both the MJO and ENSO in combination can provide extra signal compared with either the MJO or ENSO by itself. The difference between Phases 2+3 and Phases 7+8 is emphasized when displaying tracks for all TCs undergoing a 30-knot or greater RI during 24 hours (Figure 3).

6. Summary and future work

This paper showed the strong impact that both the MJO and ENSO have on RI episodes in the Atlantic basin. It began by examining ENSO's impacts on Atlantic basin RI and demonstrated that RI is much more frequent in La Niña events than in El Niño episodes with neutral ENSO events having RI frequency between cold and warm episodes. Given these relationships, RI episodes were then demonstrated to occur much more frequently in MJO Phases 1+2 than in MJO Phases 6+7, with other phases of the MJO showing relationships between these two extremes. When the MJO and ENSO were combined using the WH-Combined index, even stronger relationships were demonstrated.

The most conducive phases for RI in the Atlantic MDR occur when deep convective anomalies occur over the tropical Indian Ocean. Associated with these deep convective anomalies in the Indian Ocean are increased mid-level moisture and reduced vertical wind shear in the tropical Atlantic, both of which are critical factors for RI. When deep convective anomalies are concentrated over the central and eastern tropical Pacific, the Atlantic MDR tends to be drier and have enhanced vertical wind shear, which reduces the likelihood of RI.

One area of current research is determining whether incorporation of the daily MJO index would improve the skill of the Statistical Hurricane Intensity Prediction Scheme (SHIPS) (DeMaria *et al.*, 2005) or the recently-developed revised rapid intensity index (Kaplan *et al.*, 2010). This statistical model typically provides the best real-time forecast guidance for the National Hurricane Center, and consequently, any improvements to the SHIPS model could help prevent loss of life and property. Additional avenues for research include examining other ways of combining the MJO and ENSO to maximize skill. The impact of the MJO and ENSO on RI in other global TC basins will also be investigated.

References

Camargo, S. J., K. A. Emanuel, and A. H. Sobel, 2007: Use of a genesis potential index to diagnose ENSO effects on tropical cyclone genesis. *J. Climate*, **20**, 4819-4834.

DeMaria, M., M. Mainelli, L. K. Shay, J. A. Knaff, and J. Kaplan, 2005: Further improvements to the Statistical Hurricane Intensity Prediction Scheme (SHIPS). *Wea. Forecasting*, **20**, 531-543.

Kaplan, J., M. DeMaria, and J. A. Knaff, 2010: A revised tropical cyclone rapid intensification index for the Atlantic and Eastern North Pacific basins. *Wea. Forecasting*, **25**, 220-241.

Kistler, R., and Co-Authors, 2001: The NCEP-NCAR 50-year reanalysis: Monthly means CD-ROM and documentation. *Bull. Amer. Meteor. Soc.*, **82**, 247-267.

Klotzbach, P. J., 2010: On the Madden-Julian Oscillation-Atlantic hurricane relationship. *J. Climate*, **23**, 282-293.

Klotzbach, P. J., 2011: El Niño-Southern Oscillation's impacts on Atlantic basin hurricanes and U. S. landfalls. *J. Climate*, **24**, 1252-1263.

Madden, R. A., and P. R. Julian, 1972: Description of global-scale circulation cells in the tropics with a 40-50 day period. *J. Atmos. Sci.*, **29**, 1109-1123.

Rasmusson, E. M., and T. H. Carpenter, 1982: Variations in tropical sea surface temperature and surface wind fields associated with the Southern Oscillation/El Niño. *Mon. Wea. Rev*., **110**, 354-384.

Sampson, C. R., J. Kaplan, J. Knaff, M. DeMaria, and C. Sisko, 2011: A deterministic rapid intensification aid. *Wea. Forecasting*, **26**, 579-585.

Tang, B. H., and J. D. Neelin, 2004: ENSO influence on Atlantic hurricanes via tropospheric warming. *Geophys. Res. Lett*., **31**, L24204. doi:10.1029/2004GL021072.

Wheeler, M. C., and H. H. Hendon, 2004: An all-season real-time multivariate MJO index: Development of an index for monitoring and prediction. *Mon. Wea. Rev.*, **132**, 1917-1932.

Wolter, K., and M. S. Timlin, 1998: Measuring the strength of ENSO events - how does 1997/98 rank? *Weather*, **53**, 315-324.

Science and Technology Infusion Climate Bulletin
NOAA's National Weather Service
37th NOAA Annual Climate Diagnostics and Prediction Workshop
Fort Collins, CO, 22-25 October 2012

Short-term Climate Extremes: Prediction Skill and Predictability

Emily J. Becker[1], Huug van den Dool[1], and Malaquias Peña[2]

[1]*Climate Prediction Center, NCEP/NWS/NOAA, MD*
[2]*IMSG at Environmental Modeling Center, NCEP/NWS/NOAA, MD*

ABSTRACT

Forecasts for extremes in short term climate (monthly means) are examined to understand our current prediction capability and potential predictability. This study focuses on 2 m surface temperature and precipitation extremes over North and South America, and sea-surface temperature extremes in the Niño3.4 and Atlantic hurricane Main Development regions, using the Climate Forecast System (CFS) global climate model, for the period of 1982-2010. The primary skill measures employed are the anomaly correlation (AC) and root-mean-square error (RMSE). The success rate of forecasts is also assessed using contingency tables.

The AC, a signal-to-noise skill measure, is routinely higher for extremes in short-term climate than those when all forecasts are considered. While the RMSE for extremes also rises, especially when skill is inherently low, it is found that the signal rises faster than the noise. Permutation tests confirm that this is not simply an effect of reduced sample size. Both 2 m temperature and precipitation forecasts have higher anomaly correlations in the area of South America than North America; credible skill in precipitation is very low over South America and absent over North America, even for extremes. Anomaly correlations for SST are very high in the Niño3.4 region, especially for extremes, and moderate to high in the Atlantic hurricane Main Development Region. Prediction skill for forecast extremes is similar to skill for observed extremes. Assessment of the potential predictability under perfect-model assumptions finds that predictability and prediction skill have very similar space-time dependence. While prediction skill is higher in CFS version 2 than in CFS version 1, the potential predictability is not.

This work has been published in the *Journal of Climate* in 2012.

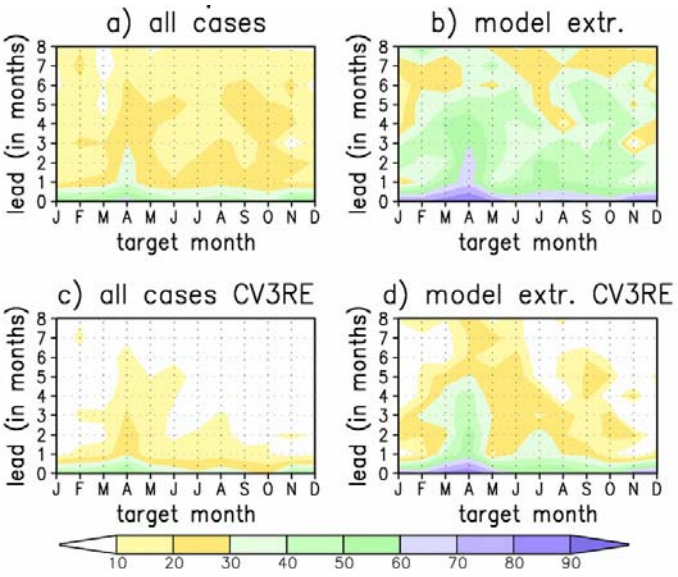

Fig. 1 CFSv2 2 m temperature anomaly correlations over North America, expressed as a function of the target month(horizontal) and lead (vertical), for a) all cases, b) when the model predicts an extreme, defined as +/- 1.645 local standard deviation, c) all cases with CV3RE applied (Cross-validation when three years are excluded. See the paper for details.), and d) predicted extremes with CV3RE applied. (From Becker *et al.* 2012)

Paper published

Becker, E. J., H. van den Dool, and M. Peña, 2012: Short term climate extremes: prediction skill and predictability. *J. Climate*. doi: http://dx.doi.org/10.1175/JCLI-D-12-00177.1.

Correspondence to: Emily Becker, Climate Prediction Center, NCEP/NWS/NOAA, 5830 University Research Court, College Park, MD 20740-3818; E-mail: Emily.Becker@noaa.gov.

4. TELECONNECTIONS AND STRATOSPHERIC IMPACTS

Science and Technology Infusion Climate Bulletin
NOAA's National Weather Service
37th NOAA Annual Climate Diagnostics and Prediction Workshop
Fort Collins, CO, 22-25 October 2012

The Influence of Teleconnections on Synoptic-Scale Circulation Patterns Affecting Western Canadian Water Resources

B. W. Newton[1], T. D. Prowse[2], and B. R. Bonsal[3]

[1]*Water and Climate Impacts Research Centre, Department of Geography, University of Victoria, Victoria, BC, Canada*

[2]*Water and Climate Impacts Research Centre, Environment Canada, Department of Geography, University of Victoria, Victoria, BC, Canada*

[3]*National Hydrology Research Centre, Environment Canada, Saskatoon, SK, Canada*

1. Introduction

Large-scale atmospheric circulation is linked to surface climate variables, such as temperature and precipitation. Indices of El Niño-Southern Oscillation (ENSO), the Pacific Decadal Oscillation (PDO), and the Pacific North American (PNA) pattern have also been shown to influence surface climate (*i.e.* Beltaos and Prowse 2009; Shabbar *et al.* 2011). Although knowledge about atmosphere-surface links and teleconnection-surface links exist, less is known about how teleconnections influence characteristics of atmospheric circulation.

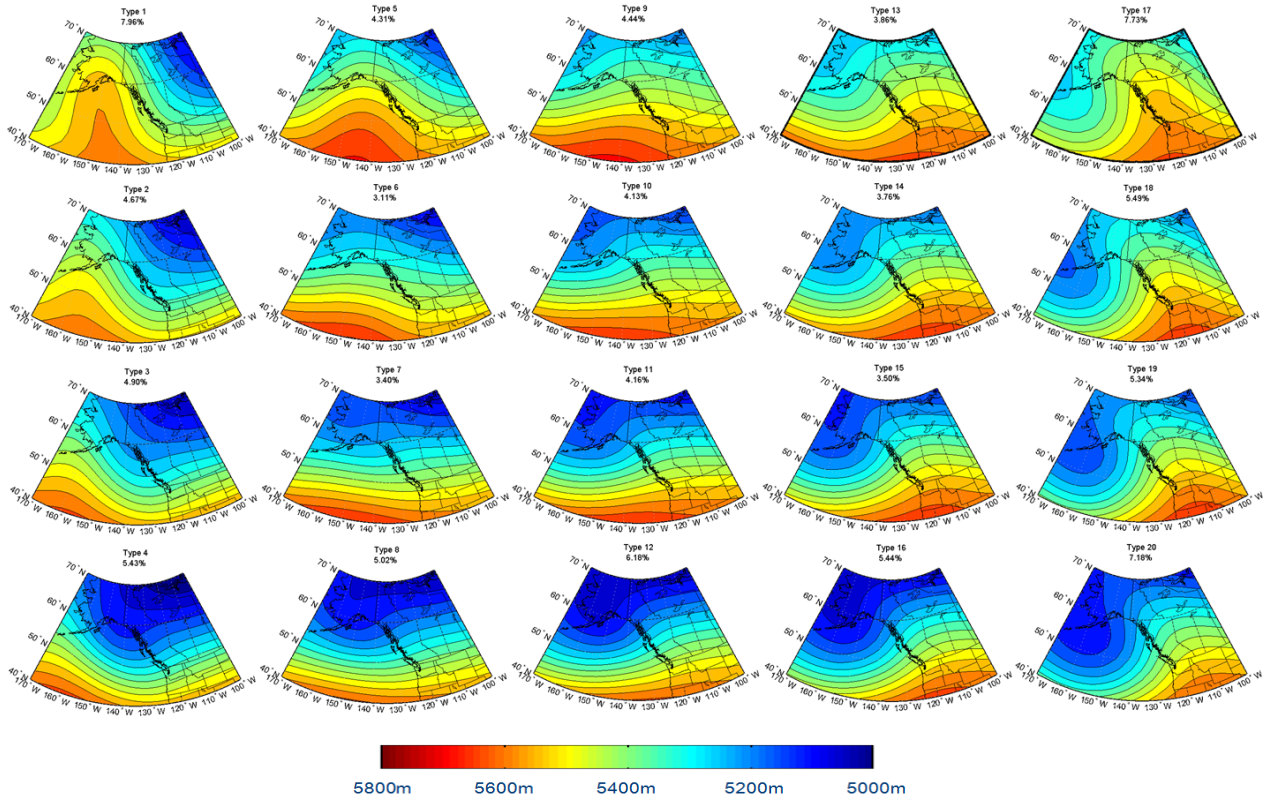

Fig. 1 Synoptic classification using SOM. Daily patterns of 500 hPa gph for 1949-2011 snow accumulation season (Nov-Apr). The array of synoptic maps is used to assess surface climate variables across the entire study region.

Correspondence to: B. W. Newton, Water and Climate Impacts Research Centre, Department of Geography, University of Victoria, Victoria, BC, Canada ; E-mail: bwnewton@uvic.ca.

Winter snow accumulation supplies an important water storage component that is released during spring freshet and provides the largest contribution to annual streamflow on rivers originating on the leeward slopes of the Rocky Mountains. The Liard, Peace, and Athabasca Rivers are tributaries to the north-flowing Mackenzie River. The largest source of freshwater to the Arctic Ocean is river discharge, and most of the flow on the Mackenzie River originates well outside the arctic (Serreze *et al.* 2003). Magnitude of snowpack and timing of snowmelt has implications for river ice dynamics (Beltaos and Prowse 2009), Arctic sea ice formation (Lammers *et al.* 2001), and feedbacks to the global climate (Lewis *et al.* 2000). The east-flowing North Saskatchewan, Red Deer, Bow, and Oldman Rivers are tributaries to the Saskatchewan River. Water demand is highest during summer months as these rivers are heavily allocated for agricultural, municipal, and industrial use, as well as used for hydroelectricity generation. This region is subject to routine droughts and pluvials affecting seasonal water availability (Shabbar *et al.* 2011). Understanding flow on the Mackenzie and Saskatchewan Rivers requires knowledge of the headwater source region, specifically snow regimes of the Rocky Mountains and links to the controlling atmospheric conditions, including synoptic climatology. This research represents a brief synopsis of a larger study evaluating the atmospheric drivers of water availability on rivers originating on the leeward slopes of the Rocky Mountains in Canada, and will contribute to our understanding of the climatic redistribution of western Canadian water resources.

71.6	**40.5**	**44.7**	**37.9**	**70.2**
39.7	**22.1**	**30.4**	**28.0**	**45.5**
36.8	**22.8**	**26.2**	**24.7**	**42.2**
56.7	**40.0**	**45.7**	**45.0**	**66.7**

Fig. 2 Synoptic pattern persistence.

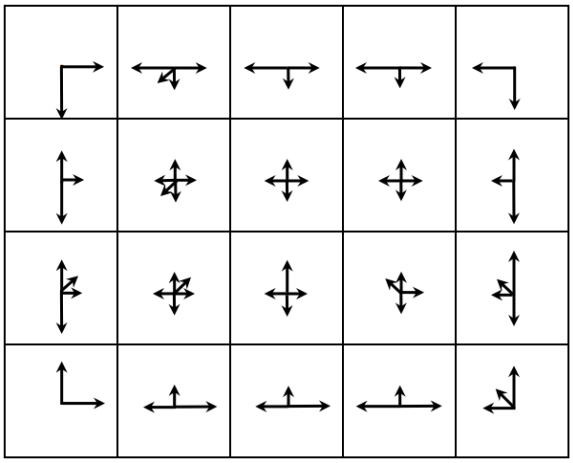

Fig. 3 Synoptic pattern trajectory.

2. Data and methodology

To assess the characteristics of dominant synoptic circulation patterns as they relate to the spatial and temporal distribution of water availability, daily mid-tropospheric circulation patterns at 500 hPa geopotential height (gph) for 1949-2011 snow accumulation seasons (Nov-Apr) were classified using self-organizing maps (SOM), an iterative training process that uses competitive and cooperative learning to cluster and project data onto an organized output array (Kohonen 2001). This research used the batch algorithm SOM as it was determined to be faster and less subjective than the sequential algorithm (Kohonen 1999; Liu and Weisberg 2005; Jiang *et al.* 2011). Daily values of PNA, and monthly values of the Southern Oscillation Index (SOI) (representing ENSO), and PDO were used to calculate a 3-month (DJF) mean. The mean value was used to classify winters into positive or negative SOI, PDO, and PNA to evaluate changes in frequency.

-0.69	**-0.42**	**-0.01**	**0.24**	**0.57**
-0.84	**-0.33**	**0.05**	**0.39**	**0.75**
-0.78	**-0.24**	**0.20**	**0.49**	**0.76**
-0.76	**-0.18**	**0.21**	**0.55**	**0.77**

Fig. 4 Average PNA value corresponding to each synoptic type.

3. Results

Daily synoptic circulation patterns were classified into 20 types (Figure 1). Persistence (Figure 2) represents the percentage of occurrences where the pattern is followed by the same pattern the following day. Trajectory (Figure 3) represents the preferential pattern shifts, which occurs primarily around the outer edge of the SOM array.

The average PNA value associated with each synoptic pattern was calculated (Figure 4), and indicates a clear pattern of strongly negative PNA in the far left column and strongly positive PNA in the far right column, a function of the organizational qualities of the SOM. Patterns 1-4 in the far left column of the SOM array were also determined to occur with a greater frequency during negative phases of PDO and positive phases of SOI, and patterns 17-20 in the far right column were found to occur with a greater frequency during positive phases of PDO and negative phases of SOI (Figure 5). Frequency differences for PDO, SOI, and PNA were assessed individually, with similar results. The strongest frequency relationships were found when isolating seasons that fit the criteria of coupled teleconnection phases, such as positive PDO, negative SOI, and positive PNA.

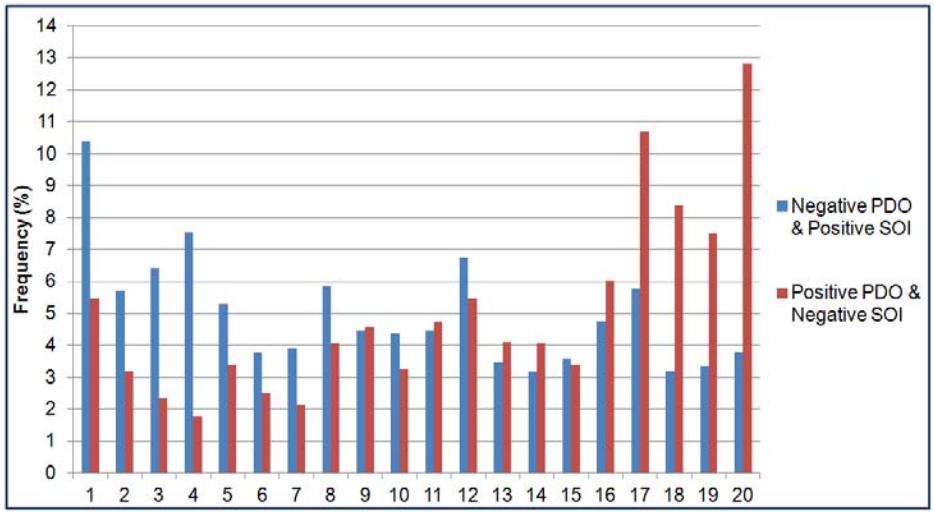

Fig. 5 Frequency (%) of occurrence for each synoptic type during negative PDO coupled with positive SOI, and positive PDO coupled with negative SOI.

Synoptic types 1-4 are associated with higher precipitation and lower temperatures throughout the study region. A ridge of high pressure centred over the Pacific Ocean results in the advection of cold arctic air south across the Rocky Mountains. Synoptic types 17-20 are associated with lower precipitation and higher temperatures. These patterns are characteristic of high pressure over the continent and a strong Aleutian Low in the North Pacific Ocean.

4. Discussion and future work

Numerous studies have described the influence of teleconnections on surface climate; few have addressed the impacts of teleconnections on synoptic-scale circulation. Synoptic types 1-4 and 17-20 were determined to experience the greatest influence from teleconnection phases, as well as exerting the greatest influence on surface climate variables. During negative phases of PDO, positive phases of SOI, and negative phases of PNA, mid-tropospheric circulation is expected to favour high pressure ridging over the Pacific Ocean and result in higher precipitation and lower temperatures. During positive phases of PDO, negative phases of SOI and positive phases of PNA, mid-tropospheric circulation is expected to favour high pressure over the continent and a strong Aleutian Low over the North Pacific Ocean. These patterns of mid-tropospheric circulation result in lower precipitation and higher temperatures on the leeward slopes of the Rocky Mountains.

Future work includes statistical time series trend analysis of synoptic type frequency to determine significant increases or decreases over time. Further work to evaluate the spatial distribution of association with surface climate across the study area will be completed using a gridded dataset of daily values of precipitation and temperature at 10km resolution.

References

Beltaos, S. and T.Pr owse, 2009: River-ice hydrology in a shrinking cryosphere. *Hydrol. Processes*, **23**, 122-144. doi: 10.1002/hyp.7165.

Jiang, N., K. Cheung, K. Luo, P.J. Beggs, and W. Zhou, 2011: On two different objective procedures for classifying synoptic weather types over east Australia. *Int. J. Climatol.* doi: 10.1002/joc.2373.

Kohonen, T., 1999: Fast evolutionary learning with batch-type self-organizing maps. *Neural Processing Letters*, **9**, 153-162.

Kohonen, T., 2001: *Self-Organizing Maps*. Springer, New York.

Lammers, R.B., A.I. Shiklomanov, C.J. Vörösmarty, B.M. Fekete, and B.J. Peterson, 2001: Assessment of contemporary Arctic river runoff based on observational discharge records. *J. Geophys. Res.*, **106**, D4, 3321-3334.

Lewis, E.L., 2000: *The Freshwater Budget of the Arctic Ocean*. Kluwer Academic Publishers, Dordrecht.

Liu, Y. and R.H. Weisberg, 2005: Patterns of ocean current variability on the West Florida Shelf using the self-organizing map. *J. Geophys. Res.*, **110**, C06003. doi: 10.1029/2004JC002786.

Serreze, M.C., D.H. Bromwich, M.P. Clark, A.J. Etringer, T. Zhang, and R. Lammers, 2003: Large-scale hydro-climatology of the terrestrial Arctic drainage system. *J. Geophys. Res.*, **108**, D2, 8160.

Shabbar, A., B.R. Bonsal, , and K. Szeto, 2011: Atmospheric and oceanic variability associated with growing season droughts and pluvials on the Canadian Prairies. *Atmosphere-Ocean*, **1**, 1-17.

Science and Technology Infusion Climate Bulletin
NOAA's National Weather Service
37th NOAA Annual Climate Diagnostics and Prediction Workshop
Fort Collins, CO, 22-25 October 2012

The Multivariate PNA Index: A New Index for Identifying MJO Impacts over North America

Carl J. Schreck III[1] and David Margolin[2]

[1]*Cooperative Institute for Climate and Satellites–North Carolina (CICS-NC), North Carolina State University and NOAA's National Climatic Data Center, Asheville, NC*
[2]*EarthRisk Technologies, Chicago, IL*

1. Introduction

The Madden–Julian Oscillation (MJO; Zhang 2005) influences weather patterns around the globe with its 30–60 day period. Recent studies have shown that it can influence temperature and precipitation patterns over North America (Becker *et al.* 2011; Zhou *et al.* 2012). These impacts are frequently diagnosed using the Wheeler–Hendon (2004) Real-time Multivariate MJO (RMM) index. The eastern United States tends to be warm when the MJO's enhanced convection is over the western Pacific (phases 5/6) and cold when that convection is over the Western Hemisphere and Africa (phase 8/1).

These impacts are driven by interactions between the MJO's tropical convection and extratropical weather patterns like the Arctic Oscillation, the North Atlantic Oscillation, and the Pacific/North American (PNA) teleconnection (Riddle *et al.* 2012 and references therein). Naturally not every MJO event produces the same extratropical response. This project develops a new index, the Multivariate PNA (MVP), to discern which MJO events will affect North American temperatures and which will not.

2. Data

Outgoing longwave radiation (OLR) from the NOAA polar-orbiting satellites will be used here as a proxy for the tropical convection associated with the MJO. The extratropical responses will be identified using streamfunction, geopotential heights, and temperatures from the NCEP–DOE Reanalysis 2. Both datasets were obtained from NOAA/ESRL/PSD. Only dates from December–February 1979/80–2010/11 are used.

3. Constructing the MVP

When the MJO affects North American temperatures, the tropical convective heating forces a Rossby wave train. For that reason, we use a combined empirical orthogonal function (EOF) of outgoing longwave radiation (OLR) and streamfunction at 850 hPa and 200 hPa. This combined EOF is calculated using data that have been filtered for 20–100 days to focus on the MJO time scale. Such data is difficult to produce in near-real time, so we project the filtered EOF onto unfiltered data to produce the principal component time series.

Figure 1 illustrates the resulting EOF loading pattern. The 200-hPa streamfunction (top panel) shows

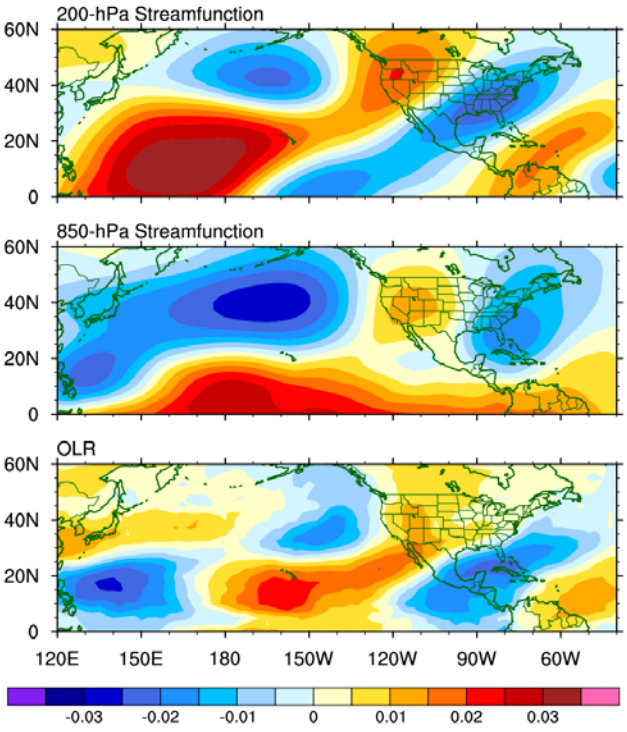

Fig. 1 EOF loading pattern for 200-hPa streamfunction (top), 850-hPa streamfunction (middle), and OLR (bottom).

Correspondence to: Carl J. Schreck III, Cooperative Institute for Climate and Satellites–North Carolina, North Carolina State University and NOAA's National Climatic Data Center, Asheville, NC; E-mail: carl@cicsnc.org.

a wave train pattern originating in the tropical Pacific, crossing North America, and then descending back to the tropical Atlantic. This pattern is reminiscent of the conventional PNA pattern, although the waveguide in the new index is shifted 5°–10° latitude farther south. The new index has a 0.57 correlation with the PNA from NOAA's Climate Prediction Center (NOAA/CPC). To reflect this connection, the new index is dubbed the "Multivariate PNA" (MVP) index.

At 850-hPa (middle panel), the streamfunction shows the low-level reflection of the wave train, along with anomalous zonal flow near Hawaii. The OLR pattern identifies anomalous convection near Hawaii that extends to the southwestern United States, like the familiar "pineapple express." Three opposite-signed OLR anomalies are also found to the north, east, and west.

4. North American impacts

As noted before, we expect to see warmth over the eastern United States when the RMM is in phase 5 and cold in phase 8. Figure 2 illustrates how we can use the MVP to discern which MJO events will produce these impacts. It shows composite anomalies of 850-hPa temperatures (shading) and 500-hPa geopotential height for phases 5 (top) and 8 (bottom). The composites are subdivided by the MVP. Days where the MVP ≤ -0.75 are on the left, $-0.75 <$ MVP $< +0.75$ are in the middle, and MVP $\geq +0.75$ are on the right. In each case, the anomalies are averaged for the pentad centered 8 days after the composite date to show the predictive potential.

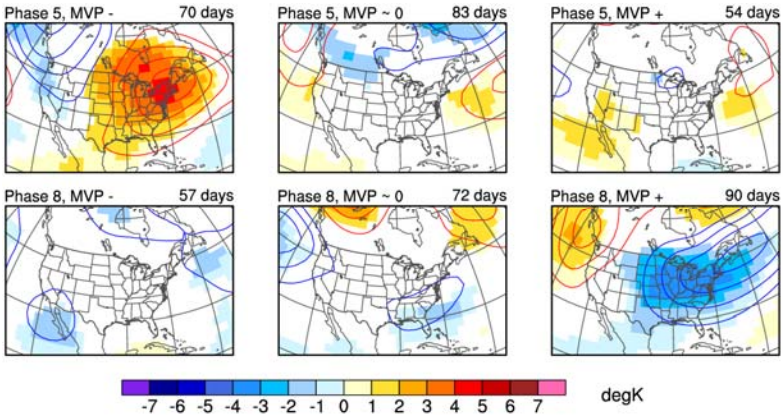

Fig. 2 Composite anomalies of 850-hPa temperature (shading) and 500-hPa geopotential height (contours) averaged 6–10 days after the RMM is > 1.0 and in phase 5 (top) or phase 8 (bottom). The composite dates are further subdivided by days when MVP ≤ -0.75 (left), $-0.75 <$ MVP $< +0.75$ (middle), and MVP $\geq +0.75$ (right). Only temperature anomalies that are 95% significant are shaded. Geopotential height anomalies are contoured every 20 m.

As discussed before, warm anomalies are generally associated with phase 5, but the top row of Fig. 2 shows that these anomalies are only observed for MVP ≤ -0.75. When the MVP is neutral or positive, that warm signal disappears. Conversely, the bottom row shows that the cold in Phase 8 only occurs for MVP $\geq +0.75$. The signal is absent for the neutral and negative phases. The number of dates used for each composite is shown in the upper right. Note that for both RMM phases, the MVP is relatively equally distributed among positive, negative, and neutral.

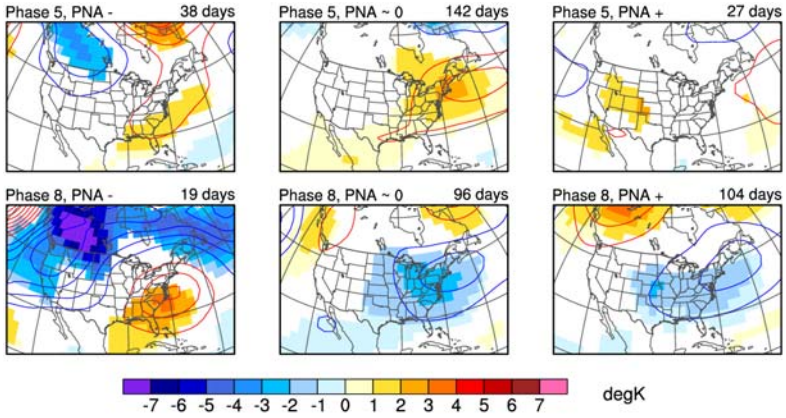

Fig. 3 As in Fig. 2, but subdivided by PNA ≤ -0.75 (left), $-0.75 <$ PNA $< +0.75$ (middle), and PNA $\geq +0.75$ (right).

Figure 3 repeats the composite analysis using NOAA/CPC's PNA index, which does not show the same sensitivity. For phase 5, the largest warm signal occurs when the PNA is neutral, which accounts for 69% of the days. A weaker signal is found when the PNA is negative, and none when it is positive. For phase 8, cold signals are observed for both the positive and neutral PNA composites. The negative PNA is actually associated with a warm signal over the

southeastern United States and a cold signal over northwestern North America. However, this composite accounts for only 9% of the total days in phase 8.

Since the MVP is focused on the North Pacific basin, it could be influenced by the El Niño–Southern Oscillation (ENSO). To investigate this possibility, Fig. 4 shows the number of days per year where the RMM is in phase 5 (top) or phase 8 (bottom) and the MVP is $\geq +0.75$ (red) or ≤ -0.75 (blue). Some degree of interannual variability is apparent, most notably the large number of negative MVP events in phase 8 during 1991/92. However, if ENSO were a driving factor, then significant ENSO years like 1982, 1997, and 1998 would stand out.

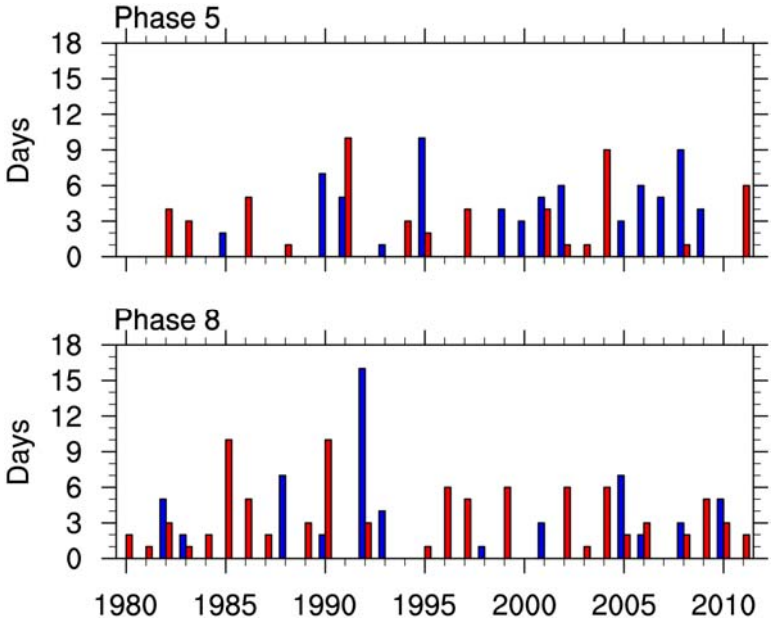

Fig. 4 Number of days per December–February when the MVP ≤ -0.75 (blue) or MVP $\geq +0.75$ (red) and the RMM is in phase 5 (top) or phase 8 (bottom).

5. Summary and future plans

This study proposes a new index, the MVP, for identifying which MJO events will influence North American temperatures and which will not. This index is based on a combined EOF of 20–100 day filtered OLR and streamfunction at 850 hPa and 200 hPa. Composites indicate that the warm anomalies in phase 5 are strongly associated with the MVP being negative, while the cold anomalies in phase 8 occur with a positive MVP.

The MVP is related to the conventional PNA, but the PNA is unable to replicate these signals. There are several possible explanations:

1) The MVP more explicitly incorporates the MJO's diabatic heating by including OLR.
2) The wave train in the MVP is shifted 5°–10° southward, which might be associated with more persistent temperature patterns.
3) The phase of the PNA is too closely related to that of the MJO to provide enough null cases that lack the expected temperature signals.

For these reason, the MVP seems to be more useful for identifying the MJO's impacts over North America.

A logical next step will be to determine why some MJO events produce a response over North America while others do not. Preliminary results suggest that the convective anomaly near Hawaii in the bottom panel of Fig. 1 might play an important role. This convection may be associated with anti-cyclonic wave breaking from the extratropics. Therefore, further research is required to determine whether the convection is driving the circulation or vice versa.

Acknowledgements. Schreck received support for this research from NOAA's Climate Data Record (CDR) Program through the Cooperative Institute for Climate and Satellites-North Carolina (CICS-NC).

References

Becker, E. J., E. H. Berbery, and R. W. Higgins, 2011: Modulation of cold-season U.S. daily precipitation by the Madden–Julian Oscillation. *J. Climate*, **24**, 5157–5166, doi:10.1175/2011JCLI4018.1.

Riddle, E., M. Stoner, N. Johnson, M. L'Heureux, D. Collins, and S. Feldstein, 2012: The impact of the MJO on clusters of wintertime circulation anomalies over the North American region. *Clim. Dyn.*, 1–18, doi:10.1007/s00382-012-1493-y.

Wheeler, M. C., and H. H. Hendon, 2004: An all-season real-time multivariate MJO index: Development of an index for monitoring and prediction. *Mon. Wea. Rev.*, **132**, 1917–1932.

Zhang, C., 2005: Madden-Julian oscillation. *Rev. Geophys.*, **43**, RG2003, doi:10.1029/2004RG000158.

Zhou, S., M. L'Heureux, S. Weaver, and A. Kumar, 2012: A composite study of the MJO influence on the surface air temperature and precipitation over the Continental United States. *Clim. Dyn.*, **38**, 1459–1471, doi:10.1007/s00382-011-1001-9.

Science and Technology Infusion Climate Bulletin
NOAA's National Weather Service
37th NOAA Annual Climate Diagnostics and Prediction Workshop
Fort Collins, CO, 22-25 October 2012

A Teleconnection Between Geopotential Height Anomalies over the North Atlantic and Precipitation in the Sahel Region of Africa

Daniel Barandiaran and Shih-Yu Wang

Department of Plants, Soils, and Climate, Utah State University, Logan, UT

ABSTRACT

This study presents initial findings on a link between inter-annual variability in atmospheric circulations over the North Atlantic and precipitation over the African Sahel (P_S). Our analysis shows that a meridionally stratified circulation wave train resembling the East Atlantic (EA) mode has a pronounced connection with P_S, and that the Climate Forecast System version 2 (CFSv2) fails to depict this EA mode and its P_S impact. Since the EA mode explains about 20% of variance of P_S, our analysis result is suggestive of a comparable portion of PS variability that is missing in CFSv2 operational forecast.

1. Introduction

The African Sahel, a semi-arid region lying along the southern edge of the Sahara Desert, is characterized by large climate variability in summer precipitation on the inter-annual and inter-decadal time scales. The El Nino-Southern Oscillation (ENSO) is known as an important modulator of the Sahel summer precipitation (P_S) (*e.g.*, Joly and Voldoire, 2009). Other climatic forcing factors that modulate P_S include sea surface temperature (SST) anomalies in the Indian Ocean (Bader and Latif, 2003) and the tropical Atlantic (Brandt *et al.*, 2010). These previous findings were mainly based upon the concept of SST-driven, tropically confined teleconnections affecting P_S. By comparison, the process of a mid-latitude influence on the Sahel climate has drawn much less attention, possibly because of the prominent Sahara heat low and the robust mid-level African high (*e.g.*, Chen 2005) potentially blocking any teleconnection influences originating from higher latitudes.

Most of the mid- to high-latitude climate oscillations, such as the North

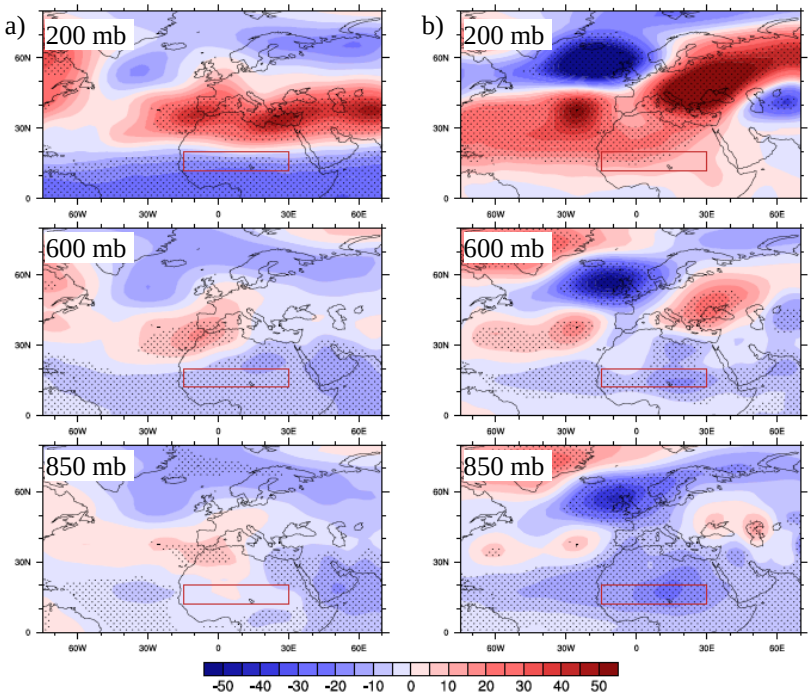

Fig. 1 Composite differences of geopotential height over the years 1950-2010 for (a) La Nina summers (normalized Nino3.4 index < -1) minus El Nino summers (normalized Nino3.4 index > 1), and (b) wet summers (normalized P_S > 1) minus dry summers (normalized P_S < -1) during ENSO-Neutral years (normalized Nino3.4 index between -1 and 1). Precipitation data were obtained from the PREC/L. Red box indicates the Sahel region. Stippling indicates statistical significance of 95% per *t*-test.

Correspondence to: Daniel Barandiaran, Department of Plants, Soils, and Climate, Utah State University, Logan, UT; E-mail: dbarandiaran@gmail.com.

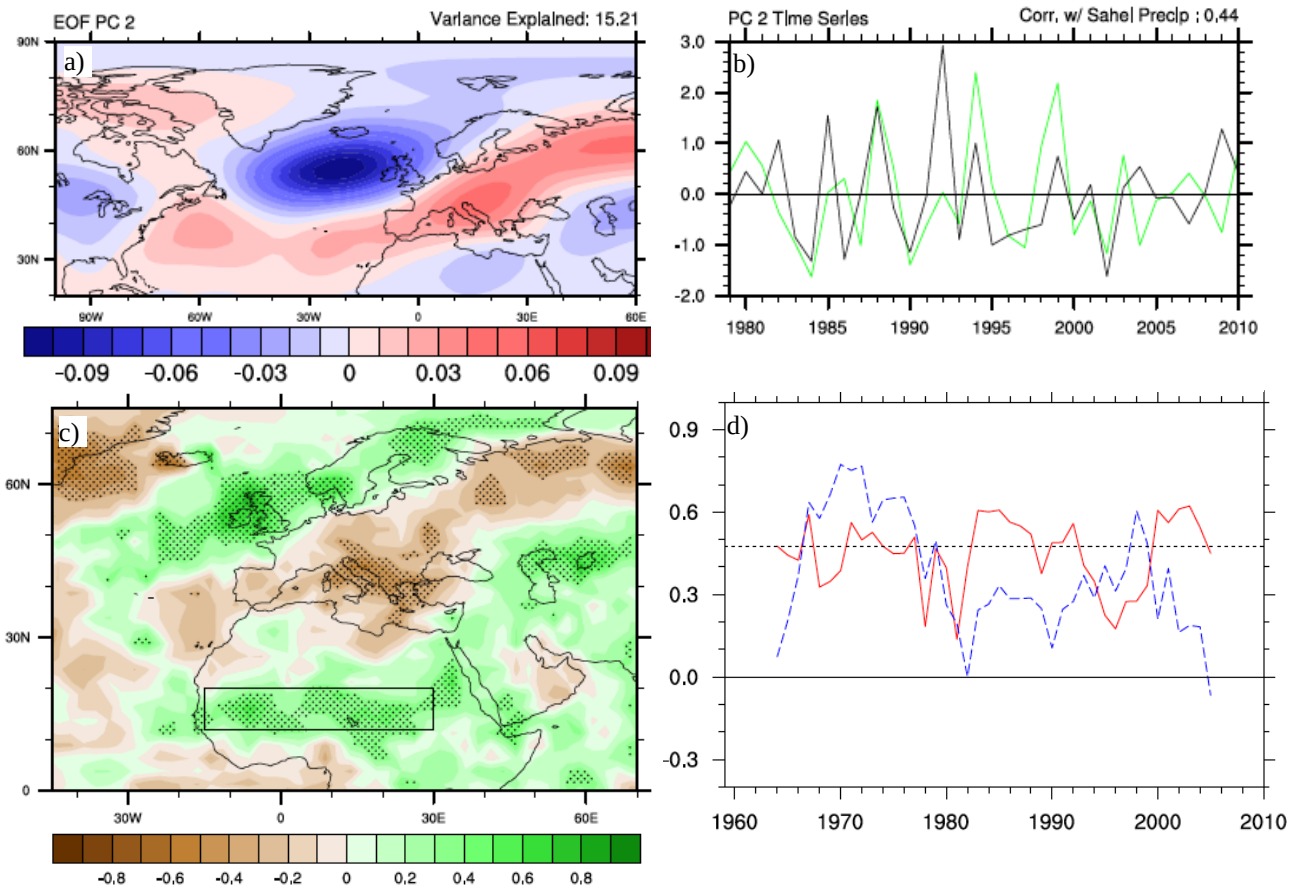

Fig. 2 (a) Second EOF of the 600mb geopotential height during the JAS season over the years 1979-2010. (b) Normalized second PC time series (black) and the normalized JAS P_S (green). (c) One-point correlation map between PC2 time series and P_S; stippling shows significance of 95% per r-test. (d) Sliding correlations of 11-year window between P_S and Nino-3.4 (red) and PC2 (blue); the horizontal dashed line indicates significance at 95%.

Atlantic Oscillation (NAO; Hurrell *et al.*, 2003), are predominately winter phenomena, even though their presence and effects during summer months have been studied (*e.g.*, Folland *et al.*, 2009). For the Sahel region, Chen and Wang (2007) noticed a connection between P_S and an atmospheric short-wave train in the North Atlantic during active ENSO years. In this study, we show a meridional wave train pattern that connects P_S with a possible higher latitude influence, regardless of the state of ENSO. Our analysis indicates that such a North Atlantic wave train is linked to the so-called East Atlantic (EA) mode, first identified by Barnston and Livezey (1987) as a center of anomalous 700mb geopotential height off the coast of Ireland with wave-like disturbances downstream across Europe. More importantly, we report that this EA-P_S linkage is missing in one of the major climate forecast models, hence representing missing variability of P_S in seasonal climate prediction.

This study utilized the National Center for Environmental Prediction (NCEP)/National Corporation for Atmospheric Research (NCAR) Reanalysis I (Kalnay *et al.*, 1996) for atmospheric data. Rain gauge observations compiled and gridded by the National Oceanic and Atmospheric Administration (NOAA) precipitation reconstruction over land (PREC/L, Chen *et al.*, 2002) were used. We also analyzed the Global Precipitation Climatology Project (GPCP, Adler *et al.*, 2003), which synthesized rain gauge and satellite derived precipitation after 1979. The reforecast outputs (or hindcast) from the NCEP Climate Forecast System version 2 (CFSv2, Saha *et al.*, 2012) were examined for the forecast skill of P_S. Our primary focus is inter-annual variability after 1979; hence, all data after 1979 have been linearly detrended to remove long-term variability. Hereafter the term P_S and all other analyses are focused on the July-September (JAS) season. P_S was defined as the average precipitation within 12°-20° N and 15° W-30° E. Precipitation and various

climate indices used in the following analyses were normalized for ease of comparison between observational and model data.

2. The North Atlantic influence on P_S

2.1 Empirical evidence

The well-known ENSO influence on P_S is illustrated in Fig. 1a by the composites of geopotential height anomalies during ENSO-active years, *i.e.* La Nina minus El Nino years based on normalized JAS Nino-3.4 index less than -1/greater than 1. These composites reflect the resultant wet conditions in the Sahel. During ENSO-active years, the largest anomalies appear at 200mb over the Mediterranean Sea and North Africa, with considerably weaker amplitudes occurring at lower levels. During La Nina (El Nino) events, the circulation anomalies result in increased (decreased) strength of the tropical easterly jet (TEJ) and enhanced (suppressed) divergence aloft, which in turn enhances (suppresses) convection over the Sahel and West Africa (*e.g.*, Nicolson and Grist 2001). By comparison, the composite circulation anomalies between anomalous rainfall years (wet minus dry, using years when |normalized P_S| > 1, using PREC/L data), computed during ENSO-neutral years in which the absolute values of normalized Nino 3.4 index are less than 1, portray a quite different circulation pattern (Fig. 1b). First, substantial circulation anomalies leading to wet conditions in the Sahel (without the ENSO influence) are persistent throughout the lower troposphere. Second, there is a northwest-southeast oriented wave train extending from Greenland to North Africa, particularly at 600mb. The "center of action" of this wave train appears to be the pronounced negative anomaly west of Ireland

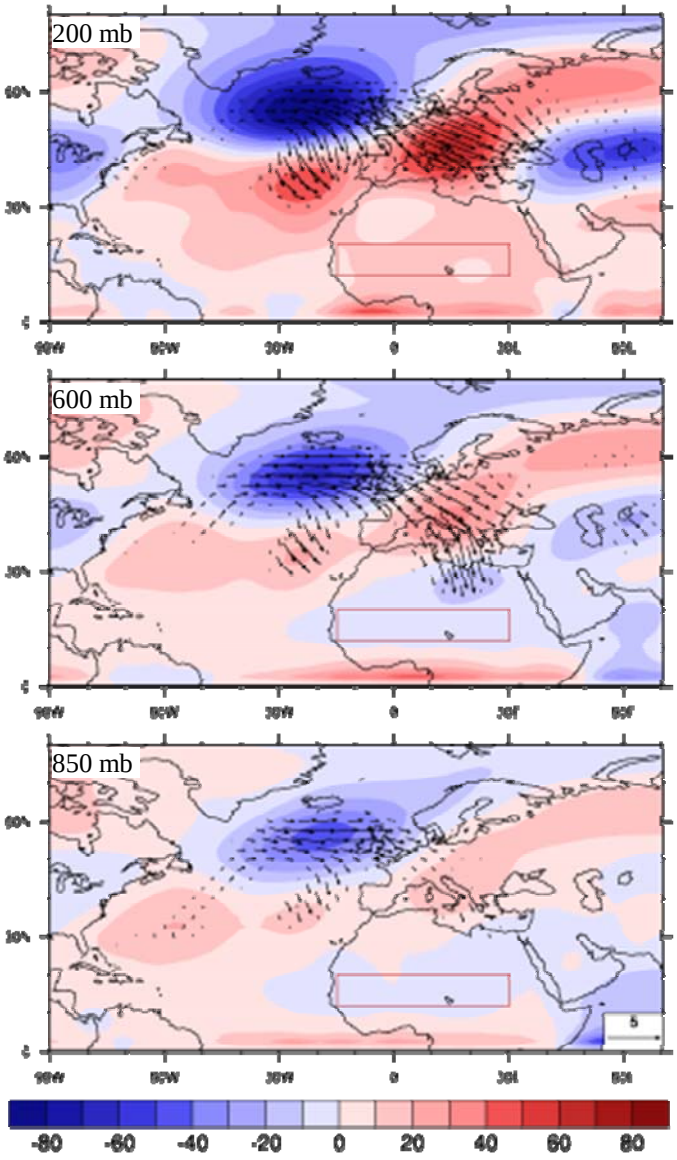

Fig. 3 Same as Fig. 1b but for 1979-2010 and with the Rossby wave activity flux (W) vectors. Vectors with the length smaller than 1 $m^2 s^{-2}$ were omitted.

The meridional wave train pattern revealed in Fig. 1b is suggestive of a teleconnection influence emerging from higher latitudes on P_S. To examine the extent and origin of this wave train, we first conducted the Empirical Orthogonal Function (EOF) analysis on the 600mb geopotential height for the JAS seasons spanning 1979-2010 over the North Atlantic region as outlined in Fig. 2a. Shown in Fig. 2a is the second EOF that resembles the EA pattern (Barnston and Livezey 1987) as well as the composite wave train in Fig. 1b. This result is in agreement with the EOF leading modes of summertime sea level pressure by Folland *et al.* (2009); *i.e.* their EOF1 was the NAO and EOF2 was an EA-like pattern. What was not shown in Folland *et al.*'s analysis, however, is the significant correlation of the second principal component (PC2) with P_S, as is evidenced in Fig. 2b (r=0.43). By contrast, the NAO (*i.e.* PC1) does not reveal any significant correlation with P_S (r = -0.07).

Based upon their correlations during the period 1979-2010, ENSO explains 26% of the variance of P_S while PC2 explains 19%. Spatial correlations between PC2 and GPCP precipitation (Fig. 2c) show

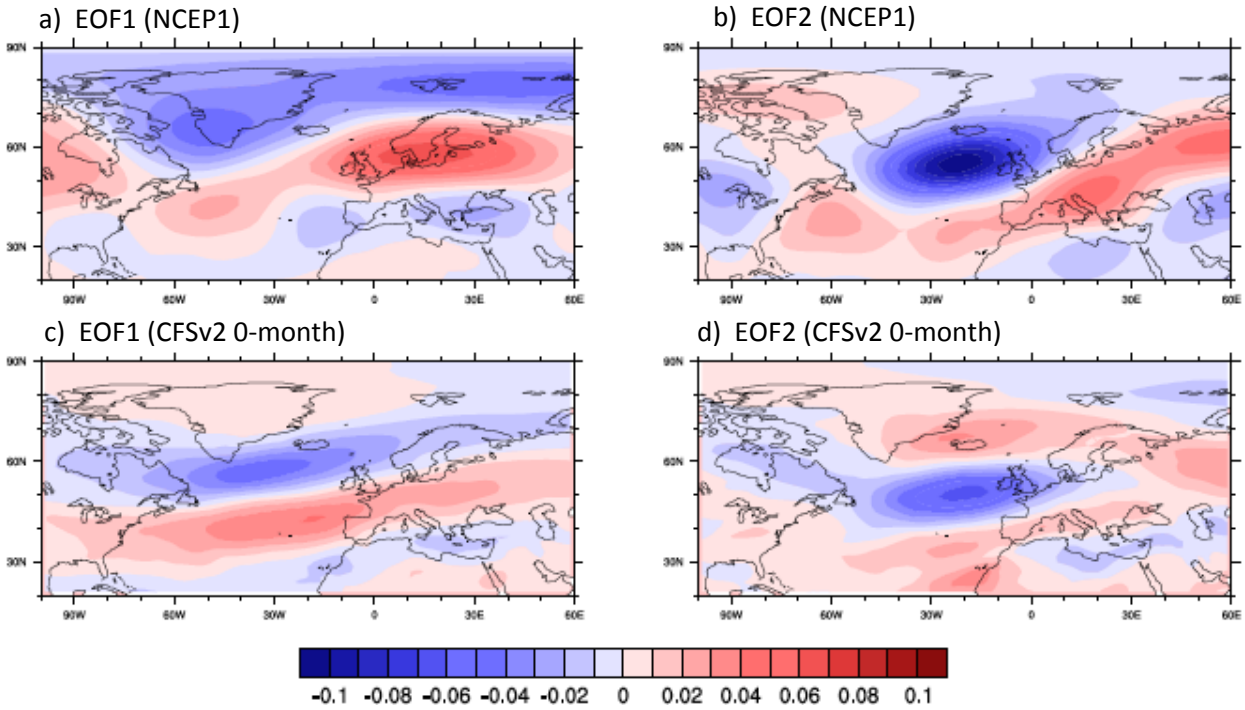

Fig. 4 EOF analysis of the 600mb geopotential height of (a) EOF1 of NCEP1, (b) EOF2 of NCEP1, (c) EOF1 of CFSv2, and (d) EOF2 of CFSv2 at 0-month lead forecast.

significant responses across the Sahel region (boxed area). The precipitation correlations also reveal a north-south stratified structure that corresponds to the EOF2 (or EA) pattern. To examine the connection of PC2 with prominent climate modes, we computed the correlations of P_S with other common climate indices including ENSO, the Arctic Oscillation (AO), the Pacific-North American Pattern (PNA), the Atlantic Multidecadal Oscillation (AMO), and the Pacific Decadal Oscillation (PDO), obtained from the NOAA Climate Prediction Center (CPC; http://www.cpc.ncep.noaa.gov/data/teledoc/). The results showed that PC2 is independent of all these climate oscillations. Moreover, only ENSO and PC2 are significantly correlated with P_S.

According to Barnston and Livezey (1987) and the CPC, which provides the EA index (http://www.cpc.ncep.noaa.gov/data/teledoc/ea.shtml), the EA index was determined using the EOF analysis over the entire Northern Hemisphere (rather than the North Atlantic domain as in this study). Because EOF analysis is sensitive to geographic domain and dataset differences, a point-based EA index approach was utilized here. Based upon the EOF2 pattern as shown in Fig. 2a, we selected three geographical locations and applied the following formula:

$$EA = Z_{600}(5^oN, 15^oE) - 3 * Z_{600}(55^oN, 22.5^oW) + 2 * Z_{600}(30^oN, 20^oE), \quad (1)$$

where Z_{600} is the 600mb geopotential height in the JAS season. This point-based EA index correlates strongly with the PC2 time series (r=0.924) and its spatial correlation with precipitation is essentially unchanged (not shown). Hereafter we refer to EA as the index built from Eq. (1), rather than PC2.

The relationship between P_S and EA was further examined by computing an 11 year sliding correlation, as shown in Fig. 2d by the center year. The linear trend within each 11-yr window was removed prior to computing the correlation to minimize the impact from inter-decadal variability. The sliding correlation of EA with P_S varies widely over time at roughly a 25 year timescale and has declined in the recent decade. The timing of this low-frequency variation does not correspond to that of either the AMO or the PDO. By comparison, the correlations between ENSO and P_S are relatively stable. A similar stabilization effect has been observed between ENSO and the all-India monsoon indices, in which the low-frequency fluctuations common in the sliding correlations between two random climatic time series are suppressed (Gershunov *et al.*

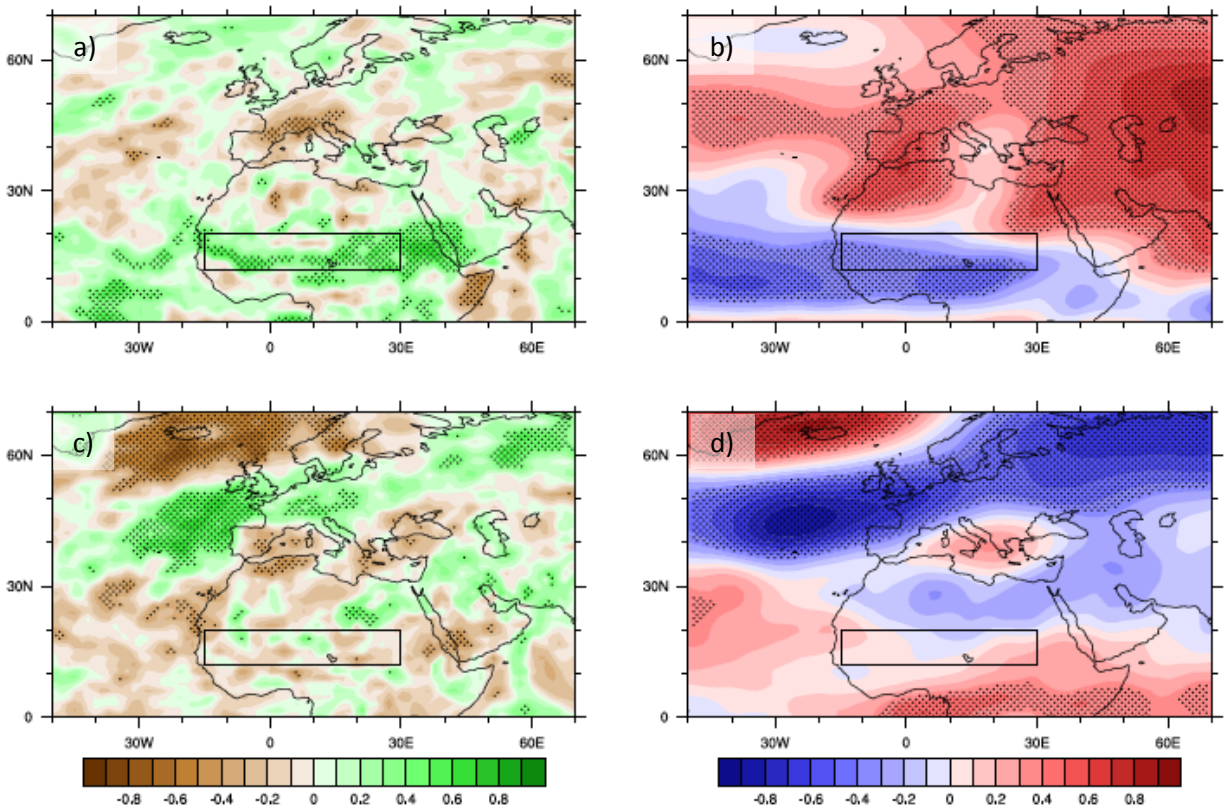

Fig. 5 Spatial correlations of CFSv2 reforecasts (1982-2010) between (a) Nino3.4 index and precipitation, (b) Nino3.4 index and the 600mb geopotential height, (c) EA index and precipitation, and (d) EA index and geopotential height. Stippling shows statistical significance of 95% per r-test. Box shows the Sahel region.

2001). At this point we do not have evidence to rule out the possibility that the fluctuating EA-P_S correlations are stochastic noise, and not a realization of multidecadal modulations.

2.2 Dynamical inference

Having established an empirical connection between EA and P_S, we next explored the dynamic mechanism of this connection by analyzing the horizontal-component Rossby wave-activity flux (*W*, derived per Takaya and Nakamura, 2001) during EA-active years (*i.e.* |EA| > 1). This *W* vector provides a measure of propagation of Rossby wave energy and enstrophy. Calculation of this wave-activity flux is not dependent on spatial or temporal averaging and therefore is suitable for any particular time period (see Takaya and Nakamura, 2001 for details).

As shown in Fig. 3, *i.e*. the wet-dry composite during ENSO neutral years, the wave-activity flux at the upper troposphere (top panel) is mainly zonal in direction and confined to north of 30° N. In the middle troposphere however (middle panel), there is a strong wave-activity flux penetrating into North Africa, moving along the downstream portion of the wave train over the Mediterranean Sea. At lower troposphere (bottom panel), the wave-activity flux crosses the Mediterranean into North Africa but does not extend as far inland as at 600mb. This *W* propagation is consistent with the EA composite (not shown) and is suggestive of the forcing mechanism leading to the middle and lower tropospheric circulation patterns associated with the Sahelian wet/dry anomalies (Fig. 1b).

The rather large wave-activity flux over North Africa at 600mb has an implication for regional circulation anomalies. It appears that the mid-level anticyclone that stations itself over the Sahara Desert can be modulated by teleconnection emanating from higher latitudes. This teleconnection may affect the position and/or intensity of the African easterly jet (AEJ) which, in turn, regulates the activity of African easterly

waves (AEWs) (Chen, 2006). Since AEWs form at both sides of the AEJ core (Chen 2006) it is possible that this injection of Rossby wave-activity energy modulates the middle-level anticyclone and the AEJ, as well as the development of these AEWs, thereby influencing P_S. Further investigation is needed for the dynamic processes of this documented EA-P_S teleconnection.

3. Forecast skill for EA

An important question derived from the aforementioned finding of the EA-P_S connection lies in its depiction in climate prediction, that is, how well do operational climate forecast models capture EA and its impact on P_S? Here we tested hindcast output from CFSv2 to evaluate the model's performance. Following the observational analysis in Fig. 2, we first conducted an EOF analysis on the 600mb geopotential height of CFSv2 at zero-month lead time. The loading patterns and time series for the EOFs were substantially different from those of the NCEP reanalysis data (Fig. 4a-b). Both EOF 1 and 2 (Fig. 4c-d) of CFSv2 exhibit a distinct zonal loading pattern, with considerably smaller magnitude and a north-south – rather than northwest-southeast – orientation as in the reanalysis data. CFSv2 apparently does not reproduce the EA, signified by the very low temporal correlation of -0.16 at 0-month forecast and essentially no correlation at 3-month forecast (r=0.01). Apparently, the EOF approach to define EA as was used in Barnston and Livezey (1987) and the CPC is not suitable for the analysis of CFSv2 outputs, hence justifying the use of the point-based EA index.

In terms of ENSO, the CFSv2 performs well in reproducing the Nino-3.4 index (r=0.97) and reasonably captures P_S (r=0.78) at 0-month forecast. At forecast month 3, CFSv2 still has a robust correlation of 0.81 for Nino-3.4, but the correlation of P_S forecast drops to 0.33. When we consider spatial correlations between modeled ENSO/EA and P_S in CFSv2 at 0-month lead forecast (Fig. 5a/c), P_S responds as expected to modeled ENSO forcing. However, there is essentially no connection between forecast precipitation and forecast EA in the Sahel. Spatial correlation with the 600mb streamfunction (Fig. 5b,d) shows that modeled circulation response to ENSO forcing is a reasonable approximation to that of observational data (Fig 1a), but the EA wave pattern does not reveal the same sign of circulation anomalies over North Africa, hence the insignificant precipitation response in CFSv2 (Fig. 5c).

4. Summary

CFSv2 has been improved in terms of forecasting ENSO, particularly SST evolutions in the Nino 3.4 region (*e.g.*, Wu *et al.* 2009). This is a promising step in forecasting the well-established connection between ENSO and P_S. Correspondingly, modeled P_S responds appropriately to ENSO forcing through the first few forecast months. However, there is a discrepancy in the variability of atmospheric circulations in the North Atlantic and North Africa between CFSv2 and observational data, in that EA is not captured at all even at 0-month forecast. Therefore, an important portion (~20%) of the P_S variance will be missing in CFSv2 forecasts. Since EA is predominately a winter mode (whereas this study only considers the summer season), an examination of model performance in atmospheric variability during the winter season could help to determine if this deficiency of forecasting EA is seasonal in nature, or is intrinsic to CFSv2 regardless of season.

In addition to its known connection with ENSO, P_S is significantly and positively correlated with EA. During the positive phase of EA, transport of Rossby wave activity brings energy from the mid-latitudes into North Africa at the middle troposphere where the core of the AEJ is located. CFSv2 fails to capture this higher-latitude variability mode, but forecasts reasonably the state of ENSO and the associated Sahel precipitation anomalies up to 3 months. In future work we will further explore the dynamical implications for the connection between P_S and this atmospheric/EA mode. We will also seek an explanation for the multidecadal fluctuations of EA's influence on P_S.

References

Adler, R. F., and Co-authors, 2003: The version-2 Global Precipiation Climatology Project (GPCP) monthly precipitation analysis (1979-present). *J. Hydrometeor.*, **4**, 1147-1167. doi: 10.1175/1525-7541(2003)004<1147:TVGPCP>2.0.CO;2.

Bader, J., M. Latif, 2003: The impact of decadal-scale Indian Ocean sea surface temperature anomalies on Sahelian rainfall and the North Atlantic Oscillation. *Geophys. Res. Lett.*, **30**, 2169. doi: 10.1029/2003GL018426.

Barnston, A. G., and R. E. Livezey, 1987: Classification, seasonality and persistence of low-frequency atmospheric circulation patterns. *Mon. Wea. Rev.*, **115**, 1083-1126. DOI: 10.1175/1520-0493(1987)115<1083:CSAPOL>2.0.CO;2.

Brandt, P., G. Caniaux, B. Bourles, A. Lazar, M. Dengler, A. Funk, V. Hormann, H. Giordani, and F. Marin, 2010: Equatorial upper-ocean dynamics and their interaction with the West African monsoon. *Atmos. Sci. Lett.*, **12**, 24-30. DOI: 10.1002/asl.287.

Chen, M. P.-P. Xie, J. E. Janowiak, and P. A. Arkin: 2002: Global land precipitation: a 50-yr monthly analysis based on gauge observations. *J. Hydrometeor.*, **3**, 249-266. doi: 10.1175/1525-7541(2002)003<0249:GLPAYM>2.0.CO;2.

Chen, T-C., 2005: Maintenance of the midtropospheric North African summer circulation: Saharan high and African easterly jet. *J. Climate*, **18**, 2943-2962. doi: 10.1175/JCLI3466.1.

—, 2006: Characteristics of African easterly waves depicted by ECMWF reanalyses for 1991-2000. *Mon. Wea. Rev.*, **134**, 3539-3566. doi: 10.1175/MWR3529.1.

—, and S.-Y. Wang, 2007: Interannual variation of the Sahel rainfall. *Geophys. Res. Abs.*, **9**, 11206. SRef-ID: 1607-7962/gra/EGU2007-A-11206.

Folland, C. K., J. Knight, H. W. Linderholm, D. Fereday, S. Ineson, and J. W. Hurrell, 2009: The summer North Atlantic Oscillation: past, present, and future. *J. Climate*, **22**, 1082-1103. DOI: 10.1175/2008JCLI2459.1.

Gershunov, A., N. Schneider, and T. Barnett, 2001: Low-frequency modulation of the ENSO-Indian monsoon rainfall relationship: signal or noise? *J. Climate*, **14**, 2486-2492. DOI: 10.1175/1520-0442(2001)014<2486:LFMOTE>2.0.CO;2.

Hurrell, J. W., Y. Kushnir, G. Ottersen, and M. Visbeck, 2003: The North Atlantic Oscillation: Climatic significance and environmental impact. *Geophys. Monogr. Series*, **134**, 279 pp. ISBN: 0-87590-994-9.

Joly, M., and A. Voldoire, 2009: Influence of ENSO on the West African monsoon: temporal aspects and atmospheric processes. *J. Climate*, **22**, 3193-3210. doi: 10.1175/2008JCLI2450.1.

Kalnay, E., and Co-authors, 1996: The NCEP/NCAR 40-year reanalysis project. *Bull. Amer. Meteor. Soc.*, **77**, 437-472. doi: 10.1175/1520-0477(1996)077<0437:TNYRP>2.0.CO;2.

Nicholson, S. E., and J. P. Grist, 2001: A conceptual model for understanding rainfall variability in the West African Sahel on interannual and interdecadal timescales. *Int. J. Climatol.*, **21,** 1733–1757.

Saha, S. S., and Co-authors, 2012: The NCEP Climate Forecast System version 2. *J. Climate* (submitted).

Takaya, K., and H. Nakamur, 2001: A formulation of a phase-independent wave-activity flux for stationary and migratory quasigeostrophic eddies on a zonally varying basic flow. *J. Atmos. Sci.*, **58**, 608.627. doi: 10.1175/1520-0469(2001)058<0608:AFOAPI>2.0.CO;2.

Wu, R., B. P. Kirtman, H. van den Dool. 2009. An analysis of ENSO prediction skill in the CFS retrospective forecasts. *J. Climate* , **22**, 1801-1818. doi: 10.1175/2008JCLI2565.1.

Science and Technology Infusion Climate Bulletin
NOAA's National Weather Service
37th NOAA Annual Climate Diagnostics and Prediction Workshop
Fort Collins, CO, 22-25 October 2012

The Signature of the Stratospheric Brewer-Dobson Circulation in Tropospheric Clouds

Ying Li and David W. J. Thompson

Department of Atmospheric Science, Colorado State University, Fort Collins, CO

1. Introduction

The Brewer-Dobson circulation (BDC) has important implications for global climate. It influences temperatures and concentrations of ozone and water vapor throughout much of the global stratosphere (Brewer 1949; Dobson 1956; Holton *et al.* 1995; Mote *et al.* 1996; Shepherd 2007). The purpose of this study is to demonstrate that variability in the BDC also has a significant influence on clouds at tropospheric levels in two key regions of the atmosphere: the tropical tropopause transition layer (TTL) and the Arctic troposphere.

2. Data and analysis method

The analyses exploit five years (June 2006 through April 2011) of remotely sensed cloud incidence data derived from the merged CALIPSO/CloudSat dataset (Stephens *et al.* 2002). The cloud fraction data are obtained from the Level 2B Geometrical Profiling-LIDAR product (2B-GEOPROF-LIDAR; version P2R04), which combines information from the CloudSat Cloud Profiling Radar (CPR) and CALIPSO lidar.

Instantaneous relationships between cloud incidence and temperature are assessed using the CloudSat European Centre for Medium-Range Weather Forecasts Auxiliary product (ECMWF-AUX). The ECMWF-AUX product is interpolated to the same spatial and temporal resolution sampled by the CloudSat radar. Relationships between cloud incidence and the meteorology on annual and interannual timescales are assessed using the European Centre for Medium Range Weather Forecasts (ECMWF) Interim Reanalysis (ERA-Interim; Simmons *et al.* 2007).

The deep, equator-pole branch of the stratospheric BDC is driven primarily by planetary scale wave breaking in the extratropics (Yulaeva *et al*. 1994; Holton *et al*. 1995; Ueyama and Wallace 2010; Zhou *et al*. 2012; Grise and Thompson 2012). The planetary wave entering in the extratropical stratosphere can be measured by the vertical flux of wave activity in the lowermost stratosphere (*e.g*., Waugh *et al*. 1999; Newman *et al.* 2001; Randel *et al*. 2002a; Polvani and Waugh 2004), which is proportional to the zonal-mean meridional eddy flux of heat at 100 hPa: $[v^*T^*]_{100\text{hPa}}$, where the brackets denote the zonal mean and asterisks denote the deviation from zonal mean. As the planetary-scale wave-driven BDC has largest amplitude in the Northern Hemisphere (NH) and during boreal winter (*e.g.*, Yulaeva *et al*. 1994; Rosenlof 1995), we focus on the wave fluxes averaged poleward of 30°N ($[v^*T^*]_{100\text{hPa, }30\text{–}90^\circ\text{N}}$), and regressions on the wave fluxes are centered on the months October–March. The fluxes are calculated from six hourly v and T and then averaged to form monthly means.

As on month-to-month timescales, stratospheric wave driving is correlated with temperatures during both the current and subsequent month, we define our index of the BDC as weighted average of ($[v^*T^*]_{100\text{hPa, }30\text{–}90^\circ\text{N}}$) formed from the previous and current months values. The corresponding weights are determined via an empirical fit of the ($[v^*T^*]_{100\text{hPa, }30\text{–}90^\circ\text{N}}$) time series to lowermost stratospheric temperatures. As noted in Ueyama and Wallace (2010), the weights applied to the previous and current months values of $[v^*T^*]_{100\text{hPa, }30\text{–}90^\circ\text{N}}$ are roughly 2 and 1, respectively. That is, the BDC index value for month i is defined as:

$$\text{BDC}(i) = 2 \times [v^*T^*]_{100\text{hPa, }30\text{–}90^\circ\text{N}}\,(i-1) + 1 \times [v^*T^*]_{100\text{hPa, }30\text{–}90^\circ\text{N}}\,(i),$$

Correspondence to: Ying Li, Department of Atmospheric Science, Colorado State University, Fort Collins, CO; E-mail: yingli@atmos.colostate.edu.

where (i) is the current month, and ($i - 1$) is the previous month. The resulting BDC index time series is then standardized so that it is dimensionless. The standardized BDC index is hereafter referred to as BDC_{NH}.

3. Results

We will first establish the robustness of the linkages between cloud incidence and tropopause temperatures in both these regions. We will then draw on the inferred linkages to motivate and support the analyses between cloud incidence and stratospheric wave driving.

3.1. Cloud incidence as a function of SST and tropopause temperature

The left and middle panels in Figure 1 examine the vertical distribution of cloud incidence over the tropical ocean as a function of sea-surface temperature (SST; Fig. 1a) and over the tropical ocean and land as a function of tropopause temperature (Fig. 1b). The right panel examines the vertical distribution of cloud incidence as a function of tropopause temperatures over the Arctic poleward of 60ºN (Fig. 1c). The key results in Figure 1 are strong linkages between tropopause temperatures and upper tropospheric clouds at both tropical and NH polar latitudes.

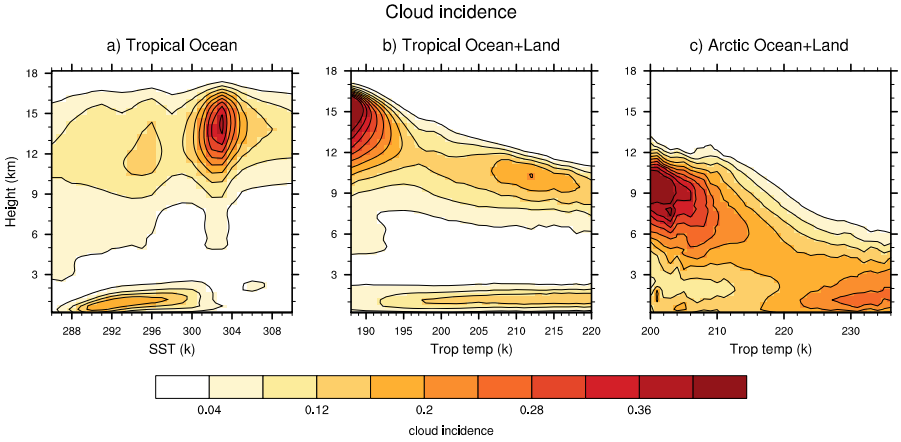

Fig. 1 Cloud incidence (shading) as a function of height and (a) sea-surface temperature (SST) over the tropical ocean, (b) tropopause temperature over the tropical ocean and land, and (c) tropopause temperature over the Arctic poleward of 60°N. Results are based on contemporaneous relationships between cloud incidence from CloudSat/CALIPSO product sea-surface and tropopause temperatures from the ECMWF-AUX product. The seasonal cycle is not removed from the data. All satellite swaths from June 2006 through April 2011 are used. There are a total of more than 2×10^8 individual profile measurements over the tropics, and more than 9×10^7 individual profile measurements over the Arctic. The bin size in all plots is 1 K.

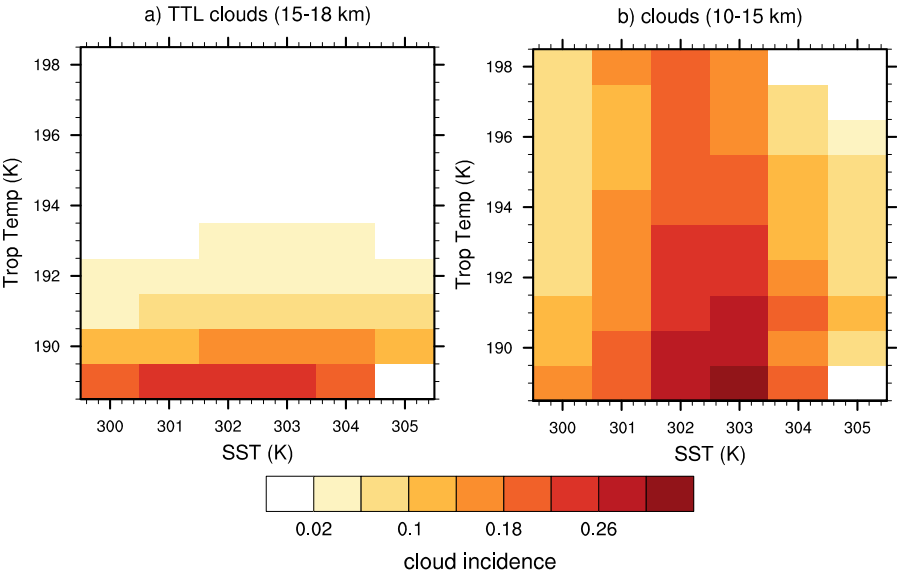

Fig. 2 Cloud incidence (shading) over the tropical ocean shown as a function of SST and tropopause temperature. Results are shown for cloud incidence averaged between (a) 15–18 km and (b) 10–15 km. Results are based on data for all months of the year, and are focused on regions where SSTs are higher than 300 K and tropopause temperatures are lower than 198 K. The seasonal cycle is not removed from the data. The bin size in all plots is 1 K.

The linkages between tropopause temperatures and upper tropical tropospheric clouds (Fig. 1b) are in part due to the coherence between tropopause temperatures and SSTs: regions of anomalous SSTs force large-scale equatorial waves, and such waves influence TTL temperatures and cirrus through adiabatic motions (*e.g.*, Boehm and Lee 2003; Norton 2006; Virts *et al.* 2010). To test the independent relationship between tropical tropopause temperatures and cloud

incidence, we show in Figure 2 the incidences of clouds between 15–18 km (top) and 10–15 km (bottom) as a function of sea-surface (abscissa) and tropopause (ordinate) temperature. The 15 km level corresponds roughly to the base of TTL (*e.g.*, Shepherd 2007; Fueglistaler *et al.* 2009). Cloud incidence between 15–18 km (Fig. 2 top) is clearly a much stronger function of tropopause temperature than of SST, whereas tropical cloud incidence between 10–15 km (Fig. 2 bottom) is a function of both tropopause and sea-surface temperature.

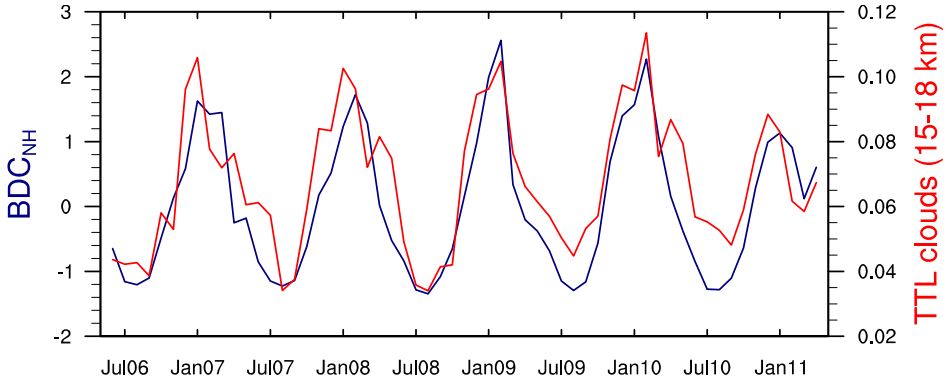

Fig. 3 Monthly-mean cloud incidence averaged 30°S–30°N and between 15–18 km (red; scale at right) and the standardized BDC_{NH} index (blue; scale at left). The BDC_{NH} index is based on the meridional eddy flux of heat and is defined in Section 2.2.

3.2 The signature of Brewer-Dobson circulation in TTL cirrus and Arctic tropospheric clouds

In this section we will build on the relationships between tropopause temperature and cloud incidence established in Figures 1–2 to demonstrate a robust link between the stratospheric Brewer-Dobson circulation and clouds in both the TTL and Arctic troposphere. The BDC index (BDC_{NH}) is based on the vertical flux of wave activity into the NH extratropical stratosphere during winter and is described in Section 2. Figure 3 confirms the coherence between the annual cycles of NH stratospheric wave driving and cloud incidence in the TTL, and support Virts and Wallace (2010)'s conclusion that the large-scale BDC plays a central role in the seasonal cycle of TTL cirrus.

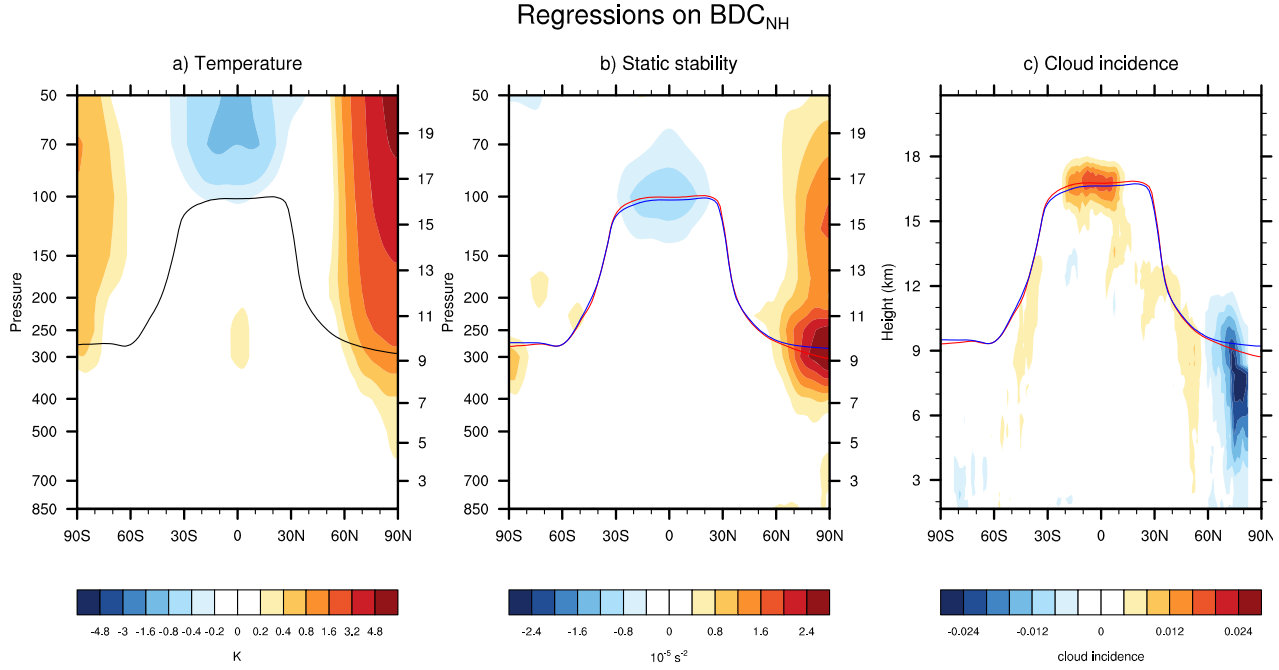

Fig. 4 Regressions of zonal-mean (a) temperature, (b) static stability and (c) cloud incidence onto standardized monthly-mean values of the anomalous BDC_{NH} index. Results are shown as a function of latitude and height and are based on October–March data from June 2006–April 2011. The seasonal cycle has been removed from the data. Units are K (temperature) and $10^{-4}s^{-4}$ (static stability). The solid black line in (a) corresponds to the climatological-mean (October–March) tropopause height. The red and blue lines in (b) and (c) indicate the climatological-mean tropopause height plus and minus the regression of tropopause height onto the standardized BDC_{NH} index, respectively.

Figures 4–5 examine the linkages between the BDC, atmospheric temperatures and tropospheric clouds on month-to-month timescales during the NH winter months October–March. Figure 4a shows monthly-mean, zonal-mean temperature anomalies regressed on standardized wintertime values of the anomalous BDC_{NH} index. The solid black line indicates the climatological-mean (October–March) tropopause height. Periods of enhanced wave driving in the extratropical stratosphere are associated with anomalously low temperatures in the tropical lower stratosphere and anomalously high temperatures in the polar stratosphere.

Figure 4b shows the corresponding changes in atmospheric static stability. Here the red and blue lines indicate the climatological-mean tropopause height plus (red) and minus (blue) the regression of tropopause height onto the wintertime values of the BDC_{NH} index. Periods of enhanced stratospheric wave driving lead to 1) anomalously high tropopause heights and anomalously low static stability at ~100 hPa in the tropics juxtaposed against 2) anomalously low tropopause heights and anomalously high static stability in the upper troposphere/lower stratosphere in the Arctic.

Figure 4c shows the corresponding changes in cloud incidence. Month-to-month variability in stratospheric wave driving is associated with a distinct pattern of near-tropopause cloudiness. Periods of enhanced stratospheric wave driving are marked by anomalously high cloud incidence near the tropical tropopause and anomalously low cloud incidence near the Arctic tropopause. The anomalies in tropical cloud incidence are limited to the tropopause region, whereas the anomalies in Arctic cloud incidence extend to the middle-upper troposphere.

The linkages between the BDC and cloud incidence revealed in Fig. 4c also highly significant. As shown in Figure 5, variability in the BDC accounts for more than 25% of the month-to-month variability in cloudiness in both the TTL and Arctic troposphere. The associated correlation coefficients are significant at the 99% confidence level based on a one-tailed test of the *t*-statistics with an effective sampling size of 24 (using the criterion given in Bretherton *et al.* 1999).

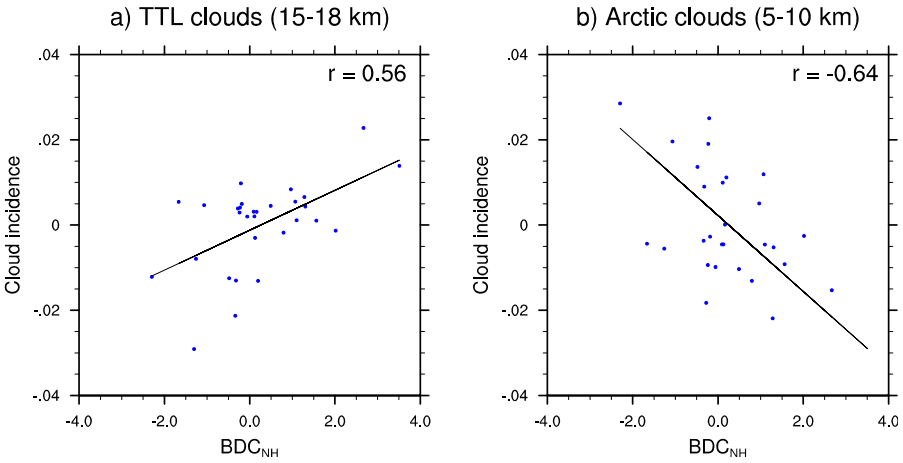

Fig. 5 Scatterplots of monthly mean values of the anomalous BDC_{NH} index (abscissa) and cloud incidence (ordinate). Cloud incidence is averaged (a) equatorward of 30° and between 15–18 km and (b) poleward of 60°N and between 5–10 km. Results are based on October–March data from June 2006–April 2011.

4. Concluding remarks

The planetary-scale stratospheric Brewer-Dobson circulation influences temperatures and static stability in the vicinity of the tropopause in both the tropics and Arctic. Periods of enhanced wave driving in the NH extratropical stratosphere are marked by lifting and cooling of the tropical tropopause juxtaposed against sinking and warming of the Arctic tropopause, and vice versa. Here we exploited ~5 years of data from the CloudSat and CALIPSO instruments to reveal that the influence of the BDC during NH winter extends to clouds in both the TTL and Arctic troposphere. The BDC accounts not only for the seasonal cycle in TTL cirrus [Fig. 3; Virts and Wallace 2010], but also for ~25% of the month-to-month variability in cloud incidence in both the TTL and Arctic troposphere during NH winter (Figs. 4c, 5). The results reveal a novel pathway through which stratospheric processes can influence tropospheric climate.

The linkages between the BDC and clouds in the TTL and Arctic troposphere are physically plausible and statistically robust. Upper tropospheric cloud incidence is linked to variability in tropopause temperatures in both the tropics and over the Arctic (Figs. 1, 2). Tropopause temperatures and static stability in both regions

are, in turn, linked to variability in the BDC (Figs. 4a, 4b). The subsequent linkages between variability in the BDC and clouds in the TTL and Arctic troposphere are significant at the 99% level (Fig. 5).

The linkages between the BDC and clouds in the TTL and Arctic troposphere have potential implications for both climate change and the ability of models to simulate such change. Climate change simulations reveal robust increases in the strength of the BDC in response to future increases in greenhouse gases (*e.g.*, Butchart and Scaife 2001; Butchart *et al.* 2006; Li *et al.* 2008; Garcia and Randel 2008; McLandress and Shepherd 2009; Butchart *et al.* 2010), and at least some observations suggest that such changes have already occurred (Thompson and Solomon 2009; Hu and Fu 2009; Young *et al.* 2012). The changes in cloudiness associated with a strengthening of the BDC may have notable radiative effects on both the TTL and Arctic troposphere. The radiative effects of the linkages documented here and the ability of climate models to simulate such linkages remain to be determined.

References

Boehm, M. T. and S. Lee, 2003: The implications of tropical Rossby waves for tropical tropopause cirrus formation and for the equatorial upwelling of the Brewer-Dobson circulation. *J. Atmos. Sci.*, **60**, 247–261.

Bretherton, C. S., M. Widmann, V. P. Dymnikov, J. M. Wallace, and I. Bladé, 1999: The effective number of spatial degrees of freedom of a time-varying field. *J. Climate*, 12, 1990–2009.

Brewer, A. W., 1949: Evidence for a world circulation provided by the measurements of helium and water vapor distribution in the stratosphere. *Quart. J. Roy. Meteor. Soc.*, **75**, 351–363.

Butchart, N. and A. A. Scaife, 2001: Removal of chlorouorocarbons by increased mass exchange between the stratosphere and troposphere in a changing climate. *Nature*, **410**, 799–802.

Butchart, N., and Co-authors, 2006: Simulations of anthropogenic change in the strength of the Brewer-Dobson circulation. *Climate Dyn.*, **27**, 727–741.

Butchart, N., and Co-authors, 2010: Chemistry-climate model simulations of 21st century stratospheric climate and circulation changes. *J. Climate*, **23**, 5349–5374, doi:10.1175/2010JCLI3404.1.

Dobson, G. M. B., 1956: Origin and distribution of polyatomic molecules in the atmosphere. *Proc. Roy. Soc. London.*, **A236**, 187–193.

Fueglistaler, S., A. E. Dessler, T. J. Dunkerton, I. Folkins, Q. Fu, and P. W. Mote, 2009: Tropical tropopause layer. *Rev. Geophys.*, **47**, RG1004, doi:10.1029/2008RG000267.

Garcia, R. R. and W. J. Randel, 2008: Acceleration of the Brewer-Dobson circulation due to increases in greenhouse gases. *J. Atmos. Sci.*, **65**, 2731–2739.

Grise, K.M. and D.W. J. Thompson, 2012: On the signatures of equatorial and extratropical wave forcing in tropical tropopause layer temperatures. *J. Atmos. Sci.*, in press.

Holton, J. R., P. H. Haynes, M. E. McIntyre, A. R. Douglass, R. B. Rood, and L. Pfister, 1995: Stratosphere-troposphere exchange. *Rev. Geophys.*, **33**, 403–439.

Hu, Y. and Q. Fu, 2009: Stratospheric warming in Southern Hemisphere high latitudes since 1979. *Atmos. Chem. Phys.*, **9**, 4329–4340, doi:10.5194/acp-9-4329-2009.

Li, F., J. Austin, and R. J. Wilson, 2008: The strength of the Brewer-Dobson circulation in a changing climate: Coupled chemistry-climate model simulations. *J. Climate*, **21**, 40–57.

Lin, P., Q. Fu, S. Solomon, and J. M.Wallace, 2009: Temperature trend patterns in Southern Hemisphere high latitudes: Novel indicators of stratospheric change. *J. Climate*, **22**, 6325–6341.

McLandress, C. and T. G. Shepherd, 2009: Simulated anthropogenic changes in the Brewer-Dobson circulation, including its extension to high latitudes. *J. Climate*, **22**, 1516–1540.

Mote, P. W., et al., 1996: An atmospheric tape recorder: The imprint of tropical tropopause temperatures on stratospheric water vapor. *J. Geophys. Res.*, **101**, 3989–4006, doi:10.1029/95JD03422.

Newman, P. A., E. R. Nash, and J. E. Rosenfield, 2001: What controls the temperature of the Arctic stratosphere during the spring? *J. Geophys. Res.*, **106**, 19 999–20 010.

Norton, W. A., 2006: Tropical wave driving of the annual cycle in tropical tropopause temperatures. Part II: Model results. *J. Atmos. Sci.*, **63**, 1420–14 331.

Polvani, L. M. and D. W. Waugh, 2004: Upward wave activity flux as precursor to extreme stratospheric events and subsequent anomalous weather regimes. *J. Climate*, **17**, 3548–3554.

Randel, W. J., F. Wu, and R. Stolarski, 2002: Changes in column ozone correlated with the stratosphere EP flux. *J. Meteor. Soc. Japan*, **80**, 849–862.

Rosenlof, K. H., 1995: Seasonal cycle of the residual mean meridional circulation in the stratosphere. *J. Geophys. Res.*, **100**, 5173–5191.

Shepherd, T. G., 2007: Transport in the middle atmosphere. *J. Meteor. Soc. Japan*, **85B**, 165–191.

Simmons, A., S. Uppala, D. Dee, and S. Kobayashi, 2007: ERA-Interim: New ECMWF re-analysis products from 1989 onwards. *ECMWF Newsletter*, **110**, 25–35, ECMWF, Reading, United Kingdom.

Stephens, G. L. and Coauthors, 2002: The CloudSat mission and the A-train: A new dimension of space-based observations of clouds and precipitation. *Bull. Amer. Meteor. Soc.*, **83**, 1771–1790, doi:10.1175/BAMS-83-12-1771.

Thompson, D. W. J. and S. Solomon, 2009: Understanding recent stratospheric climate change. *J. Climate*, **22**, 1934–1943.

Ueyama, R., and J. M. Wallace, 2010: To what extent does 485 high latitude wave forcing drive tropical upwelling in the Brewer-Dobson circulation? *J. Atmos. Sci.*, **67**, 1232–1246.

Virts, K. S., J. M. Wallace, Q. Fu, and T. P. Ackerman, 2010: Tropical tropopause transition layer cirrus as represented by CALIPSO lidar observation. *J. Atmos. Sci.*, **67**, 3113–3129.

Waugh, D., W. Randel, S. Pawson, P. Newman, and E. Nas, 1999: Persistence of the lower stratospheric polar vortices. *J. Geophys. Res.*, **104**, 27191–27201.

Young, P. J., K. H. Rosenlof, S. Solomon, S. C. Sherwood, Q. Fu, and J.-F. Lamarque, 2012: Changes in stratospheric temperatures and their implications for changes in the BrewerDobson circulation. *J. Climate*, **25**, 1759–1772, doi:10.1175/2011JCLI4048.1.

Yulaeva, E., J. Holton, and J. M. Wallace, 1994: On the cause of the annual cycle in tropical lower-stratospheric temperatures. *J. Atmos. Sci.*, **51**, 169–174.

Zhou, T., M. A. Geller, and W. Lin, 2012: An observational study on the latitudes where wave forcing drives Brewer-Dobson upwelling. *J. Atmos. Sci.*, **69**, 1916–1935.

Science and Technology Infusion Climate Bulletin
NOAA's National Weather Service
37th NOAA Annual Climate Diagnostics and Prediction Workshop
Fort Collins, CO, 22-25 October 2012

The Equal Frequency of Stratospheric Sudden Warmings in El Nino and La Nina

Amy H. Butler[1], C.I. Garfinkel[2], D.W. Waugh[2], M.M. Hurwitz[3], and L.M. Polvani[4]

[1]*Climate Prediction Center, NCEP/NWS/NOAA, College Park, MD*
[2]*Department of Earth and Planetary Science, Johns Hopkins University, Baltimore, MD*
[3]*NASA Goddard Space Flight Center, Greenbelt, MD*
[4]*Lamont-Doherty Earth Observatory, Columbia University, Palisades, MD*

ABSTRACT

The effect of El Niño-Southern Oscillation (ENSO) on the frequency and character of Northern Hemisphere major mid-winter stratospheric sudden warmings (SSWs) is evaluated using a meteorological reanalysis data set and comprehensive chemistry-climate models. There is an apparent inconsistency between the impact of opposite phases of ENSO on the seasonal mean vortex and on SSWs: El Niño leads to an anomalously warm, and La Niña leads to an anomalously cool, seasonal mean polar stratospheric state, but both phases of ENSO lead to an increased SSW frequency. A resolution to this apparent paradox is here proposed: the region in the North Pacific most strongly associated with precursors of SSWs is not strongly influenced by El Niño and La Niña teleconnections. In the observational record, both La Niña and El Niño lead to similar anomalies in the region associated with precursors of SSWs and, consistent with this, there is a similar SSW frequency in La Niña and El Niño winters. A similar correspondence between the penetration of ENSO teleconnections into the SSW precursor region and SSW frequency is found in the comprehensive chemistry-climate models (Fig. 1). The inability of some of the models to capture the observed relationship between La Niña and SSW frequency appears related to whether the modeled ENSO teleconnections result in extreme anomalies in the region most closely associated with SSWs. Finally, it is confirmed that the seasonal mean polar vortex response to ENSO is only weakly related to the relative frequency of SSWs during El Niño and La Niña.

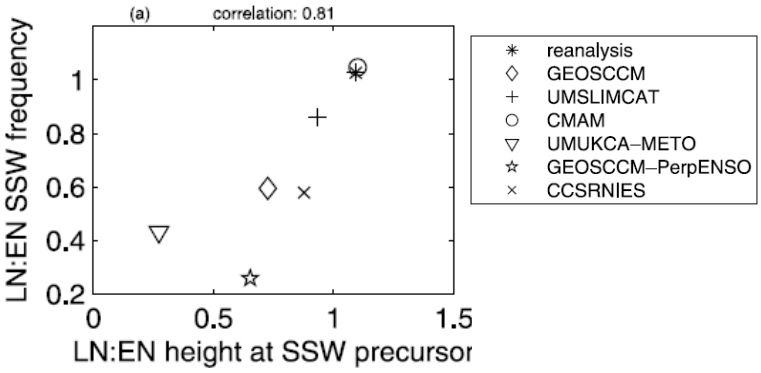

Fig.1 (*c.f.* Figure 5, Garfinkel *et al.* 2012). The relationship between the ratio of La Niña SSW frequency to El Niño SSW frequency (y-axis), and the ratio of La Niña to El Niño extreme negative height anomalies in the SSW precursor region, for reanalysis and models (each marker represents one data source).

This work has been published in *Journal of Geophysical Research* in 2012.

Paper published

Garfinkel, C.I., A.H.Butler, D.W. Waugh, M.M. Hurwitz, and L.M. Polvani, 2012: Why might SSWs occur with similar frequency in El Nino and La Nina winters? *J. Geophys. Res.*, **117**, D19106, doi: 10.1029/2012JD017777.

Correspondence to: [1]Amy H. Butler, Climate Prediction Center, National Center for Weather & Climate Prediction, College Park, MD; E-mail: amy.butler@noaa.gov. [2] Chaim Garfinkel, Department of Earth and Planetary Sciences, Johns Hopkins University, Baltimore, MD; E-Mail: cig4@jhu.edu.

5. DROUGHT AND HYDROCLIMATE

MONITORING AND PREDICTION

Science and Technology Infusion Climate Bulletin
NOAA's National Weather Service
37th NOAA Annual Climate Diagnostics and Prediction Workshop
Fort Collins, CO, 22-25 October 2012

Objective Blends of Multiple Ensemble-Mean NLDAS Drought Indices

Youlong Xia[1,2], Michael Ek[1], Christa Peters-Lidard[3], David Mocko[3],
Justin Sheffield[4], and Eric F. Wood[4]

[1]*Environmental Modeling Center (EMC), NCEP/NOAA/NWS, College Park, MD*
[2]*IMSG at NOAA/NCEP/EMC, College Park, MD*
[3]*Hydrological Sciences Laboratory, NASA/GSFC, Greenbelt, MD*
[4]*Department of Environmental and Civil Engineering, Princeton University, Princeton, NJ*

1. Introduction

The multi-institution North American Land Data Assimilation project (NLDAS) has experienced four stages since it was initiated in 2000 (Mitchell *et al.* 2004). The first stage established infrastructure including selection of land surface models, generation of surface forcing data, and collection of soil and vegetation datasets, and in-situ and satellite-retrieved observations. Four model groups ran their models separately for a 3-year period (from 1 October 1997 to 30 September 1999). NCEP Environmental Modeling Center's land-hydrology group ran the community Noah model, Princeton University's land group ran the VIC model, NASA Goddard Space Flight Center's hydrology group ran the Mosaic model, and National Weather Service's Office of Hydrologic Development ran the SAC hydrological model. The model outputs were evaluated and compared with in-situ observations and satellite-retrieved products. Overall results showed that all four models are able to capture broad features for these validated variables such as energy fluxes (*e.g.*, net radiation, sensible heat, latent heat, and ground heat), water fluxes (*i.e.*, evapotranspiration, total runoff) and state variables (*i.e.*, soil temperature, soil moisture, land surface temperature, snow cover fraction, snow water equivalent). The validation tools and overall results are detailed in Mitchell *et al.* (2004).

The second stage focused on improving model physics, tuning model parameters and improving surface forcing data quality and reliability based on the findings from the first stage, and further expanding the short-term (*i.e.*, 3 years) model products to long-term (> 30 years) model products. The NCEP NLDAS team improved Noah simulation in cold season (Livneh et al. 2010) and warm season (Wei *et al.* 2012) through collaboration with University of Washington. The Princeton Land group improved the VIC simulation by calibrating model parameters (Troy *et al.* 2008), and the NCEP NLDAS team also improved SAC simulation by using climatologically averaged observed potential evaporation (Xia *et al*. 2012a), while Mosaic was improved little. For surface forcing data, the CPC gauge precipitation has been bias-corrected by PRISM (Parameter-elevation Regressions on Independent Slopes Model, Daly *et al.* 1994) precipitation to reduce the impact of topography on gauge precipitation. Four models were retrospectively run from 1 January 1979 to 31 December 2008. After then, they are run in a near-realtime mode (with a 3 and half day lag).

The third stage moved toward evaluating and validating the quality and reliability of long-term NLDAS products using as many as available in-situ observations and satellite-retrieved products (short-term *vs.* long-term, different time scales from hourly to annual, different spatial scales from site and basin to continental United States). These observations include energy fluxes (*e.g.*, downward shortwave and longwave radiation, upward shortwave and longwave radiation, net radiation, sensible heat flux, latent heat flux, ground heat flux, *etc.*), water fluxes (*e.g.*, evapotranspiration, streamflow), and state variables (*e.g.*, soil moisture, soil temperature, land surface/skin temperature, snow water equivalent, snow cover fraction). Evaluation/validation works have made significant progress during the recent two years. An overall evaluation and comparison was detailed in Xia *et al.* (2012a, 2012b). Overall results show that the NLDAS products generated from the stage 2 have better quality when compared to those generated from stage 1, due

Correspondence to: Youlong Xia, Environmental Modeling Center, NCEP/NOAA, College Park, Maryland;
E-mail: youlong.xia@noaa.gov.

to both model and surface forcing data improvement. The simulated total runoff was evaluated against the observed streamflow at 986 small-medium size basins and 8 large size basins which were measured by the U.S. Geological Survey (USGS). In west coast and eastern U.S., all four models are able to capture the broad features of observed streamflow. Four- model ensemble mean outperforms any individual model in term of errors. The similar conclusion can be found for the validation of simulated evapotranspiration. The simulated soil moisture was evaluated using three observational datasets (Xia *et al.* 2012c): 20-year (1985-2004) monthly mean soil moisture from Illinois (17 sites), 6-year (1997-2003) daily mean soil moisture from Oklahoma Mesonet (72 sites), and 8-year (2002-2009) daily soil moisture from Soil Climate Analysis Network (SCAN, 121 sites) over the continental United States. The results show that simulation skills of all four models are quite good in term of anomaly correlation for both daily and monthly time scales although simulated soil moisture magnitude shows large errors, where some models may overestimate and other models may underestimate observed soil moisture. Like streamflow and evapotranspiration evaluations, the four-model ensemble mean shows the most robust simulation skills over continental United States when compared to any individual model.

The focus of fourth stage is to apply long-term NLDAS products to support the National Integrated Drought information System (NIDIS, drought.gov) and U.S. operational drought monitoring and prediction. One key application of the near real-time NLDAS is its drought monitoring over continental United States, shown at the "NLDAS Monitor" tab of the NLDAS website (Sheffield *et al.* 2012; NCEP/EMC NLDAS website: http://www.emc.ncep.noaa.gov/mmb/nldas/; NASA NLDAS website: http://ldas.gsfc.nasa.gov/nldas/NLDASnews.php). At the same time, the NLDAS team also uses a cron job to routinely provide four-model ensemble mean daily, weekly, and monthly percentiles of top 1m soil moisture, total column soil moisture, total runoff and evapotranspiration to the U.S. drought monitor author group to directly support the USDM. This team also provides NLDAS drought indices to support CPC monthly drought briefing and seasonal drought outlook. However, these NLDAS drought indices are not comprehensively assessed as there are few reference drought datasets. The USDM (http://droughtmonitor.unl.edu/), an operational product (Svoboda *et al.* 2002), has generated many statistics (*i.e.*, drought area percentages for the forty-eight states). How to use these statistics to improve U.S. operational drought monitoring is still a challenging issue. This study will develop an objectively blended approach by establishing the linkage between NLDAS products and USDM statistics. The approach will use an optimization method to search for optimally blended weights and equations by minimizing the root mean square error (RMSE) between drought area percentage derived from an NLDAS and from USDM. In turn, the USDM drought area percentage will be used to evaluate simulation skills of optimally blended NLDAS drought index.

2. Methodology

Weekly drought area percentages were downloaded from the USDM archives website (http://droughtmonitor.unl.edu/dmtabs_archive.htm) for five categories and 48 states. This dataset covers a 12-year period from 2000 to 2011. Five drought categories are from abnormally dry to exceptional (D0-D4), moderate drought to exceptional (D1-D4), severe drought to exceptional (D2-D4), extreme drought to exceptional (D3-D4), and exceptional (D4-D4). Monthly mean drought percentages were calculated using the number of days as weights to average weekly values. For NLDAS, percentiles of monthly mean top 1m soil moisture (SM1), total column soil moisture (SMT), evapotranspiration (ET), and total runoff (Q) derived from four-model ensemble were used as four NLDAS drought indices. A linear combination of the four indices was used as the blend in this study. We calculated monthly drought area percentage from the blend for forty-eight states using land mask, state mask, and the USDM drought categories. 10-year monthly drought area percentages were used to construct our error function (the last 2 years were used for validation as the USDM authors have referenced NLDAS products since 1 January 2010). The root mean square error E can be defined as:

$$E = \frac{1}{MT}\sum_{t=1}^{MT}\sqrt{\frac{1}{C}\sum_{c=1}^{C}(A_{t,c} - O_{t,c})^2} \qquad (1)$$

where MT is total number of months (120 in this study), C is the number of drought categories (5 in this study), $A_{t,c}$ and $O_{t,c}$ are the drought percentage area from the blended NLDAS drought index and the USDM, respectively. The ranges of all four weights are selected to be from 0 to 1. By an optimization process, Very Fast Simulated Annealing (VFSA, Xia 2007) automatically searches for optimal weights to minimize the error function E. The optimization process was performed for each state separately (Xia *et al.* 2013, "Application of USDM Statistics in NLDAS-2: Objective Optimal Blended NLDAS drought Index over the Continental United States", in preparation for Journal of Geophysical Research).

The basic evaluation method for this study includes bias, root mean square error (RMSE), correlation coefficients, and Nash-Sutcliffe efficiency (Nash and Sutcliffe 1970). The Nash-Sutcliffe efficiency is defined as:

$$NSE = 1 - \frac{\sum_{t=1}^{MT}(A_t - O_t)^2}{\sum_{t=1}^{MT}(O_t - \overline{O})^2} \qquad (2)$$

In equation (2) A_t and O_t are, respectively, drought area percentage derived from NLDAS and USDM, and $\overline{A}$ and $\overline{O}$ are their mean values for any given time period. The NSE is a measure of the drought area percentage simulation skill of the method as compared to the mean USDM drought area percentage, and ranges in value from minus infinity (poor model skill) to one (perfect model skill). An efficiency of 0 ($NSE = 0$) indicates that the model simulations are as accurate as the mean of the USDM data, whereas an efficiency less than zero ($NSE < 0$) occurs when the USDM mean is a better predictor than the model.

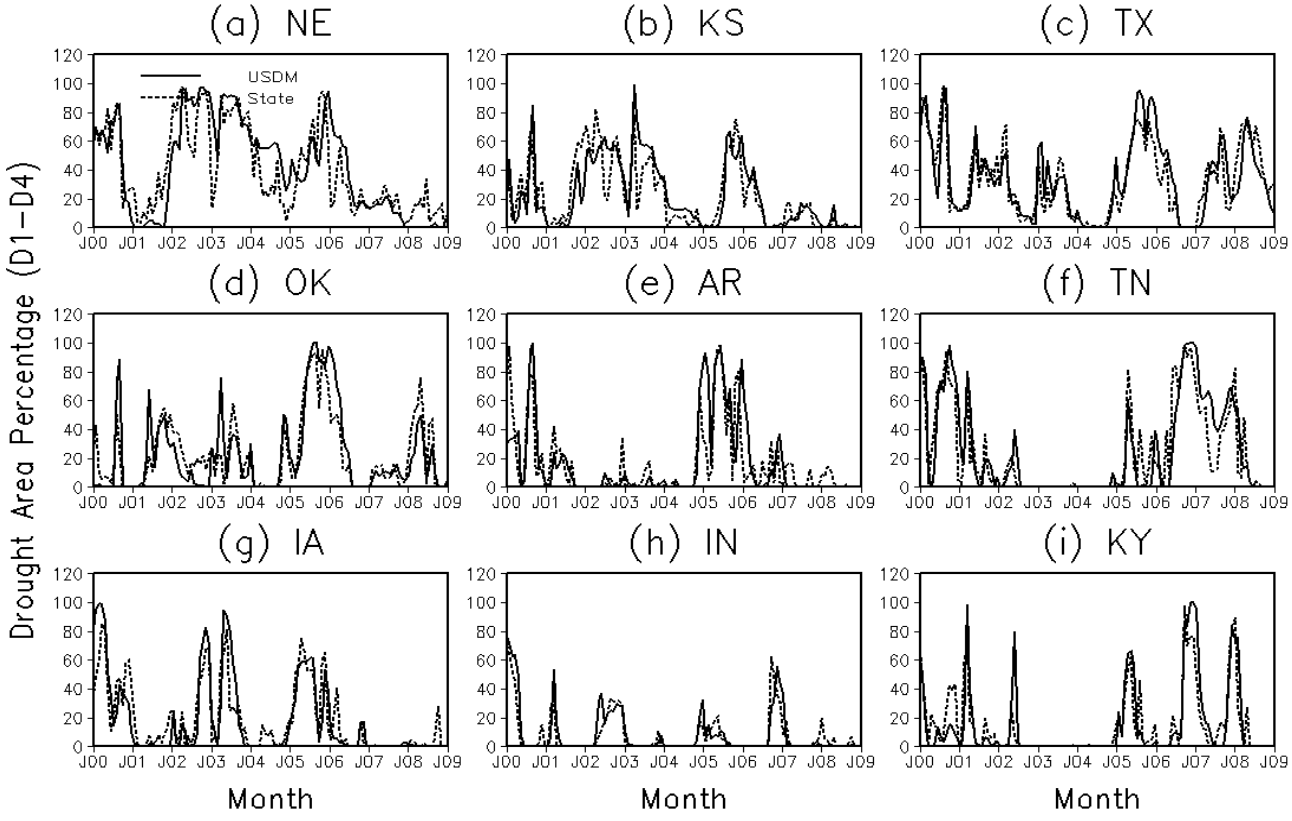

Fig 1 Comparison of drought area percentage for D1-D4 derived from USDM and objective NLDAS blend (represented State in Fig.1) in (a) Nebraska (NE), (b) Kansas (KS), (c) Texas (TX), (d) Oklahoma (OK), (e) Arkansas (AR), (f) Tennessee (TN), (g) Iowa (IA), (h) Indiana (IN), and (i) Kentucky (KY) for January 2000 to December 2009.

3. Results

Figure 1 and Figure 2 show the comparison between USDM and NLDAS drought area percentage (D1-D4) for nine states and different periods: the training period (2000-2009) and the validation period (2010-2011), respectively. These states have the highest correlation for both training and validation period. The

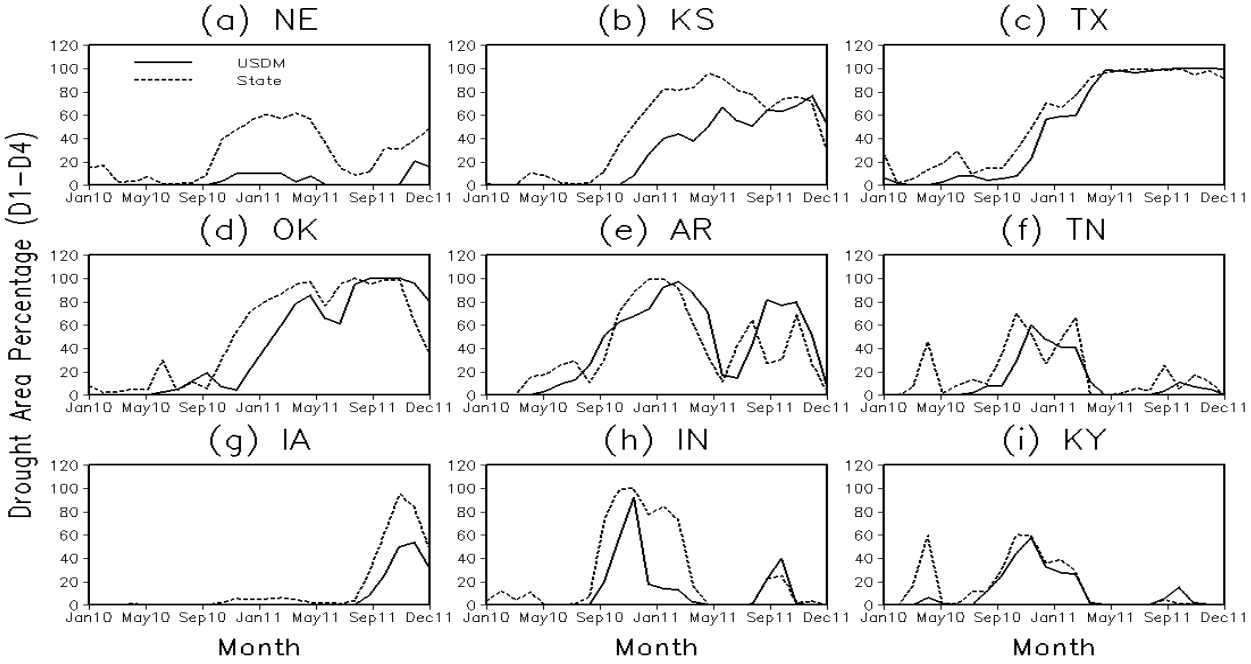

Fig. 2 The same as Figure 1 except for the validation period from January 2010 to December 2011.

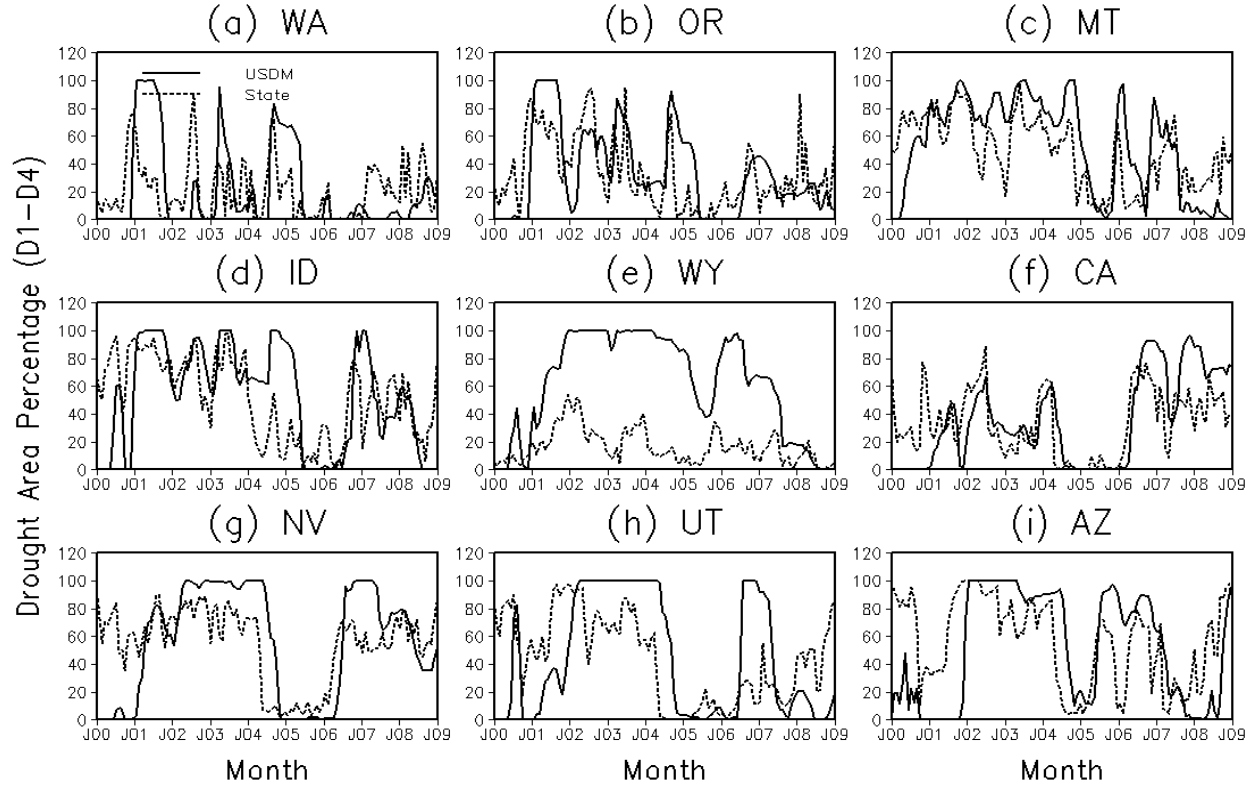

Fig. 3 The same as Figure 1 except for (a) Washington (WA), (b) Oregon (OR), (c) Montana (MT), (d) Idaho (ID), (e) Wyoming (WY), (f) California, (g) Nevada (NV), (h) Utah (UT), and (i) Arizona (AZ).

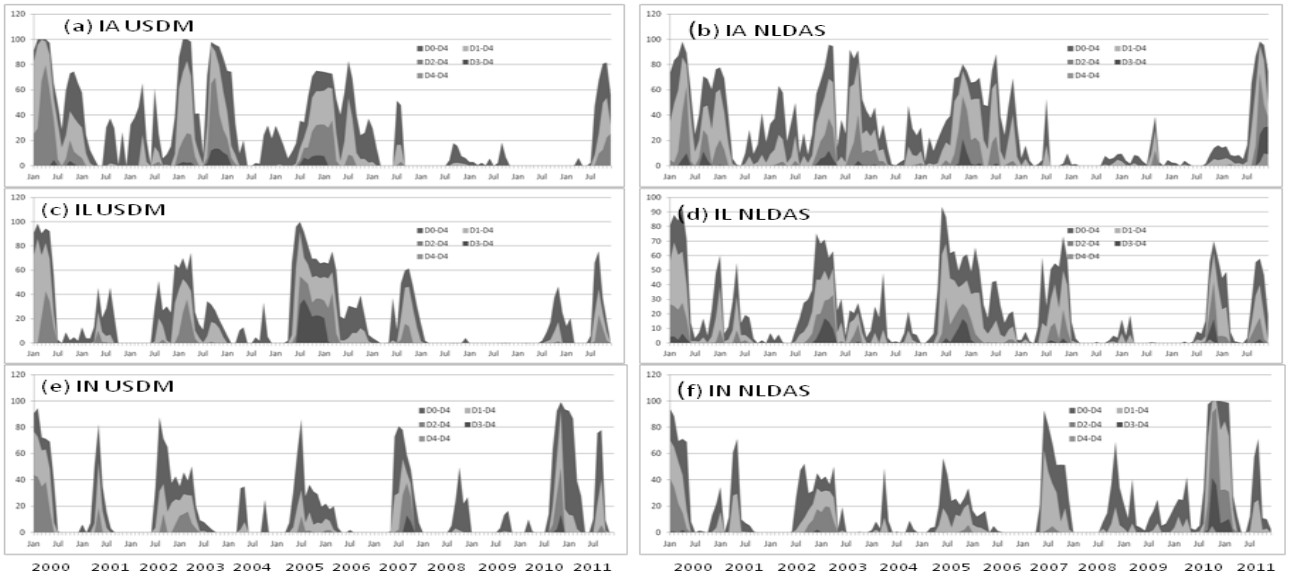

Fig. 4 Comparison of drought area percentages for five drought categories (D0-D4, D1-D4, D2-D4, D3-D4, D4-D4) derived from USDM (left panel) and objective NLDAS blend (right panel). The data covers the period from January 2000 to December 2011. From top panel to bottom panel represent Iowa (IA), Illinois (IL), and Indiana (IN).

results show that the objective NLDAS blend can capture variability and magnitude of monthly drought events very well for both the training period and validation period although the blend overestimates USDM drought area percentage for almost all nine states during the validation period. The performance of the objective blend varies from state to state. Basically, most states in Southern and Southeastern U.S. have quite good performance, and the states in Northeastern, Midwestern, and Western U.S. have low simulation skills. An example for nine states over western U.S. is shown in Figure 3. The objective NLDAS blend shows quite low simulation skill over western U.S. regions for both monthly magnitude and variability, in particular for Washington and Wyoming. The possible reason may be (1) inaccurate precipitation data and (2) low simulation skills for soil moisture, ET and Q (Xia *et al.* 2012a, 2012b). As indicated by Mo *et al.* (2012), the number of precipitation gauges has significantly decreased since 2002. Therefore, precipitation estimates may be not representative for that region. Moreover, because of complex topography, snow processes, and frozen soil processes, combined with inaccurate precipitation over the western mountainous region, further results in poor simulation of soil moisture, ET and Q in that region. Figure 4 shows monthly variation of drought area percentage for 5 drought categories in three states derived from USDM (left panel) and objective NLDAS blend (right panel). The results show that the NLDAS blend quite well captures the monthly magnitude and variability of the USDM drought area percentage for these three states, in particular for the first two drought categories. The inability of the objective NLDAS blend to capture USDM drought area percentages for severe drought or above categories is due to their small sample sizes. Therefore, a long-term USDM product (*i.e.*, 30 years) can be expected to improve severe drought simulation. The spatial distribution of Nash-Sutcliffe efficiency for three drought categories (*i.e.*, D0-D4, D1-D4, and D2-D4) was shown in Fig. 5 for the training period (left panel) and the validation period (right panel). The results show that objective NLDAS blend has quite good simulation skills in southern and southeastern states, and poor simulation skills in western, mid-northern, and northeastern states, in particular for the validation period and the severe drought case. The simulation skills of objective NLDAS blends are reduced from the training period to the validation period for most states. The reduction of the simulation skills also occurs when drought categories vary from D0-D4 to D3-D4. The reason for both reductions may be due to the short record-length of USDM data.

4. Summary and future direction

Currently NLDAS is a quasi-operational system to support U.S. operational drought monitoring and seasonal hydraulic prediction, in particular for the National Integrated Information System including U.S.

Drought Monitor (USDM) and Monthly Drought Briefing. Detailed information about NLDAS can be found at NOAA (http://www.emc.ncep.noaa.gov/mmb/nldas) and NASA (http://ldas.gsfc.nasa.gov/nldas/) websites. The system consists of a retrospective 29-year (1979-2008) historical execution and a near real-time daily update execution using four land surface models (NCEP/Noah, NASA/Mosaic, NWS/OHD/SAC, and VIC developed by Princeton University and University of Washington) on a common 1/8th degree grid using common hourly land surface forcing. The non-precipitation surface forcing is derived from the NCEP retrospective North American Regional Reanalysis (NARR), and now realtime NCEP operational Regional Climate Data Assimilation System (RCDAS). The precipitation forcing is anchored to daily gauge-only precipitation over Continental United Sates (CONUS) that applies Parameter-elevation Regressions on Independent Slopes Model (PRISM) corrections. This daily precipitation analysis is then temporally disaggregated to hourly precipitation amounts using radar products. The NARR-based surface downward solar radiation is bias-corrected using seven years (1997-2004) of satellite-derived solar radiation retrievals.

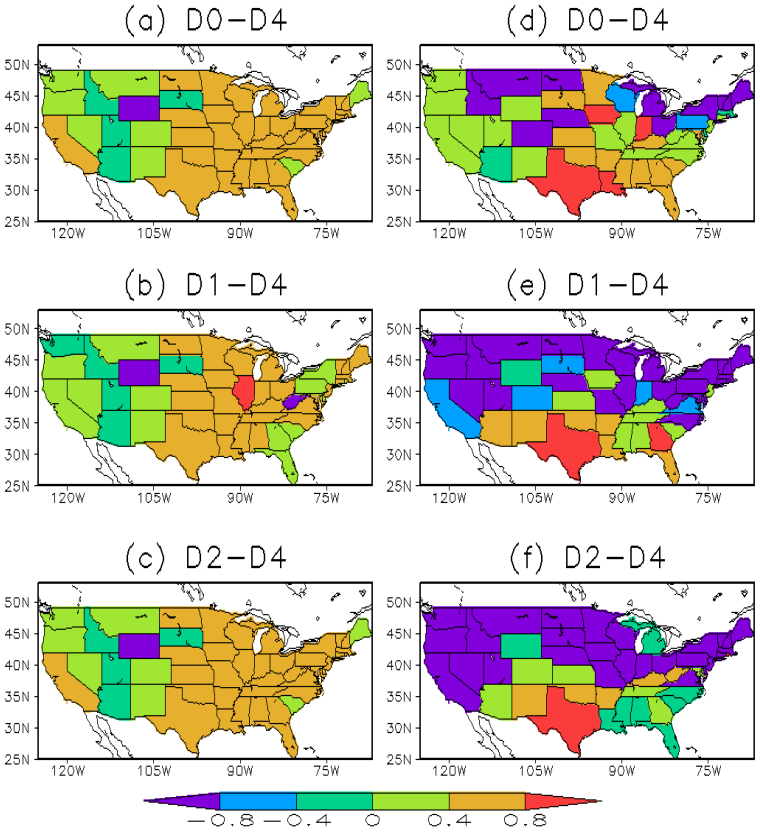

Fig. 5 Spatial distribution of Nash-Sutcliffe efficiency (NSE) for three drought categories (*i.e.*, D0-D4, D1-D4, and D2-D4) and different periods: the training period (left panel) and the validation period (right panel). Negative NSE indicates poor simulation for USDM drought area percentages.

The 29-year NLDAS retrospective run is used to derive the climatology of each of the four land models. Then current near real-time (past week, past month) land states (*e.g.* soil moisture, snowpack), and water fluxes (*e.g.* evaporation, total runoff, streamflow) of each of the four models from daily executions are depicted as anomalies and percentiles with respect to their own model climatology. The simulated streamflow, soil moisture, snowpack, and evapotranspiration from the four models are well evaluated and validated using in-situ observations from the U.S. Geological Survey, Illinois, Oklahoma, and CONUS soil moisture, and evapotranspiration from U.S. surface flux measurement sites. This evaluation provides a basis to apply NLDAS products. One key application of the near real-time updates is drought monitoring over CONUS, shown at the "NLDAS Drought" tab of the NLDAS website. NLDAS ensemble mean drought indices are directly provided to the U.S. Drought Monitor author group through a daily cron job.

NLDAS has become mature enough and will be implemented in NCEP operations in the near future. At the same time, we recognize that the current NLDAS is not an "actual" land data assimilation system because remotely-sensed estimates of land-surface states such as soil moisture and snowpack, and in-situ observations such as streamflow and soil moisture, are not yet assimilated into current version of NLDAS. The NCEP/EMC NLDAS team is collaborating with the NASA Goddard Hydrological Sciences Laboratory to add their Land Information System (LIS; Kumar *et al.* 2006) to the current NLDAS system which would allow assimilation of remotely-sensed data and in-situ observations, *e.g.* via an ensemble Kalman filter approach.

The comparison analysis of drought area percentages shows that the objective NLDAS blend is able to capture broad features of drought area percentage such as magnitude and monthly variability for the first two categories in many states which are mainly located in the South, Southeast, High Plains and Midwest regions. However, there is still significant room for improvement for enhancing simulation skills, in particular for most states of the Western and Northeast regions, and for the strongest drought events (D3-D4, D4-D4). Impact of accurate gauge precipitation on simulation skills in the Western region will need to be addressed in the future work by rerunning the four NLDAS models using a retrospective gauge precipitation dataset. In addition, after more independent inputs such as observed streamflow (*e.g.*, percentile) from USGS, remote sensing drought indices (*e.g.*, Evaporative Stress Index, Ground Water Storage), and Climate Prediction Center (CPC) operational drought indices (*e.g.*, standard precipitation index, Palmer Drought Index, Palmer Hydrological Drought Index, Objectively Blended Drought Indicators) will be used to blend with the four NLDAS drought indices used in this study, further improvement can be expected. It should be noted that the objective NLDAS blend is easily reproducible, which is quite different from the USDM, which is based on a combination of objective and subjective analysis, making it not easily reproducible. Therefore, this approach can be used to reconstruct long-term drought area percentages and drought indices.

Acknowledgment. The NLDAS project is sponsored by the Modeling, Analysis, Predictions, and Projections (MAPP) of Climate Program Office (CPO).

References

Daly, C., R. P. Neilson, and D. P. Phillips, 1994: A statistical-topographic model for mapping climatological precipitation over mountainous terrain. *J. Appl. Meteorol.*, **33**, 140-158.

Kumar, S.V., C.D. Peters-Lidard, Y. Tian, P.R. Houser, J. Geiger, S. Olden, L. Lighty, J.L. Eastman, B. Doty, P. Dirmeyer, J. Adams, K. Mitchell, E. F. Wood and J. Sheffield, 2006: Land Information System - An interoperable framework for high resolution land surface modeling. *Environmental Modelling & Software*, **21**, 1402-1415. doi:10.1016/j.envsoft.2005.07.004.

Livneh, B., Y. Xia, K. E. Mitchell, M. B. Ek, and D. P. Lettenmaier, 2010: Noah LSM snow model diagnostics and enhancements. *J. Hydrometeor*, **11**, 721–738

Mitchell, K. E., and Co-authors, 2004: The multi-institution North American Land Data Assimilation System (NLDAS): Utilizing multiple GCIP products and partners in a continental distributed hydrological modeling system. *J. Geophys. Res.*, **109**, D07S90, doi:10.1029/2003JD003823.

Mo, K. C., L.-C. Chen, S. Shukla, T. J. Bohn, and D. P. Lettenmaier, 2012: Uncertainties in North American Land Data Assimilation Systems over the contiguous United States. *J. Hydrometeor*, **13**, 996–1009.

Nash, J. E. and J. V. Sutcliffe, 1970: River flow for forecasting though conceptual models part 1-A discussion of principle. *J. Hydrology*., **10,** 282-290.

Sheffield, J., Y. Xia, L. Luo, E. F. Wood, M. Ek, K. E. Mitchell, and the NLDAS Team, 2012: Drought monitoring with the North American Land Data Assimilation System (NLDAS): A framework for merging model and satellite data for improved drought monitoring. *Remote Sensing of Drought: Innovative Monitoring Approaches*, B. Wardlow, M. Anderson and J. Verdin (eds.), p. 270, Taylor and Francis, London, United Kingdom.

Svoboda, M., and Co-authors, 2002: The drought monitor. *Bull. Amer. Meteor. Soc.*, **83**, 1181-1190.

Troy, T. J., E. F. Wood, and J. Sheffield, 2008: An efficient calibration method for continental-scale land surface modeling. *Water Resour. Res.*, **44**, W09411, http://dx.doi.org/10.1029/2007WR006513

Wei, H., Y. Xia, K. E. Mitchell, and M.B. Ek, 2012: Improvement of the Noah land surface model for warm season processes: evaluation of water and energy flux simulation. *Hydrological Processes*, doi: 10.1002/hyp.9214.

Xia, Y., 2007: Calibration of LaD model in the northeast of the United States using observed annual streamflow. *J. Hydrometeor.*, **8**, 1098-1110.

Xia, Y., and Co-authors, 2012a: Continental-scale water and energy flux analysis and validation for the North American Land Data Assimilation System project phase 2 (NLDAS-2): 1. Intercomparison and application of model products. *J. Geophys. Res.*, **117**, D03109, doi:10.1029/2011JD016048.

Xia, Y., and Co-authors, 2012b: Continental-scale water and energy flux analysis and validation for North American Land Data Assimilation System project phase 2 (NLDAS-2): 2. Validation of model-simulated streamflow, *J. Geophys. Res.*, **117**, D03110, doi:10.1029/2011JD016051.

Xia, Y., and Co-authors, 2012c: Evaluation of multi-model simulated soil moisture in NLDAS-2, *J. Hydrology* (submitted).

Science and Technology Infusion Climate Bulletin
NOAA's National Weather Service
37th NOAA Annual Climate Diagnostics and Prediction Workshop
Fort Collins, CO, 22-25 October 2012

Monitoring and Maintenance of a Cold-Season Drought

Er Lu

Nanjing University of Information Science & Technology, Nanjing, China,
and Climate Prediction Center, NCEP/NWS/NOAA, Maryland, U.S.

1. Introduction

A once-in-a-century severe drought swept across Southwest China during fall 2009 and the subsequent winter. It made over 16 million people and 11 million livestock short of drinking water, and devastated crops in more than 4 million hectares of farmland with making a fourth of them yield no harvest. The goal of this study is to monitor the drought at a daily scale and examine the regional atmospheric anomalies that fostered the severe drought.

2. Monitoring the drought at a daily scale

The weighted average of precipitation (WAP) developed by Lu (2009) is used to monitor the drought. The suggested form of the index for the general monitoring of drought at a daily scale is

$$WAP = 0.1\sum_{n=0}^{44} 0.9^n P_n$$

which combines the precipitation (P) of the recent 45 days (n = 0, 1 , …, 44) with weights that decay with time. Although the period-averaged negative anomaly of precipitation (figure not shown) can also indicate the drought, WAP can provide more details of the drought process. Figure 1 shows that the drought in Yunnan and Guizhou, two provinces of the Southwest, is severer-than-normal almost every day during the long period of the drought.

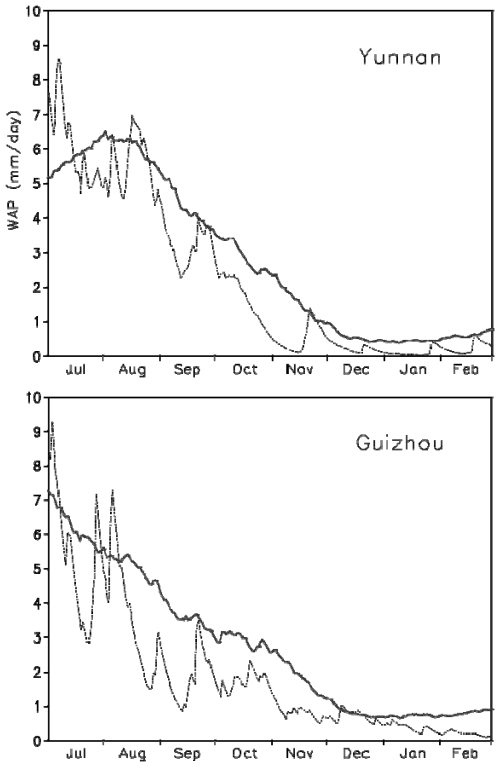

Fig. 1 Daily WAP of the 2009-2010 cold-season drought (thin) and the climatic mean (thick) for Yunnan (upper) and Guizhou (lower) Provinces.

3. Regional atmospheric anomalies of the cold-season drought

a. Contributions from less water vapor and warmer air temperature

Atmospheric circulation is important to precipitation; its ultimate effect is to increase the water vapor in the local air and lower the air temperature, through transporting water vapor and invading cold air, and thus make the air become saturated.

Lu and Takle (2010) concluded, from large spatial samples, a tight positive relation between precipitation and relative humidity at interannual timescale. This relation is broader than the conventionally recognized water vapor-precipitation link.

The relative humidity of the 2009-2010 cold-season drought has negative anomaly in the Southwest (Fig. 2), which reflects not only the role of the less-than-normal water vapor in the region but the effect of the warmer-than-normal temperature as well. Their contributions to the drought can be compared with the precipitation-relative humidity relation.

Correspondence to: Er Lu, Nanjing University of Information Science & Technology, Nanjing, China;
E-mail: elu@nuist.edu.cn.

Denote the lower-than-normal relative humidity of the drought ($P_{dry} < P_{nor}$) as $r_{dry} < r_{nor}$, or $D_r \equiv r_{dry}/r_{nor} < 1$. With expressing relative humidity r in terms of specific humidity q and saturation vapor pressure e_s at temperature T, it can further be written as

$$D_r = D_q D_T < 1,$$

where

$$D_q \equiv q_{dry} / q_{nor}$$

and

$$D_T \equiv e_s (T_{nor}) / e_s (T_{dry})$$

measure the contributions of the less water vapor and warmer air temperature to the decrease of relative humidity.

Figure 3 shows that, over the Southwest, D_q ranges from 1 to 0.6, whereas D_T from 1 to 0.8, and their minima both appear in the severest drought area. This suggests that at the interannual timescale (*i.e.*, comparing this drought year with the normal year), while less water vapor contributes more, warmer air temperature also contributes significantly to the formation of the severe drought.

b. Changes in atmospheric circulation and water vapor transport

Figure 4 shows that the water vapor transport field of the 2009-1010 cold-season drought is pretty similar in spatial pattern to the climatic mean, and the major difference is in the strength; the vapor transport of this drought is weaker than normal across the Southwest.

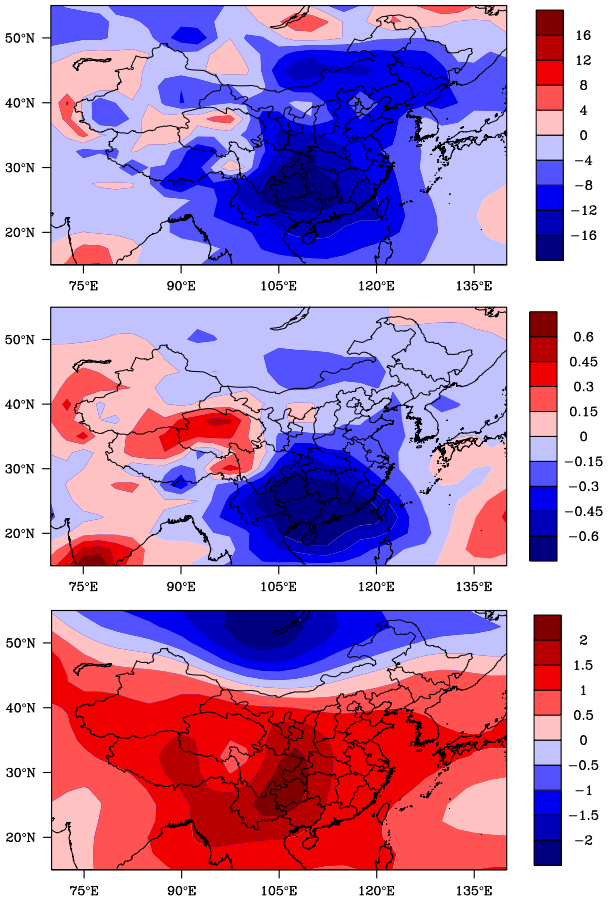

Fig. 2 Anomalies of relative humidity (%, top), specific humidity (g kg^{-1}, middle), and temperature (K, bottom) at 600hPa of the 2009-2010 cold-season drought, relative to the climatic mean.

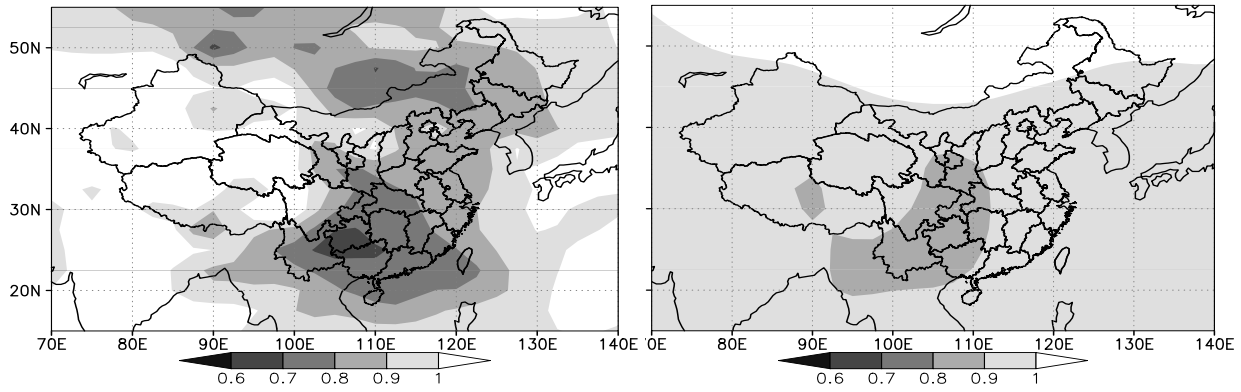

Fig. 3 D_q (left) and D_T (right) at 600hPa calculated with data of the 2009-2010 cold-season drought and the climatic mean.

This is different from the 1999 summer drought over North China (Ding et al. 2003), during which vapor transport has a significant anomaly in the track, and the strength is not weak from the source of vapor and along the track. The southwest monsoon transports water vapor along the low latitudes all the way to the east, and water vapor cannot reach North China. Since summer is the rainy season of the region, the normal

transport of water vapor can lead to much precipitation, which sometimes can even form floods. If the vapor transport in a particular year is along the normal track but just weaker in strength, it can still bring precipitation. This precipitation might be less than normal, but would be far from forming a severe drought. To form severe drought in the summer of the region, the transport of water vapor needs to have a significant change in track.

By contrast, the Southwest severe drought analyzed in this study maintains mainly in cold season. It is normally very hard to form persistent strong precipitation at this time of the year. To form severe drought in cold season, a weakening in the strength of vapor transport can be sufficient, and there is no need to have a major change in the transport track.

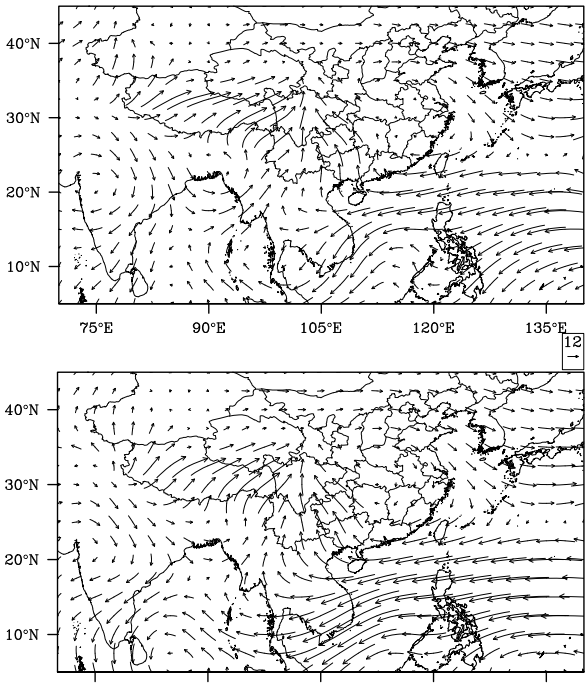

Fig. 4 Water vapor transport (g kg^{-1} m s^{-1}, 850hPa) of the 2009-2010 cold-season drought (upper) and the climatic mean (lower).

c. The higher-than-normal pressure at upper levels

Figure 5 shows that there is positive anomaly of geopotential height at the upper level in the Southwest, while negative anomaly at the lower level. Geopotential thickness thus has a positive anomaly in the region, which manifests the warmer-than-normal air temperature of the drought. The dominance between the warmer air temperature and the upper-level higher pressure needs to be further analyzed.

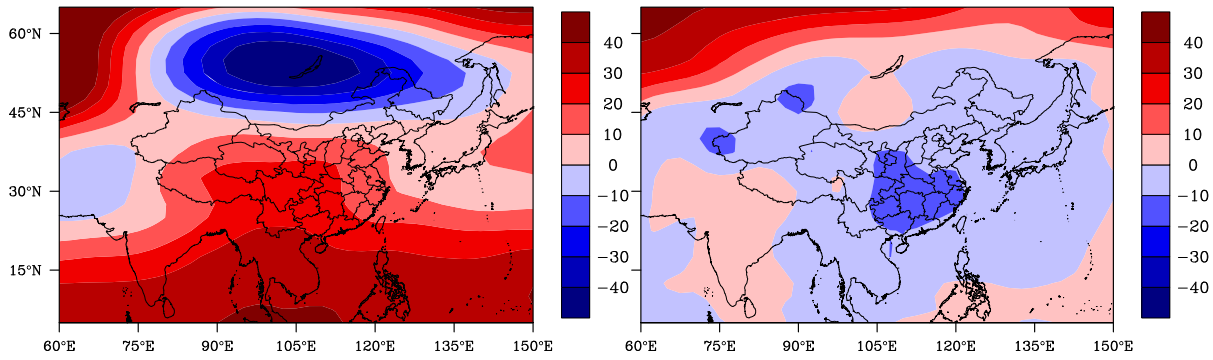

Fig. 5 Anomalies of geopotential height (gpm) at 200 (left) and 925hPa (right) of the 2009-2010 cold-season drought, relative to the climatic means.

d. The effect of warmer air temperature on cold-season drought

In summer, the East Asian monsoon season, water vapor transport and convergence are strong. Making the air saturated is easy, even if the air is much warmer than normal. Strong and persistent vapor supply can lead to heavy rain and even floods. So, heavy rain and floods in summer are dominated dynamically by the atmospheric circulation and the related water vapor transport.

In cold season, though water vapor transport is weak, light to moderate rains are still expectable. Whether air temperature can be low, relative to the season, is key to formation of precipitation. If it is low, weak precipitation may form from time to time, which may still efficiently mitigate the drought. Warmer air temperature is therefore particularly important to the formation of the cold-season drought.

e. The positive feedback in the regional atmosphere

With weaker water vapor transport and convergence, warmer air temperature is not helpful to the saturation of the air, and thus can help bring a clear weather. Whereas the clear weather can in turn warm the air through less cloud, stronger solar radiation, and thus more sensible heat from the surface. Such warmer temperature - less precipitation positive feedback, an inherent mechanism in the regional atmosphere, can facilitate the maintenance of the severe cold-season drought.

4. Summary

The 2009-2010 cold-season severe drought can be well monitored at a daily scale with the WAP index. Water vapor is less than normal during the drought. The atmospheric circulation and water vapor transport do not show significant anomalies in the track. To form drought in the cold season, a weakening in the strength of vapor transport can be sufficient. Air temperature is much warmer than normal during the drought. Though it has less influence on summer precipitation, which is dynamically controlled, air temperature is particular important to the formation of cold-season drought. The warmer air temperature in the cold season makes the air harder to saturate, and thus harder to form even light rains. Moreover, the warmer temperature - less precipitation feedback in the regional atmosphere can facilitate the maintenance of the cold-season drought.

References

Ding, Y., and Co-authors, 2003: Analysis on large-scale conditions of severe flood and drought events in East Asia during the 1990s. In "Study on severe flood and drought disasters in China and their physical mechanisms", China Meteorological Press (in Chinese).

Lu, E., 2009: Determining the start, duration, and strength of flood and drought with daily precipitation: Rationale. *Geophys. Res. Lett.*, **36**, L12707, doi:10.1029/2009GL038817.

Lu, E., and E. S. Takle, 2010: Concurrent variations of water vapor and temperature corresponding to the interannual variation of precipitation in the North American Regional Reanalysis., *J. Geophys. Res.*, **115**, D11101, doi:10.1029/2009JD012956.

Science and Technology Infusion Climate Bulletin
NOAA's National Weather Service
37th NOAA Annual Climate Diagnostics and Prediction Workshop
Fort Collins, CO, 22-25 October 2012

Factors Driving the Persistence of ENSO-Led Winter Rainfall Deficits into Late-Spring and Early-Summer over Texas

D. Nelun Fernando[1,2,3], Rong Fu[2], Kingtse C. Mo[4], Bridget R. Scanlon[5], Ruben Solis[3], Lei Yin[2], Adam Bowerman[2], and Robert Mace[3]

[1]*Visiting Scientist Programs, University Corporation for Atmospheric Research, Boulder, CO*
[2]*Department of Geological Sciences, Jackson School of Geosciences, University of Texas at Austin, Austin, TX*
[3]*Water Science and Conservation, Texas Water Development Board, Austin, TX*
[4]*Climate Prediction Center, NOAA/NWS/NCEP, College Park, MD*
[5] *Bureau of Economic Geology, Jackson School of Geosciences, University of Texas at Austin, Austin, TX*

1. Introduction

The 2011 exceptional drought over Texas was unusual because of its rapid intensification over the late-spring/early-summer 2011. Combined reservoir storage across the state dropped by 20%, and more regionally, in less than one year. Such a rapid reduction in reservoir storage, in a system designed to cope with multi-year droughts, caught water managers by surprise. Improved predictability of drought intensification in the spring could help decision makers, tasked with water resources management, adopt suitable measures to both reduce

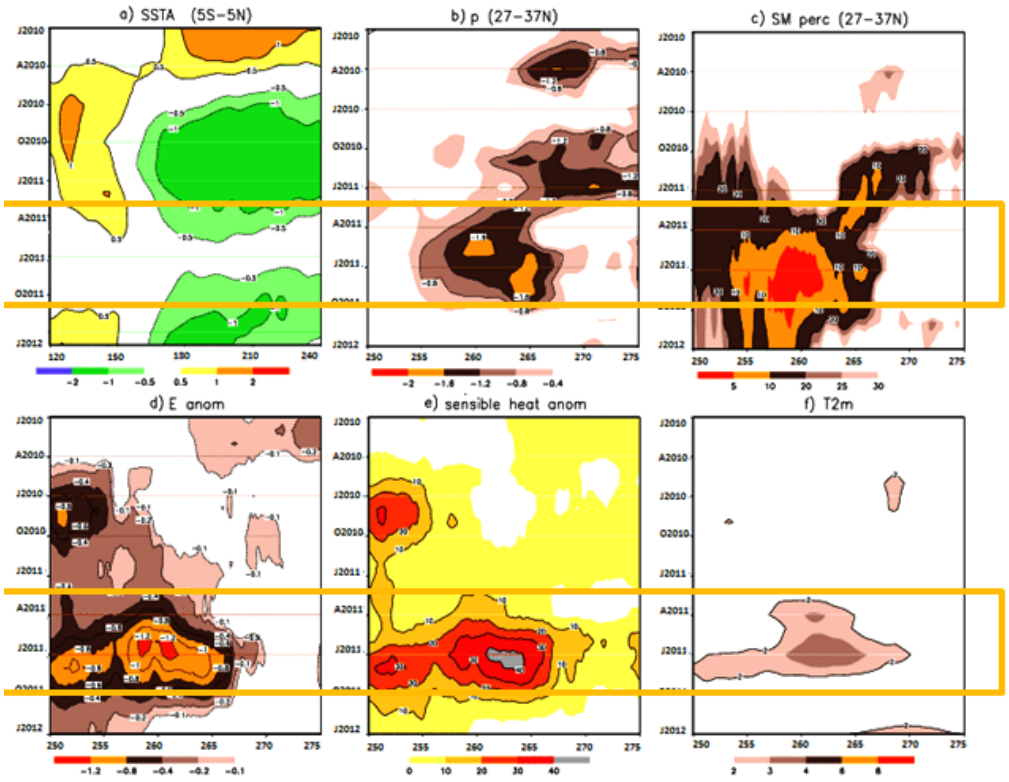

Fig. 1 Time-longitude plots of (a) sea surface temperature anomalies in the Nino3.4 region, (b) rainfall anomalies, (c) soil moisture percentiles, (d) evaporation anomalies, (e) sensible heat anomalies and (f) 2-meter temperature anomalies over Texas. SSTs are from the ERSST2 dataset (Smith *et al.* 1996) and precipitation is from the CPC unified precipitation dataset (Xie *et al.* 2010). Anomalies are calculated from a 1950-2010 climatology. Soil moisture percentiles, evaporation and sensible heat anomalies, and 2-meter temperature anomalies are from NLDAS based surface hydrology fields available at http://www.cpc.ncep.noaa.gov/products/Drought/Monitoring/.

Correspondence to: D. Nelun Fernando, Department of Geological Sciences, Jackson School of Geosciences, University of Texas at Austin, Austin, TX 78712; E-mail: nelun.fernando@jsg.utexas.edu.

evaporative loss from reservoirs and prepare contingency plans to cope with an impending reduction in water supply over the summer. We investigate factors that led to the spring intensification of the drought with the aim of improving drought predictability for Texas.

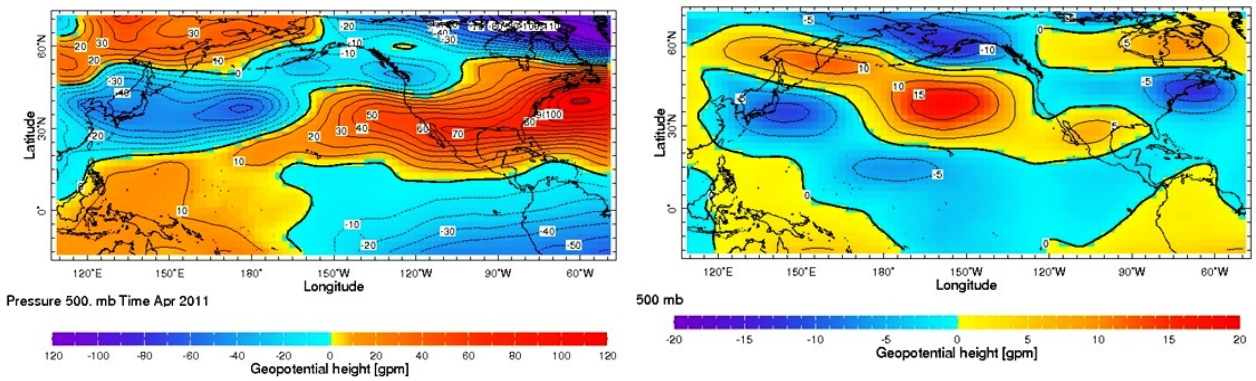

Fig. 2 (a) 500 hPa height anomalies in April 2011 and (b) 500 hPa height anomaly composite in 23 La Niña years. Dataset used is NCEP-R1 (Kistler *et al.* 2001) with 1981-2010 climatology. Zonal means have been removed.

2. Spring intensification of the drought

La Niña conditions played an important role in the initiation of the drought in the fall of 2010. Rainfall deficits over Texas commenced in the fall of 2010 coincident with the La Niña event that began in the summer of 2010 and peaked in the fall of 2010 (Fig. 1, panels a-b). The most marked reduction in rainfall and soil moisture occurred from April 2011 onwards and peaked in the summer of 2011 (Fig. 1, panels b-c). With the reduction in rainfall and soil moisture, there was a reduction in evaporation and an increase in sensible heating and surface (2 meter) temperature (Fig. 1, panels d-f). The reduction in evaporation and the increases in sensible heating and 2-meter temperatures are also most prominent from April 2011 onwards.

Why is April an important milestone for the drought event of 2011? April happens to be the normal start of the rainfall season over Texas and, in 2011 we see a drastic reduction in rainfall right at the start of the rainfall season. Rainfall in April can be from the passage of frontal systems and from convective storms. Therefore, we examined large-scale circulation anomalies induced by La Niña, the local thermodynamic environment over Texas and synoptic events as candidate factors driving April rainfall deficits.

3. Large-scale circulation anomalies induced by La Niña

The ridge at 500 hPa in April 2011 over Texas (Fig. 2(a)) was stronger and had a more zonal pattern over the Pacific compared with the composite pattern of 500 hPa height anomalies in 23 La Niña years from 1949 to the present (Fig. 2(b)).

4. Local thermodynamic factors and synoptic events

There was a sudden sharp increase in convective inhibition at the end of April 2011 (Fig. 3 – red line). An interesting feature to note from past intense drought events is that there is a similar increase in convective inhibition – albeit not as strong as in 2011 – in the drought events of 1918, 1925 and 1956.

An examination of lower-

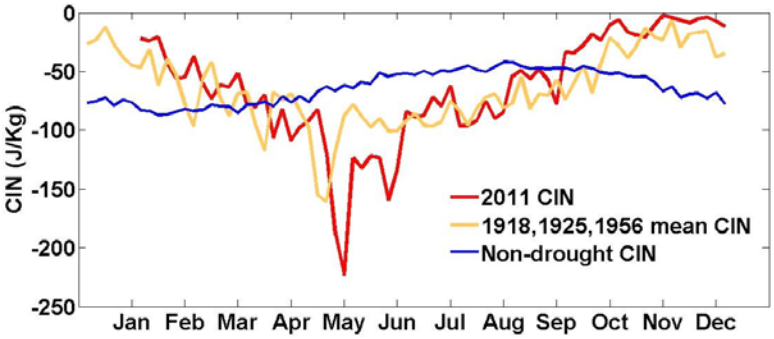

Fig. 3 Pentadal convective inhibition (CIN) in 2011 (red), mean convective inhibition in drought years of 1918, 1925 and 1956 (orange) and mean convective inhibition in non-drought years (blue). Dataset for 2011 convective inhibition is CFSv2 realtime data available from 1 February onwards (Saha *et al.* 2011). Dataset for historical droughts and non-droughts is the NOAA/ESRL/PSD 20th Century Reanalysis (Compo *et al.* 2011).

tropospheric circulation anomalies shows that there were anomalously strong westerly winds at 850 hPa in April 2011 (Fig. 4). Wind speeds during the bursts of abnormally strong westerlies at the end of April 2011 were more than twice the climatological wind speed for that time of year (Fig. 5 (b)). At the same time as the anomalous westerlies, we see an increase in surface temperature and dewpoint (Fig. 5(a)), negative relative vorticity (Fig.5(c)) and increases in 500 hPa height (Fig. 5(d)) implying that the westerlies advected temperature and negative vorticity eastward. The high terrain to the west of Texas had abnormally high surface temperatures in March and April, with anomalies reaching 5 ºK (not shown). Therefore, thermal advection due to increased westerly flow over a warmer-than normal terrain in the spring increased convective inhibition and contributed to the establishment of a 500 hPa height anomaly (*i.e.* the mid-tropospheric high pressure system) in late-April 2011.

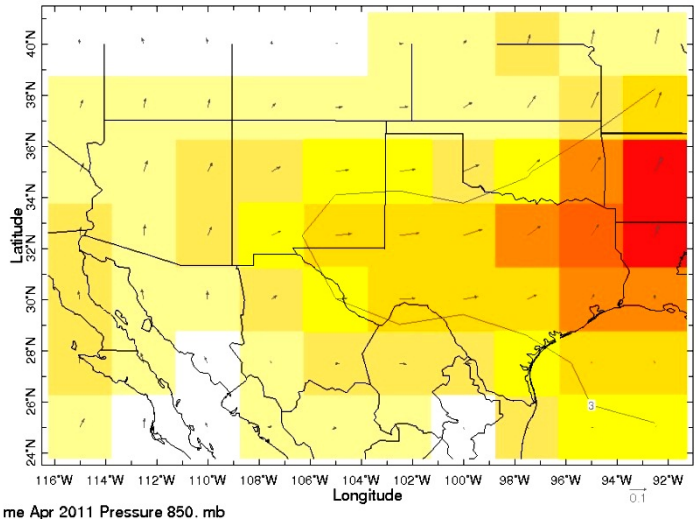

Fig. 4 Vector wind anomaly at 850 hPa in April 2011 showing the westerly flow over Texas. Dataset used is NCEP-R1 with anomalies calculated from a 1981-2010 climatology.

We find that the anomalous strengthening of the zonal winds at 850 hPa is a characteristic feature in the 12 severe-to-extreme droughts experienced over Texas since 1895 that had persistent negative rainfall anomalies from winter through summer (Fig. 6). Results suggest that February SST anomalies in the central Pacific, specified by the NINO4 index, is an important driver of the low level westerly wind anomalies in April over Texas.

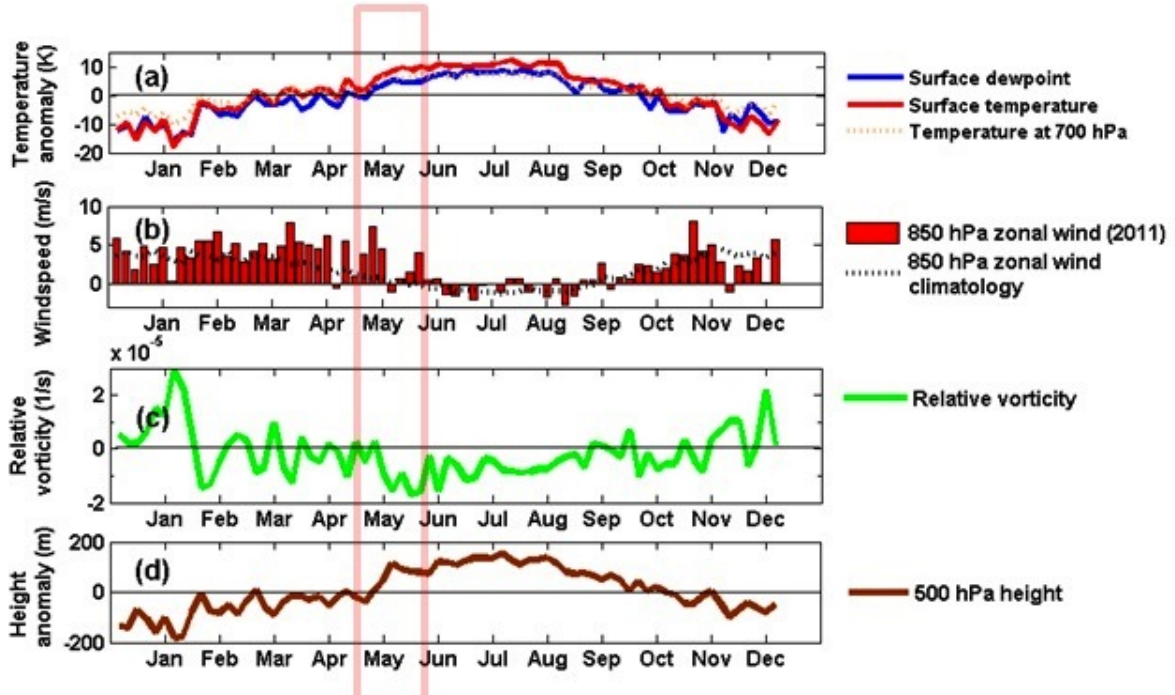

Fig. 5 Area-averaged (for the domain of Texas) pentadal surface temperature and dewpoint and temperature at 700 hPa (a), pentadal zonal winds at 850 hPa in 2011 and climatology (b), pentadal relative vorticity anomalies (c), and pentadal 500 hPa height (d). Data are from NCEP-R1 fields with anomalies calculated from a 1981-2010 climatology.

5. Conclusion

La Niña induced a reduction in winter precipitation over Texas in DJF 2010/2011. This led to a cumulative decrease in column soil moisture from the winter through the spring of 2011 that drove increases in sensible heating and surface temperature. La Niña also induced the mid-tropospheric high at 500 hPa that set up large scale subsidence over Texas. Surface heating due to soil moisture deficits and large-scale subsidence increased convective inhibition in late-spring. The sharp increase in convective inhibition in late-April and early-May was due to strengthened westerlies at 850 hPa that advected warm and dry air eastward from the Mexican Plateau and west Texas. The finding that strengthened westerlies at 850 hPa in April in past intense drought events as well has implications for improving drought predictability. Soil moisture feedback can influence summer drought intensity when rainfall deficits (hence, soil moisture deficits) are established in winter/spring. This finding underscores the need for improved real-time monitoring of soil moisture.

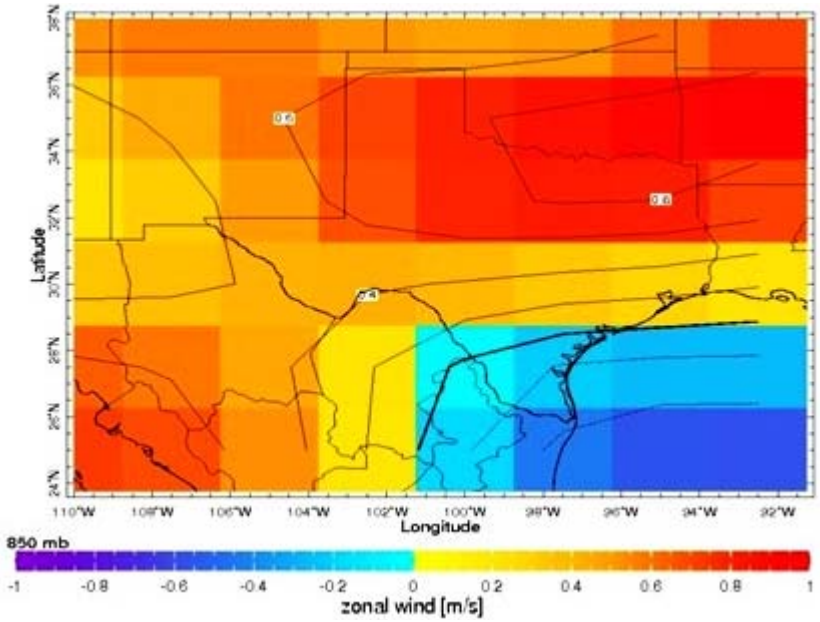

Fig. 6 Anomalous zonal wind composite for 12 severe-to-extreme drought years with rainfall deficits in winter through summer. Data are from NCEP-R1 with a 1981-2010 baseline climatology use in the calculation of anomalies.

The findings reported in this summary are included in an article currently in review by *PNAS-Plus*.

References

Compo, G. P., and Co-authors, 2011: The Twentieth Century Reanalysis Project. *Quart. J. Royal Meteor. Soc.*, **137,** 1-28.

Kistler, R., E., and Co-authos, 2001: The NCEP-NCAR 50-Year Reanalysis: Monthly Means CD-ROM and Documentation. *Bull. Amer. Met. Soc.*, **82**, 247-267.

Saha, S., and Co-authors, 2011: The NCEP Climate Forecast System Version 2. Submitted to *J. Climate* (http://cfs.ncep.noaa.gov/cfsv2.info/CFSv2_paper.pdf).

Smith, T. M., R. W. Reynolds, R. E. Livezey, and D. C. Stokes, 1996: Reconstruction of historical sea surface temperatures using empirical orthogonal functions. *J. Climate*, **9,** 1403-1420.

Xie, P. P., M. Chen, and W, Shi, 2010: CPC unified gauge based analysis of global daily precipitation. *AMS 24th Conf. on hydrology*, Jan 18-21, 2010, Atlanta, GA.

Science and Technology Infusion Climate Bulletin
NOAA's National Weather Service
37th NOAA Annual Climate Diagnostics and Prediction Workshop
Fort Collins, CO, 22-25 October 2012

Tree-Ring Extension of Precipitation Variability at 12-km Grid Points in Eastern Nevada: Implications for Drought Analysis

Franco Biondi

DendroLab, University of Nevada, Reno, NV

1. Introduction

Preparing for future hydroclimatic variability benefits from an assessment of the duration, magnitude, and intensity (or peak value) for both dry and wet spells. Given that climatic episodes recorded by the instrumental record are not likely to cover the entire spectrum of potential future scenarios (Milly *et al.*, 2008), water managers can "hedge their bets" by examining long (*i.e.*, multi-century) proxy records of climate at seasonal to annual time steps (Biondi and Strachan, 2012). Until recently, these records were only available at relatively coarse spatial scales, such as the 2.5×2.5° grid spacing of the North American Drought Atlas (Cook and Krusic, 2004). However, km-scale spatial intervals can now be achieved using a combination of more intense sampling and advanced statistical techniques. In particular, kriging is a geostatistical technique commonly used for optimal interpolation of environmental data (Isaaks and Srivastava, 1989), and space-time geostatistical models can improve kriging estimates when long temporal sequences of observations exist at relatively few points on the landscape (Christakos, 2000).

In the Great Basin of North America, ecotonal environments characterized as lower forest border sites are ideally suited for tree-ring reconstructions of hydroclimatic variability. I present here how space-time kriging was applied to a network of 22 precipitation records developed from single-leaf pinyon (*Pinus monophylla*) tree-ring samples in eastern Nevada, within the Great Basin of North America (Figure 1).

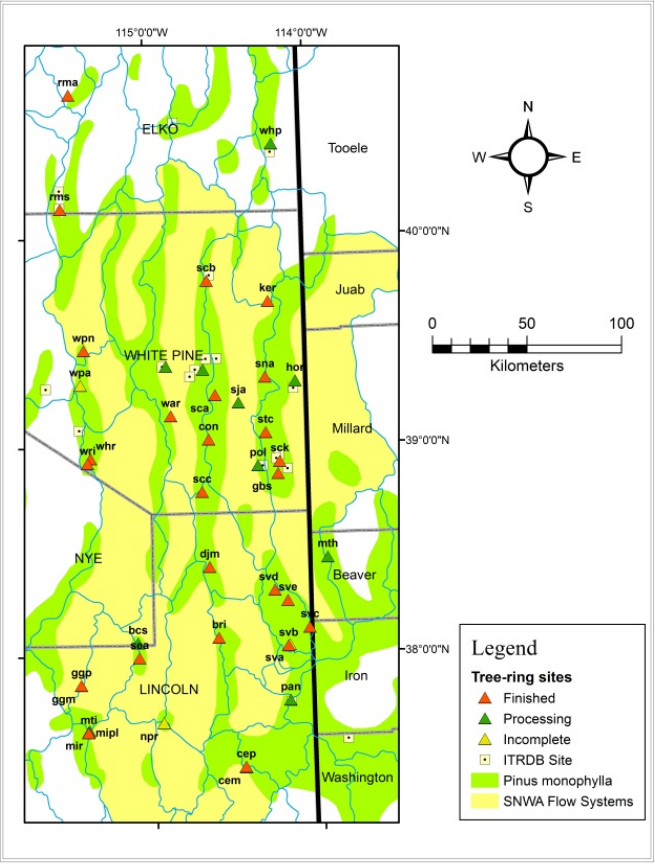

Fig. 1 Map of the study area, showing the Nevada-Utah border (heavy vertical line), county lines (gray lines) and names (uppercase), subwatershed boundaries (blue lines), distribution of single-leaf pinyon pine (*Pinus monophylla*, green areas), location of tree-ring sites (lowercase 3-letter codes), either new (triangles) or from the ITRDB database (squares), and hydrographic basins of interest to the Southern Nevada Water Authority (SNWA Flow Systems).

2. The tree-ring network and precipitation reconstructions

A total of 22 tree-ring sites (5 from the ITRDB dataset) in eastern Nevada distributed over 500 m of elevation (~1930-2430 m) and a geographical area of ~ 230 (N-S) × 155 (E-W) km were selected based on

Correspondence to: Franco Biondi, DendroLab, Dept. of Geography, MS 0154, University of Nevada, Reno, NV 89557; E-mail: fbiondi@unr.edu.

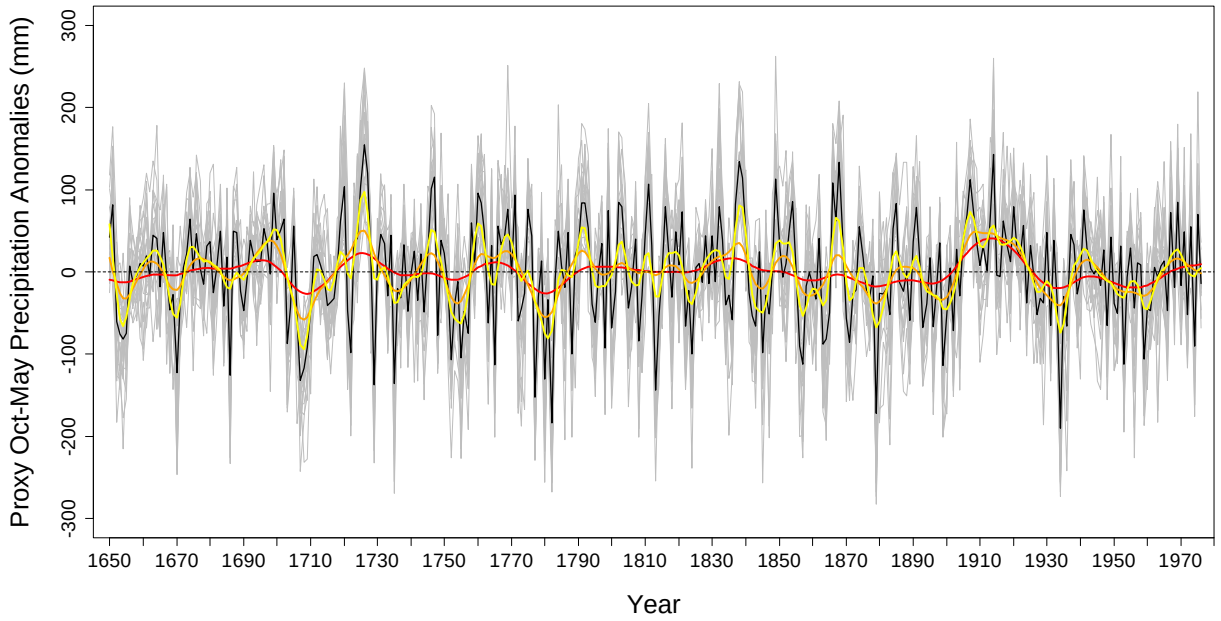

Fig. 2 The average (black) of the 22 site reconstructions (gray) of October-May total precipitation anomalies (mm) was smoothed with a 30-year (red), 15-year (orange), and 7.5-year (yellow) cubic spline to highlight interannual and interdecadal patterns.

their correlation with local precipitation data obtained from the PRISM 4 × 4 km database (Daly *et al.*, 1994). Each site tree-ring chronology was computed as follows:

$$\overline{I}_t = \underset{i=1,\ldots,n_t}{median}\left(\frac{w_t}{y_t}\right)_i$$

where $\bar{I}_t$ = chronology value in year t = median annual index; n_t = number of samples in year t, with $n_t \geq 3$; w = crossdated ring width (mm, with 1000th digit resolution) of sample i in year t; y = value of sample i in year t computed by fitting a cubic smoothing spline with 50% frequency response at a period of 100 years to ring width series i; w_t / y_t = index value of sample i in year t. Site chronologies were obtained by fitting a cubic smoothing spline (Cook and Peters, 1981) to each ring-width series to avoid known issues that affect other types of standardization functions, such as modified negative exponentials (Biondi and Qeadan, 2008).

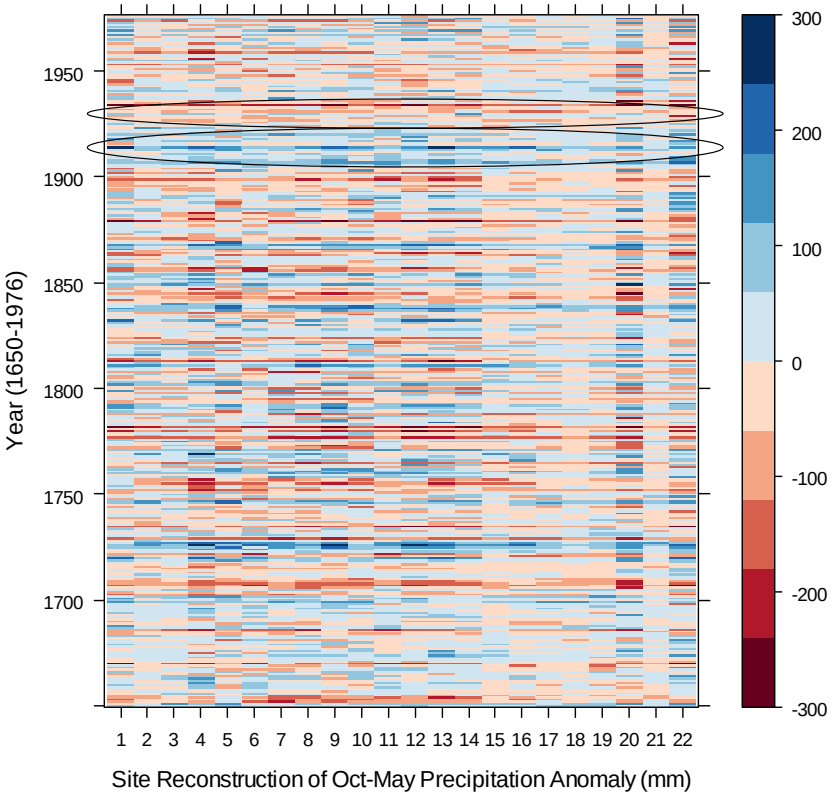

Fig. 3 Pseudo-color plot of the 22 reconstructions of October-May total precipitation anomalies, showing temporal patterns at annual resolution (y-axis). The color scale for the anomalies, divided into 10 intervals over a 600-mm range, is displayed on the right. The early 1900s pluvial and the "Dust-Bowl" drought that followed it were highlighted with black ellipses.

The period in common among all tree-ring chronologies, *i.e.* 1650-1976, was used to reconstruct October-May total precipitation using the Line of Organic Correlation (LOC) method (Biondi and Strachan, 2011). The LOC method was used because it maintains the variability found in the instrumental record (Helsel and Hirsch, 2002), and is particularly well adapted to reproduce long-term features of hydroclimatic anomalies (Figures 2 and 3).

Individual, annually resolved site reconstructions were then combined using spatio-temporal kriging to produce 327 annual maps (from 1650 to 1976) on a 12 × 12 km spacing, for a total of 315 grid nodes. I performed space-time estimation (Fassó and Cameletti, 2009) using public-domain software (R Development Core Team, 2012). Elevation was treated as a covariate in order to compute a single kriging estimate for each two-dimensional grid point location (rather than predict over all possible altitudes), and still take elevation into account. Inter-annual patterns at the km-scale were quantified by the duration, magnitude, and intensity (peak value) of past episodes (as done by Biondi *et al.*, 2008). By considering how modern interannual variability compares to that of previous records, recent changes can be placed in a long-term context to estimate the likelihood of severe and sustained drought.

3. Space-time interpolation and drought analysis

Space-time variograms showed an exponential behavior up to about 200 km with no temporal autocorrelation, *i.e.* beyond the 1-year lag the spatial dependence was essentially zero. The annual mean of the 315 grid point estimates was used to identify wet and dry episodes. The three driest years were 1934, 1879, and 1782, and the three wettest years were 1914, 1868, and 1726 (Figure 4). Greater spatial variability

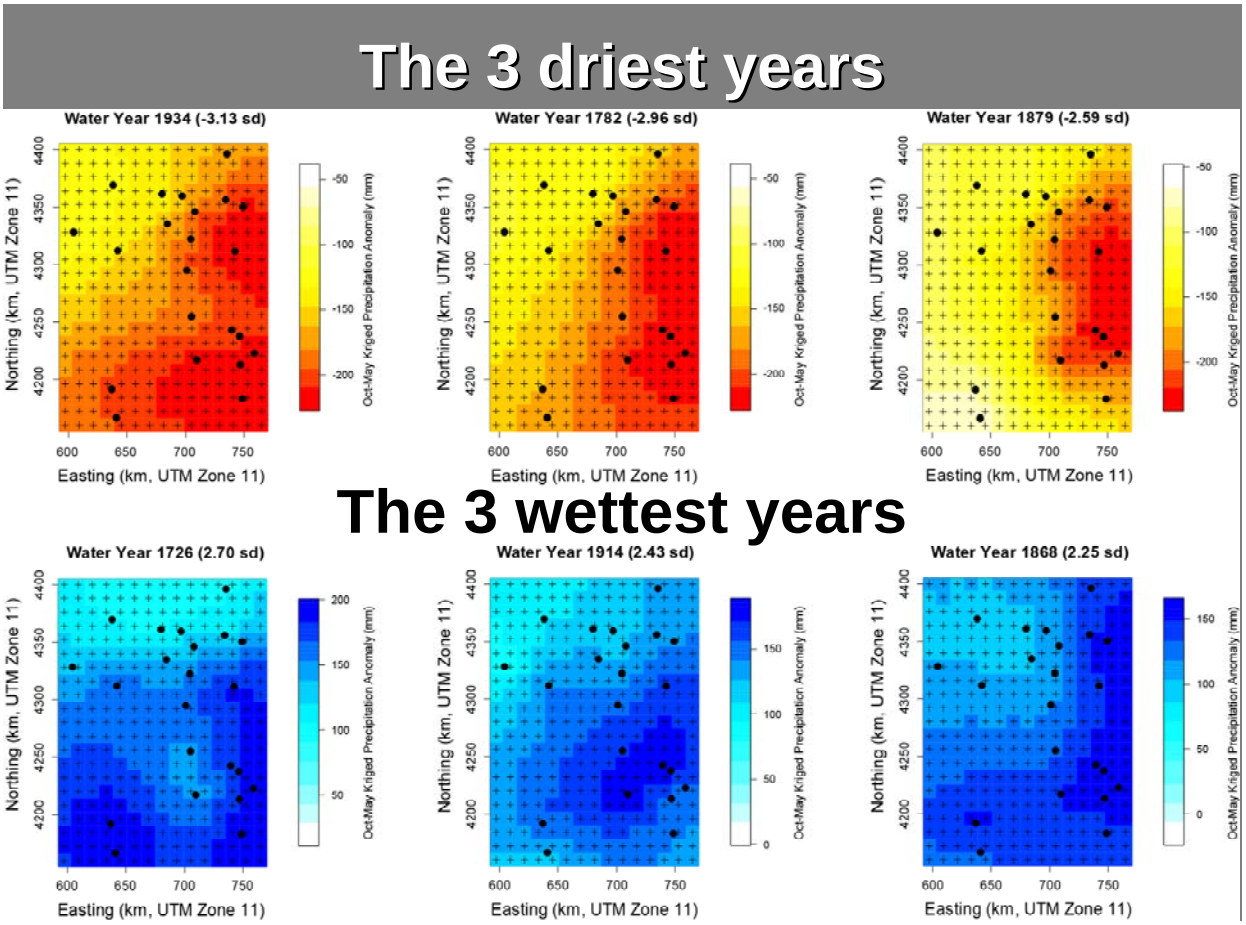

Fig. 4 Pseudo-color plots for space-time interpolated reconstructions of October-May total precipitation anomalies (mm). The color scale for the anomalies, divided into 12 intervals over a 190-mm range, is displayed on the right. The location of tree-ring chronologies (solid black circles) and 12-km grid points (black crosses) is also shown.

emerged during wet periods, whereas dry spells were more synchronous over the landscape. At the annual time scale, the most remarkable episode in the entire reconstruction was the early 1900s pluvial, followed by the late 1800s drought. The 1930s 'Dust Bowl' drought was in 8th position, making it a remarkable hydro-climatic episode for at least the past few centuries. After smoothing the annual values with a 7.5-year cubic spline to emphasize interannual variability, the early 1900s pluvial remained the strongest episode, but the 1930s drought became the second strongest one. Therefore, the early-1900s pluvial, a most remarkable episode in the last few centuries, biases the instrumental record, but water management policies in eastern Nevada basins could use the 1920-30's drought as a relevant worst-case scenario.

Besides showing how regional drought severity varies across the Great Basin, these results directly address the needs of water managers with respect to planning for 'worst case' scenarios of drought duration and magnitude. For instance, it is possible to analyze which geographical areas and hydrographic basins are more likely to be impacted during the most extreme droughts, at annual or multiannual timescales AND at the km-spacing used by regional climate models. This approach allows water managers not only to evaluate drought patterns for single watersheds, but also to determine if episodes that occurred during the instrumental period can be used for long-term planning, thereby increasing their ability to design management practices aimed towards resiliency to future changes.

Acknowledgements. I thank J.D. Salas, L. Saito, and J. Leising for helpful discussions of statistical and hydrological issues. I am also extremely grateful to all the people and DendroLab personnel, especially Scotty Strachan, who contributed, either in the field or in the laboratory, to the development of the tree-ring network. This research was supported, in part, by Southern Nevada Water Authority, by the Office of the Vice President for Research at the University of Nevada, Reno, and by the US National Science Foundation under Cooperative Agreement EPS-0814372 and Grant No. P2C2-0823480. The views and conclusions contained in this document are those of the author and should not be interpreted as representing the opinions or policies of the funding agencies.

References

Biondi, F., T.J. Kozubowski, A.K. Panorska, L. Saito, 2008: A new stochastic model of episode peak and duration for eco-hydro-climatic applications. *Ecological Modelling*, **211**, 383-395.

—, and F. Qeadan, 2008: A theory-driven approach to tree-ring standardization: Defininig the biological trend from expected basal area increment. *Tree-Ring Research*, **64**, 81–96.

—, and S. Strachan, 2011: Tree-ring extension of precipitation variability for Eastern Nevada: Implications for drought analysis in the Great Basin Region, USA. Abstract H42G-08, *Fall Meeting of the American Geophysical Union*, San Francisco, CA.

—, and S. Strachan, 2012: Dendrohydrology in 2050: Challenges and opportunities. *Toward a Sustainable Water Future: Visions for 2050*, W.M. Grayman, D.P. Loucks and L. Saito, Eds., American Society of Civil Engineers (ASCE), Reston, Virginia., 355-362.

Christakos, G., 2000: *Modern Spatiotemporal Geostatistics*. Oxford University Press.

Cook, E.R., and P.J. Krusic, 2004: *The North American Drought Atlas*. Lamont-Doherty Earth Observatory.

—, and K. Peters, 1981: The smoothing spline: A new approach to standardizing forest interior tree-ring width series for dendroclimatic studies. *Tree-Ring Bulletin,* **41**, 45-53.

Daly, C., R.P. Neilson, and D.L. Phillips, 1994: A statistical-topographic model for mapping climatological precipitation over mountainous terrain. *J. of Appl. Meteor*., **33**, 140-158.

Fassó, A., and M. Cameletti, 2009: The EM algorithm in a distributed computing environment for modelling environmental space-time data. *Environmental Modelling & Software*. **24**, 1027-1035.

Helsel, D.R., and R.M. Hirsch, 2002: Statistical methods in water resources. *Techniques of Water-Resources Investigations Book 4, Chapter A3*, United States Geological Survey.

Isaaks, E.H., and R.M. Srivastava, 1989: An Introduction to Applied Geostatistics. *Oxford University Press, New York*.

Milly, P.C.D., J.L. Betancourt, M. Falkenmark, R.M. Hirsch, Z.W. Kundzewicz, D.P. Lettenmaier, and R.J. Stouffer, 2008: Stationarity is dead: Whither water management? *Science*, **319**, 573-574.

R Development Core Team, 2012: R: A language and environment for statistical computing, Version. 2.15.0. R Foundation for Statistical Computing, Vienna, Austria.

Science and Technology Infusion Climate Bulletin
NOAA's National Weather Service
37th NOAA Annual Climate Diagnostics and Prediction Workshop
Fort Collins, CO, 22-25 October 2012

Comparison of Dynamically and Statistically Downscaled Seasonal Climate Forecasts for the Cold Season over the United States

Jin-Ho Yoon[1], L. Ruby Leung[1] and James Correia Jr.[1,2]

[1]*Pacific Northwest National Laboratory, Richland, WA*

[2]*NOAA/Storm Prediction Center and Cooperative Institute for Mesoscale Meteorological Studies, University of Oklahoma, Norman, OK*

ABSTRACT

This study compares two approaches, dynamical and statistical downscaling, for their potential to improve regional seasonal forecasts for the United States (U.S.) during the cold season. In the Multi-RCM Ensemble Downscaling (MRED) project, seven regional climate models (RCMs) are used to dynamically downscale the Climate Forecast System (CFS) seasonal prediction over the conterminous U.S. out to 5 months for the period of 1982–2003. The simulations cover December to April of next year with 10 ensemble members from each RCM with different initial and boundary conditions for the corresponding ensemble members. These dynamically downscaled forecasts of precipitation (P) and surface air temperature (T) are compared with statistically downscaled forecasts produced by two bias correction methods of Bias Correction and Spatial Disaggregation (BCSD) and Bayesian merging applied to both the CFS and RCM forecasts.

The RCMs generate finer-scale features that are missing from CFS in terms of both climatology and anomaly from the long-term mean. However, forecast skill of the downscaled P and T can vary for different metrics used in the cross validation. In terms of temporal anomaly correlation (AC), it is found that RCMs and statistical downscaling methods generally are somewhat higher than CFS, especially in the Northwest and North Central regions. For this skill measure, some RCMs can even outperform the multi-model ensemble or combined dynamical-statistical methods. For skill measured by spatial correlation, RCMs and statistical downscaling also provide additional values in addition to CFS. The Bayesian method performs poorly for AC because of the large ensemble spread in the forecasts. Using RMSE as the metrics (Fig. 1), we find that a couple of RCMs can reduce forecast errors compared to CFS, but some RCMs have higher RMSE due to the overprediction of precipitation in the Northwest and Northern California. However, the RCMs combined with

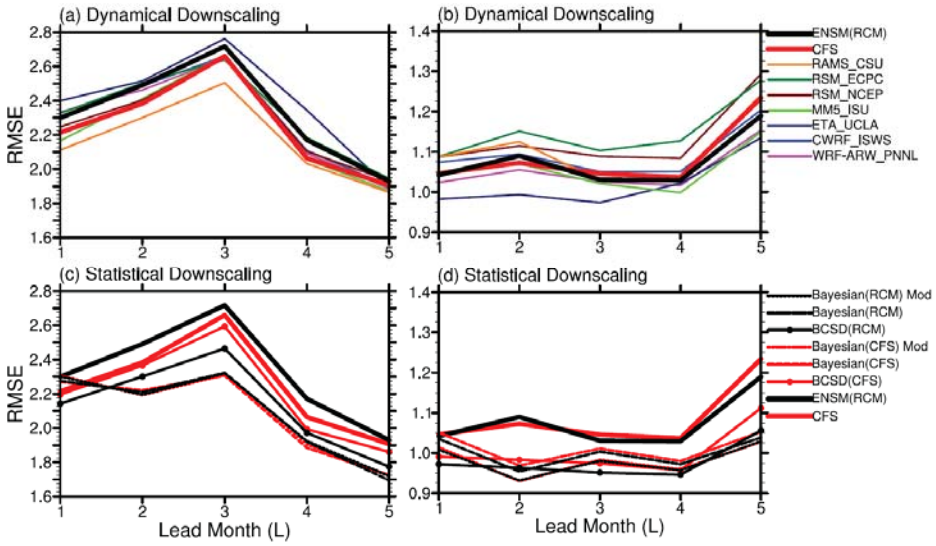

Fig. 1 Root Mean Squared Error (RMSE) of Surface air temperature (a and c) and precipitation (b and d) averaged over the contiguous U.S. RMSE of all the regional climate models are in the top panels (a and b) and statical downscaling methods in the bottom (c and d). Y axis in the left column (a and c) is deg C and that in the right column (b and d) is in mm/day.

Correspondence to: Jin-Ho Yoon, Pacific Northwest National Laboratory, Richland, WA;
E-mail: Jin-Ho.Yoon@pnnl.gov.

statistical bias correction stand out clearly. At the first-month lead, simple BCSD of all seven RCMs do surprisingly well. At the longer leads, the Bayesian merging applied to either CFS or RCMs does a good job. Improvement of forecast skill can be found over the mountainous regions, especially the western U.S. during the winter season.

This work has been published in *J. Geophys. Res* in 2012.

Paper published

Yoon, J.-H., L. Ruby Leung, and J. Correia Jr., 2012: Comparison of dynamically and statistically downscaled seasonal climate forecasts for the cold season over the United States, *J. Geophys. Res.*, 117, D21109, doi:10.1029/2012JD017650.

6. GLOBAL CLIMATE CHANGE IMPACT ON SEASONAL VARIABILITY AND PREDICTION

Science and Technology Infusion Climate Bulletin
NOAA's National Weather Service
37th NOAA Annual Climate Diagnostics and Prediction Workshop
Fort Collins, CO, 22-25 October 2012

Is Global Warming Changing the ENSO Precursor in the Western North Pacific?

Shih-Yu Wang[1], Michelle L'Heureux[2], and Jin-Ho Yoon[3]

[1]*Utah Climate Center/Dept. Plants, Soils, and Climate, Utah State University, Logan, Utah*
[2]*NOAA Climate Prediction Center, College Park, Maryland*
[3]*Pacific Northwest National Laboratory, Richland, Washington*

1. Introduction

Recently, Wang *et al.* (2012) found that the boreal winter sea surface temperature anomalies (SSTA) in the western North Pacific (WNP) are strongly correlated to the development of the El Niño-Southern Oscillation (ENSO) by the following winter. Wang *et al.* (2012) defined the WNP index in two ways: (1) more simply by using de-trended SSTA averaged from 122°–132°E to 18°–28°N (a white box in Figure 1a) or (2) the second leading Maximum Covariance Analysis (MCA) of SSTA and 10m wind anomalies in the western Pacific from 90°E-170°W to 10°S-30°N (Figure 1a). In this study, the WNP will refer to the combined pattern of anomalous SST and winds, which is analogous to the Pacific Meridional Mode (PMM) located in the eastern half of the North Pacific. Both the PMM and WNP are linked to an SSTA dipole with significant anomalies off the equator in the Northern Hemisphere subtropics with opposing SSTAs located in the deep tropics. The PMM and WNP are thought to be linked to the "Seasonal Footprinting Mechanism (SFM)" (Vimont *et al.* 2003a,b; Alexander *et al.* 2010), when the atmospheric circulation over the extratropical North Pacific during the boreal winter (linked to the North Pacific Oscillation/NPO) establishes an SSTA pattern that persists through the following year and eventually influences ENSO. Wang *et al.* (2012) suggested that the location of the WNP SSTA dipole and associated wind anomalies (Figure 1a) may exert a more direct influence than the PMM on the degree of oceanic Kelvin wave activity preceding ENSO events (McPhaden 2004; Roundy and Kiladis 2007).

Here we report new observational and modeling evidence that, since the mid-20th century, there is a growing association between the WNP and the development of ENSO by the following year. The stronger relationship between the WNP and ENSO appears to be linked to increased greenhouse gas (GHG) in the atmosphere, and it may reflect the energetic west-to-east development of ENSO in recent decades (Wang and An 2002; Guan and Nigam 2008). Furthermore, a greater link between the WNP and ENSO one year later provides a plausible pathway by which anthropogenic climate change may influence ENSO and perhaps provide greater predictive skill in seasonal ENSO outlooks.

2. Data sources

To mitigate potential errors in historical SST data and reanalysis methods, three monthly SST datasets are utilized: (1) the Hadley Centre SST (HadISST) (Rayner *et al.* 2003), (2) the NOAA Extended Reconstructed SST (ERSST) Version 3b (Smith *et al.* 2008), and (3) the Kaplan long-term SST anomalies (Kaplan *et al.* 1998). Atmospheric winds are obtained from the NCEP/NCAR Global Reanalysis (NCEP1) that begins in 1948 (Kalnay *et al.* 1996). In addition, to examine the long-term changes in the WNP and ENSO, historical simulations with the Community Earth System Model version 1 (CESM1) are analyzed. Deser *et al.* (2011) showed the Community Climate System Model (CCSM4) – predecessor of the CESM1 but sharing the same ocean model – demonstrates significantly improved ENSO variability. This study uses three CMIP5 sets of historical single-forcing experiments that are driven by (a) greenhouse gas forcing only (GHG), (b) aerosol forcing only (Aerosol), and (c) natural forcing only including solar and volcano (Natural). Each experiment produced a two-member ensemble initialized from long-stable preindustrial (1850) control

Correspondence to: Shih-Yu Wang, Utah Climate Center/Dept. Plants, Soils, and Climate, Utah State University, Logan, Utah; E-mail: simon.wang@usu.edu.

runs up to 2005. In addition, we utilize a 350-year fully coupled CESM1 simulation without any external forcings. This long-term control simulation is useful to depict the natural variability of the WNP and ENSO.

3. Results

a. Strengthening of the WNP (DJF) and ENSO (DJF+1yr) association

Throughout this analysis, the WNP index is based on the second leading MCA mode of the western North Pacific SSTA and anomalous surface winds, but the major findings are also reproduced using an index of the box average SSTA. In order to align with above-average anomalies associated with the WNP box average, the positive phase of the MCA/WNP is defined by the anomalous pattern of SST and winds shown in Figure 1a. Figure 1b shows the 25-year sliding correlation between the WNP index during boreal winter (December-February, DJF) and the Niño-3.4 index (average SSTA for 170°-120°W, 5°S-5°N) during the following winter (DJF+1yr). The x-axis corresponds to the final year of the correlation window. A strong increase in correlations between the WNP and ENSO (DJF+1yr) is evident among all three SST datasets (Figure 1b). Here, the WNP and Niño-3.4 indices are linearly de-trended within each 25-year moving window in order to examine the interannual correlations between the WNP and ENSO irrespective of multi-decadal or longer trends. We note that either removing a single, fixed trend over the entire analysis period or keeping the trend results in similar increases in the correlation with a difference less than 0.1 (not shown). This increase is particularly robust for moving windows that begin with 1960 as the initial year.

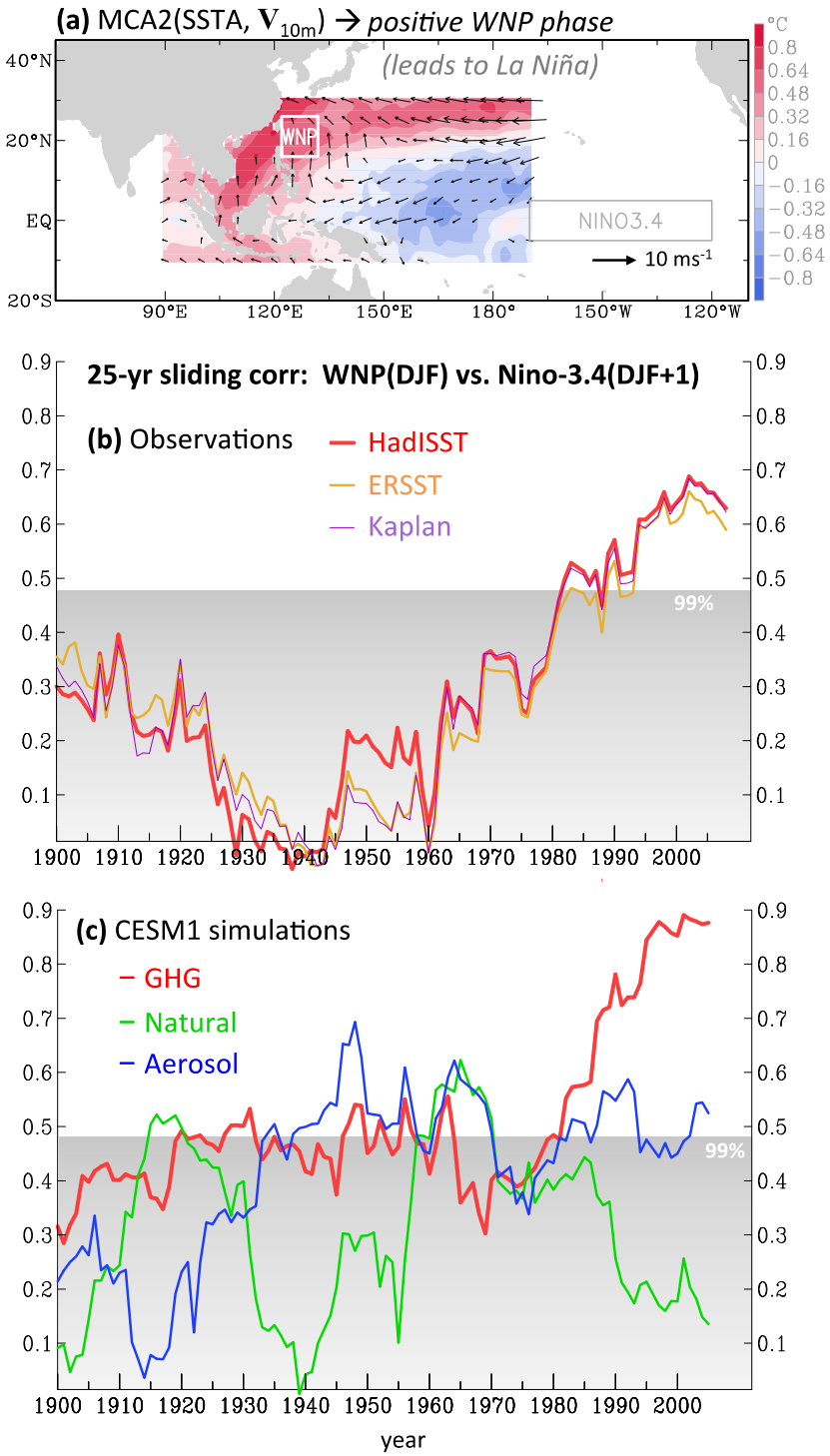

Fig. 1 (a) MCA-2 of WNP SSTA and surface wind anomalies in DJF, adopted from Wang et al. (2012). The PC time series of MCA2 is used as the WNP index. Outlined areas represent an alternative WNP index domain and the Niño-3.4 index domain. (b) 25-year sliding correlations betwenn the WNP (DJF) and Niño-3.4 (DJF+1yr) indices using three SST datasets. Years on the x-axis represent the final year of the 25-year sliding window. The top of gray area indicates the 99% significance level. (c) Same as (b) but for the three CESM1 experiments.

The correlation has increased to as high as 0.7 in the most recent part of the record. This result is robust regardless of the length of the sliding windows (not shown).

Figure 2a shows one-point correlation maps between SSTA and the WNP index at lead times of zero-year (left) and one-year (right), using HadISST data for the period 1958-2010 (Wang *et al.* 2012). The WNP index is inverted, so the map can be interpreted as the negative WNP phase that precedes El Niño. During DJF, strong correlations are evident along the East Asian coastline and along the Kuroshio Extension. In the following winter (DJF+1yr), the WNP is related to a significant basin-wide El Niño SSTA pattern.

The WNP-ENSO association is examined using CESM1 simulations forced by the GHG, Natural, and Aerosol forcings to understand the role of external forcings (Figures 2b-2d). The correlations between the WNP and SSTA based on the forcing experiments for DJF (left) and DJF+1yr (right) during 1958-2005 bear a strong resemblance with the observations. Key aspects of the WNP relationship with SSTA are broadly reproduced, with the exception of opposing correlations in the eastern Indian Ocean. Furthermore, Figure 1c shows 25-year sliding correlations between de-trended values of the WNP (DJF) and Niño-3.4 indices one year later (DJF+1yr) for the three CESM1 single forcing experiments. A considerable amount of decadal variability of the correlation between the WNP and ENSO is observed among the forcing experiments. While the Aerosol and Natural forcing experiments show significant correlations between the WNP and ENSO for periods between ~1940/50 through 1960/70, only the GHG forcing provides evidence for strong increase in

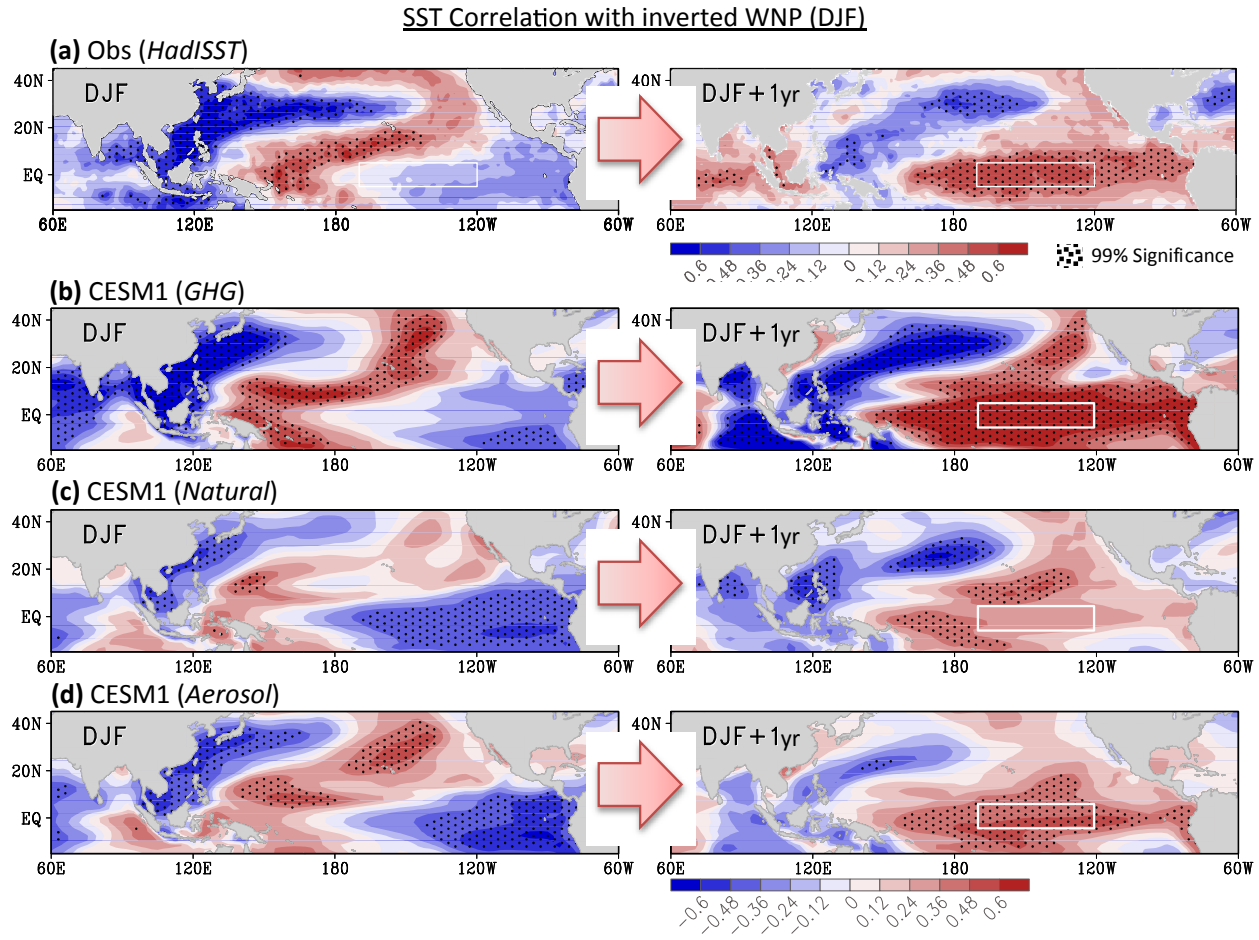

Fig. 2 (a) Corelation maps of SSTA with the inverted WNP index for zero-lead DJF (left) and one-year lead, DJF+1yr (right) using the HadISST and NCEP1 data for the period 1958-2010. All variables are detrended. The Niño-3.4 area is outlined. Dotted values are significance at the 99% level per a t-test. (b)-(d) Same as (a) but for the CESM1 simulations from the GHG, Natural, and Aerosol forcing experiments for the period 1958-2005.

the correlations that begins during ~1950-1970 and continues through the present. The GHG-only experiment indicates correlations as strong as ~0.9 between the WNP (DJF) and ENSO (DJF+1yr) in the recent decade while the Natural-only experiment indicates an insignificant relationship. Because these experiments are free runs, the specific years among the model experiments cannot be directed compared. Thus, the only robust comparison in Figure 1c is that neither the Aerosol-only run nor the Natural-only run produces a sustained period of significant correlations as large, or for long, as the GHG-only experiment.

b. Shifts in the strongest SST trends and the WNP (DJF) - ENSO (DJF+1yr) association

To better understand why the de-trended, interannual relationship between the WNP (DJF) and ENSO (DJF+1yr) has increased, we split the dataset into two halves: 1950-1979 and 1980-2008. The year 1950 is chosen as a starting point due to greater reliability in the observed datasets over the tropical Pacific after that time (Bunge and Clarke 2009; L'Heureux *et al.* 2012). To further suppress sampling errors, two SST datasets (HadISST and ERSST) are averaged together. Figures 3a and 3b show the SSTA correlations and the low-level wind regressions in DJF with the DJF+1yr Niño-3.4 index (the length of the vectors are weighted by the correlation). Comparing the two halves, the most striking and pronouced change in the recent era is the stronger regression/correlation between ENSO (DJF+1yr) and the previous DJF low-level wind anomalies curling southward and then eastward in the western equatorial Pacific just north of Papua New Guinea. Also evident is a stronger out-of-phase SSTA correlation between the subtropical western North Pacific and western equatorial Pacific (~160°E-180°). This result mirrors the inverse of Figure 1a and strongly implies that one of the canonical initiating mechanisms for ENSO onset has become more active recently: namely, the generation of oceanic Kelvin waves by wind stress anomalies over the western equatorial Pacific.

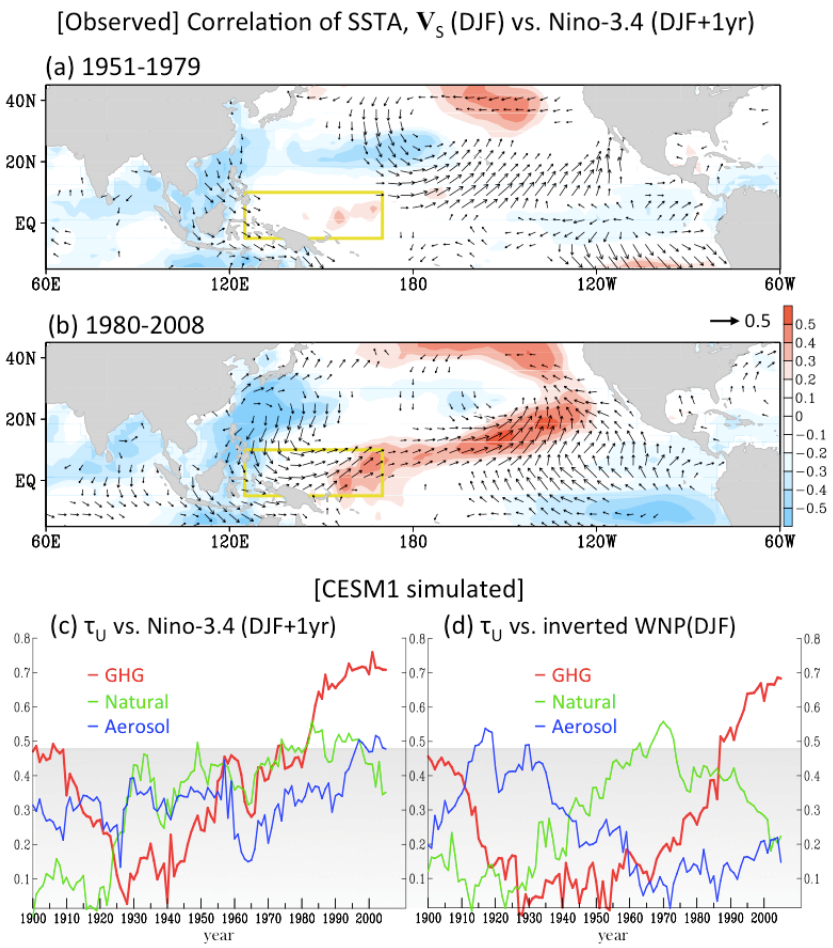

Fig. 3 Correlation map of DJF SSTA (shadings) and regression of surface winds weighted by the correlation (vector length) against the DJF+1yr Niño-3.4 index during the periods of (a) 1951-1979 and (b) 1980-2008, using the NCP1 wind and averaged HadISST-ERSST data. The plotted values exceed significance at the 95% level. (c) Similar to the 25-year sliding correction in Fig. 1b and 1c, but for the DJF surface wind stress (τ_U) (averaged in the yellow box in a, b) and the DJF+1yr Niño-3.4 index from the three CESM1 experiments. (d) Same as (c) except for correlations between τ_U and the inverted DJF WNP index.

Given that low-level wind anomalies in the western equatorial Pacific are optimally situated to influence the generation of oceanic Kelvin waves that affect the development of ENSO, we show in Figures 3c and 3d the CESM1 25-year sliding correlations of the de-trended surface zonal wind stress averaged for 120°-170°E, 5°S-10°N (τ_U) with the de-trended Niño-3.4 (DJF+1yr) and WNP (DJF), respectively. Among all the forcings, only the GHG-only forcing illustrates the pronounced upward correlation of low-level wind stress in the

equatorial western Pacific and the WNP with ENSO beginning in the mid-20th century. The increased correlations of the low-level winds provide more evidence for a GHG-driven increasing relationship between the WNP and ENSO development by the following year.

c. The changing ENSO precursor pattern

Why are there stronger correlations of the low-level winds in the western tropical Pacific and the WNP (DJF) with ENSO (DJF+1yr) index in the recent decades? To further examine the extent of which the low-level wind fields may change the ENSO-WNP link, Figure 4 presents composites of DJF SSTA and winds one year prior to El Niño in (a) and La Niña in (b), using a ±0.5°C threshold in the DJF Niño-3.4 index. The composite differences between the two eras, which are not de-trended, emphasize the change in the preceding SSTA and winds from the earlier period to the most recent period. The bottom panel is the difference between the top (a) and middle (b) panels and demonstrates how the differences between El Niño and La Niña preconditions are changed in the recent era and, as expected, largely replicate the ENSO correlations shown in Figure 3b. Unlike the correlations in Figure 3, this composite stratification allows for an examination of how the precursor SSTs have changed for El Niño and for La Niña separately. Interestingly, a comparison between Figures 4a and 4b reveals that positive SST trends east of Taiwan/south of Japan are greater prior to La Niña whereas these positive trends are relatively muted prior to El Niño. On the equatorial Western Pacific, positive SST trends are stronger prior to El Niño (~160°E-180) relative to those prior to La Niña. The differences (Figure 4c) mirror the correlations (Figure 3b) with both depicting a SSTA dipole and strong curvature of the winds connecting the subtropical WNP to the equator. Thus, it appears SST trends prior to ENSO events have changed location with relatively greater amplitudes collocated with the positive anomalies in the WNP dipole. This sharpening of the positive SST anomalies appears to arise in a strengthened WNP-ENSO relationship in the interannual timescales. However, why the GHG-associated SST trends vary between El Niño and La Niña in a manner that more strongly amplifies the above-average regions of the WNP dipole is unclear.

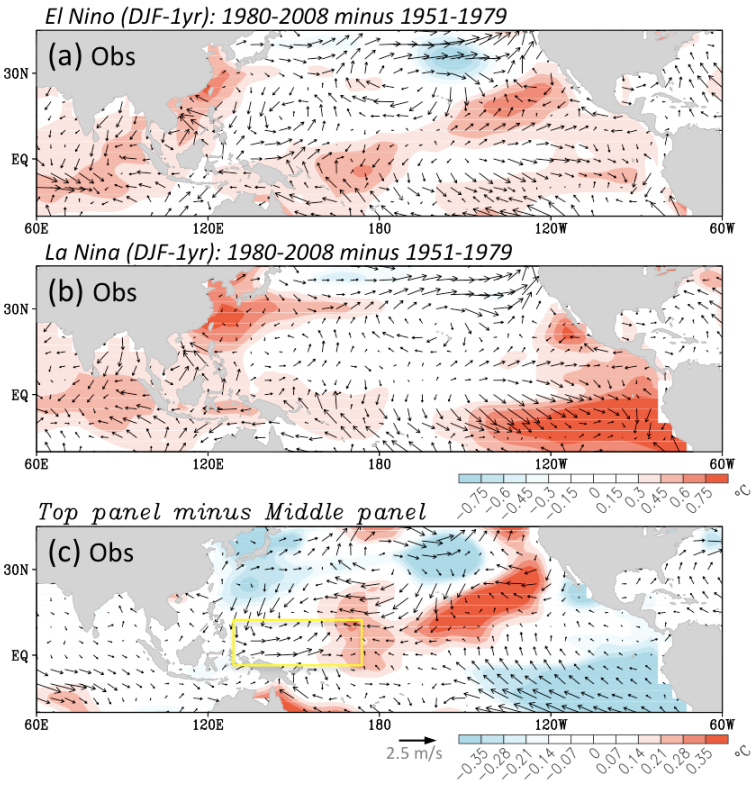

Fig. 4 Composite differences of SSTA (shading) and surface wind (vector) prior to (a) El Niño (DJF-1yr) and (b) La Niña (DJF-1yr) between the two eras of 1951-1979 and 1980-2008. (c) Differences between (a) and (b). The wind fields are averaged from 20CR and NCEP1 while the SSTA fields are averaged from HadlSST and ERSST.

4. Summary

While the WNP index is significantly correlated to the development of ENSO by the following winter, the analysis presented here further suggests that this relationship between the WNP and ENSO has significantly increased since the mid-20th century. The stronger WNP-ENSO association occurs on interannual timescales based upon de-trended data, so is not the direct result of the SST warming trends. CESM1 single forcing experiments suggest that the increased relationship is forced by increasing GHG in the atmosphere. The recent era is characterized by strengthening of the low-level wind anomalies in the equatorial western Pacific one year prior to ENSO, and an AMIP-style run implies this strengthening is due to shifts in the location of positive SST trends relative to El Niño or La Niña (one year previously). Prior to El Niño, the

region of positive SST trends occurs near the typical region of above-average SSTA in the western equatorial Pacific, whereas prior to La Niña, positive SST trends reinforce the above-average SSTA near southeastern Asia.

It is hypothesized that this shift in SST trends, which sharpens and amplifies the above-average SST region of the WNP dipole, arises in a strengthening WNP-ENSO relationship on interannual timescales. Analysis of the 350-year CESM1 preindustrial control simulation reveals that fluctuations in the leading North Pacific SSTA pattern of multi-decadal (30-year) variability mirror the variability in the correlations between the WNP and ENSO. While the control simulation only reflects coupled climate variability without external forcings, CESM1 suggests anthropogenic forcings, particularly GHG, have facilitated and even accelerated such a WNP-ENSO relationship. In recent decades, both the GHG-forcing experiment and the observations indicate unprecedented correlations closer to 0.7-0.9 between WNP and ENSO the following winter.

These results provide an important example of how lower frequency changes, like anthropogenic climate change, can directly impact intraseasonal-to-interannual climate variations. Provided that prediction tools can adequately capture the WNP-ENSO connection, if GHG are increasing the WNP-ENSO relationship then this may suggest potentially more skillful ENSO forecasts at one-year lead and increased confidence in seasonal predictions during the decades to come.

References

Alexander, M. A., D. J. Vimont, P. Chang, and J. D. Scott, 2010: The Impact of Extratropical Atmospheric Variability on ENSO: Testing the Seasonal Footprinting Mechanism Using Coupled Model Experiments. *J. Climate*, **23,** 2885-2901.

Bunge, L., and A. J. Clarke, 2009: A Verified Estimation of the El Niño Index Niño-3.4 since 1877. *J. Climate*, **22,** 3979-3992.

Deser, C., and Coauthors, 2011: ENSO and Pacific Decadal Variability in the Community Climate System Model Version 4. *J. Climate*, **25,** 2622-2651.

Guan, B., and S. Nigam, 2008: Pacific Sea Surface Temperatures in the Twentieth Century: An Evolution-Centric Analysis of Variability and Trend. *J. Climate*, **21,** 2790-2809.

Kalnay and Co-authors, 1996: The NCEP/NCAR 40-year reanalysis project. Bull. Amer. Meteor. Soc., 77, 437–470.

Kaplan, A., M. Cane, Y. Kushnir, A. Clement, M. Blumenthal, and B. Rajagopalan, 1998: Analyses of global sea surface temperature 1856-1991. *J. Geophys. Res*., **103,** 18567-18589.

L'Heureux, M. L., D. C. Collins, and Z.-Z. Hu, 2012: Linear trends in sea surface temperature of the tropical Pacific Ocean and implications for the El Nino-Southern Oscillation. *Clim. Dynamics***,** 1-14.

McPhaden, M. J., 2004: Evolution of the 2002/03 El Niño. *Bull. Amer. Meteor. Soc*., **85,** 677-695.

Rayner, N. A., and Coauthors, 2003: Global analyses of sea surface temperature, sea ice, and night marine air temperature since the late nineteenth century. *J. Geophys. Res*., **108,** 4407.

Roundy, P. E., and G. N. Kiladis, 2007: Analysis of a Reconstructed Oceanic Kelvin Wave Dynamic Height Dataset for the Period 1974‚Äì2005. *J. Climate*, **20,** 4341-4355.

Smith, T. M., R. W. Reynolds, T. C. Peterson, and J. Lawrimore, 2008: Improvements to NOAA's Historical Merged Land–Ocean Surface Temperature Analysis (1880–2006). *J. Climate*, **21,** 2283-2296.

Vimont, D. J., D. S. Battisti, and A. C. Hirst, 2003b: The Seasonal Footprinting Mechanism in the CSIRO General Circulation Models. *J. Climate*, **16,** 2653-2667.

Vimont, D. J., J. M. Wallace, and D. S. Battisti, 2003a: The Seasonal Footprinting Mechanism in the Pacific: Implications for ENSO. *J. Climate*, **16,** 2668-2675.

Wang, B. W., and S. A. An, 2002: A mechanism for decadal changes of ENSO behavior: roles of background wind changes. *Clim. Dynamics*, **18,** 475-486.

Wang, S.-Y., M. L'Heureux, and H.-H. Chia, 2012: ENSO prediction one year in advance using western North Pacific sea surface temperatures. *Geophys. Res. Lett.*, **39,** L05702.

Science and Technology Infusion Climate Bulletin
NOAA's National Weather Service
37th NOAA Annual Climate Diagnostics and Prediction Workshop
Fort Collins, CO, 22-25 October 2012

Weakened Interannual Variability in the Tropical Pacific Ocean Since 2000

Zeng-Zhen Hu[1], Arun Kumar[1], Hong-Li Ren[2,3], Hui Wang[1,4],
Michelle L'Heureux[1], and Fei-Fei Jin[2]

[1]*Climate Prediction Center, NCEP/NWS/NOAA, MD*
[2]*Department of Meteorology, the University of Hawaii, Honolulu, HI*
[3]*Laboratory for Climate Studies, National Climate Center, CMA, Beijing, China*
[4]*WYLE Science, Technology and Engineering Group, McLean, VA*

ABSTRACT

In this paper an interdecadal shift in the variability and mean state in the tropical Pacific Ocean is investigated in the context of changes in the El Niño–Southern Oscillation (ENSO). Compared with 1979-1999, the interannual variability in the tropical Pacific was significantly weaker in 2000-2011, and this shift can be seen as coherent changes in both the atmospheric and oceanic mean state and variability (Fig. 1). For example, the equatorial thermocline tilt became steeper during 2000-2011, which was consistent with positive (negative) sea surface temperature anomalies, increased (decreased) precipitation, and enhanced (suppressed) convection in the western (central and eastern) tropical Pacific, which reflected an intensification of the Walker circulation. We propose that the combination of a steeper thermocline slope with stronger surface trade winds has hampered the zonal migration of the warm water along the equatorial Pacific. As a consequence, the variability of the warm water volume was reduced and thus ENSO variability also decreased. Through Zebiak-Cane model experiments, it is preliminarily confirmed that both too large and too small thermocline slopes (and too strong and too weak wind stress) can potentially lead to the suppression in ENSO variability.

This work has been published in *Journal of Climate* in 2012.

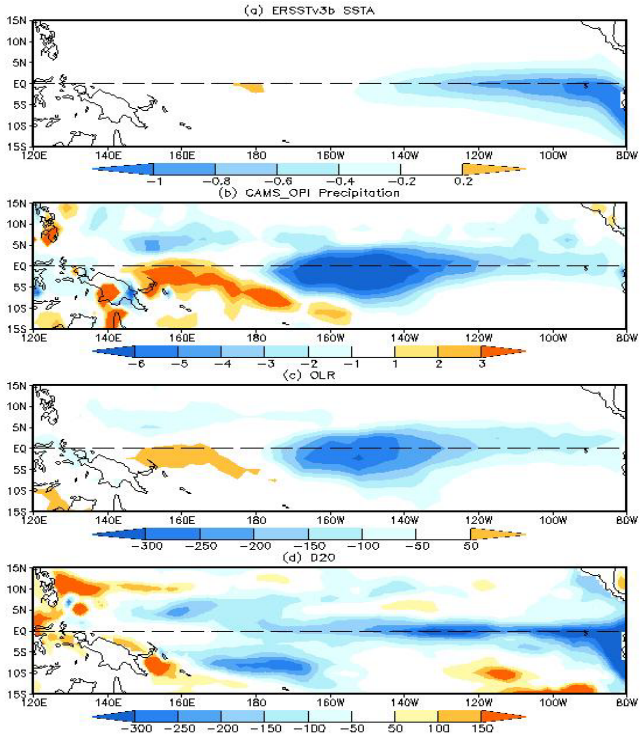

Fig. 1 Variance differences of (a) ERSSTv3b SST, (b) CAMS_OPI precipitation, (c) OLR, and (d) D20 between the means in Jan 2000-Dec 2011 and in Jan 1979-Dec 1999. The units are $(^oC)^2$ in (a), $(mm/day)^2$ in (b), $(W/m^2)^2$ in (c), and m^2 in (d).

Paper published

Hu, Z.-Z., A. Kumar, H.-L. Ren, H. Wang, M. L'Heureux, and F.-F. Jin, 2012: Weakened interannual variability in the tropical Pacific Ocean since 2000. *J. Climate* (online release; doi: http://dx.doi.org/10.1175/JCLI-D-12-00265.1).

Correspondence to: Zeng-Zhen Hu, Climate Prediction Center, NCEP/NWS/NOA, 5830 University Research Court, College Park, MD 20740-3818; E-mail: Zeng-Zhen.Hu@noaa.gov.

7. SETTING UP AN OPERATIONAL FRAMEWORK

Science and Technology Infusion Climate Bulletin
NOAA's National Weather Service
37th NOAA Annual Climate Diagnostics and Prediction Workshop
Fort Collins, CO, 22-25 October 2012

Web-Based Reanalysis Intercomparison Tools (WRIT) to Allow Easy Analysis and Comparison of Reanalyses and Other Datasets

Catherine A. Smith, Gilbert P. Compo, and Don K. Hooper

Cooperative Institute for Research in Environmental Sciences, University of Colorado, and NOAA/Earth System Research Laboratory, Boulder, Colorado

1. Motivation

There are currently at least 8 major reanalysis datasets available for scientists to study. Each dataset uses a different model, diferent observations and different assimilation algorithms. Comparing the reanalysis fields to each other and to observations may yield insights into climate processes. A host of issues make this difficult. The reanalysis data are available from different organizations, are stored in different formats with different file name architecture, have differing resolutions, file attributes, variable names, and units. Generally speaking, users have to download the data, convert it to a useable format, store it locally, change variable names, re-grid if needed, convert units and write code general enough that applications such as NCL, GrADS, IDL, or others can be used to read each dataset and compare the desired variables. Even if the dataset can be read via OPEnDAP or a similar remote protocol, most of this work is still needed. All of these tasks take time, effort and money. Our group at PSD has expertise both in storing and making reanalysis datasets available and in creating web-based climate analysis tools that have been widely used throughout the meteorological community. To overcome some of the obstacles in reanalysis inter-comparison, we have created a web-based reanalysis inter-comparison tool (WRIT), which allows users to easily plot and compare reanalysis datasets. Users may still want to download and analyze data but by using the page, they can test hypotheses and create basic plots to both narrow down scientific questions and have basic results. WRIT also facilitates the mission of the Reanalyses Intercomparison and Observations web-site (http://reanalyses.org) as a convenient toolkit for the study of these datasets.

2. Project overview

The reanalyses datasets we chose to make available now are the NCEP/NCAR Reanalysis I (Kalnay *et al.* 1996), NCEP/DOE Reanalysis 2 (Kanamitsu *et al.* 2002), ECMWF Interim Reanalysis (Dee *et al.* 2011), NASA Modern Era Reanalysis for Research and Applications (MERRA) (Rienecker *et al.* 2011), NCEP Climate Forecast System Reanalysis (CFSR) (Saha *et al.* 2010), and the NOAA-CIRES 20th Century Reanalysis V2 (20CR) (Compo *et al.* 2011) with more to be added later. Basic attributes are given in Table 1. The earliest reanalysis starts in 1871 and some are available near present. We have these pressure level variables: geopotential height, zonal and meridional winds, omega, air temperature, relative humidity and specific humidity. Each dataset outputs on different pressure levels but they generally start at 1000mb and go up as high as 1mb. We have a common set of levels available for all datasets that we use when making cross-

Reanalysis	Year Range at PSD	Levels/Output Resolution at PSD*
NCEP/NCAR R1	1948-present	17/2.5x2.5
NCEP/DOE R2	1979-Jun 2012	17/2.5x2.5
MERRA	1979-2012	31/1.25x1.25
20th Century	1871-2010	24/2.0x2.0
ERA Interim	1979-2011	30/1.5x1.5
NCEP CFSR	1979-Mar 2011	37/2.5x2.5

Table 1 Characteristics of the Reanalysis datasets as stored at NOAA/ESRL PSD.

Correspondence to: Catherine A. Smith, Cooperative Institute for Research in Environmental Sciences, University of Colorado, and NOAA/Earth System Research Laboratory, Boulder, Colorado; E-mail: cathy.smith@noaa.gov.

section comparisons. Single level variables include 2m air temperature, 10m zonal and meridional winds, sea level pressure and precipitation rate. For comparison with observations, we also have available the U of Delaware V3.01 (Willmott and Matsuura 1995) land air temperature and precipitation dataset, NOAA's GHCN_CAMS air temperature (Fan and van den Dool 2008), NOAA/NASA global precipitation analysis (GPCP) (Adler *et al.* 2003), Climatic Research Unit (CRU) air temperature (Mitchell and Jones 2005) and the NOAA precipitation analyses (Chen *et al.* 2002) over land. These datasets can be directly compared with 2m air temperature and precipitation from reanalyses. Comments and suggestions can be made at reanalysis.org. Additionally, user plots can be posted there.

Initially, we have developed three web tools. These are available from the URL http://esrl.noaa.gov.psd/writ/ and include

1. Monthly/Seasonal plotting page: Plots composites and differences from the datasets including maps and vertical cross-sections
2. Monthly Timeseries:
3. Trajectory Plotting Tool:

We plan to add more tools later including shorter time-scales and more analyses types.

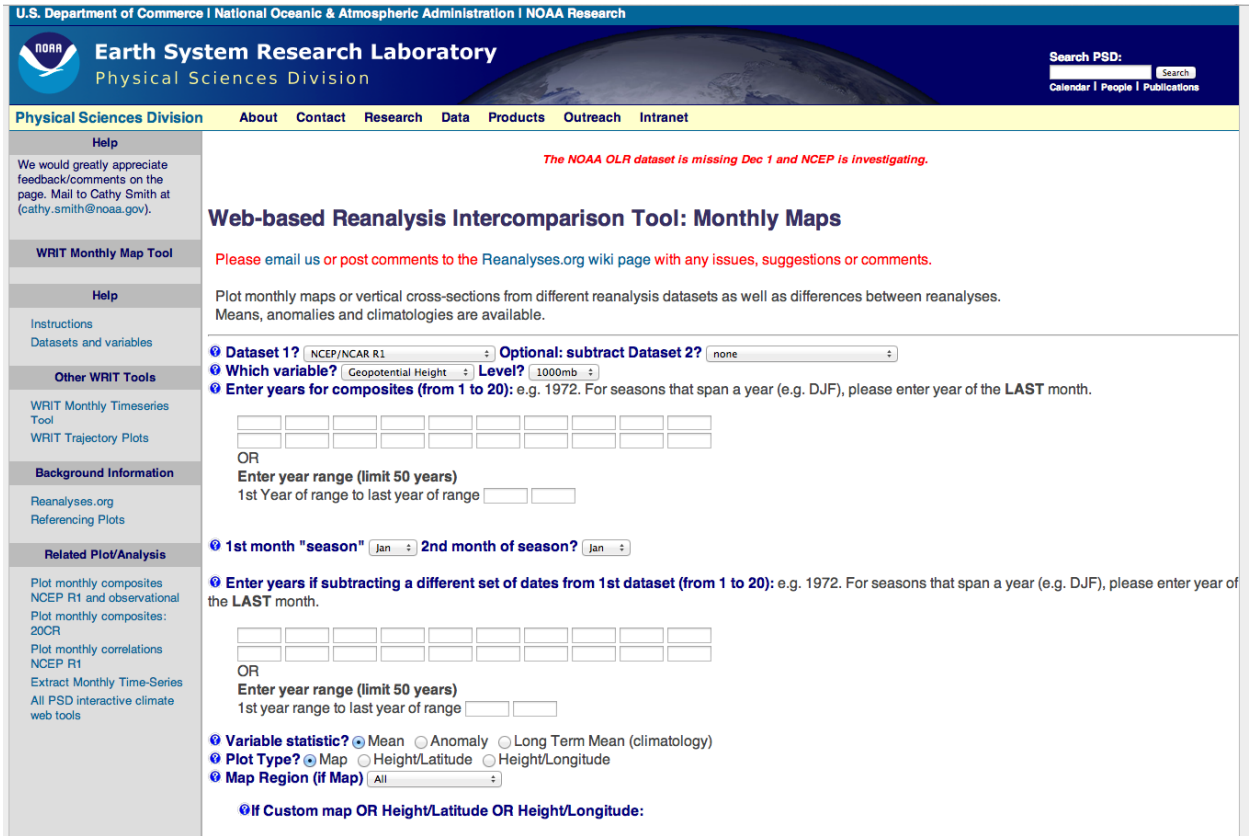

Fig. 1 Web Page Interface for Monthly Map Page showing user options.

3. Code development

The web tools are coded similarly. All use HTML web forms that have all necessary options available. The form variables are sent to a Perl program that reads in and validates the options. The Perl program also returns the locations of the data files needed from each dataset. They also create the temporary files needed for the web and pass along the variables needed for analysis and for plotting. We use NCL for both the monthly plotting and the time-series pages. NCL reads in files easily and has many built-in routines for meteorological processing (such as creating climatologies or calculating area averages). The code performs

the necessary analysis. This includes taking into account the differing grids and grid resolutions, attributes, levels, etc. When necessary, plots or cross-sections are interpolated to the same grid, converting from low to higher resolution. The Perl routine processes the results from the NCL script and also generates KML/Google Earth for the monthly plotting page.

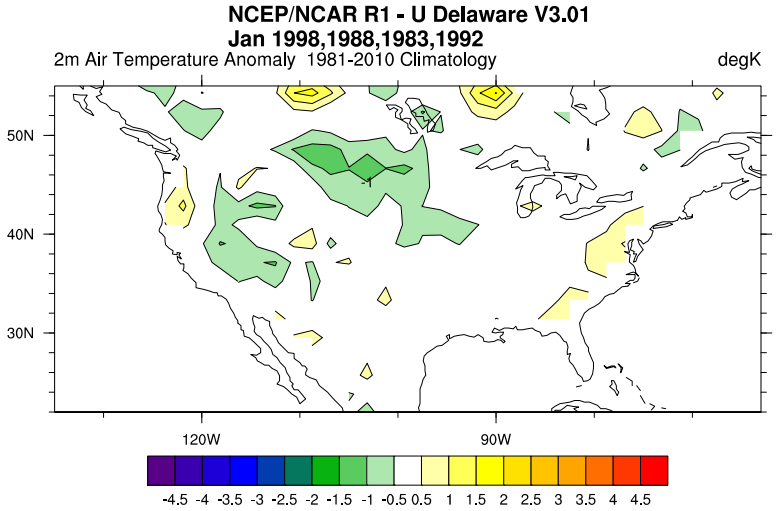

Fig. 2 Difference between the NCEP/NCAR R1 and the U of Delaware 2m air temperatures for January El Niño composite.

4. Features highlight

a) First page: Monthly Plotting Page

The interface, shown in Fig. 1, allows users to select one or two datasets, the level(s), the type of plot (map, latitude/height or longitude/height), the statistic (mean, anomaly, long term mean) and plotting options. They can also select a season and one or more years (for example, creating an El Nino composite). If two datasets are chosen, each grid or cross-section is calculated and then the resulting output differenced. Results are returned as images, NetCDF files and KML. Shown in Fig. 2 is a map of the difference between the NCEP/NCAR R1 and the U of Delaware 2m air temperatures for composite wintertime El Niño's. Fig. 3 shows the difference between zonally averaged winds for the 20CR dataset for 1970-1979 compared to 1990-1999.

b) Second page: Time Series Differences

The interface for this page (not shown) is similar to the one used in the mapping page. The reanalysis datasets are the same as the mapping page but has just one observed dataset (more will be added). Selections include dataset, one or two variables/levels, area for 1st dataset, area for 2nd dataset, season, type of statistic and type of output plot. The types include two timeseries plots (same or different axis), difference of two timeseries, scatter plots, auto or cross correlation and distribution. Statistics from each plot (mean, median, standard deviation) are returned. Also returned is the correlation between two timeseries and the actual grid bounds used in each dataset (as grids differ for the different reanalyses). Shown in Fig. 4 is the difference of precipitation in the eastern tropical Pacific (4ºN-4ºS, 120ºE-160ºE) between the NCEP/NCAR R1 and the GPCP V2 dataset. Fig. 5 shows a scatter plot of 20CR vs. ERA-Interim zonally averaged 2 m air temperature south of 70ºS.

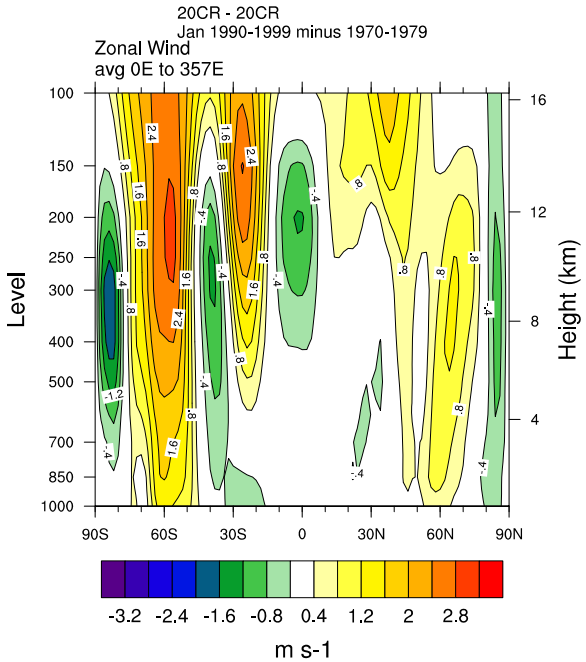

Fig. 3 Plot produced from the WRIT Monthly Mapping Page, showing the cross-section of January zonal mean of zonal wind difference between 1970-1979 and 1990-1999 for the 20CR.

c) Third page: Trajectory Tool

Finally, we have created a trajectory plotting tool that uses the three different reanalysis datasets in which we have 4-times daily data available: NCEP/NCAR R1, NCEP/DOE R2 and the 20CR. Users can select a start/end time, an initial level and location and plot the trajectory based on the 3-D winds from the reanalyses. The trajectory

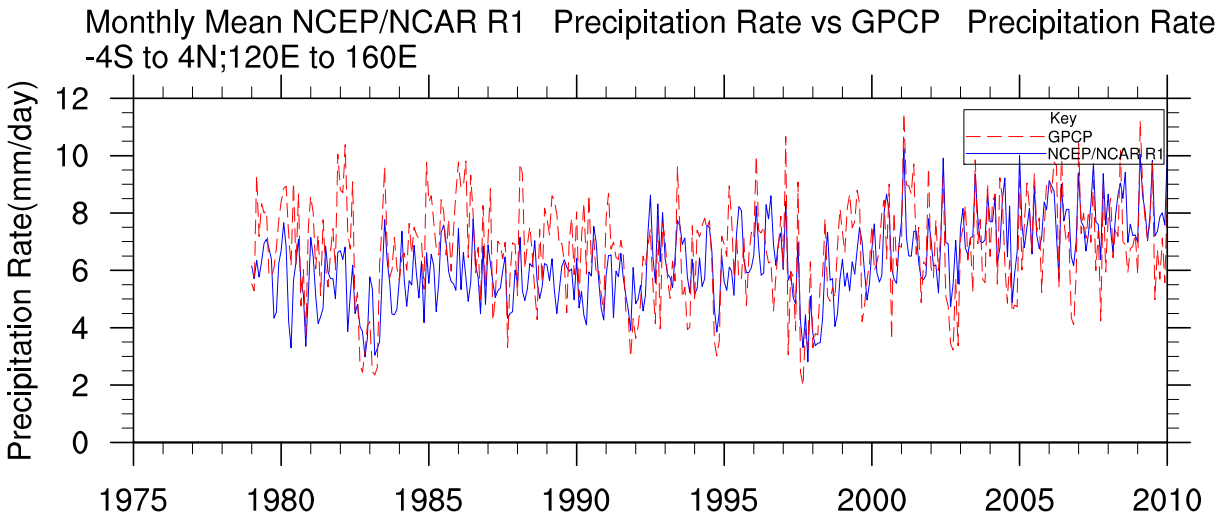

Fig. 4 Plot is produced from the WRIT Time-Series Page, showing a comparison between the NCEP/NCAR R1 precipitation and that of the GPCP observational dataset over the eastern Tropical Pacific.

can be forward or backward. The trajectory code was obtained from the U of Australia in Melbourne courtesy of Ian Simmonds. It is based on 3-D advective model that is solved using a 4th order Runge-Kutta scheme. The trajectory is calculated using a time step of 1 hour and the results plotted on a map and are available as KML and in a Google Earth Web plugin. Plotted in Fig. 6 is a trajectory for the 20CR dataset for wintertime (October 28 1991; the so-called "Perfect storm") for the starting location 48ºN; 310ºE. Also plotted is the pressure level at each trajectory point. Users can download the NetCDF files containing the trajectory points.

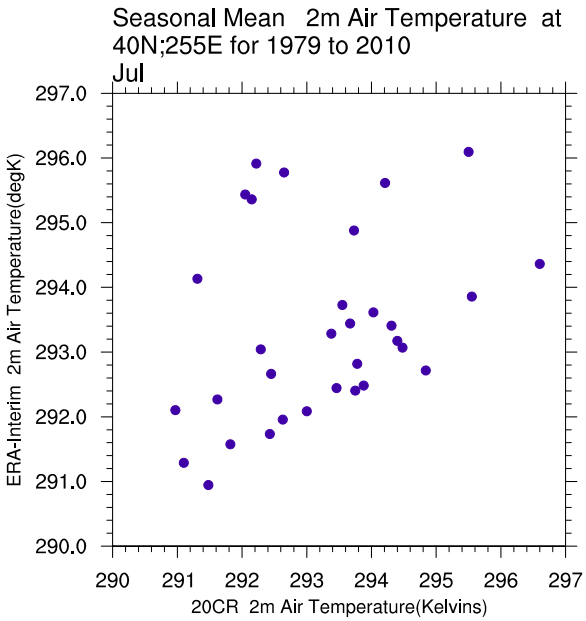

Fig. 5 Scatter plot produced from the WRIT Monthly Time-Series Webpage showing 2m air temperature for July over Boulder, CO (40ºN; 255ºE) for the 20CR dataset vs. the ERA-Interim dataset.

5. Summary/discussions and future works

a) More features

We plan to add more observational datasets to the mapping and time series webpage. We also hope to add one or more reanalyses datasets to the trajectory tool. Features we plan to add to the mapping page include more observational datasets, the ability to obtain dates to composite with from a user supplied date file or from a climate index (*e.g.* highest PNA months). For time series, we will add climate indices as well as user files input via FTP. We may also look at fitting distributions. We may add additional plots such as whisker plots. Users can leave comments and suggestions at http://reanalyses.org/atmosphere/web-based-reanalysis-intercomparison-tools-writ

b) Other issues

We started the project by attempting to use files via OPEnDAP. While we have many datasets at PSD, we cannot store all of them as we hoped that by being able to access datasets remotely, we could make available more datasets and variables. This was only partially successful. While we could read our own data via OPEnDAP easily, other datasets took too long depending on how their server was set up. In addition, we

had to rely on the metadata supplied at the source. In some cases the metadata was lacking, hard to use and/or in error. The metadata issues are likely addressable but access time remains an unresolved issue.

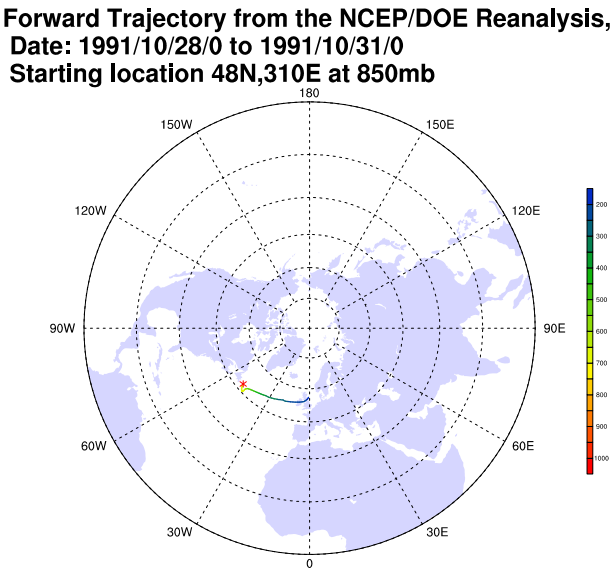

Fig. 6 Trajectory plot made from the WRIT Trajectory Webpage showing the forward trajectory of a point started at 850mb, 48ºN, 210ºE on 0Z Oct 28 1991 using the NCEP/DOE Reanalysis 2 dataset.

References

Adler, R.F., G.J. Huffman, A. Chang, R. Ferraro, P. Xie, J. Janowiak, B. Rudolf, U. Schneider, S. Curtis, D. Bolvin, A. Gruber, J. Susskind, and P. Arkin, 2003: The Version 2 Global Precipitation Climatology Project (GPCP) Monthly Precipitation Analysis (1979-Present). *J. Hydrometeor*., **4**, 1147-1167.

Chen, M., P. Xie, J. E. Janowiak, and P. A. Arkin, 2002: Global Land Precipitation: A 50-yr Monthly Analysis Based on Gauge Observations. *J. of Hydrometeor*., **3**, 249-266.

Compo, G.P., J.S. Whitaker, P.D. Sardeshmukh, N. Matsui, R.J. Allan, X. Yin, B.E. Gleason, R.S. Vose, G. Rutledge, P. Bessemoulin, S. Brönnimann, M. Brunet, R.I. Crouthamel, A.N. Grant, P.Y. Groisman, P.D. Jones, M. Kruk, A.C. Kruger, G.J. Marshall, M. Maugeri, H.Y. Mok, Ø. Nordli, T.F. Ross, R.M. Trigo, X.L. Wang, S.D. Woodruff, and S.J. Worley, 2011: The Twentieth Century Reanalysis Project. *Quart. J. Roy. Meteorol. Soc*., **137,** 1-28. doi: 10.1002/qj.776

Dee, D. P., and Co-authors, 2011: The ERA-Interim reanalysis: Configuration and performance of the data assimilation system. *Quart. J. Roy. Meteorol. Soc*., **137**, 553-597. doi 10.1002/qj.828.

Fan, Y., and H. van den Dool, 2008: A global monthly land surface air temperature analysis for 1948-present. *J. Geophys. Res*., **113**, D01103, doi:10.1029/2007JD008470.

Kalnay, E., and Co-authors, 1996: The NCEP/NCAR 40-year reanalysis project. *Bull. Amer. Meteor. Soc*., **77**, 437-470.

Kanamitsu, M., W. Ebisuzaki, J. Woollen, S.-K. Yang, J. J. Hnilo, M. Fiorino, and G. L. Potter, 2002: NCEP–DOE AMIP-II Reanalysis (R-2). *Bull. Amer. Meteor. Soc*., **83**, 1631–1643. doi:10.1175/BAMS-83-11-1631.

Mitchell, T.D., and P.D. Jones, 2005: An improved method of constructing a database of monthly climate observations and associated high-resolution grids. *Int. J. Climatol.*, **25**, 693-712. doi: 10.1002/joc.1181.

Rienecker, M.M., and Co-authors, 2011: MERRA - NASA's Modern-Era Retrospective Analysis for Research and Applications. *J. Climate*, **24**, 3624-3648. doi: 10.1175/JCLI-D-11-00015.1.

Saha, S., and Coauthors, 2010: The NCEP Climate Forecast System Reanalysis. *Bull. Amer. Meteor. Soc.*, **91**, 1015–1057. doi: 10.1175/2010BAMS3001.1 .

Willmott, C. J. and K. Matsuura, 1995: Smart interpolation of annually averaged air temperature in the United States. *J. Appl. Meteor*., **34**, 2577-2586.

Science and Technology Infusion Climate Bulletin
NOAA's National Weather Service
37th NOAA Annual Climate Diagnostics and Prediction Workshop
Fort Collins, CO, 22-25 October 2012

Enhancement of Local Climate Analysis Tool (LCAT) to Better Serve NWS Staff and Users

Marina Timofeyeva, Fiona Horsfall, Annette Hollingshead, and Jenna Meyers

Climate Service Division, OCWWS/NWS/NOAA, MD

Understanding and provision of integrated environmental information is one of the top priorities in the new Weather-Ready Nation strategy recently introduced by the National Weather Service (NWS) at the US National Oceanic and Atmospheric Administration (NOAA). The ability to identify and predict local climate impacts on weather and water is critical because most climate-sensitive decisions occur at the local level such as cities, counties and states.

Climate serves as a driving force in the frequency of extreme weather and water events. Public warnings on the occurrence of climate events and their possible impacts, such as fresh water shortages in the Pacific Islands during El Niño events, provide actionable information to help build communities' resilience to weather and water elements. Efficient local service is a key component for the effective dissemination of climate information. The NWS is presently working towards developing a local climate analysis tool (LCAT) to enable office staff and technical users to access, manipulate, and interpret climate data, and characterize climate variability and change linkages to weather and water elements.

To ensure the relevance of the tool to end users, the LCAT Integrated Working Team identifies requirements and sets priorities for development. LCAT's capabilities are being developed to respond to the needs of NOAA staff providing operational climate services, as well as those of external technical users making climate-sensitive decisions. External technical user groups include:

- Natural resource managers (such as hydrologists, planning and operational engineers of water reservoirs and energy turbines using water, nuclear, wind, and solar sources of power generation)
- Wildlife managers including fisheries, national parks, and marine sanctuaries
- Researchers working on climate information applications for national security including agriculture, environment, transportation and military matters.

The LCAT Integrated Working Team is using different ways to identify requirements, including literature surveys, reviews of user logs maintained by NWS local offices, and direct engagement with users, such as through the Annual Climate Prediction Application Science Workshop[1].

The enabling role of LCAT

LCAT is an online interactive tool that will enable local users to conduct regional and local climate studies using state-of-the-art station and reanalysis gridded data and various statistical techniques. LCAT uses the principles of artificial intelligence to respond to queries, in particular, through use of machine technology that responds intelligently to input from users (Figure 1). The user translates customer questions into primary variables and issues, and LCAT pulls the most relevant data and analysis techniques to provide information back to the user, who in turn responds to their customer. Most responses take on the order of 10 seconds, which includes providing statistics, graphical displays of information, and translations for users, metadata, and a summary of the user request to LCAT. The results are used to provide services to guide local decision makers in weather- and climate- sensitive actions and to deliver information to the general public. LCAT

[1] http://www.nws.noaa.gov/om/csd/index.php?section=meetings

Correspondence to: Marina Timofeyeva, Climate Service Division, OCWWS/NWS/NOAA,, 1325 East West Highway, Silver Spring, MD 2091; E-mail: marina.timofeyeva@noaa.gov.

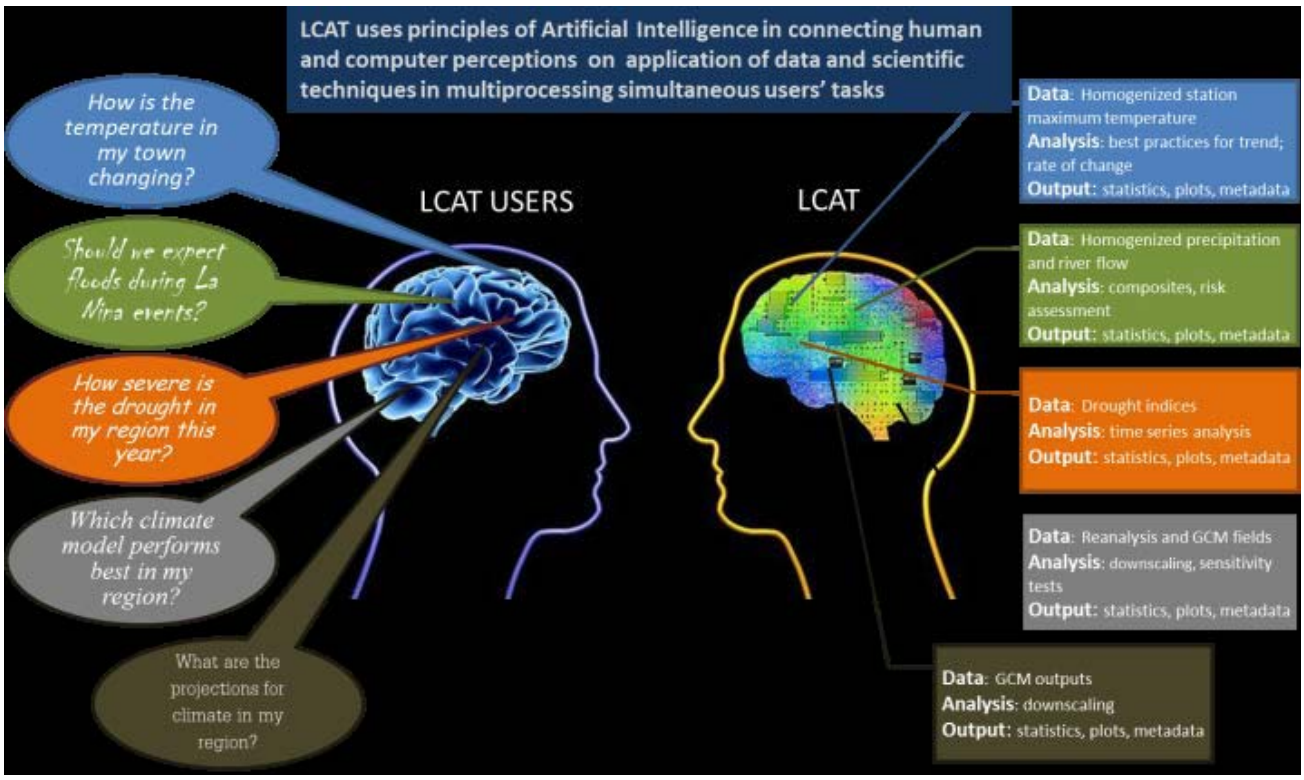

Fig. 1 LCAT mimics human abilities to listen, think, reach out for information, and respond multiple users' inquiries at the same time.

augments current climate reference materials with relevant regional and local information. Its main emphasis is to enable studies of extreme meteorological and hydrological events such as tornadoes, floods, droughts and severe storms. LCAT will close a very critical gap in NWS local climate services because it provides analysis of climate variables beyond average temperature and total precipitation. NWS external partners and government agencies will benefit by incorporating LCAT's output easily into their own analysis and delivery systems.

Present and near-term capabilities

NWS has identified five existing requirements for local climate information:

- Local impacts of climate change (Figure 2)
- Local impacts of climate variability
- Drought severity studies
- Climate studies for water resources
- Diagnostics of extreme meteorological and hydrological events.

The methodologies for the first four requirements have been included in LCAT phase one implementation.

The local rate of climate change is defined as a slope of the mean trend estimated from the ensemble of three trend techniques: hinge, optimal climate normals (running mean for optimal time periods), and the exponentially-weighted moving average (Figure 2).

Root mean squared error is used to determine the best trend fit to observations with the least error. Analysis of ensemble information allows assessment of mean climatological data and uncertainty due to the trend fitting techniques.

Studies of the impacts of climate variability on local extremes use compositing techniques applied to various definitions of local variables, from specified percentiles to critical thresholds. Drought studies combine the visual capabilities of Google maps with statistical estimates of drought severity indices.

Climate studies for water resources applications include:

- Current and expected maps of water resources (Figure 3)
- Site-speci5fic, interactive information on forecast ensemble distribution for water resources and their expected evolution
- Historical analogues of present and expected river flow
- The relationship between water parameters and climate variability indices

NWS is leveraging internal and external NOAA partnerships to develop methodologies for the requirement on the attribution of extreme meteorological and hydrological events. This section of LCAT will include references to explain the climatological drivers for extreme events such as the 2010 heat wave and drought in Russia, the 2011 Missouri River flood and the unusually warm March in the eastern USA in 2012.

The near-term development plan includes the incorporation of various climate variability indices such as North Atlantic, Arctic, Madden Julian, Pacific Decadal and other oscillations with documented impacts of weather and water parameters. In addition, LCAT will have access to NOAA's severe weather data sets, which will enable climatological and impact studies of frequencies in tornados (Figure 4), floods, snowstorms, heat waves,

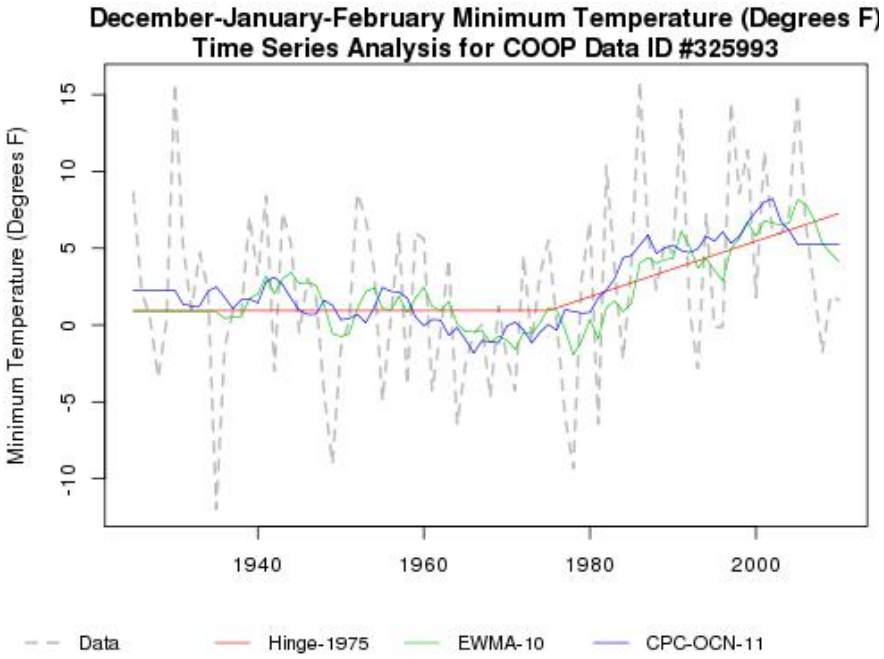

Fig. 2 LCAT options for climate change local studies include fitting different trends to the local climate time series, computation of rate of change (1.7^0C per 30-year period), and de-trended time series for further studies of climate variability impacts.

Fig. 3 LCAT section on Climate Studies for Water Resources Applications is currently developing as a stand-alone feature with future incorporation into LCAT framework.

lightning and other extreme events. For example, a pilot study analyzed the relationship between tornados and El Niño Southern Oscillation (ENSO) events, helping to identify areas with significant tornados and an enhanced number of tornado days during La Niña events in the central USA region. The plan also includes developing numerous options for user-defined climate analysis, such as tuning to strong climate events using multiple indices of climate variability and critical percentiles of data distributions.

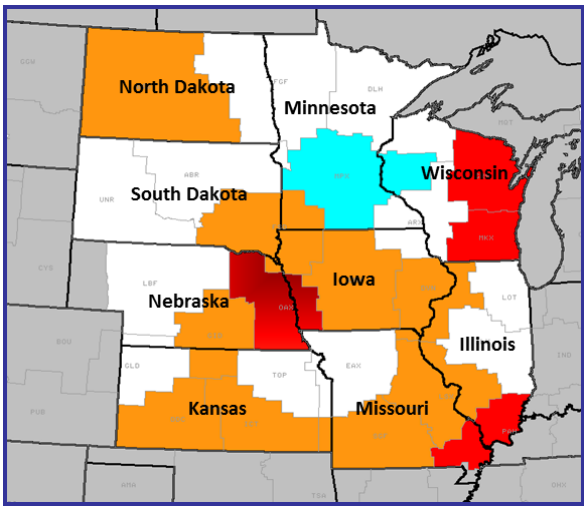

Fig. 4 Results of a pilot study helps to identify areas with significant tornados and enhanced numbers of tornado days during La Niña events in the central U.S. Orange polygon is the area with enhanced significant tornados; cyan – area with diminished significant tornados; red – area with enhanced number of tornado days.

Future goals and applications

Future plans for LCAT include building the capability to extend it to existing data visualization tools and adding options for three-dimensional and multiple-site graphical capabilities. Additionally, LCAT will be developed for climate studies in key environmental and economic sectors. For example, to support marine sanctuaries and coastal systems, LCAT will have access to NOAA global sea level, tidal and coastal surges monitoring data, which will enable climate studies at specific harbors or marsh habitats. To support renewable energy decisions, LCAT will use global surface observation, satellite and reanalysis wind, cloud cover, and solar insulation data to allow the analysis of local climatology at different heights of the atmosphere anywhere on Earth. Extension to reanalysis data will enhance LCAT global applications and enable the potential use of data from Global Circulation Models for model inter-comparison on regional scales. The LCAT development plan also includes potential access to demographic and biological data to help with holistic environmental climatological analysis.

User engagement

LCAT was beta tested by approximately 40 NOAA staff, who were eager to start local climate studies. Several training events took place to engage beta testers:

• Live webinars were recorded and provided to users for further reference

• A training workshop was held, that included instructions on using LCAT, information on data and methods used for analyses, practice sessions, and discussions to collect user feedback

• Fact sheets were developed describing LCAT capabilities

Feedback from beta testers identified new requirements to be added to the tool prior to operational implementation for internal use by NOAA. LCAT's application for NOAA's external use requires the engagement of users and integration of new requirements. LCAT's development is an iterative process of user engagement that includes identifying user needs, formulating requirements, and setting priorities; coordinating with subject matter experts on best practices for use of appropriate data and scientific methods to respond to these needs; building and testing new LCAT capabilities; training, and user feedback.

This continuous development will ensure that LCAT provides the analysis tools and capabilities to meet the needs of a wide range of stakeholders, enabling the interpretation and dissemination of climate data to support climate-sensitive decisions.

Science and Technology Infusion Climate Bulletin
NOAA's National Weather Service
37th NOAA Annual Climate Diagnostics and Prediction Workshop
Fort Collins, CO, 22-25 October 2012

Weather and Climate Analyses Using the New NVAP-MEaSUREs Global Water Vapor Dataset

Thomas H. Vonder Haar[1,2], Janice L. Bytheway[1,3], and John M. Forsythe[1,2]

[1] *Science and Technology Corporation, METSAT Division, Fort Collins, CO*
[2] *Cooperative Institute for Research in the Atmosphere (CIRA), Fort Collins, CO*
[3] *Department of Atmospheric Science, Colorado State University, Fort Collins, CO*

ABSTRACT

The NASA Water Vapor Project (NVAP) dataset is a global (land and ocean) water vapor dataset created by merging multiple sources of observed atmospheric water vapor to form a global data base of total and layered precipitable water vapor. Under the NASA Making Earth Science Data Records for Research Environments (MEaSUREs) program, NVAP has been reprocessed and extended. The NVAP-MEaSUREs (NVAP-M) dataset features multiple production streams geared towards varied user needs, and biases in the original dataset caused by algorithm and input changes were removed by relying on peer reviewed algorithms and inputs. This extension increases NVAP's 14-year coverage to include 22 years (1988-2009) of data. The resulting data set provides new information on the seasonal and interannual variability of water vapor at both global and regional scales (Fig. 1). The availability of both total and layered precipitable water also allows for the study of water vapor at various levels of the atmosphere. NVAP-M continues the NVAP legacy wide-ranging uses, from studies of weather features, regional circulations, to assimilation into and validation of climate models.

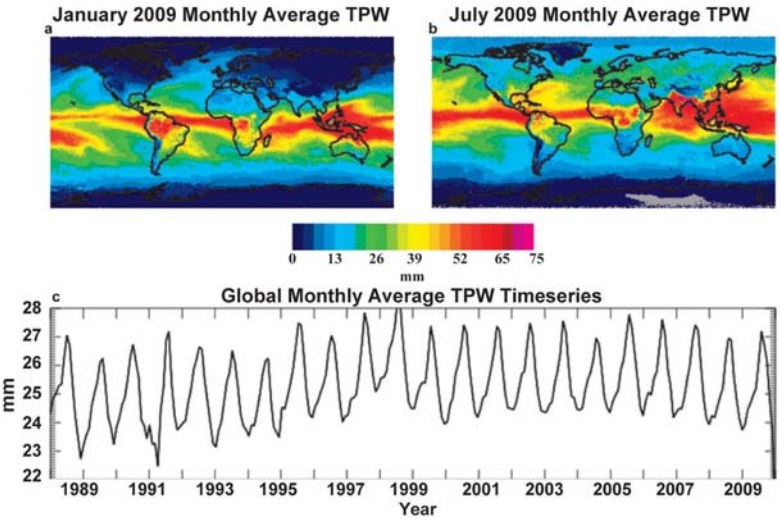

Fig. 1 Seasonal and interannual variability from NVAP-M Climate: monthly average total precipitable water (TPW) for (a) January and (b) July2009. (c) The time series of global monthly average TPW.

This work has been published in *Geophysical Research Letters* in 2012.

Paper published

Vonder Haar, T. H., J. L. Bytheway, and J. M. Forsythe, 2012: Weather and climate analyses using improved global water vapor observations. *Geophysical Research Letters*, **39**, L15802, doi:10.1029/2012GL052094.

Correspondence to: John M. Forsythe, Science and Technology Corporation, METSAT Division, 4033 Buckskin Trail, Laporte, CO 80535. E-mail: John.Forsythe@colostate.edu .

APPENDIX

Commentary

The New Normal

Kevin E. Trenberth
Chair, GEWEX Scientific Steering Group

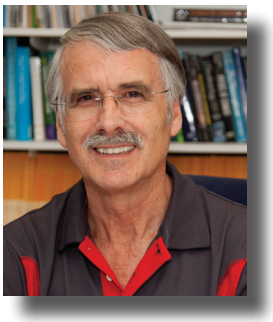

The answers I frequently get to the question "What is climate?" are commonly along the lines of "the average weather" or "climate is what we expect and weather is what we get." Firstly, those are statistical statements, and secondly, an average is obviously dependent upon the time of the average. If it is a very "long-term" average to avoid interannual variability, then by definition there is no climate change. This conundrum was recognized back in the 1970s when it was proposed that we speak about "climate states." This perhaps relates to what is now commonly known as a "base period." The classic base period is a 30-year period (as defined by the World Meteorological Organization) that traditionally gets updated. Hence we went from the 1961–1990 normal to the 1971-2000 normal, and now 1981–2010 is the "New Normal."

For the U.S., the new normal is about 0.3°C warmer than the previous normal in minimum temperature and 0.1°C for maximum temperature overall. Globally, the new normal for sea-surface temperatures (SSTs) is over 0.3°C warmer in many places, although some regions have cooled. We must remember that the new normal vs. the old is actually the 2000s minus the 1970s divided by three. So, an overall change of about 0.2°C is actually a warming between those decades of 0.6°C.

Too little attention has been paid to the fact that the normals are now changing a lot (i.e., climate change is happening). When we speak about how anomalous the recent climate has been, we often fail to factor in the differences associated with the new normal. This clearly colors perceptions about the degree to which things are indeed anomalous or abnormal.

Given all of these considerations, how then can we talk about climate change in a more enlightened way? We have "climate dynamics" as a growing field, and the climate is indeed continually varying and changing. Therefore, I suggest that simply using statistics is not good enough. Instead I suggest that we think about and define climate in a different way, and we do this from a physical standpoint.

"Weather" happens in the atmosphere. Most of it is internal to the atmosphere and arises from instabilities, whether it is convective instability that gives rise to clouds and thunderstorms, or baroclinic instability that leads to major cyclones and anticyclones, cold and warm fronts, and all the associated day-to-day weather.

"Climate" happens when the atmosphere interacts non-trivially with the rest of the climate system and externalities. The climate system consists not just of the atmosphere, but also the oceans, land, land-surface water, and cryosphere. The externalities include the orbit of the Earth around the sun, changes in the sun, changes in the Earth (e.g., continental drift), changes in the composition of the atmosphere, and anthropogenic effects. The diurnal cycle is a climate phenomenon and so is the annual cycle of the seasons. The El Niño–Southern Oscillation (ENSO) is a climate phenomenon as it is inherently a coupled phenomenon.

The atmosphere is always being conditioned by climate influences. Hurricanes are treated as a weather phenomenon, but it is increasingly clear that the cold wake churned up behind a hurricane through strong winds, causing mixing and huge surface fluxes that produce evaporative cooling of the ocean, play a vital role in the hurricane's subsequent development and track. Therefore, is a hurricane really a climate phenomenon or a weather phenomenon? What about the Madden-Julian Oscillation?

All storms interact with the Earth's surface, but for years we have run atmospheric models with specified fixed SSTs for numerical weather prediction (NWP). This means that we are indeed dealing with weather. However, increasingly the evidence suggests that this is actually a limitation in NWP and that having the SSTs respond and feed back into weather systems is essential, especially for second week weather forecasts and those beyond.

Issues of Attribution and How We Talk about It

All too often we hear meteorologists say, "it was due to the jet stream," "it was a thunderstorm that stalled," "it was the blocking anticyclone," or "it was tropical storm Irene," and so on. The explanation is given in terms of the weather phenomenon. That is, in fact, not an explanation or attribution at all! Instead, it is a description of the other aspects of the event: a more complete description of the phenomenon. The flood was due to the storm and the drought was due to the blocking anticyclone, etc.

As an explanation, the question should be, "why did that weather phenomenon behave the way it did?" In particular, what influences external to the atmosphere were playing a role and what climate factors were in play? Why did the blocking anticyclone last as long as it did and why was it so intense? Why was there enough rain in this weather system to cause flooding? As soon as we ask these different kinds of questions, we can talk sensibly about attribution and causes through the external influences on the weather. The main cause we can point to is almost always anomalous SSTs and the predominant influence of ENSO on anomalous weather patterns.

For example, we can say that the reason we had "snowmaggedon" in Washington, DC in 2010 is: (1) we had winter and there was plenty of cold continental air; (2) there was a storm in the right place; and (3) the unusually high SSTs in the tropical Atlantic Ocean (1.5°C above normal) led to an exceptional

amount of moisture flowing into the storm, which resulted in very large snow amounts. It is this last part that then relates to anomalous external influences on the atmosphere.

Human Effects on Climate and Weather

Without doubt, the SSTs in the Atlantic Ocean were warmer by about 0.5°C due to human influences, and so by itself that led to a 4 percent increase in moisture flowing into the storm. There is a lot of natural variability, and the Atlantic Multi-decadal Oscillation and other things are in play, at times adding to and at times subtracting from the human component. Human-induced climate change occurs on long timescales, and 20 years is a reasonable estimate for noticeable significant changes. Once we realize that, it becomes clear that the proper way to think about this is that there is an underlying new normal of a warmer background that the shorter-term variability is superposed upon. Of course, this is linear thinking and some effects are clearly nonlinear, but it works quite well and clears the mind on how to talk about and think of human influcences.

How big is the human component? The natural flow of energy through the climate system is equivalent to about 240 Wm^{-2}. The carbon dioxide radiative forcing is about 1.6, greenhouse gas forcing is about three, and net forcing with aerosols is about 1.6 Wm^{-2}. Water vapor feedback roughly doubles that, so the net value is 1–2 percent of the natural flow. Of course the system has responded and the water vapor feedback is part of that response, so that the net imbalance in energy at the top of the atmosphere is closer to 1 Wm^{-2} or less than 1 percent. It is small on a day-to-day basis and negligible, but it is always in one direction. It builds up in time and accumulates; hence the main effect on climate and weather is not the instantaneous effect but the changed environment in which all weather systems are operating in the "new normal." In particular, the main memory is in the oceans, and the oceans have warmed by 0.5°C since the 1970s and the atmosphere above the oceans is warmer and moister as a result. On average the water vapor has increased by 4 percent since the 1970s over the oceans.

Since all storms reach out about four times the radius of their precipitating area to grab moisture and bring it into the storm, most storms are influenced by ocean changes. The storms are bigger in winter and a storm dumping snow in the Ohio River valley is bringing in moisture from 3500 km away from the Gulf of Mexico and the subtropical Atlantic. In summer the storms are smaller and there is greater dependence on land moisture and recycling.

What does the science community say? "You can't blame a single event on climate change." As a result the media loses interest and the public immediately turns off. What nonsense! When we break records like we did in 2012 in the U.S., at a rate of nine hot records to one cold one for the first 6 months, it is a clear signal of climate change. Just because we zoom in on one of those records or events doesn't make it otherwise. The odds are that most of these records would not have occurred without climate change! It won't be the same this year, but the odds are that similar events will occur somewhere (currently it seems in Australia). We are experiencing climate change in action.

We can talk about it in terms of changing odds, as many others have done. The odds have increased for these kinds of extremes to occur. But we can also talk about it in physical terms. In particular, we have a new normal! The environment in which all weather events occur is different than it used to be. All storms, without exception, are different. Even if 95 percent of them look just like the ones we used to have, they are not the same.

In that respect, another way of looking at it is to regard the new normal as a shift in the seasons. The amplitude of the annual cycle of SSTs is only 2°C in the Southern Hemisphere and up to 5°C in the Northern Hemisphere. So a 0.6°C increase is like moving the seasons by 1–3 weeks toward summer. The resulting weather is familiar but it occurs at a somewhat different time of year. In 2012 we had June temperatures in March in the U.S.! This means that we may be missing the core winter and in summer we venture into unknown territory.

This commentary is intended to provide food for thought and encourage readers to think seriously about how to better communicate these issues of changing climate and changing risk of extremes with climate change.

The above commentary is the text of a banquet speech Kevin Trenberth delivered at the NOAA 37th Climate Diagnostics and Prediction Workshop in Fort Collins, 22–25 October 2012.

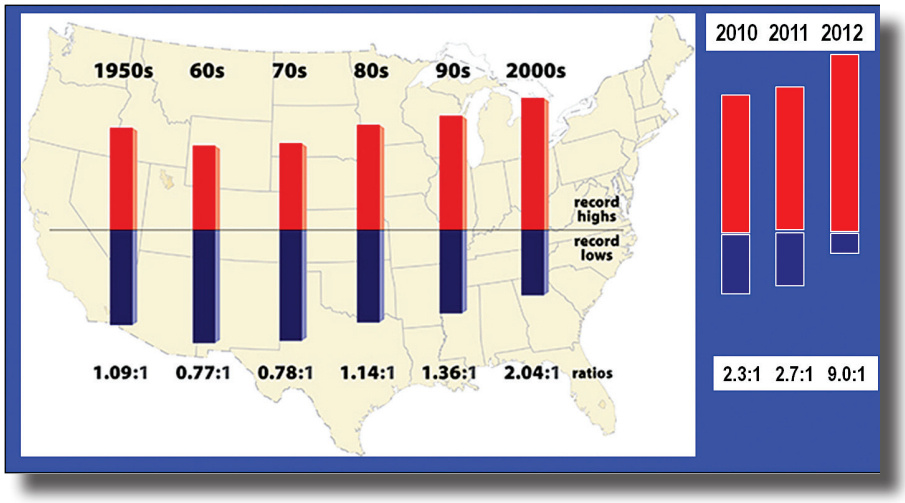

The ratio of record daily highs (red) to record daily lows (blue) at about 1,800 weather stations in the 48 contiguous United States from January 1950 to September 2009 (Meehl et al., GRL, 2009). Updated at right using NOAA data through June 2012; from climatecommunication.org.

NWS Science and Technology Infusion Climate Bulletin

Featured Special Collections

(http://www.nws.noaa.gov/ost/climate/STIP/Collections.htm)

Climate Prediction Science and Technology Digest

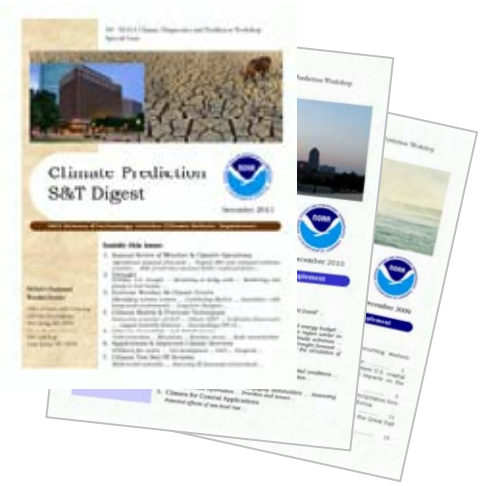

1. 36th Annual Climate Diagnostics and Prediction Workshop Digest
2. 35th Annual Climate Diagnostics and Prediction Workshop Digest
3. 34th Annual Climate Diagnostics and Prediction Workshop Digest
4. 33rd Annual Climate Diagnostics and Prediction Workshop Extended Summaries

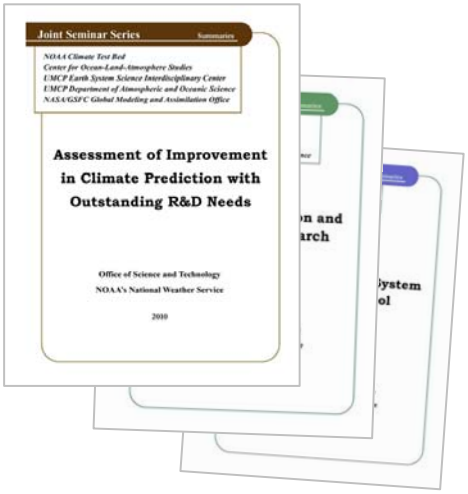

NOAA Climate Test Bed Joint Seminar Series Extended Summaries Collection Volume

1. Unified Modeling, Seamless Prediction and Integrated Services (2010-2011)
2. Assessment of Improvement in Climate Prediction with Outstanding R&D Needs (2009-2010)
3. Research to Operation and Operation to Research (2008-2009)
4. CFS as a Prediction System and Research Tool (2007-2008)

S&T Infusion Lecture Series & Notes

1. Notes About CPC's Seasonal Prediction
2. Uncertainty and Ensemble Forecast